Topological states in aperiodic, non-Hermitian and electronically correlated systems

Topologische toestanden in aperiodische, niet-Hermitische en elektronisch gecorreleerd systemen
(met een samenvatting in het Nederlands)

Etats topologique dans les systèmes apériodique, non-Hermitien et electroniquement corrélés
(avec un resumé en français)

Proefschrift

ter verkrijging van de graad van doctor aan de Universiteit Utrecht
op gezag van de
rector magnificus, prof. dr. Henk Kummeling,
ingevolge het besluit van het College voor Promoties
in het openbaar te verdedigen op

dinsdag 10 december 2024 des middags te 4.15 uur

door

Anouar Moustaj

geboren op 05 maart 1993
te Marrakesh, Marokko

Promotoren:
Prof. dr. C. de Morais Smith
Prof. dr. M.I. Katsnelson

Beoordelingscommissie:
Prof. dr. E.J. Bergholtz
Prof. dr. R.A. Duine
Prof. dr. A. Jagannathan
Prof. dr. M.J. Verstraete
Prof. dr. J. van Wezel

Dit proefschrift werd mede mogelijk gemaakt met financiële steun van de Nederlandse Organisatie voor Wetenschappelijk Onderzoek (NWO) onder het TOPCORE-project met projectnummer OCENW.GROOT.2019.048.

Contents

List of publications **v**

Introduction **vii**

1 Preliminaries **1**
1.1 Symmetry protected topological phases 2
1.1.1 Symmetries 2
1.1.2 Classification 6
1.2 Bulk-Boundary Correspondence 8
1.2.1 Example 1: SSH model 9
1.2.2 Example 2: The Haldane model 11
1.2.3 The role of interactions 14
1.2.4 Applications beyond noninteracting electrons 16
1.3 Non-Hermitian Systems 17
1.3.1 Modification of the topological classification 18
1.3.2 Example: Hatano-Nelson model 21
1.3.3 Example: NH SSH model 23
1.4 Aperiodic Systems 27
1.4.1 Symbolic dynamics 28
1.4.2 Example Hamiltonian: Fibonacci sequence 29
1.4.3 Classification of aperiodic systems 30
1.4.4 Topology in a quasiperiodic chain 31

I Topological Phases **35**

2 Emergent non-Hermitian models **37**
2.1 Introduction 38
2.2 Isospectral Reduction 39
2.3 Emergent Hatano-Nelson model 41
2.4 Emergent non-Hermitian SSH Model 44
2.4.1 Onset of the NHSE 44
2.4.2 Topological Edge Modes 46
2.5 Generalized construction principles 48
2.5.1 Emergent Hatano-Nelson models 48
2.5.2 Emergent NH SSH model 51

2.6 Conclusion . . . 53
2.A Detailed calculations for the NHSE and topology . . . 53
2.A.1 Constraints on the NHSE . . . 53
2.A.2 Determining the topological transition energies of the four-band model . . . 54
2.A.3 The 10-band model . . . 55
2.A.4 Quantization of the winding number . . . 55
2.B Topological Phase Transitions in the Emergent NH SSH Model . . . 57
2.C Additional information for construction principles . . . 58

3 Non-Hermitian Field Theory 61
3.1 Introduction . . . 62
3.2 Topological Field Theory of Two-Band Models . . . 63
3.3 Effect of Disorder . . . 65
3.4 NH SSH model . . . 66
3.5 NH s-wave Superconducting Chain . . . 69
3.6 Comparison to Numerical Calculations of Disorder in the discrete case 71
3.7 Conclusions . . . 73
3.A Energy vorticity in the continuum limit . . . 74
3.B Derivation of the disorder averaged Green's function . . . 74
3.C Calculations for the non-Hermitian SSH model . . . 76

4 Topological phases of the interacting SSH model: an analytical study 79
4.1 Lattice SSH model . . . 82
4.1.1 Symmetries and Topology . . . 83
4.1.2 Interactions and the continuum limit . . . 84
4.1.3 Generalization: extended SSH model . . . 85
4.2 Polarization as a response to an external field: non-interacting case . 86
4.2.1 Lattice Model . . . 86
4.2.2 Continuum polarization of the SSH model . . . 89
4.3 Effects of Interactions . . . 90
4.3.1 Expectations from scaling properties . . . 90
4.3.2 Polarization for the Thirring model . . . 92
4.3.3 Perturbation theory . . . 96
4.4 Conclusion . . . 100
4.A Quantization of the winding number . . . 101
4.A.1 Lattice model . . . 101
4.A.2 Continuum model . . . 102
4.B Thirring and sine-Gordon models . . . 102
4.C Derivation of the scaling behavior of Green's function in momentum space . . . 105
4.D Scaling dimension in quantum field theory . . . 106

II Aperiodic Systems **109**

5 Impurities in Quasicrystals **111**
5.1 Introduction . . . 112
5.2 The Model . . . 113
5.2.1 Fibonacci Tight-Binding Model . . . 113
5.2.2 Renormalization of the Chains . . . 117
5.3 The Tribonacci chain . . . 120
5.3.1 The Tribonacci Hamiltonian . . . 121
5.3.2 The Rauzy fractal . . . 122
5.3.3 Multifractal properties . . . 123
5.4 Introducing Disorder in the Fibonacci chain . . . 125
5.4.1 Organizing Disorder: Renormalization Path . . . 125
5.4.2 Localization Properties . . . 131
5.5 Conclusion . . . 135
5.A Finite-size Scaling of IPR and Size Dependence of Overlap Integrals 136
5.B Perturbative calculation of the IPR . . . 137

6 Spectral Properties of Coupled Fibonacci Chains **141**
6.1 Introduction . . . 142
6.2 A single Fibonacci chain . . . 142
6.3 Methods . . . 145
6.3.1 Numerical methods . . . 145
6.3.2 Analytical methods . . . 145
6.4 Uniform coupling . . . 147
6.5 Non-uniform coupling . . . 149
6.5.1 Coupling only A or only B-sites . . . 150
6.5.2 Defect-coupling . . . 150
6.6 Quasiperiodic coupling . . . 152
6.6.1 Decimation Procedure. . . . 153
6.6.2 Effective Couplings and Energy Corrections . . . 154
6.7 Coupling through intermediate sites . . . 158
6.8 Conclusions . . . 160
6.A Determination of effective hopping amplitudes and energy corrections of the quasiperiodic coupling case . . . 161
6.A.1 v_A cluster . . . 161
6.A.2 v_B cluster . . . 163
6.A.3 Table of energy corrections . . . 164

7 Topology in Aperiodic Systems **165**
7.1 Introduction . . . 166
7.2 Signatures of nontrivial states . . . 167
7.3 Aperiodic Systems . . . 169
7.4 Topological Charge Pumping of Aperiodic Systems . . . 170
7.4.1 Charge transport as a polarization current . . . 171
7.4.2 Bott-Index formulation of quantized charge pumping . . . 172
7.4.3 Aperiodic systems . . . 174

7.5 Topological Signatures in Aperiodic Systems 176
7.5.1 Inversion-symmetric aperiodic chains 177
7.5.2 Polarization 178
7.5.3 Entanglement Spectrum 181
7.6 Conclusion 182
7.A Berry phase and edge state level crossing 183
7.B Entanglement Spectrum of Quadratic Hamiltonians 184

Conclusions and outlook **187**

Layman Summary **191**

Samenvatting **199**

Resumé **207**

Acknowledgement **215**

Curriculum Vitae **217**

List of publications

The author of the thesis acknowledges the financial support through the project TOPCORE with the number OCENW.GROOT.2019.048 of the research program OC ENW-GROOT, which is financed by the Dutch Research Council (NWO).

Publications which are part of this thesis

Note: names in bold are (shared) first authors.

Chapter 2 is based on

- [1] **L. Eek**, **A. Moustaj**, M. Röntgen, V. Pagneux, V. Achilleos, and C. Morais Smith. Emergent non-Hermitian models. Phys. Rev. B, **109** 045122 (2024).
  AM, LE, and MR conceptualized the project and wrote the manuscript. AM and LE performed calculations equally and obtained most of the results. MR provided all the graphs that resulted in the correct isospectral reduction. VP, VA, and CMS supervised the project and provided feedback on the manuscript.

Chapter 3 is based on

- [2] **A. Moustaj**, **L. Eek**, and C. Morais Smith. Field theoretical study of disorder in non-Hermitian topological models, Physical Review B, **105** L180503 (2022).
  AM, LE, and CMS conceptualized the project. AM and LE performed the calculations equally and obtained all the results. AM and LE wrote the manuscript. CMS supervised and provided feedback on the manuscript.

Chapter 4 is based on

- [3] **E. Di Salvo**, **A. Moustaj**, **C. Xu**, L. Fritz, A. K. Mitchell, C. Morais Smith, and D. Schuricht. Topological phases of the interacting SSH model, arXiv 2408.01421 (2024).
  ES, AM and CX conceptualized the project, performed calculations, and wrote the manuscript. LF, AKM, CMS, and DS supervised the project and provided feedback on the manuscript.

Chapter 5 is based on the following publications:

- [4] **A. Moustaj**, S. Kempkes, and C. Morais Smith, Effects of disorder in the Fibonacci quasicrystal, Phys. Rev. B **104** 144201 (2021).
  AM, SK, and CMS conceptualized the project. AM performed calculations and wrote the manuscript. SK and CMS supervised the project and gave feedback on the manuscript.

- [5] **J. P. J. Krebbekx**, A. Moustaj, K. Dajani, and C. Morais Smith, Multifractal properties of Tribonacci chains, Phys. Rev. B **108** 104204 (2023).
  JPJK, AM, KD, and CMS conceptualized the project. JPJK performed all the calculations and wrote the manuscript. AM, KD, and CMS supervised the project and provided feedback on the manuscript.

Chapter 6 is based on

- [6] **A. Moustaj**, **M. Röntgen**, C. V. Morfonios, P. Schmelcher, and C. Morais Smith, Spectral properties of two coupled Fibonacci chains, New J. Phys. **25**, 093019 (2023).
  AM, MR, and CVM conceptualized the project. AM and RM performed the calculations and wrote the manuscript. PS and CMS supervised the project and provided feedback on the manuscript.

Chapter 7 is based on

- [7] **A. Moustaj**, J. P. J. Krebbekx, and C. Morais Smith, Anomalous polarization in one-dimensional aperiodic insulators, arXiv 2404.14916 (2024).
  AM conceptualized the project. AM performed all the calculations and wrote the manuscript. JPJK performed the initial analysis on charge pumping during his master thesis. JPJK and CMS provided feedback on the manuscript.

Publications which are not part of this thesis

- [8] **L. Eek**, M. Röntgen, A. Moustaj, and C. Morais Smith, Higher-order topology protected by latent crystalline symmetries, arXiv 2405.02704 (2024).
  LE and AM conceptualized the project. ME provided insights and graphs to perform calculations on. LE performed all the calculations and wrote the manuscript. AM, MR, and CMS supervised the project and provided feedback on the manuscript.

- [9] **Z. Osseweijer**, L. Eek, A. Moustaj, M. Fremling, and C. Morais Smith, Haldane model on a Sierpinski gasket, arXiv 2407.20075 (2024) (accepted for publication in Phys. Rev. B).
  LE, AM, and CMS conceptualized the project. ZO performed all the calculations and wrote the manuscript. LE, AM, MF, and CMS supervised the project and provided feedback on the manuscript.

- [10] **A. Moustaj**, **L. Eek**, M. Rontgen, and C. Morais Smith, Latent Haldane models, (arXiv 2411.08202) (2024).
  AM and LE conceptualized the project and performed calculations. AM and MR wrote the manuscript. CMS supervised the project.

- [11] **L. Eek**, **A. Moustaj**, and C. Morais Smith, Nearest-neighbour hopping Chern insulators, (in preparation) (2024).
  AM and LE conceptualized the project. AM and LE performed calculations and wrote the manuscript. CMS supervised the project and provided feedback on the manuscript.

- [12] **M. Stålhammar**, **A. Moustaj**, and C. Morais Smith, Properties of fractal exceptional nodal band band structures in two and three dimensions, (in preparation) (2024).
  MS, AM, and CMS conceptualized the project. AM and MS performed calculations and wrote the manuscript. CMS supervised the project and provided feedback on the manuscript.

Introduction

" *The language of science is a language under stress. Words are being made to describe things that seem indescribable in words — equations, chemical structures, and so forth. Words do not, cannot mean all they stand for, yet they are all we have to describe experience. By being a natural language under tension, the language of science is inherently poetic*", Roald Hoffmann – Nobel Prize of Chemistry.

Symmetries and dimensionality are crucial in describing many phases of matter. For a long time, Laudau's paradigm of spontaneous symmetry breaking of local order parameters prevailed in this regard. While this approach is powerful and applicable to many phases of matter, it fails to capture numerous classical and quantum phase transitions. For instance, the Kosterlitz-Thouless phase transition (classical) [13] and transitions between quantum Hall plateaus (quantum) [14] require new mechanisms to describe them. This is because they involve global properties described by topological quantities rather than local geometric ones.

The focus of this thesis is on a subset of phases of matter known as symmetry-protected topological phases [15, 16]. Specifically, we explore the concept of topological insulators and their applications beyond traditional electronic band theory [17]. The defining characteristic of these systems is the bulk-boundary correspondence. For instance, a topological insulator is insulating in the bulk but conducting at the edges. More broadly, bulk properties, described by topological invariants, can predict the behavior of the system's boundaries. These observable features remain robust and are protected by the underlying symmetries, maintaining their integrity even when the system undergoes various perturbations, provided the topological invariants remain unchanged.

The theoretical understanding of the field culminated when it was realized that the Altland-Zirnbauer classification of random matrix theory could be applied to topological insulators and superconductors [18]. This classification relied on the realization of three discrete symmetries — time-reversal, particle-hole, and chiral symmetries — alongside the system's dimensionality.

Soon after, the first natural extension of this classification emerged with the discovery that crystalline symmetries could also give rise to phases not predicted by the original classification. This concept was further refined, allowing for a novel bulk-boundary correspondence: topological properties in D-dimensions predict the behavior of the $(D-n)$-dimensional boundaries, where $2 \leq n \leq D$. This new type of

system is called a higher-order topological insulator [19]. Additionally, obstructed atomic limits were also discovered as a weaker version of topological phases, characterized by fractionalized corner charges predicted from bulk topological properties of insulators [20, 21].

Topological phases have also been extended to aperiodic systems, demonstrating unique properties not found in periodic crystals [22–24]. Quasiperiodic systems exhibit discrete spatial symmetries that are otherwise forbidden in regular crystalline materials. This has enabled, for example, the observation of five-fold or eight-fold rotational symmetric insulators with the corresponding corner charges [25]. Moreover, one-dimensional multilevel charge pumping in quasiperiodic chains was also theoretically predicted and experimentally observed [23, 24].

Finally, the subsequent enrichment arose from the understanding that systems described by non-Hermitian Hamiltonians inherently permit a broader spectrum of possibilities and, consequently, a greater number of topological phases [26, 27]. This expansion is not surprising, given the reduced constraints on non-Hermitian Hamiltonians. As a result, the Altland-Zirnbauer classification extends from ten symmetry classes for Hermitian systems to thirty-eight symmetry classes for non-Hermitian systems.

Given these developments over the last two decades, one of the questions we sought to answer is whether other topological phases exist beyond those predicted by current classifications. This motivated our multifaceted approach, exploring aperiodic systems, non-Hermitian systems, and electronic systems with electron-electron interactions. Notable results along this direction include the discovery of a hidden class of topological phases protected by so-called latent symmetries [1] and the realization that aperiodic systems can host a variant of the obstructed-atomic-limit phase [7].

Following the quest to uncover these results, we have developed various methods and studied different properties of topological and aperiodic systems. Those findings are part of this thesis. On the topological front, we developed a field theoretical approach to study the effect of disorder in driving a non-Hermitian topological phase transition [2]. Additionally, we examined the impact of fermionic interactions in a one-dimensional Hermitian topological insulator, employing various analytic tools to derive exact results. Our findings indicate that the topological phase remains unchanged except for charge renormalization and additional non-Fermi liquid contributions [3].

In the case of aperiodic systems, we investigated how impurities affect the quasiperiodic ordering of a Fibonacci chain [4]. We also generalized the construction of the Fibonacci chain to a Tribonacci chain, providing a physical platform for the Rauzy fractal [5]. Lastly, we explored the diverse spectral properties of two coupled Fibonacci chains [6].

We will next provide an outline of the thesis with more details on the research results.

Outline of the thesis

This thesis is split into two parts. The first part covers various subjects on topological phases, while the second is dedicated to aperiodic systems. The structure is as follows.

In Chapter 1, we introduce the various subjects in more detail. Specifically, we explain how topological phases of matter are classified and how they are applied to multiple areas of condensed-matter physics. We then go on with Chapter 2, where we study the application of latent symmetries and isospectral reductions to predict the existence of topological phases in otherwise complicated one-dimensional non-Hermitian systems. Specifically, we investigate how the isospectral reduction of a class of periodic graphs results in energy-dependent Hatano-Nelson and non-Hermitian SSH models. This allows us to predict various non-Hermitian and topological features on these graphs, such as the non-Hermitian skin effect and topological edge modes.

In Chapter 3, we provide tools to analyze generic one-dimensional non-Hermitian two-band models at their topological phase transition. To this end, we develop a field-theoretical description of a continuum model near the gap-closing and derive expressions for the spectral winding number. We study how this winding changes under the influence of disorder by analyzing the behavior of the disorder-averaged Green function and then apply our analysis to two examples: a non-Hermitian SSH model and a non-Hermitian s-wave superconductor.

In Chapter 4, we examine the influence of interactions on the topological phases of a fermionic SSH model. We derive an analytic expression for the polarization of the system, which in the non-interacting case is equal to the winding number topological invariant. We then study how this winding number changes under the influence of interactions by examining the low-energy quantum field theory, specifically the Thirring model. Using non-perturbative methods, we derive the modification of the polarization and conclude that the topological phases remain intact, except for a charge renormalization that contains a term arising from the non-Fermi liquid behavior of the model.

For the second part of the thesis, we begin in Chapter 5 with the study of the Fibonacci quasicrystal. We first introduce the model and its generalization to the Tribonacci chain, followed by a brief demonstration of multifractality in both models. We also show how the Rauzy fractal finds application in the study of wavefunctions of the Tribonacci quasicrystal. We then examine the effect of impurities on the quasiperiodic ordering of the Fibonacci quasicrystal, finding that, depending on the position of the impurity, one can track how disorder sets in using the concept of renormalization paths.

In Chapter 6, we study the spectral properties of a system of coupled Fibonacci chains. By implementing their coupling in various ways, we observe different resulting behaviors, such as the coexistence of extended and critical eigenstates and the formation of flat bands in a quasiperiodic system.

Finally, in Chapter 7, we return to the notion of topology in aperiodic systems. We study how multilevel topological charge pumping occurs in various representatives of aperiodic systems, namely, the Fibonacci quasicrystal, the Tribonacci

quasicrystal, and the Thue Morse chain. During the pumping procedure, we find times when the chain exhibits features typical of obstructed atomic limits, such as degenerate boundary states with half-charges due to the presence of inversion symmetry. We then conclude the thesis with final remarks and an outlook.

Chapter 1

Preliminaries

Commonly used symbols and acronyms

Symbol/Acronym	Meaning
SPT	Symmetry Protected Topological
TI	Topological Insulator
AZ	Altland-Zirnbauer
TRS	Time-Reversal Symmetry
PHS	Particle-Hole Symmetry
CS	Chiral Symmetry
SLS	Sublattice Symmetry
$\mathcal{H}$	Second Quantization Hamiltonian
H	First Quantization Hamiltonian
$H(\mathbf{k})$	Bloch Hamiltonian
BZ	Brillouin Zone
BBC	Bulk-Boundary Correspondence
SSH	Su–Schrieffer–Heeger
PBC	Periodic Boundary Conditions
OBC	Open Boundary Conditions
NH	Non-Hermitian
NHSE	Non-Hermitian Skin Effect
PT	Parity-Time
EP	Exceptional Point

1.1 Symmetry protected topological phases

In the last two decades, considerable effort has been made to characterize and classify exotic quantum phases of matter [15, 28, 29]. Indeed, the discovery of topological phases rendered the universal Landau classification insufficient, prompting the search for another theory. This required a deeper understanding of the types of order present in the systems; orders which can change even though the symmetries of the ground states are preserved. Since these phases are inherently quantum mechanical, entanglement is thought to play a prominent role in the way they manifest. Along this line of thought, and through the advances of quantum information theory [30], many quantifiable tools of entanglement have been constructed and used to probe quantum phase transitions. For example, bipartite entanglement between two parts of a larger system is an instrumental concept. One can obtain it from the spectrum of a reduced-density matrix corresponding to the subsystem of interest. The latter is also often known as the entanglement spectrum and is a good measure of the presence of topological edge states [31–33]. Moreover, the concept of topological order arises when patterns of long-range entanglement exist within a system. Ground states of such systems exhibit long-range entanglement, a characteristic that the notion of topological entanglement entropy can quantify. These are usually strongly correlated states of matter, giving rise to interesting phenomenologies, such as effective matter fields with fractionalized quantum numbers (e.g., anyons), interacting through emergent gauge fields [34–37].

On the other hand, other types of phases exist, which, although not having *true* topological order, are referred to as symmetry-protected topological states (SPT). These phases have ground states that are short-range entangled, with symmetries enforcing topological protection [38]. It has been shown in a seminal paper that all one-dimensional (1D) gapped ground states are short-range entangled [29]. Typical examples include topological insulators (which we will mainly be concerned with) and integer spin-chains in the Haldane phase [39]. A general definition for such phases is that their ground state can be expressed as a product state of local Hilbert spaces, and these product states cannot be smoothly deformed into each other without breaking the "protecting" symmetry. In the absence of symmetry, all product states can be smoothly deformed to the same so-called trivial product state. When symmetries are present, some phases may be topologically nontrivial, examples of which include the Kitaev chain, the SSH chain, or the previously mentioned Haldane phase of integer spin chains [39–41].

1.1.1 Symmetries

Let us restrict the discussion to a particular set of SPTs. We will now consider the symmetries that were considered in the original formulation of the Altland Zirnbauer (AZ), or ten-fold classification [18]. It was originally formulated to describe disordered electron systems in a setup of normal-metal-superconductor interface. It generalized the threefold Wigner-Dyson classification of random matrices by considering time-reversal symmetry (TRS), particle-hole symmetry (PHS), and chiral (or sublattice) symmetry (CS). These are symmetries that are not unitarily realized on the single-particle Hamiltonian, and their combinations correspond exactly to the

ten possibilities of symmetric spaces of Hermitian matrices, the Cartan classes. We shall now briefly describe how these symmetries act at the level of noninteracting Hamiltonians. To this end, we shall write a generic second-quantized Hamiltonian as

$$\mathcal{H} = \sum_{I,J} H_{IJ} \hat{\psi}_I^\dagger \hat{\psi}_J,$$

where $\psi_I^\dagger$ and ψ_I are the creation and annihilation operators for fermions in a state described by a multi-index I, which can describe any internal degree of freedom contained in the single-particle Hilbert space. For simplicity, it is typically assumed that the system is regularized by a lattice, such that I could, for example, represent lattice sites i, spin σ, orbital degrees of freedom n, etc. The single-particle Hamiltonian is then given by

$$H = \sum_{I,J} H_{IJ} \left|I\right\rangle \left\langle J\right|,$$

where $|I\rangle = |i\rangle \otimes |\sigma\rangle \otimes |n\rangle \cdots$ is a single-particle state in the local Hilbert space. Next, we will describe how each of the three symmetries acts on the single-particle Hamiltonian and how each symmetry can be characterized by a specific numerical value.

Time-Reversal. We start with transformations that invert the flow of time, $\hat{T} : t \to -t$. Under this operation, the classical position transforms trivially while the classical momentum operator undergoes inversion. Requiring this to hold for the quantum mechanical operators,

$$\hat{T}\hat{\mathbf{x}}\hat{T}^{-1} = \hat{\mathbf{x}},$$
$$\hat{T}\hat{\mathbf{p}}\hat{T}^{-1} = -\hat{\mathbf{p}},$$

means that in order to preserve the canonical commutation relations $[\hat{x}_i, \hat{p}_j] = i\hbar\delta_{ij}$, the TR operator must be anti-unitary, i.e., it can be written as a complex conjugation operator K followed by a unitary operator U, $\hat{T} = UK$. For the spin operator, the only way for the spin commutation relation to hold under TR,

$$\hat{T}[\hat{S}_i, \hat{S}_j]T^{-1} = T(i\hbar\epsilon_{ijk}S_k)\hat{T}^{-1},$$

is that the action of TR on the spin operator is given by

$$\hat{T}\hat{\mathbf{S}}\hat{T}^{-1} = -\hat{\mathbf{S}}.$$

The spin operators for fermions are typically given by the irreducible representation of the $SU(2)$ group spanned by Pauli matrices, σ_i with $i \in \{1, 2, 3\}$. In this case, the TR operator is represented by anti-unitary 2×2 matrices, where the unitary part of $\hat{T}$ takes the typical form $U = e^{i\phi}\sigma_2$. Applying the TR operator twice results in $\hat{T}^2 = -\mathbb{1}$. This holds in general for any half-integer representation of spin $1/2$ and is, in fact, related to the fundamental antisymmetric nature of fermionic operators in general. For integer spin, the result is $\hat{T}^2 = \mathbb{1}$.

The action of TR on the creation and annihilation operators takes the form

$$\hat{\mathcal{T}}\psi_I\hat{\mathcal{T}}^{-1} = \sum_J \left(U_T^\dagger\right)_{IJ}\psi_J, \quad \hat{\mathcal{T}}\psi_I^\dagger\hat{\mathcal{T}}^{-1} = \sum_J \psi_J^\dagger\left(U_T\right)_{JI}, \quad \hat{\mathcal{T}}i\hat{\mathcal{T}}^{-1} = -i,$$

where U_T is a unitary matrix acting on single-particle states in the local Hilbert space. Here, $\hat{\mathcal{T}}$ is the anti-unitary TR operator acting in Fock space. For TR to be a symmetry, it must commute with the second-quantized Hamiltonian, $\left[\hat{\mathcal{T}}, \mathcal{H}\right] = 0$. This essentially results in the following action on the single-particle Hamiltonian,

$$U_T H^* U_T^\dagger = H$$

Thus, the single-particle TR operator can be identified with three numbers:

$$\begin{aligned}
&\mathcal{T} = 0; \quad \text{no symmetry},\\
&\mathcal{T} = +1; \quad \text{TRS with } \hat{T}^2 = 1,\\
&\mathcal{T} = -1; \quad \text{TRS with } \hat{T}^2 = -1,
\end{aligned}$$

and its action on the single-particle Hamiltonian is given by

$$\hat{T}H\hat{T}^{-1} = H,$$

where $\hat{T} = U_T K$.

Particle-Hole Symmetry. The next anti-unitarily realized symmetry is particle-hole symmetry (PHS), also known as charge conjugation symmetry. It is commonly found in Bogoliubov-de Gennes Hamiltonians of mean-field superconductors. Its action turns creation operators into annihilation operators, and it is unitarily realized on Fock space,

$$\hat{\mathcal{C}}\psi_I\hat{\mathcal{C}}^{-1} = \sum_J \left(U_C^{*\dagger}\right)_{IJ}\psi_J^\dagger, \quad \hat{\mathcal{C}}\psi_I^\dagger\hat{\mathcal{C}}^{-1} = \sum_J \psi_J\left(U_C^*\right)_{JI}, \quad \hat{\mathcal{C}}i\hat{\mathcal{C}}^{-1} = i.$$

Here, ψ_I is typically a Nambu spinor, and I also contains a particle-hole index. Invariance of the second-quantized Hamiltonian results in the following condition on the first-quantized Hamiltonian

$$U_C H^* U_C^\dagger = -H,$$

making the first-quantized charge-conjugation operator an anti-unitary operator, $\hat{C} = U_C K$. Similar to the case of TRS, it is possible for the square of $\hat{C}$ to have a -1 phase. To understand this, note that since U_C is a unitary operator, $\hat{C}^2 = U_C U_C^* = e^{i\gamma}\mathbb{1}$ is also a unitary operator and must be proportional to the identity. By examining the triple product $U_C U_C^* U_C$, it follows that $e^{i\gamma}U_C = e^{-i\gamma}U_C$, leading to $e^{i\gamma} = \pm 1$.

We can, once again, identify the single-particle PH operator with three numbers:

$$\begin{aligned}
&\mathcal{C} = 0; \quad \text{no symmetry},\\
&\mathcal{C} = +1; \quad \text{PHS with } \hat{C}^2 = 1,\\
&\mathcal{C} = -1; \quad \text{PHS with } \hat{C}^2 = -1,
\end{aligned}$$

and its action on the single-particle Hamiltonian is given by

$$\hat{C}H\hat{C}^{-1} = -\hat{C},$$

where $\hat{C} = U_C K$.

Chiral Symmetry. The last of the three fundamental discrete symmetries is chiral symmetry (CS), or, as it is most commonly realized in condensed matter, sublattice symmetry (SLS). It can be viewed as a combination of both TRS and PHS,

$$\hat{\mathcal{S}} \equiv \hat{\mathcal{T}} \circ \hat{\mathcal{C}}.$$

This kind of symmetry arises, for example, when considering a lattice composed of two distinct groups of cells forming their own sublattices, such that couplings only occur between sublattices and not within a sublattice. In this scenario, the local Hilbert space V_H can be decomposed into a direct sum of the two sublattice blocks, $V_H \sim A \bigoplus B$. The single-particle Hamiltonian then only has components in the off-diagonal blocks, which encode the coupling information between the two sublattices.

Its action will once again turn creation operators into annihilation operators, but this time, it is also anti-unitarily realized on Fock space,

$$\hat{\mathcal{S}}\psi_I\hat{\mathcal{S}}^{-1} = \sum_J \left(U_S^{*\dagger}\right)_{IJ}\psi_J^\dagger, \quad \hat{\mathcal{S}}\psi_I^\dagger\hat{\mathcal{S}}^{-1} = \sum_J \psi_J\left(U_S^*\right)_{JI}, \quad \hat{\mathcal{S}}i\hat{\mathcal{S}}^{-1} = -i,$$

where $U_S = U_T U_C^*$. Requiring invariance of the second-quantized Hamiltonian yields directly the following condition on the first-quantized Hamiltonian

$$\hat{S}H\hat{S}^{-1} = -H.$$

Contrary to the other two cases, the operator $\hat{S} = U_S$ is unitary, and therefore, there are only two possible numbers that can characterize it,

$$\mathcal{S} = 0; \quad \text{no symmetry},$$
$$\mathcal{S} = +1; \quad \text{PHS with } \hat{S}^2 = 1.$$

Table 1.1 summarizes the results discussed in this subsection.

Table 1.1: Summary of the discussion on symmetries, with the number $\mathcal{N}$ that characterizes them, the realizations in first- and second-quantization, and the action on the first-quantized Hamiltonian H.

Symmetry	$\mathcal{N}$	First-quantization	Second-quantization	Action on H
TRS	$0, \pm 1$	Anti-unitary	Anti-unitary	$\hat{T}H\hat{T}^{-1} = H$
PHS	$0, \pm 1$	Anti-unitary	Unitary	$\hat{C}H\hat{C}^{-1} = -H$
CS	$0, +1$	Unitary	Anti-unitary	$\hat{S}H\hat{S}^{-1} = -H$

1.1.2 Classification

The theoretical framework for the classification of single-particle Hamiltonians is based on the anti-unitary symmetries from the previous section. The most general statement that can be made concerning SPT states of matter is that they are ground states of a many-body system that are adiabatically distinct from a trivial product of single-particle states. For systems with translational invariance, the classification is neatly achieved by using K-theory. It has been shown that the generalized homotopy group of a Bloch Hamiltonian taking values in the d-dimensional Brillouin zone (BZ) T^d and belonging to a certain classifying space R_q can be written as [42]

$$\pi(T^d, R_q) = \pi_0(R_{q-d}) \bigoplus \left[\bigoplus_{s=0}^{d-1} \binom{d}{s} \pi_0(R_{d-s}) \right].$$

The classifying spaces R_q are the sets of real symmetric matrices under the constraint of anti-unitary symmetries, and with eigenvalues ± 1. They are labeled by the integer $q \mod 8$ and correspond to the eight real Cartan classes. A similar equation can be posed for the complex classifying spaces C_q, corresponding to the set of Hermitian matrices labeled by the integer $q \mod 2$, and associated with the two complex Cartan classes [see Table 1.2]. The first part of this equation, $\pi_0(R_{q-d})$, appears in the ten-fold classification [see Table 1.3] and is independent of translation symmetry. It is the homotopy classes of maps from two points to the space R_{q-d}, classifying it into inequivalent path-connected components. The second part is attributed to translation symmetry, which in 3D allows for the existence of weak topological insulators (TIs). These can be understood as periodic stacks of 2D strong TIs [43].

Table 1.2: Identification of the Bloch Hamiltonian's coset spaces with the appropriate Cartan class and the corresponding symmetries. Table based on Ref. [44].

Cartan label	$\mathcal{T}$	$\mathcal{C}$	$\mathcal{S}$	Coset space	Label
Complex case:					
A	0	0	0	$U(M+N)/U(M) \times U(N)$	C_0
AIII	0	0	1	$U(N) \times U(N)/U(N)$	C_1
Real case:					
AI	1	0	0	$O(M+N)/O(M) \times O(N)$	R_0
BDI	1	1	1	$O(N) \times O(N)/O(N)$	R_1
D	0	1	0	$O(2N)/U(N)$	R_2
DIII	-1	1	1	$U(2N)/\mathrm{Sp}(2N)$	R_3
AII	-1	0	0	$\mathrm{Sp}(M+N)/\mathrm{Sp}(M) \times \mathrm{Sp}(N)$	R_4
CII	-1	-1	0	$\mathrm{Sp}(N) \times \mathrm{Sp}(N)/\mathrm{Sp}(N)$	R_5
C	0	-1	0	$\mathrm{Sp}(2N)/U(N)$	R_6
CI	1	-1	1	$U(N)/O(N)$	R_7

These classes arise when one tries to identify a unique feature of the Bloch Hamiltonian $H(\mathbf{k})$, which has an occupied subspace that is well separated from the rest of the energy bands. In order to do this, one resorts to the procedure of spectral flattening, whereby $H(\mathbf{k})$ is adiabatically flattened to $\mathcal{H}(\mathbf{k})$, which now only contains two eigenspaces with eigenvalues $E = -1$ (occupied subspace of dimension M) and $E = 1$ (empty subspace of dimension N). The deformed Hamiltonian can be written as

$$H(\mathbf{k}) = \mathcal{U}(\mathbf{k}) Q \, \mathcal{U}^\dagger(\mathbf{k}),$$

where $Q = \mathbb{1}_N \oplus (-\mathbb{1}_M)$. All information is thus encoded in the matrices $\mathcal{U}(k)$. For example, when no symmetry is imposed (class A), we have $\mathcal{U}(k) \in U(M+N)$. In order to have inequivalent descriptions of $\mathcal{H}(\mathbf{k})$, we must ignore any block diagonal matrices

$$\mathcal{U}(\mathbf{k}) = \begin{pmatrix} u_1(\mathbf{k}) \in U(N) & 0 \\ 0 & u_2(\mathbf{k}) \in U(M) \end{pmatrix},$$

as they cannot change $H(\mathbf{k})$ from Q. Thus, we are interested in classifying matrices in the coset space $\mathcal{U}(\mathbf{k}) \in U(M+N)/U(M) \times U(N)$. These coset spaces take different shapes when one further imposes the three anti-unitary symmetries from Section 1.1.1. By evaluating the homotopy class $\pi_0(X)$, where X is a placeholder for the classifying spaces, one obtains a topological invariant distinguishing the possible different ground states that can arise given a certain symmetry class and dimension. Whenever they are labeled by $\mathbb{Z}$ or $2\mathbb{Z}$, there is a countable infinity of such ground states, while if they are labeled with $\mathbb{Z}_2$, only two topologically

Table 1.3: The classification table using $\pi_0(X)$, where X is a placeholder for any classifying space C_q or R_q . The first column contains the Cartan labels, while the rest of the columns denote the spatial dimension of the bulk Hamiltonian. Each entry corresponds to the associated homotopy class $\pi_0(C_{q-d})$ for the complex case, or $\pi_0(R_{q-d})$ for the real case. Notice the *Bott periodicity* [45] of period 8 for real spaces and 2 for complex spaces. Table based on Ref. [44].

Cartan label / d	0	1	2	3	4	5	6	7
Complex case								
A	$\mathbb{Z}$	0	$\mathbb{Z}$	0	$\mathbb{Z}$	0	$\mathbb{Z}$	0
AII	0	$\mathbb{Z}$	0	$\mathbb{Z}$	0	$\mathbb{Z}$	0	$\mathbb{Z}$
Real case								
AI	$\mathbb{Z}$	0	0	0	$2\mathbb{Z}$	0	$\mathbb{Z}_2$	$\mathbb{Z}_2$
BDI	$\mathbb{Z}_2$	$\mathbb{Z}$	0	0	0	$2\mathbb{Z}$	$\mathbb{Z}_2$	$\mathbb{Z}_2$
D	$\mathbb{Z}_2$	$\mathbb{Z}_2$	$\mathbb{Z}$	0	0	0	$2\mathbb{Z}$	$\mathbb{Z}_2$
DIII	0	$\mathbb{Z}_2$	$\mathbb{Z}_2$	$\mathbb{Z}$	0	0	0	$2\mathbb{Z}$
AII	$2\mathbb{Z}$	0	$\mathbb{Z}_2$	$\mathbb{Z}_2$	$\mathbb{Z}$	0	0	0
CII	0	$2\mathbb{Z}$	0	$\mathbb{Z}_2$	$\mathbb{Z}_2$	$\mathbb{Z}$	0	0
C	0	0	$2\mathbb{Z}$	0	$\mathbb{Z}_2$	$\mathbb{Z}_2$	$\mathbb{Z}$	0
CII	0	0	0	$2\mathbb{Z}$	0	$\mathbb{Z}_2$	$\mathbb{Z}_2$	$\mathbb{Z}$

distinct ground states exist [see Table 1.3]. For a further in-depth study of the classification, we refer the reader to the reviews from Refs. [16, 44].

1.2 Bulk-Boundary Correspondence

An interesting feature of SPT's is the bulk-boundary correspondence (BBC). That is, the topological properties of the bulk can be used to determine unusual features observed at the boundary of such systems. For example, the BBC for 2D TRS broken insulators states that whenever the bulk Hall resistivity of the system is quantized (and equal to a topological invariant), there exists gap traversing states, which are located on the boundary of the system [46]. This makes the system a conductor at the boundary, while it is insulating in the bulk. On the other hand, a 2D TI respecting TRS will exhibit the quantum spin Hall effect, where the boundary states carry spin currents instead of charge currents. This type of behavior does not only exist in 2D but also in 3D and in 1D, albeit when subjected to different symmetry constraints [20]. In 3D, for example, a strong TI is one that respects TRS and has conducting surface states, which are very robust due to spin-momentum locking and cannot be destroyed by the presence of disorder or any symmetry-respecting perturbation [43, 47]. It also features a rich variety of additional effects, such as quantized magnetoelectric polarizability, providing a realization of axion electrodynamics in a condensed matter setting [48, 49]. In 1D, systems possessing inversion symmetry may feature a quantized polarization density. This fact can be attributed to two significant results: the formulation of the polarization as a Berry phase [50], and the fact that the Berry phase is quantized to $\phi = 0, \pi$ for inversion symmetric systems [51]. In this case, it is possibile to have anomalous polarization corresponding to fractionalized charges on the two boundaries of the system. The overarching theme in all of these situations is that one can compute bulk quantities of these systems and relate them to a corresponding boundary observable. Additionally, they are called topological insulators because these bulk quantities are often expressed as topological invariants [16, 44]. For example, if an inversion-symmetric 1D system also possesses SLS, then it is possible to define a winding number ν, which is directly proportional to the quantized Berry phase, $\phi = \pi\nu$. Another example would be a TRS broken 2D system, in which the Hall conductivity is quantized and given by a Chern number [52]. This is the reason why properties related to these topological invariants are very robust, as long as one respects the symmetries of the system.

Continuum Dirac Hamiltonians and index theorems. Near a gap closing, topological insulators (TIs) can be described using a continuum approximation. Due to the linear dispersion relations of TIs, the real-space Hamiltonian results in a massive relativistic Dirac equation [53]. The key distinction between a trivial and a topological phase typically lies in the sign of the mass of the Dirac fermion. This insight enables an understanding of the topological boundary modes in terms of index theorems of elliptic differential operators, which include the Dirac operator.

The easiest example is provided by the Jackiw-Rebbi problem, a 1D Dirac

equation with a spatially varying mass term that changes sign at the origin,

$$H = i\hbar v_F \sigma_x \partial_x + m(x) v_F^2 \sigma_z, \tag{1.1}$$

where v_F is the Fermi velocity and

$$m(x) = \begin{cases} +|m|, & \text{if } x > 0, \\ -|m|, & \text{if } x < 0. \end{cases}$$

The zero-energy state is given by

$$\Psi(x) = \sqrt{\frac{v_F|m|}{2\hbar}} \begin{pmatrix} i \\ 1 \end{pmatrix} e^{-m(x)xv_F/\hbar}.$$

It is bound to the interface between the two regions at $x = 0$, representing the interface between the trivial and topological insulator. Moreover, the analytical index of the Dirac differential operator is found to count the number of boundary modes. This provides a physical intuition for the Atiyah-Singer index theorem [54] and formalizes the BBC.

We will now describe two examples in more detail to familiarize ourselves with the quantitative tools required to perform these analyses.

1.2.1 Example 1: SSH model

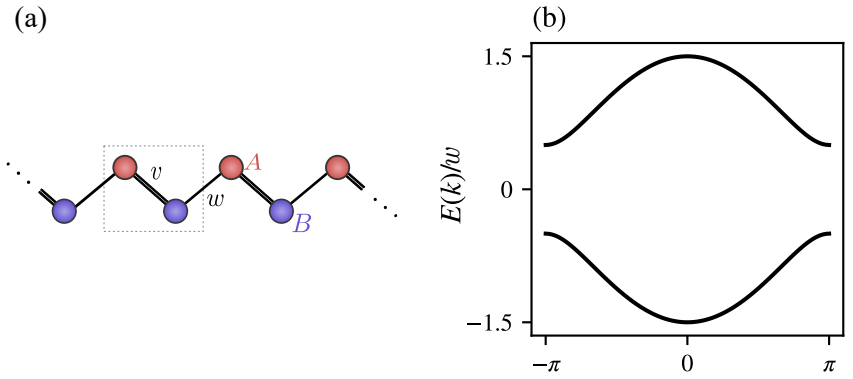

Figure 1.1: (a) The SSH chain, with sublattice A (top) and B (bottom) colored in red and blue, respectively. A choice of unit cell is shown by the dotted box. The intracell hopping is v, and the intercell hopping is w. (b) Dispersion relation for parameter choice $v = 0.5w$.

The Su–Schrieffer–Heeger (SSH) model was originally conceived to describe the behavior of electrons and the emergence of solitonic defects in a polyacetylene molecule [41]. It is a nearest-neighbor tight-binding model for spinless electrons hopping on a chain with two alternating bonds [see Fig. 1.1(a)]. The Hamiltonian

of the SSH model is

$$\begin{aligned}\mathcal{H} &= v\sum_{j=1}^{N} c_{A,j}^{\dagger}c_{B,j} + w\sum_{j=1}^{N} c_{B,j}^{\dagger}c_{A,j+1} + \text{h.c.},\\ &= \int_{-\pi/a}^{\pi/a} \frac{\mathrm{d}k}{2\pi} \begin{pmatrix} c_{A,k}^{\dagger}, & c_{B,k}^{\dagger}\end{pmatrix} H(k) \begin{pmatrix} c_{A,k} \\ c_{B,k}\end{pmatrix}.\end{aligned} \tag{1.2}$$

where v and w are intracell and intercell hopping, respectively, and $c_{X,j}$ ($c_{X,j}^{\dagger}$) is the annihilation (creation) operator for an electron at site X in the unit cell j. The sum in the first line runs over cell indices, A, B refer to the two sites inside a unit cell of length a, and we imposed periodic boundary conditions (PBC) at the ends of the chain. In the second line, the momentum space formulation is given, where we have taken the limit $N \to \infty$. Unless otherwise stated, we set $\hbar = a = 1$ for simplicity. The single-particle Bloch Hamiltonian

$$H(k) = d_x(k)\sigma_x + d_y(k)\sigma_y, \tag{1.3}$$

where $d_x(k) = v + w\cos k$, $d_y(k) = -w\sin k$ and σ_i's are Pauli matrices. The two energy bands [see Fig. 1.1(b)] are given by

$$\begin{aligned}E_{\pm} &= \pm\sqrt{d_x^2 + d_y^2},\\ &= \pm\sqrt{v^2 + w^2 + 2vw\cos k}.\end{aligned}$$

We see that it is possible for the bands to close the gap when $v = \pm w$, at $k = 0$ ($v = -w$) and $k = \pi$ ($v = w$). These gap closings correspond to a topological phase transition.

Symmetry, topology, and BBC. The model possesses two symmetries: SLS, acting on the momentum-space Hamiltonian as

$$\sigma_z H(k)\sigma_z = -H(k),$$

and inversion symmetry, acting as

$$\sigma_x H(k)\sigma_x = H(-k).$$

The former allows for the definition of a winding number invariant [16], while the latter forces the quantization of this winding number to just two values [51]. For a chiral symmetric gapped Hamiltonian, the winding number is defined as [16]

$$\nu = \int_{-\pi}^{\pi} \frac{\mathrm{d}k}{4\pi i} \operatorname{tr}\left[\sigma_z H^{-1}(k)\partial_k H(k)\right] \tag{1.4}$$

which is equivalent to the topological statement that these phases are classified by the first homotopy group of the circle $\pi_1(S^1) = \mathbb{Z}$. For the SSH chain, this invariant yields

$$\nu = \begin{cases} 0, & \text{if } |v| > |w|,\\ 1, & \text{if } |v| < |w|.\end{cases} \tag{1.5}$$

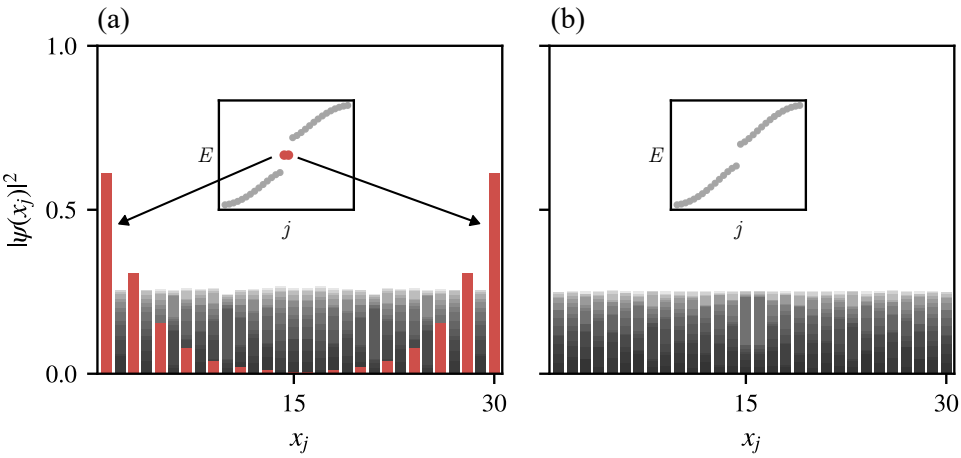

Figure 1.2: Probability density of eigenstates as a function of position along the chain, in the (a) topological phase and (b) trivial phase. The OBC spectrum is shown in the insets, where bulk modes are shown in gray and zero-energy edge modes in red.

We can relate the winding number to the Berry phase of the system at half-filling, which is given by

$$\phi = \int_{-\pi}^{\pi} \mathrm{d}k \, \langle u_-(k)| \, i\partial_k \, |u_-(k)\rangle \, ,$$

where $|u_-(k)\rangle$ is the lower band's Bloch state. It is quantized by virtue of inversion symmetry to $\phi = 0, \pi$, with the same condition as for the winding number in Eq. (1.5).

According to the modern theory of polarization [50], the Berry phase is closely related to the position of Wannier centers inside unit cells and, as such, indicates the presence/absence of a "topological" polarization given by

$$P = \frac{e\phi}{2\pi} \mod e = \begin{cases} 0, & \text{if } \nu = 0, \\ \dfrac{e}{2}, & \text{if } \nu = 1. \end{cases} \tag{1.6}$$

The mod e always appears in the definition of absolute polarization. It accounts for the 2π ambiguity of the Berry phase and for the ambiguity in the choice of a unit cell [50]. This polarization manifests itself in the form of a BBC: if the system has open boundaries, there will be half-quantized charges sitting at the boundary of the system when the system is at half-filling. This is because one electron will occupy two degenerate edge states in the open boundary condition (OBC) system [see Fig. 1.2]. This is the simplest example of a concept known as a filling anomaly in topological crystalline insulators [55].

1.2.2 Example 2: The Haldane model

The second example we will consider is the Haldane model, which realizes the anomalous quantum Hall effect on a hexagonal lattice [56]. It has been dubbed as

the "hydrogen atom" of TIs [57]. It is relatively straightforward and enables a fully analytic understanding of most of its properties, offering significant insights into the key features of more complex and realistic models of TIs.

In 1988, Haldane understood that an external magnetic field is not necessary to realize the anomalous quantum Hall effect. The essential requirement is simply to break TRS. He considered a 2D hexagonal lattice in which the total flux per unit cell is zero. One can incorporate this effect into a tight-binding model by including next-nearest neighbor complex hoppings, for which the phase is determined by the directionality (i.e., clockwise or not) of the path between the sites.

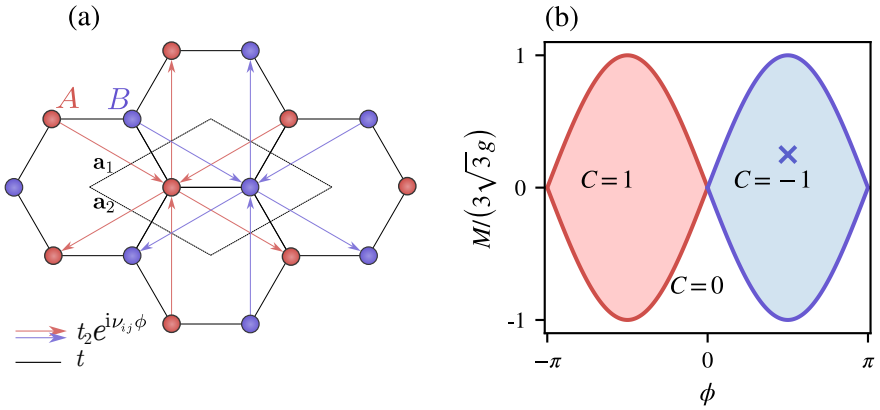

Figure 1.3: (a) Sketch of the Haldane model. The arrows indicate the direction of the phase convention used. (b) Phase diagram of the Haldane model. The Chern number is indicated, and a cross marks the parameters selected for the example shown in Fig. 1.4.

In graphene, this model corresponds to carbon atoms sitting on the vertices of a honeycomb lattice, with valence electrons hybridizing their electronic wavefunctions and for which the strongest overlap on the plane is formed by σ orbitals. The anomalous Hall effect is then artificially implemented by adding a term that breaks TRS. Additionally, an inversion symmetry-breaking term, known as the Semenoff mass, is included to account for a different on-site potential at each type of atomic site. The system is depicted in Fig. 1.3(a), and its topological phase diagram is shown in Fig. 1.3(b). The colored lobes in the diagram indicate the topological phases with a nonzero Chern number, which we will introduce shortly. The Hamiltonian for this model reads

$$\mathcal{H} = t \sum_{\langle i,j \rangle} c_i^\dagger c_j + t_2 \sum_{\langle\langle i,j \rangle\rangle} e^{i\nu_{ij}\phi} c_i^\dagger c_j + M \sum_j (-1)^j c_j^\dagger c_j,$$

where t is the nearest-neighbour hopping parameter, t_2 is the next-nearest neighbour hopping strength, and M is the Semenoff mass. Additionally, we have $\nu_{ij} = \text{sign}\left[(\mathbf{d}_{ik} \times \mathbf{d}_{kj}) \cdot \hat{\mathbf{z}}\right] = \pm 1$, where $\mathbf{d}_{ik}$ is the vector pointing from site i to its nearest-neighbour site k. Working out the Bloch Hamiltonian, we obtain

$$H(\mathbf{k}) = \begin{pmatrix} M + t_2 f_\phi(\mathbf{k}) & t\left(1 + e^{i\mathbf{k}\cdot\mathbf{a}_1} + e^{i\mathbf{k}\cdot\mathbf{a}_2}\right) \\ t\left(1 + e^{-i\mathbf{k}\cdot\mathbf{a}_1} + e^{-i\mathbf{k}\cdot\mathbf{a}_2}\right) & -M + t_2 f_{-\phi}(\mathbf{k}) \end{pmatrix}$$

where

$$f_\phi(\mathbf{k}) = 2\big[\cos(\mathbf{k}\cdot\mathbf{a}_1 - \phi) + \cos(\mathbf{k}\cdot\mathbf{a}_2 + \phi) + \cos(\mathbf{k}\cdot\mathbf{a}_3 + \phi)\big],$$

with $\mathbf{a}_1$ and $\mathbf{a}_2$ the lattice vectors shown in Fig. 1.3(a), and $\mathbf{a}_3 = \mathbf{a}_1 - \mathbf{a}_2$.

Symmetry, topology, and BBC. By setting $t_2 = M = 0$, the system becomes a gapless semimetal, which in its low-energy approximation has Dirac-type quasiparticles with relativistic dispersions [58]. The model possesses a combination of three important symmetries: TRS, inversion, and C_3. TRS ensures that the gapless points happen at the two TR partners that are also invariant under C_3: these are the two high-symmetry points $\mathbf{K}$ and $\mathbf{K}'$, satisfying $\mathbf{K}\cdot\mathbf{a}_i = 2\pi/3,\ 4\pi/3$ and $\mathbf{K}'\cdot\mathbf{a}_i = 4\pi/3,\ 2\pi/3$, for $i = 1, 2$ respectively. As long as the C_3 symmetry is preserved, these Dirac points are globally protected. Breaking inversion symmetry with $M \neq 0$ opens a trivial gap, as both Dirac points must open simultaneously due to TRS. Near that transition, the low-energy Dirac fermions acquire masses with opposite signs. On the other hand, breaking TRS with $t_2 \neq 0$ does not have to involve the two Dirac nodes simultaneously. As a consequence, when both types of symmetry-breaking terms are present, the low-energy theory at K and K' become independent of each other and describe massive Dirac fermions, realizing the parity anomaly of quantum field theory in a condensed-matter setting [56]. Ultimately,

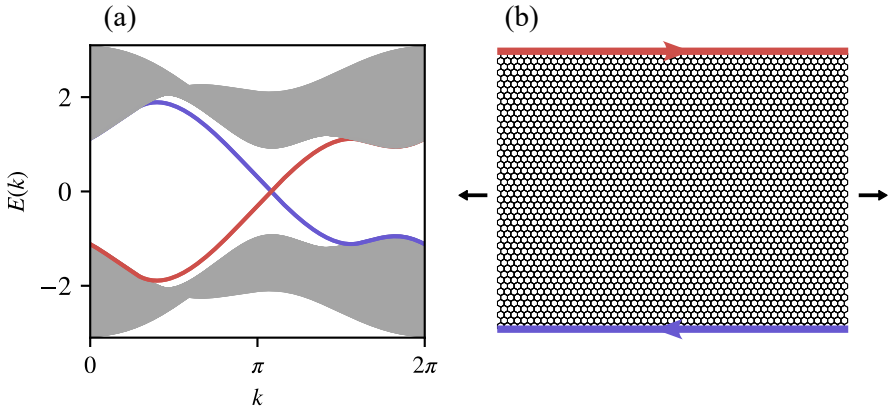

Figure 1.4: (a) Spectrum of a zigzag strip of the Haldane model. The bulk eigenstates are displayed in gray, and the edge modes traverse the bulk gap and are indicated in red and blue. The parameters are chosen to lie on the blue phase in Fig. 1.3(b), marked by the blue cross. (b) Sketch of the strip used and chiral edge states with their direction indicated by the colored arrow. The black arrow indicates that this is an infinite strip of finite width.

the reason why this case is dubbed a TI is because the gap-traversing edge states, which are shown in Fig. 1.4, always exist when the Hall conductivity is quantized and nonzero,

$$\sigma_{xy} = \frac{e^2}{h}C,$$

where C is an integer, the Chern number. It can be calculated for a band insulator through the TKNN formula [52],

$$C = \sum_n \int_{\text{B.Z.}} \frac{d^2k}{2\pi} F_{xy}^{(n)}(\mathbf{k}),$$

where the sum runs over all occupied bands and $F_{xy}^{(n)}(\mathbf{k})$ is the Berry curvature of the n^{th} band, defined by

$$F_{xy}^{(n)} = -i \left[\left\langle \frac{d\psi_n(\mathbf{k})}{dk_x} \middle| \frac{d\psi_n(\mathbf{k})}{dk_y} \right\rangle - \left\langle \frac{d\psi_n(\mathbf{k})}{dk_y} \middle| \frac{d\psi_n(\mathbf{k})}{dk_x} \right\rangle \right],$$

with $\psi_n(\mathbf{k})$ the n^{th} band's Bloch state. In this case, since we are describing a two-band model at half-filling, we only consider the lower band to compute the Chern number, yielding $C = \pm 1, 0$, depending on the parameter choices [see phase diagram in Fig. 1.3(b)].

One remarkable feature of these chiral topological edge modes is their resilience to Anderson localization [59]. In the presence of sufficiently strong random disorder, Anderson localization is inevitable for any system that is adiabatically connected to an atomic limit [16, 60]. One of the consequences of having a nontrivial Chern number is the obstruction to Wannierization of the electronic wavefunctions [61]. Therefore, the ground state of a TI is not adiabatically connected to an atomic limit, providing an intuitive understanding of the lack of Anderson localization. This is very clearly explained in the effective non-linear sigma models that are obtained when performing disorder averaging [62]. A topological term arises, which is responsible for holding the system at criticality, and hence, the system does not cross over to the disordered phase [44].

1.2.3 The role of interactions

The impact of interactions on TIs and superconductors is not universally understood. For instance, the previously described classification can collapse, or be reduced, by introducing symmetry-preserving interactions, meaning that the system can be adiabatically connected to a trivial phase without closing the gap [63, 64]. In some scenarios, interactions have no effect at all, and the topological phases described by the single-particle picture remain robust [65]. Conversely, interactions may also induce new topological phases that do not exist in their absence [66, 67]. We shall briefly give examples for a few cases.

Integer Quantum Hall Effect. In the case of the integer quantum Hall effect, the effect of interactions can be studied because the conductivity is an observable and is also well-defined in the presence of interactions. It turns out that its quantized nature survives the effect of interactions [65], and hence, this phase is insensitive to interactions. The same holds true for the quantum spin Hall effect, which is a topological phase protected by TRS. The helical edge states present in this system are, just like the chiral counterpart in the quantum Hall effect, not only robust to backscattering from disorder but also from interactions [68].

We note that this does not mean that interactions never give rise to interesting effects. If the spin degree of freedom is taken into account, the $\nu = 1$ quantum Hall phase gives rise to the so-called quantum Hall ferromagnet due to the Coulomb interactions and a strong Zeeman effect [69]. This system features a wide variety of interesting phenomena, such as topological skyrmion excitations, and exhibits behaviors akin to those found in a fractional quantum Hall effect phase rather than a typical integer phase.

Fractional Quantum Hall Effect. One cannot talk about the integer quantum Hall effect without referring to its more intricate counterpart, the fractional quantum Hall effect [70]. This phase of matter cannot be understood by using non-interacting fermions and must be treated using the full machinery of many-body physics. As its name indicates, the fractional quantum Hall effect has plateaus appearing at fractional fillings ν, resulting in a Fermi energy within Landau levels. A fully global microscopic theory of the fractional quantum Hall effect, describing the origin of the incompressibility of the ground state, is still an open question [14], but the composite fermion theories have been able to explain many experimental observations [70]. Many fractions ν can be understood as an integer quantum Hall effect of composite fermions, where the quasiparticle picture is that of one electron attached to magnetic flux quanta. The fractional quantum Hall effect is a phase of matter with long-range entanglement and possesses true topological order [38]. The implications are profound, with many exotic properties, such as anyons with fractional statistics yielding the promise of topologically-protected quantum computing [30].

Experimental realization of a bosonic many-body topological phase of the SSH model. In Ref. [71], the SSH model was experimentally realized, and a many-body topological phase of interacting hard-core bosons was achieved. Unlike their fermionic counterparts, the many-body bosonic representation of the protecting symmetry permits next-nearest neighbor couplings, which break SLS in the single-particle picture. Remarkably, this implies that the many-body topological phase remains intact, despite the addition of such perturbations.

Purely interacting topological phases. The above example is also intrinsically linked to the Haldane phase of quantum spin chains with integer spins as degrees of freedom. This is a prototype of an SPT phase, which solely exists because the system is strongly correlated. The result is a gapped phase of a chain of integer spin with half-integer spins at the boundary [39]. Another example in 2D is the existence of a fractional TI [66]. The simplest model revealing them consists of spinful electrons with decoupled spin degrees of freedom, each of which is described by a fractional quantum Hall phase, similar to how a TRS noninteracting TI is built out of two decoupled integer quantum Hall insulators with opposite chiralities [72]. We note that these SPT phases also have true topological order, marked by a nonzero topological entanglement entropy [73].

Other examples of interaction-driven topological phases are found in the highly correlated electrons in the f-shell of SmB_6, which form a state dubbed the topo-

logical *Kondo*-insulator [74]. Another example of a correlated topological insulator is the topological *Mott* insulator [75].

General comments on classification of interacting phases. For 1D systems, a complete classification of gapped phases has been provided in terms of group cohomology [29]. Since all gapped phases are short-range entangled in 1D, matrix-product states are a sufficient tool to completely classify gapped quantum phases in 1D [76]. In this description, the concept of symmetry fractionalization lies behind the existence of nontrivial SPT phases. That is, one can study how *projective representations* of a symmetry group G act on these states. Two projective representations are different if their phase factors $\alpha_1(g_1, g_2)$ and $\alpha_2(g_1, g_2)$ are inequivalent. The classification of such phase factors is done in 1D by the second cohomology group $H^2(G, \mathbb{C})$. If this group contains more than one element, then topologically distinct quantum phases exist.

In higher dimensions, similar attempts have been made at classifying interacting topological phases, but contrary to the 1D case, there is no complete classification yet. However, one can construct a host of bosonic SPTs by using tensor networks, a generalization of Matrix-Product-States, and categorize them with $H^{d+1}(G, U(1))$ [16]. For fermionic systems, a group supercohomology approach was applied to categorize SPT phases [77]. Complementary to these approaches, cobordism has also been used to classify some SPT phases. It combines the concepts of invertible topological field theories and cobordisms, a concept from algebraic topology used to classify manifolds [78–80].

Finally, this last point connects to a more physical perspective that extends to interacting theories. It leverages the relationship between BBC and the concept of quantum anomalies. [81]. The basic idea is that edge theories cannot exist in isolation; they require a bulk theory to cancel anomalous contributions to their effective field theory action. In other words, edge theories of SPT phases can have various types of quantum anomalies, which necessitate a topological term from the bulk theory to cancel them [44]. The mechanism operates as follows: since every TI (or superconductor) possesses a massive Dirac Hamiltonian in its low-energy effective field theory, we can couple this Hamiltonian to a background gauge field, determined by the gauge symmetry of the underlying Dirac Hamiltonian. For a superconductor lacking internal symmetry, this coupling is with a background metric, essentially coupling it to gravity. After integrating out the fermionic degrees of freedom, we obtain a pure gauge field action, which is gauge invariant in a bulk theory without boundaries. However, if a boundary is introduced, an additional contribution emerges. This contribution must then cancel the quantum anomaly of the "isolated" boundary theory.

1.2.4 Applications beyond noninteracting electrons

Beyond their existence in systems of noninteracting fermions, topological states and their bulk-boundary phenomenology appear in a variety of other platforms that exhibit wave-like behavior. Many realizations of typical toy models were accomplished on mechanical, photonic, and electrical platforms [82–86]. The underlying principle is that the effective descriptions of these systems, when placed on lat-

tices with appropriate geometries, can lead to similar matrix equations involving a "Hamiltonian" that is equivalent to the single-particle Hamiltonian describing fermions in a topological phase. For this reason, these platforms display the same phenomenology and features of topologically protected boundary states as those observed in fermionic systems.

One advantage they offer is the ease of implementation, allowing for the testing of novel predictions about topological systems that are challenging to control in microscopic systems. Additionally, these platforms enable exploration beyond the framework of noninteracting fermions described by a Hermitian Hamiltonian. Indeed, they have revived interest in the study of non-Hermitian (NH) Hamiltonians, as the ten-fold classification of Hermitian Hamiltonians becomes much richer when considering NH ones. The ease of controlling lattice sites and couplings in these arrays allows for the implementation of nonreciprocal couplings, as well as gain and loss. The interplay between these factors provides a more intricate phenomenology, which will be discussed in depth in the next section.

1.3 Non-Hermitian Systems

In recent years, the study of NH physics has gained significant attention due to its profound impact on the fields of condensed matter, meta-materials, acoustics, and photonics [87–90]. For example, NH platforms offer enhanced sensing capabilities [87], can exhibit Majorana bound states near exceptional points (EPs) [88]—where *both* eigenvectors and eigenvalues become degenerate— and provide opportunities for utilizing topological edge modes in the field of active matter [89, 90]. In addition, the non-conservative and non-unitary dynamics of NH systems have led to the discovery of phenomena that challenge the conventional notions of symmetry and stability [26, 27, 91, 92]. Among these, the NH skin effect (NHSE), manifesting itself as an accumulation of modes at the boundaries of the system, has been intensely studied in the past few years [93–98]. The NHSE has been realized in multiple platforms, such as acoustic crystals [96], electric circuits [97], and optical lattices using ultra-cold atoms [99]. Moreover, the interplay between NH physics and topology has given rise to novel topological phases [27, 100, 101]. Indeed, when considering Hamiltonians that are no longer Hermitian [18, 27], the AZ classification for noninteracting fermions is enlarged from 10 to 38 classes. Additionally, the BBC generally no longer holds and requires substantial modifications to account for boundary phenomena [91, 102].

Most platforms that realize topological phases of matter are subject to their environment and are rarely well-isolated. In fact, one could argue that the most natural prescription for effective Hamiltonians describing such systems must include NH contributions. For instance, mechanical systems commonly experience damping or losses due to the underlying lattice to which they are attached. Similarly, topoelectric platforms face resistances across circuits that dissipate currents as heat, while photonic platforms encounter inefficiencies in the transmission of electromagnetic waves due to, for example, complex refractive indices.

NH systems are inherently non-conservative and offer a way to describe systems coupled to an environment without the need to model the environment explicitly.

The concept of parity-time (PT) symmetry has significantly contributed to the popularity of NH descriptions [103, 104]. PT symmetry arises, for instance, when there is a balance between gain and loss in a system. When a Hamiltonian is PT-symmetric, its eigenvalues can either be real or come in complex-conjugate pairs. The occurrence of real eigenvalues prompted a reevaluation of the necessary ingredients to formulate the postulates of quantum mechanics using PT-symmetric operators instead of Hermitian ones [104]. Moreover, when the eigenvalues of the Hamiltonian are real, the eigenstates also exhibit PT symmetry. In contrast, if the eigenvalues are complex, the eigenstates do not preserve PT symmetry, indicating a *PT-symmetry broken phase* [105].

PT-symmetric models have interesting consequences across different platforms. For example, in optical systems, PT-symmetric setups offer enhanced and cleaner laser emission [106], unidirectional invisibility [107], and enhanced sensing capabilities [108]. Moreover, some of these effects are caused by the unique feature of NH systems that allows EPs in parameter space to exist [92].

Typical setup for a NH description. Finally, let us exemplify a case where a NH Hamiltonian model is useful. Consider a system composed of arrays of evanescently coupled waveguides [109]. The paraxial Helmholtz equation describing the propagation of the electric field envelope along the z-direction is given by [110]

$$i\frac{\lambda}{2\pi}\partial_z\mathcal{E}(x,y,z) = -\left[\frac{\lambda^2}{8\pi^2 n_0}\left(\frac{\partial^2}{\partial x^2}+\frac{\partial^2}{\partial y^2}\right) - \Delta n(x,y,z)\right]\mathcal{E}(x,y,z),$$

where λ is the wavelength of incoming electromagnetic radiation, $\mathcal{E}$ is the electric field amplitude, n_0 is the waveguide's bulk refractive index, and $\Delta n(x,y,z) = n_0 - n(x,y,z)$ is the deviation of the refractive index. By identifying the wavelength with Planck's constant, $\lambda \leftrightarrow h$, time with propagation direction $t \leftrightarrow z$, particle mass with bulk index of refraction $m \leftrightarrow n_0$, and the potential with the change in refractive index, $\Delta n \leftrightarrow -V$, the setup can emulate the Schrödinger equation. By carefully controlling light amplification and attenuation, together with variations of individual waveguides' profile along the z-direction, one obtains gain/loss and nonreciprocal effects that make the Hamiltonian NH [111, 112]. The tight-binding limit can also be achieved by carving out a sharply varying Δn, such as a square wave modulation [92]. Similar descriptions that involve an emulation of a NH Hamiltonian can be achieved in electric circuits, governed by Kirkchoff's law, and where the admittance matrix takes the role of a Hamiltonian and impedances the role of wavefunctions [86].

1.3.1 Modification of the topological classification

Modification of symmetries. One of the main consequences of non-Hermiticity is that transposition and complex conjugation, which are equivalent for Hermitian matrices, must be treated separately. We will describe how the symmetries defined previously in Section 1.1.1 are modified by studying their actions on the single-particle Hamiltonian matrices and use the notation of Ref. [27]. Each operation will now contain a unitary part and either a complex conjugation or a transposition. We consider the following separate symmetry operations:

- TRS, T_+, and TRS†, C_+: unitary operators with $T_+T_+^* = \pm 1$ and $C_+C_+^* = \pm 1$, acting on the first-quantized Hamiltonian as

$$T_+ H^* T_+^{-1} = H,$$
$$C_+ H^T C_+^{-1} = H.$$

- PHS, C_-, and PHS†, T_-: unitary operators with $C_-C_-^* = \pm 1$ and $T_-T_-^* = \pm 1$, acting on the first-quantized Hamiltonian as

$$T_- H^T T_-^{-1} = -H,$$
$$C_- H^* C_-^{-1} = -H.$$

- Chiral symmetry (CS), $\Gamma = T_+ \circ C_-$: unitary combination of TRS and PHS with $\Gamma^2 = 1$, acting on the first-quantized Hamiltonian as

$$\Gamma H^\dagger \Gamma^{-1} = -H.$$

- Sublattice symmetry (SLS), S: a symmetry operator distinct from Γ, satisfying $S^2 = 1$ and acting on the first-quantized Hamiltonian as

$$SHS^{-1} = -H.$$

- Pseudo-Hermiticity, η: Hermitian and unitary operator with $\eta = \eta^\dagger$ and $\eta^2 = 1$, acting on the first-quantized Hamiltonian as

$$\eta H^\dagger \eta^{-1} = H.$$

On top of all these possibilities, one must recognize the equivalence between TRS and PHS†. This can be seen from the fact that if a Hamiltonian H is symmetric under TRS, then another Hamiltonian iH is symmetric under PHS†. Moreover, in the Hermitian case, CS and SLS were identical because $H = H^\dagger$, whereas now they constitute separate symmetries. Finally, we now also have pseudo-Hermiticity as an additional symmetry operation, forcing eigenvalues of the Hamiltonian to be real whenever eigenvectors have a nonvanishing η norm.

The combinations of TRS, PHS, and CS yield the same two complex AZ classes and eight real AZ classes as the ones found in Section 1.1.1. Similarly, the combinations TRS†, PHS†, and CS result in an additional six distinct classes after identifying equivalences with the previous 10. Finally, when considering the action of SLS and the combination with all other symmetries, 22 other distinct classes emerge, yielding a total of 38 symmetry classes. For a full classification based on their topological character and definitions of topological invariants, we refer the reader to Refs. [26, 27].

The concept of a gapped phase is also modified when one considers NH Hamiltonians. Since energies are generally complex, one must distinguish between two types of gaps: a point gap and a line gap (see Fig. 1.5). The former is a novel type of gapped phase that arises even when the system considered has only one band,

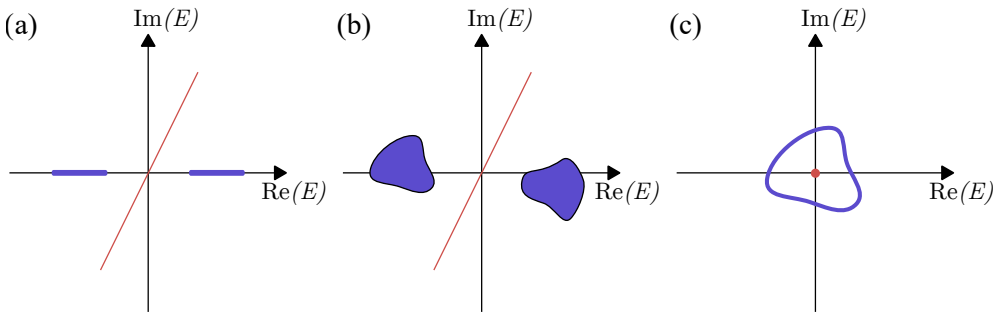

Figure 1.5: Types of energy spectra. a) Hermitian bands on the real axis (blue), separated by a line gap (red). b) NH bands, with generic complex values, are also separated by a line gap. c) One NH band enclosing a reference energy $E = 0$: this is an example of a point gap.

as exemplified in Fig. 1.5 (c). In this scenario, it is impossible to collapse the loop of energy eigenvalues (in blue) without crossing the base energy E_b (in red). This type of phase is characterized by a spectral winding number, which is defined in odd spatial dimensions $d = 2n + 1$ as [27]

$$W_{2n+1}(E_b) \equiv \frac{n!}{(2\pi i)^{n+1}(2n+1)!} \int_{\mathrm{BZ}} \mathrm{tr}\left[(H - E_b)^{-1} dH\right]^{2n+1},$$

where dH must be understood as a differential form. The expression can be generalized to any base energy by replacing $H \to H - E_b$. In 1D, this becomes

$$W_1(E_b) = \int_{-\pi}^{\pi} \frac{dk}{2\pi i} \partial_k \log\det(H - E_b). \tag{1.7}$$

Modified BBC. One challenge encountered when studying NH systems is the sometimes dramatically different behavior of Hamiltonians with OBC and PBC, leading to a breakdown of the conventional BBC. [92]. In 1D, for example, it is often observed that the spectra of PBC Hamiltonians form closed loops in the complex energy plane, whereas the spectra with OBC form arcs that lie within these loops. Another dramatic consequence of non-Hermiticity is the possible presence of the NHSE, which can be understood as the "pile-up" of all eigenmodes on one boundary of the system. The NHSE is often captured by the spectral winding Eq. (1.7), which is nonzero for all OBC eigenenergies, as they are enclosed within the PBC spectrum. Its sign also indicates the direction of the NHSE. The reason for this significant difference between the two systems is the increased sensitivity of NH matrices to perturbations [113]. By considering the term connecting the boundaries as a perturbation of the OBC Hamiltonian, it becomes clear how sensitive the Hamiltonian is to this change [114]. Another topological argument for the large contrast was given in Ref. [114], where it was observed that the structure of the complex energy eigenvalues changes drastically as it undergoes a series of transitions through EP. These are points in parameter space where eigenvalues *and* eigenvectors become degenerate. At these points, the matrix becomes defective, as

its algebraic multiplicity (the degree of the characteristic polynomial) exceeds its geometric multiplicity (the dimension of its eigenspace).

Some properties of NH matrices. Before we continue, we give a brief overview of the tools and terminology needed to analyze NH matrices. In contrast to their Hermitian counterparts, one needs to consider both left and right eigenvectors to construct a complete basis. Consider a generic diagonalizable NH matrix $M \in \mathbb{C}^{N\times N}$. Its eigenvalue equations can be cast in two ways:

$$\begin{aligned} M\left|j\right\rangle_R &= \lambda_j \left|j\right\rangle_R, \quad \left\langle j\right|_L M = \lambda_j \left\langle j\right|_L, \\ \Rightarrow M^\dagger \left|j\right\rangle_L &= \lambda_j^* \left|j\right\rangle_L, \end{aligned} \tag{1.8}$$

where $j \in \{1, \cdots, N\}$, $\lambda_j \in \mathbb{C}$ is the j^{th} eigenvalue, and the subscripts R and L denote right and left eigenvectors. These eigenvectors can be used to form a complete *biorthogonal* basis [91], in the sense that one has ${}_L\left\langle j|k\right\rangle_R = \delta_{jk}$ and

$$\begin{aligned} \mathbb{1} &= \sum_j \left|j\right\rangle_R \left\langle j\right|_L, \\ A &= \sum_{j,k} A_{jk} \left|j\right\rangle_R \left\langle k\right|_L. \end{aligned} \tag{1.9}$$

That is, there is a resolution of the identity, and we can also expand an arbitrary matrix A in this basis.

In the following, we will discuss two paradigmatic models of NH Hamiltonians: the Hatano-Nelson model and the NH SSH model. They will help to illustrate some of the essential concepts involved in studying NH Hamiltonians. Using these examples, we will also explore how to recover a notion of BBC and determine topological phase transitions.

1.3.2 Example: Hatano-Nelson model

The paradigmatic example of a NH Hamiltonian comes from a simplified version of the Hatano-Nelson model [115]. It was originally used to describe the depinning of flux lines from columnar defects in superconductors, viewed as a localization transition in a disordered bosonic NH Hamiltonian. There, non-Hermiticity results from the introduction of an imaginary vector potential in the effective bosonic theory. Later, in the literature, one refers to the Hatano-Nelson model as the following nonreciprocal 1D tight-binding Hamiltonian without disorder [92]

$$H = (v+g)\sum_i \left|i\right\rangle_R \left\langle i+1\right|_L + (v-g)\sum_i \left|i+1\right\rangle_L \left\langle i\right|_R,$$

where v is a regular hopping amplitude and g is the Hermiticity-breaking parameter. The Bloch Hamiltonian for this chain is given by

$$H(k) = 2v\cos k + 2ig\sin k, \tag{1.10}$$

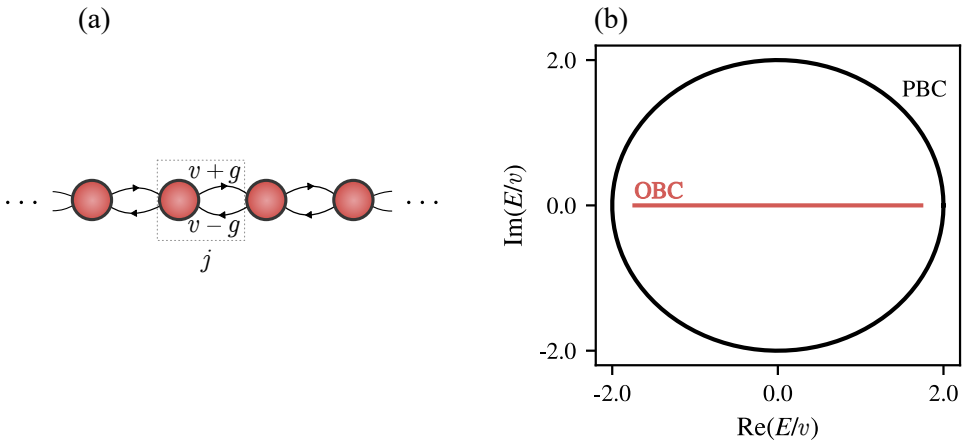

Figure 1.6: The Hatano Nelson model. a) Sketch of the chain, with the j^{th} unit cell shown inside the gray box. The nonreciprocity of the hoppings is indicated by the arrows. b) Spectrum of the chain in the complex energy plane. PBC is shown in black, and OBC in red. The parameters chosen for the plot are $g = 0.5v$.

where $k \in (-\pi, \pi]$. Since this is a one-band model, Eq. (1.10) is also the dispersion relation. The OBC version of this Hamiltonian is a simple tridiagonal Toeplitz matrix, for which the eigenvalues have a closed-form expression [116], given by

$$E(q) = 2\sqrt{v^2 - g^2}\cos(q), \tag{1.11}$$

with "quasi-momentum" $q \in (-\pi, \pi]$. A sketch of this chain is shown in Fig. 1.6 (a), while its spectrum is shown in Fig. 1.6 (b). In the latter the discrepancy between the PBC spectrum (black) and OBC spectrum (red) is evident. This discrepancy also arises in the way how eigenstates behave. While the PBC eigenstates are typical Bloch waves, the OBC eigenstates take the form

$$|q\rangle_R = \sqrt{\frac{2}{N+1}} \sum_{j=1}^{N} \left(\frac{v+g}{v-g}\right)^{j/2} \sin(qj)\,|j\rangle_R\,. \tag{1.12}$$

which suggests the introduction of the quantity

$$\kappa \equiv \frac{1}{2}\log\left(\frac{v-g}{v+g}\right), \tag{1.13}$$

whose amplitude determines an inverse length scale (in units where the lattice constant $a = 1$). These states are very different from Bloch states, and all of them localize towards one end of the chain, as determined by κ, indicative of the NHSE. We shall, therefore, from now on, refer to $1/\kappa$ as the skin length scale. In Fig. 1.7, two examples of the NHSE are shown, with the corresponding spectral winding numbers and their respective skin length scales. A phase transition takes place at $g = 0$ and is captured by the spectral winding number and a change in the sign of κ. This transition is accompanied by a reversal of the direction of the NHSE,

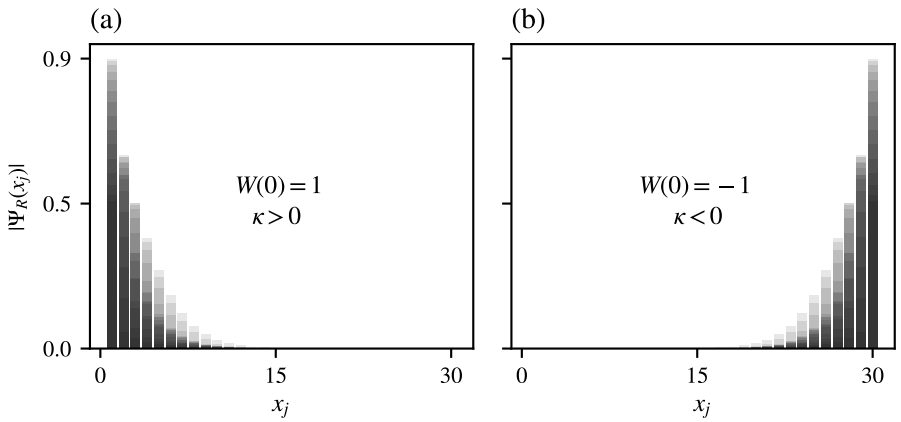

Figure 1.7: Accumulation of right eigenstates of the Hatano-Nelson model on (a) the left side of the chain, marked by a positive κ and spectral winding $W(0) = 1$, and (b) the right side of the chain, marked by a negative κ and spectral winding $W(0) = -1$.

as shown in Fig. 1.7. Finally, another important transition can be observed from Eq. (1.11). At $v = \pm g$, the eigenvalues turn from fully real into fully imaginary, marking the passage through an EP. We will describe these using the following example.

1.3.3 Example: NH SSH model

We now turn our attention to the NH SSH model. Similar to its Hermitian counterpart discussed in Section 1.2.1, this model serves as a quintessential example for investigating NH topological phases. Specifically, we focus on the scenario where non-Hermiticity arises from nonreciprocal hoppings. Other variants have also been explored, including models featuring additional gain and loss while preserving PT symmetry [117]. In our case, the model is described by the Hamiltonian matrix

$$H = (v+g)\sum_i |i,A\rangle_R \langle i,B|_L + (v-g)\sum_i |i,B\rangle_L \langle i,A|_R + w\sum_i \Big(|i,B\rangle \langle i+1,A| + \text{h.c.} \Big), \tag{1.14}$$

where, just like Eq. (1.2), v and w are Hermitian hopping parameters, but now we also include the Hermiticity-breaking parameter g within each unit cell. The model is depicted in Fig. 1.8(a) and its complex spectrum in Fig. 1.8(b). The Bloch Hamiltonian is once again given by

$$H(k) = d_x(k)\sigma_x + d_y(k)\sigma_y,$$

but now the components of the vector $\mathbf{d}(k)$ are complex-valued. In particular, we have $d_x(k) = v + w\cos k$ and $d_y(k) = ig + w\sin k$. The dispersion relation is given

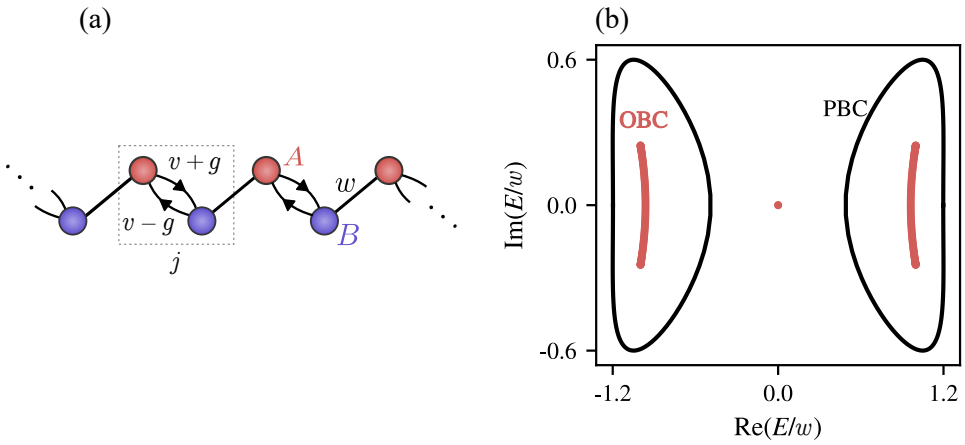

Figure 1.8: NH SSH model. a) Depiction of the chain, with unit cell j in gray. The intracell hoppings v and intercell hopping w are shown, with the nonreciprocity parameter g applied only to the hoppings inside the unit cell, as marked by the direction of the arrows. b) Spectrum of the chain in the complex energy plane. PBC is shown in black, and OBC in red. The parameters chosen for the plot are $v = 0.3w$ and $g = 0.4w$. The OBC spectrum was computed numerically for a chain of $N = 200$ sites.

by

$$E_{\pm}(k) = \pm\sqrt{v^2 + w^2 - g^2 + 2vw\cos k - 2igw\sin k}, \tag{1.15}$$

and is shown in Fig. 1.8(b) (black), together with a numerically calculated OBC spectrum (red). The latter depicts two degenerate zero-energy eigenvalues, which correspond to the topological edge modes of the model. However, because of the NHSE, they remain concealed if one were to only look at the left or right eigenvectors. To properly observe them, it is necessary to introduce the biorthogonal wavefunction amplitude for the n^{th} mode,

$$\mathcal{A}_n(x_j) = {}_L\langle\psi_n(x_j)|\psi_n(x_j)\rangle_R\,. \tag{1.16}$$

Equation (1.16) is plotted in Fig. 1.9. We observe two distinct phases: topological edge modes are depicted in Fig. 1.9(a) in red, while Fig. 1.9(b) illustrates the absence of topological edge modes.

Taking a closer look at Eq. (1.15), the transition between the two phases is expected to happen when the gap closes at

$$\begin{aligned} v &= -w \pm g, \\ v &= w \pm g. \end{aligned} \tag{1.17}$$

This is also what is predicted by a naive application of the BBC. To this end, we employ the winding number for the chiral symmetric system, defined in Eq. (1.4). We first note that it can be rewritten as the winding of the $\mathbf{d}$ vector in the plane, which is further split into two because it is complex-valued. The full expression

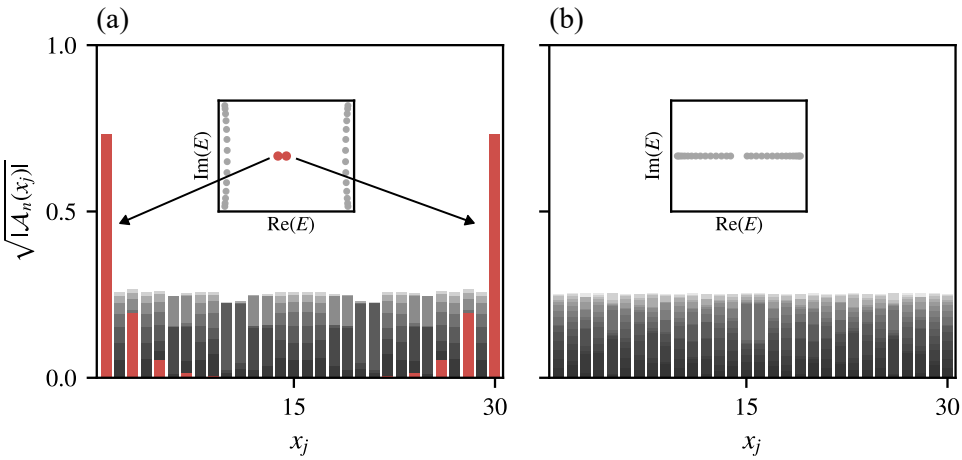

Figure 1.9: Biorthogonal wavefunction amplitude as a function of position in (a) the topological phase, with $(v, g) = (0.3w, 0.4w)$, and (b) the trivial phase with $(v, g) = (1.3w, 0.4w)$. Insets show the complex energy spectrum, with the edge modes highlighted in red in (a). The system size is $N = 30$ in both cases.

can be written as [118]

$$\begin{aligned} \nu &= \frac{1}{2}\left(\nu_1 + \nu_2\right), \\ \nu_i &= \int_{-\pi}^{\pi} \frac{\mathrm{d}k}{2\pi} \partial_k \theta_i, \end{aligned} \tag{1.18}$$

where the angles are given by

$$\begin{aligned} \tan\theta_1 &= \frac{\mathrm{Re}(d_y) + \mathrm{Im}(d_x)}{\mathrm{Re}(d_x) - \mathrm{Im}(d_y)}, \\ \tan\theta_2 &= \frac{\mathrm{Re}(d_y) - \mathrm{Im}(d_x)}{\mathrm{Re}(d_x) + \mathrm{Im}(d_y)}. \end{aligned}$$

These individual angles have an interpretation as winding numbers around EPs in the real $\mathbf{d}$-plane [118]. It can also be shown that the difference of the individual windings yields the spectral winding number Eq. (1.7) around the base energy $E = 0$ [118],

$$W(0) = \frac{1}{2}\left(\nu_1 - \nu_2\right).$$

Unfortunately, these topological indices do not capture the true topological phases of the OBC system, which is to be expected since OBC and PBC are very different from each other. A direct calculation of the zero-energy eigenstates of the OBC Hamiltonian, using a transfer-matrix approach, yields the following condition for their existence

$$\begin{aligned} |v| &< \sqrt{|w^2 - g^2|}, \\ |v| &< \sqrt{|w^2 + g^2|}, \end{aligned} \tag{1.19}$$

which indeed is completely different from Eq. (1.17).

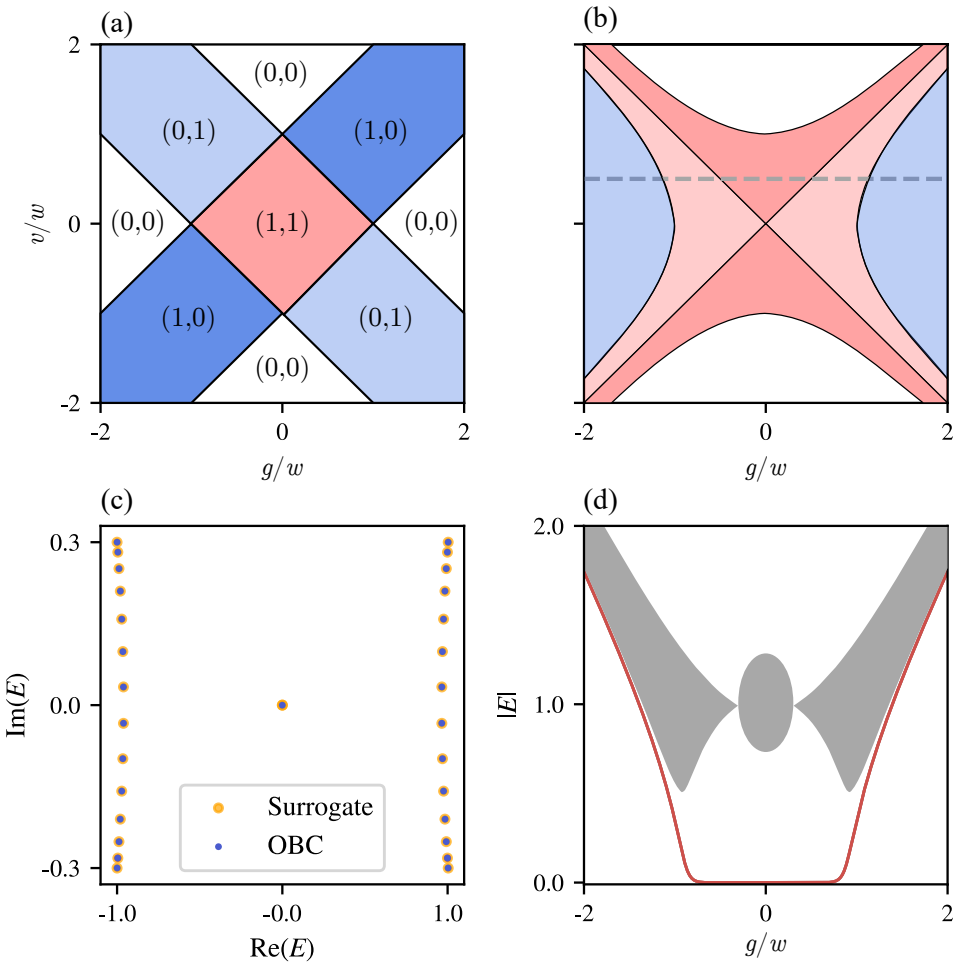

Figure 1.10: (a) Phase diagram using PBC and the winding numbers (ν_1, ν_2) from Eq. (1.17). The red region is the only one having an integer quantized generalized winding $\nu = (\nu_1 + \nu_2)/2 = 1$. The blue regions all have half-quantized generalized winding numbers. (b) Phase diagram using the surrogate Hamiltonian and the winding number Eq. (1.4), together with Eq. (1.21). The chiral winding number predicts a nonzero value in the red region. (c) Example of the complex energy spectrum of the surrogate Hamiltonian (orange) and the OBC Hamiltonian (blue). (d) Energy spectrum as a function of the nonreciprocity parameter g along the gray line shown in (b). The topological edge mode is shown in red, while all the other modes are shown in gray.

One way to recover a BBC is by constructing the so-called *surrogate* Hamiltonian [119]. This cancels the effect of the NHSE and allows one to work with a PBC Hamiltonian, whose spectrum is almost identical to the OBC spectrum. The

surrogate Hamiltonian is obtained through the placement $k \to k + i\kappa$, where κ is the skin localization length. This results in the following surrogate Hamiltonian for the SSH model

$$H_{\text{sur}}(k) = \begin{pmatrix} 0 & v + g + w\sqrt{\frac{v+g}{v-g}}e^{-ik} \\ v - g + w\sqrt{\frac{v-g}{v+g}}e^{ik} & \end{pmatrix}, \tag{1.20}$$

which, at the level of the real space Hamiltonian, amounts to a replacement of $w \to we^{\kappa}$ for the intercell hopping to the right, and $w \to we^{-\kappa}$ for the intercell hopping to the left. One can construct a full phase diagram by computing the winding number Eq. (1.4) for the surrogate Hamiltonian, and by imposing the condition for EPs $d_x^2 + d_y^2 = 0$, yielding

$$\text{Re}(d_x) = \mp\text{Im}(d_y) \quad \text{and} \quad \text{Re}(d_y) = \pm\text{Im}(d_x). \tag{1.21}$$

In this case, there are two lines, $v = \pm g$, of EPs in the phase diagram. This separates what has been dubbed "Hermitian" topological phases from the "non-Hermitian" ones [120]. In Fig. 1.10(a) and Fig. 1.10(b), one can see the difference between the phase diagrams obtained from Eq. (1.17), using the generalized winding number (ν_1, ν_2), and the one obtained from Eq. (1.19), using the winding number of the surrogate Hamiltonian Eq. (1.20). Indeed, we see that the chiral winding number now correctly predicts the topological phase transition given by Eq. (1.19). Note that the blue and light-red regions are disconnected by the two lines of EPs from the darker red region, which represents the "Hermitian" topological phase. We can also see in Fig. 1.10(c) that the OBC spectrum and the Surrogate spectrum are identical when computed numerically for a $N = 30$ site chain. Finally, Fig. 1.10 shows the recovery of a non-Bloch BBC, where the zero-energy topological edge states (in red) appear around the same transition points predicted in the phase diagram in Fig. 1.10(b) along the gray dotted line. We can also see the collapse of the eigenstates happening at the EPs determined by the condition Eq. (1.21).

1.4 Aperiodic Systems

Aperiodic systems are materials and structures that lack translational symmetry, meaning that they do not exhibit a periodic repetition in their atomic or molecular arrangements. Unlike crystals, which have repeating unit cells and long-range order, aperiodic systems have order without periodicity, presenting unique and complex structural properties. Quasicrystals are a well-known class of aperiodic systems discovered in 1984 by Dan Shechtman [121], who observed diffraction patterns with sharp peaks indicating long-range order without periodic repetition. Quasicrystals can exhibit symmetries, such as five-fold rotational symmetry, that are forbidden in traditional crystallography. Aperiodic systems often have unique electronic properties, such as unusual electronic band structures and transport phenomena. This can lead to a host of curious material properties, such as low thermal conductivity, low friction coefficients, high hardness, corrosion resistance, and superplasticity [122, 123]. Their utility ranges from heat-insulating materials, through coating that increases hardness, all the way to medical implants, where

prosthetics made from quasicrystalline materials have shown minimal cytotoxicity effects [124, 125].

From a more fundamental perspective, these systems have aroused significant curiosity for their theoretical understanding. For example, by studying spin chains under the influence of aperiodic modulations, it has been shown that depending on the fluctuations of the aperiodic sequence, it is possible to access different universality classes of quantum phase transitions [126–128]. On another front, single-particle Hamiltonians on 1D quasicrystals were investigated using various techniques, such as renormalization schemes and trace maps [129–132]. Amongst many interesting results, it was discovered that the spectrum is singular continuous and the eigenstates are neither localized nor delocalized, but are *critical* and exhibit multifractal behavior [130, 133–136]. More recently, theoretical and experimental works have shown that it is possible to observe topological charge pumping in quasiperiodic chains [22, 23, 137]. Additionally, it was found that the critical states emerge from a cascade of localization-delocalization transitions [138]; It was also shown that it is possible to control edge states by manipulating local structures in various aperiodic systems due to the presence of local symmetries [139]. Aperiodic modulations may have other interesting implications on physical systems. We refer the reader for a comprehensive review to Refs. [125, 140]

1.4.1 Symbolic dynamics

One way to obtain aperiodic order is by generating structures using deterministic rules. This is usually done by encoding sequences of symbols using an inflation rule. The mathematical study of such structures is called symbolic dynamics [141]. That is the study of dynamical systems formed by a set of symbols subjected to the repeated application of a function that maps the set of symbols to the set of combinations of symbols.

In order to exemplify this method, we consider finite-size words $W \in \mathcal{V}$, where $\mathcal{V}$ denotes the set of finite words that can be generated from an alphabet $\mathcal{A} = \{a_0,\ a_1,\ \cdots, a_m\}$ of inequivalent symbols. These words can be constructed by repeatedly applying a substitution rule $\sigma : \mathcal{A} \to \mathcal{V}$. The substitution rule imposes recurrence relations on words, which makes it easy to generate them. Suppose one starts with the "seed" letter a_0. We call the word *uniquely* generated by applying the rule σ to the seed letter n times the n^{th} approximant of the aperiodic sequence. Below, we give a few examples of aperiodic sequences that we use throughout this work.

Fibonacci sequence. The Fibonacci words can be generated from the binary alphabet $\mathcal{A} = \{A, B\}$ by applying the following recursion relation,

$$\begin{aligned} &W_n = W_{n-1}W_{n-2},\ \text{for } n > 1, \\ &W_0 = A,\ W_1 = AB, \end{aligned} \tag{1.22}$$

In the above equation, the product of words means that they are concatenated. This is an example of a 1D quasicrystal, as it can be obtained via a cut-and-project scheme from a regular 2D square lattice [142].

Tribonacci sequence. The Tribonacci word is an extension of the Fibonacci word, and it is also a quasicrystal. However, its cut-and-project scheme results from a 3D cubic lattice instead [5]. The alphabet generating the word is composed of three letters $\mathcal{A} = \{A, B, C\}$, and the recursive scheme to generate the word is

$$\begin{aligned} W_n &= W_{n-1}W_{n-2}W_{n-3}, \text{ for } n > 2, \\ W_0 &= A,\ W_1 = AB,\ W_2 = ABAC. \end{aligned}$$

Thue-Morse sequence. The two previous words are examples for which the Pisot substitution conjecture holds [143, 144]. The characteristic matrix of the substitution dynamics has a polynomial of degree equal to its dimension. This makes their diffraction spectrum pure-point. It is for this reason that they can be called quasicrystals [142]. The Thue-Morse chain is not generated by a Pisot substitution and is an example of an aperiodic chain that is not a quasicrystal. It has a singular-continuous diffraction spectrum [145]. The sequence is generated by repeatedly applying the substitution rule $\sigma(A) = AB$ and $\sigma(B) = BA$ to the binary alphabet. Alternatively, it can be generated by the following recurrence relation

$$\begin{aligned} W_n &= W_{n-1}\overline{W_{n-1}},\ n > 0, \\ W_0 &= A, \end{aligned}$$

where $\overline{W_N}$ is the bit-wise negated word: $A \to B$ and $B \to A$. That is, the n generation word is obtained by concatenating the $n-1$ generation word with its bit-wise negated version.

Rudin-Shapiro sequence. Finally, the last example of an aperiodic chain that we investigate is the Rudin-Shapiro chain [146]. This system is different from the previous three in the sense that it features an absolutely continuous diffraction spectrum. However, it is still an open question as to which type of spectral measure the energy spectrum belongs [125]. In order to generate the binary Rudin-Shapiro sequence, we use the following two-step procedure: We first impose the substitution rule on the four-letter alphabet $\mathcal{A} = \{A, B, C, D\}$:

$$\sigma : \begin{cases} A \mapsto AB, \\ B \mapsto AC, \\ C \mapsto DB, \\ D \mapsto DC. \end{cases}$$

This is then followed by the second step, which identifies $A, B \to A$, and $C, D \to B$. In this way, starting with the seed A, we obtain the Rudin-Shapiro binary sequence, which starts as $AAABAABAAAABBBAB\cdots$.

1.4.2 Example Hamiltonian: Fibonacci sequence

Let us apply the Fibonacci sequence from Eq. (1.22), which is an example of a quasicrystal in 1D. The n^{th} iteration of the Fibonacci word, W_n, will be referred

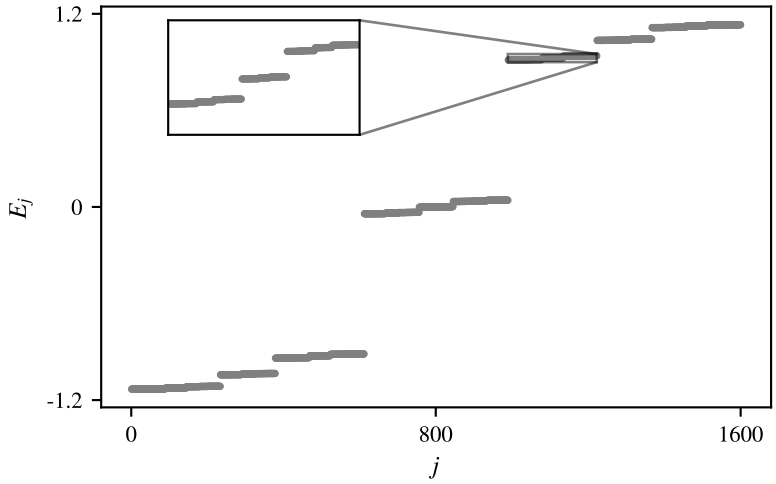

Figure 1.11: Energy spectrum of the $n = 16$ approximant Fibonacci chain, with $F_{16} = 1597$ sites. The trifurcating structure can be seen at different energy scales. Self-similarity is also visible when looking at the inset of the upper cluster's lowest quasi-band. The modulation strength has been set to $\rho \equiv t_A/t_B = 0.2$.

to as the n^{th} approximant, the size of which will be denoted by $|W_n| = F_n$. This sequence has the property

$$\lim_{n\to\infty} \frac{F_{n+1}}{F_n} = \frac{1+\sqrt{5}}{2} \equiv \phi,$$

where ϕ is called the *golden ratio*. The Fibonacci sequence is often represented in terms of word size and takes the form $\{F_n\}_{n=0}^{\infty} = \{1, 1, 2, 3, 5, 8, 13, \dots\}$. Another property is that each term can be generated recursively through:

$$F_{n+2} = F_{n+1} + F_n,$$

with $F_0 = F_1 = 1$.

Consider now the following nearest-neighbor 1D tight-binding Hamiltonian,

$$H = \sum_j t_j \left|j\right\rangle \left\langle j+1\right| + \text{h.c.}$$

By encoding the Fibonacci sequence in the hopping parameters $t_j \in \{t_A, t_B\}$, one obtains a fractal, self-similar energy spectrum, as seen in Fig. 1.11. The eigenstates of this Hamiltonian are said to be critical [130, 133, 140] and are thought to be responsible for most of the unusual properties observed in quasicrystals. We shall study this model in more detail in Chapter 5.

1.4.3 Classification of aperiodic systems

Having explored various examples of aperiodic sequences, including a detailed examination of the quasiperiodic case and its application in a tight-binding Hamil-

tonian, a natural question emerges: what differentiates these sequences from one another, both mathematically and physically? The classification of such sequences is then done from a measure theory perspective. According to the Lebesgue's decomposition theorem, the decomposition of a Borel measure on $\mathbb{R}^n$ is given by

$$\mu = \mu_{\mathrm{AC}} + \mu_{\mathrm{SC}} + \mu_{\mathrm{PP}},$$

where μ_{AC} is the absolutely continuous part, μ_{SC} is the singular continuous part, and μ_{PP} is the pure-point part [147]. For example, the hydrogen atom's Hamiltonian contains both an absolutely continuous part and a pure-point part in its spectrum.

Table 1.4: Examples of aperiodic systems and their classification. Question marks are present when the classification is still an open question [125].

Energy \ Diffraction	μ_{AC}	μ_{SC}	μ_{PP}
μ_{AC}	Spiral Lattice [148]?		Crystalline matter
μ_{SC}	Rudin-Shapiro?	Thue-Morse	Fibonacci
μ_{PP}	Amorphous matter		

Another important result in the study of aperiodic structures is the *gap labeling theorem*, which relates the properties of the energy spectrum to the singularities of the diffraction spectrum, or Fourier spectrum, of the underlying aperiodic lattice [149, 150]. Since the Fourier and energy spectra are intimately connected, the generic classification scheme is framed in terms of their respective spectral measures and interrelationships. Curiously, a singular continuous energy spectrum was once considered irrelevant in physics until the discovery of quasicrystals. Despite having a pure-point Fourier spectrum typical of periodic lattices, the Fibonacci chain exhibits an energy spectrum that is singular continuous and supported on a Cantor set of measure zero [133]. It was also shown that both the Fourier and the energy spectra are singular continuous for the Thue-Morse chain [132, 145]. A few more examples are given in Table 1.4, which is based on the review article from Ref. [125].

1.4.4 Topology in a quasiperiodic chain

Three experimental realizations of topological quasiperiodic systems are especially noteworthy [22, 23, 137]. In Ref. [22], the authors observed topological properties of quasicrystals using photonic waveguides to simulate a tight-binding Hamiltonian. The dependence on the phason angle of the quasicrystal was used to detect "topological phase transitions". That is, they smoothly interpolated between two quasiperiodic chains and observed a closing of the gap whenever the topological gap

labels on either side of the interface were distributed differently. These observations can be interpreted as topological phase transitions between phases characterized by different bulk properties.

In Refs. [23, 137], the authors studied boundary properties of the quasicrystals through pumping procedures, which cause boundary modes to traverse bulk gaps after completing a pumping cycle. Specifically, in Ref. [137], light was topologically pumped across a system of coupled single-mode waveguides. The change in quasiperiodic modulation was driven by ϕ, the phason angle, by varying the distance between the waveguides along the propagation direction z. This effectively parametrizes the Hamiltonian as $H[\phi(z)]$, which is then used to perform an adiabatic pumping cycle. The quasicrystal in this work was constructed using the André-Aubry-Harper model [151], which contains a cosine modulation of the potential incommensurate with the lattice. In Ref. [23], on the other hand, photonic topological pumping was realized for a discrete Fibonacci quasicrystal. This was possible because of a topological equivalence between the two models, implemented by a potential that smoothly interpolates between the two limits [152]. This potential was used to construct a generalized experimental setup, which allowed the study of the equivalence of the topological gaps and the pumping across them.

Given that the experimental observations of the topological properties of quasicrystals rely on a dimensional extension, we shall next describe how such this is achieved.

Chern Numbers from a 2D parent Hamiltonian. The André-Aubry-Harper model is represented by a tight-binding Hamiltonian in 1D, where the on-site potential (or the hopping parameter) is modulated by a periodic function whose period is incommensurate with the lattice. For a system with on-site modulation, the Hamiltonian is

$$\mathcal{H}(\phi) = -g\sum_j c_j^\dagger c_{j+1} + \sum_j V_j(\phi) c_j^\dagger c_j + \text{h.c.}, \tag{1.23}$$

where g is the hopping parameter, $c_j^{(\dagger)}$ is the annihilation (creation) operator of an electron at site $x_j = ja$, and $V_j(\phi) = V_0\cos(2\pi\tau x_j + \phi)$, with V_0 the strength of the on-site potential and τ the incommensurate period, i.e. some irrational number.

The topological properties associated with the gaps of this 1D model may be obtained due to the residual phason degree of freedom ϕ, which makes the potential $V_j(\phi)$ be 2π-periodic and allows for a dimensional extension to a 2D parent Hamiltonian. Interpreting ϕ as the momentum k_y in the orthogonal direction to the 1D chain, one obtains the 2D parent Hamiltonian

$$\mathcal{H}_{2D} = \sum_{m,n}\left(gc_{m,n}^\dagger c_{m+1,n} + V_0\frac{e^{2\pi i\tau m}}{2}c_{m,n}^\dagger c_{m,n+1} + \text{h.c}\right).$$

This is the well-known Hofstadter Hamiltonian of a rectangular lattice in the presence of a uniform magnetic field, with τ flux quanta per unit cell [153]. Now, $c_{m,n}^{(\dagger)}$ is the annihilation (creation) operator of an electron in a site labeled by two integers

(m, n), corresponding to the coordinates on a 2D lattice. When using a rational approximant $\tau_d = p_d/q_d$, with $p_d, q_d \in \mathbb{Z}$, it is possible to analyze the problem using magnetic translation groups and calculate the band structure of the magnetic BZ [154]. The unit cell is q_d times smaller than the real space one, and as such, one obtains q_d bands. There is a Chern number associated with each of those bands [52],

$$C_l = \int \frac{dk_x dk_y}{2\pi} F_{xy}^{(l)}(\mathbf{k}),\ l \in \{1, \cdots, q_d\}, \tag{1.24}$$

where $F_{xy}^{(l)}(\mathbf{k}) = \partial_x \mathcal{A}_y^{(l)} - \partial_y \mathcal{A}_x^{(l)}$ is the Berry curvature, $\mathcal{A}_\alpha^{(l)}(\mathbf{k}) = \langle u_l(\mathbf{k})| \partial_\alpha |u_l(\mathbf{k})\rangle$ is the Berry connection, and $|u_l(\mathbf{k})\rangle$ is the Bloch state corresponding to the l^{th} band. Recall that this topological quantity is proportional to the Hall conductivity σ_H of an electronic system at a certain filling characterized by an integer l_F, corresponding to the last band below the Fermi energy E_F [52]:

$$\sigma_H = \frac{e^2}{h} \sum_{l \leq l_F} C_l.$$

In this case, the BBC tells us that the Hall conductivity is generated by the conducting channels associated to the chiral, gapless edge states.

Going back to the 1D quasicrystal, it turns out that the Berry curvature is independent of the phason degree of freedom ϕ, therefore allowing the Chern numbers to be identified with the gap labels of the chain [137]. However, the notion of BBC is only recovered by sweeping through ϕ, as it forces boundary modes to cross the bulk gaps. This is a universal feature of topological charge pumps, independent of the model considered, and is even robust in the presence of electronic interactions and disorder [155]. The absence of anti-unitary symmetries protecting the topology of the system is responsible for this robustness.

Finally, we note that when $\tau = (\sqrt{5} - 1)/2$ (in units of the lattice constant a), which is the inverse of the golden ratio, the Hamiltonian Eq. (1.23) is topologically equivalent to the Fibonacci Hamiltonian, obtained by a discrete Sturmian sequence replacing the on-site potential: $V_j(\phi) \to v_j = \pm 1$ [130]. The Fibonacci word is generated by the discrete function

$$v_j = 2\left(\left\lfloor \frac{j+2}{\tau} \right\rfloor - \left\lfloor \frac{j-1}{\tau} \right\rfloor\right) - 1 = \pm 1.$$

This equivalence is based on the generalized interpolating Harper-Fibonacci (HF) potential function [152]

$$V_{\text{HF}}^{(\beta)}(x_j, \phi) = \frac{\tanh\left\{\beta\left[\cos(2\pi\tau x_j + \phi) - \cos(\pi\tau)\right]\right\}}{\tanh\beta},$$

for which the $\beta \to 0$ limit corresponds to the Harper modulation, and the $\beta \to \infty$ limit to the Fibonacci modulation. Consequently, the Fibonacci chain shares the topological properties of the André-Aubry-Harper model. This specific insight allowed to experimentally verify that the critical states of the Fibonacci chain emerge through a cascade of localization-delocalization transitions [138].

Part I

Topological Phases

Chapter 2

Emergent non-Hermitian models

Commonly used symbols and acronyms

Symbol/Acronym	Meaning
NH	Non-Hermitian
SSH	Su–Schrieffer–Heeger
NHSE	Non-Hermitian Skin Effect
ISR	Isospectral Reduction
PBC	Periodic Boundary Conditions
OBC	Open Boundary Conditions
$\mathcal{R}_S(E, H)$	Effective Hamiltonian for subsystem S at energy E
$H(k)$	Bloch Hamiltonian
$H_R(k, E)$	Reduced Bloch Hamiltonian energy E
$A(E)$	On-site energy of reduced models at energy E
$T_{\pm}(E)$	Nonreciprocal hoppings of reduced models at energy E
v, w	Hopping amplitudes
g	Nonreciprocity parameter
κ	Skin length scale
$\mathcal{W}$	Winding number of sublattice-symmetric Hamiltonian
ξ	Edge state penetration depth

2.1 Introduction

The investigation of toy models has been instrumental in shaping a theoretical comprehension of non-Hermitian (NH) systems. The Hatano-Nelson and the non-Hermitian Su-Schrieffer-Heeger (NH SSH) models [41, 115, 117], for instance, have become paradigmatic examples of systems hosting the NH skin-effect (NHSE) and a non-Bloch bulk-boundary correspondence, respectively. The same phenomena may occur upon departing from these idealized models but may be more challenging to describe. One way to bridge this difficulty is to reduce the complicated problem into one defined by simpler models, with additional features revealed through the reduction process.

An interesting technique— initially introduced for analyzing graphs and network models—that may be used for this purpose is the so-called isospectral reduction (ISR) [156]. The idea behind the ISR is to reduce the matrix dimensionality while preserving the spectrum of the original Hamiltonian H. This is achieved by recasting the original linear eigenvalue problem into a non-linear one. The reduced dimensionality simplifies certain tasks and may, in particular, reveal hidden structures of the system [157]. Pivoting around these favorable properties, the ISR has been applied to different problems, for instance, to yield better eigenvalue approximations [158] or to study pseudo-spectra of graphs and matrices [159]. In physics, the ISR is often encountered as an effective Hamiltonian. One example is the Brillouin-Wigner perturbation theory, where the partitioning is done in terms of degenerate subspaces of an unperturbed Hamiltonian [160]. Another example would be integrating out degrees of freedom, where the partitioning is done in Fock space, or integrating out high momentum modes [161]. In that context, the reduction provides a suitable starting point for perturbation theory. In treating scattering problems in open systems, for example, the ISR is similar to a Feshbach-Fano partitioning [162].

In the last few years, the ISR has also been applied to uncover hidden—so-called latent—symmetries [163] [1]. Latent symmetries become apparent after reduction and have been studied in several applications, including quantum information transfer [167], the design of lattices with flat bands [168] or the explanation of accidental degeneracies [169]. Very recently, latent symmetries have also been explored in waveguide networks [170, 171], including a possible application in the secure transfer of information [172].

In this work, we propose to apply the ISR to a range of one-dimensional (1D) non-Hermitian tight-binding models, such that they reduce to the paradigmatic Hatano-Nelson and the NH SSH models. This method allows us to predict the existence of various topological phases and non-standard NHSE and uncover various hitherto unexplored properties. As an example of the unusual characteristics of this class of models, our approach reveals that they exhibit an energy (or frequency)-dependent NHSE, where eigenstates can localize on either end of the systems. This energy dependence also influences the degree of localization of the NHSE.

[1] We note that it has recently been shown [164] that the concept of latent symmetry is, for the particular case of latent reflection symmetries, equivalent to the graph-theoretical concept of cospectrality [165]. A good overview of the properties of cospectrality is given in Chapter 3 of [166].

Similar behavior was recently observed in a system of coupled ring-resonators [173, 174], for which we extend the theoretical understanding. In addition, we find various topological states pinned at different non-zero energies, protected by a latent spectral symmetry that is only revealed upon applying the ISR.

As a consequence of this energy dependence, their exponential envelopes vary, a feature that is also straightforwardly explained and predicted upon using the ISR. Throughout this work, we restrict our attention to systems from which the Hatano-Nelson [115] and the NH SSH [41, 117] models emerge. It should be noted that one could also engineer other types of systems from which different models would emerge through the ISR. Indeed, the particular case of an asymmetric Hermitian system from which the conventional SSH model emerges has been recently demonstrated [175].

This article is structured as follows: in Section 2.2, we lay down the primary tool for analyzing our models. That is the ISR, which amounts to constructing an effective Hamiltonian model that is already well understood. This is used on a minimal example, where we do not a priori expect non-reciprocity to be present. The ISR allows an intuitive understanding of why the NHSE would arise in such a setup. In Section 2.3, we extend our analysis to a slightly more complex case and apply the ISR to a quasi-one-dimensional system, resulting in an "emergent" Hatano-Nelson model [115]. In this setup, we can predict the existence of an energy-dependent NHSE. In Section 2.4, we add a connection between the unit cells that leads to an "emergent" NH SSH model [117], from which a complete understanding of the topological phases can be drawn. In Section 2.5, we generalize the construction principle for which the analysis done for the previous models can be applied. Finally, in Section 2.6, we conclude by summarizing our results.

2.2 Isospectral Reduction

Given a Hamiltonian H, it is possible to partition a choice of basis into a set S and its complement $\overline{S}$ so that H can be written in block-form as

$$H \equiv \begin{pmatrix} H_{S,S} & H_{S,\overline{S}} \\ H_{\overline{S},S} & H_{\overline{S},\overline{S}} \end{pmatrix} . \tag{2.1}$$

By partitioning the eigenvalue problem $H|\psi\rangle = E|\psi\rangle$ [where $|\psi\rangle \equiv (|\psi_S\rangle, |\psi_{\overline{S}}\rangle)^T$] into the different subsets S and $\overline{S}$ and subsequently eliminating $|\psi_{\overline{S}}\rangle$, we obtain the non-linear eigenvalue problem

$$\mathcal{R}_S(E,H)|\psi_S\rangle = E|\psi_S\rangle . \tag{2.2}$$

Here,

$$\mathcal{R}_S(E,H) = H_{S,S} - H_{S,\overline{S}}\left(H_{\overline{S},\overline{S}} - E\mathbb{1}\right)^{-1} H_{\overline{S},S} , \tag{2.3}$$

is the effective Hamiltonian for the subsystem S. In the language of graph theory, $\mathcal{R}_S(E,H)$ is known as the ISR of H to S [176].

In this work, we show how the ISR allows us to understand the behavior of systems without making approximations. This is done by recognizing that the

ISR of a system may yield another (energy-dependent) known model, which is well understood. In this case, the properties of the known reduced system can be used to make predictions for the full system. However, it should be emphasized that the energy-dependent parameters that result from this construction are not truly physical. We shall now illustrate this using a simple but important example.

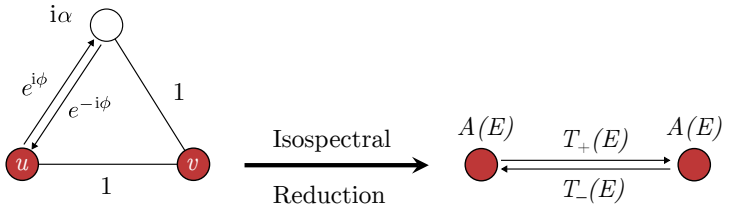

Figure 2.1: Isospectral reduction of the lossy, complex hopping model on the left to the red sites $S = \{u, v\}$ yields the non-reciprocal effective model on the right. Circles denote sites, and lines denote couplings.

A conventional and intuitive reason for the NHSE to appear is understood through the lens of nonreciprocity. An exemplary illustration of this phenomenon can be found in the Hatano-Nelson model [115]. Alternatively, the NHSE can be induced by a combination of on-site gain/dissipation and complex couplings, but this mechanism may appear less intuitive [177]. Consider the system depicted on the left-hand side of Fig. 2.1. It is a three-site non-Hermitian tight-binding Hamiltonian, with complex hopping parameters and one site featuring an imaginary on-site term. Specifically, if we enumerate the sites such that u, v are the first two, the Hamiltonian is given by

$$H = \begin{pmatrix} 0 & 1 & e^{i\phi} \\ 1 & 0 & 1 \\ e^{-i\phi} & 1 & i\alpha \end{pmatrix}.$$

The resulting effective model on the right-hand side is obtained through an ISR to the red sites. This reduced model exhibits a new on-site potential and hopping amplitudes, given by

$$A(E) = \frac{1}{E - i\alpha},$$
$$T_\pm(E) = 1 + \frac{e^{\pm i\phi}}{E - i\alpha},$$

respectively. Notice how the hopping displays asymmetry in its magnitude, i.e., $|T_+(E)| \neq |T_-(E)|$, thereby indicating non-reciprocity within the model, in the same way as the Hatano-Nelson model. By employing an ISR, both avenues for realizing the NHSE can be unified – directly by non-reciprocal couplings or reciprocal couplings but non-Hermitian on-site potentials.

In the following sections, we will modify our prototypical model slightly to have interesting and emergent phenomena taking place. By considering a one-dimensional chain of fully connected four-site models instead of three-site ones, like

in Fig. 2.1, we can obtain an energy-dependent NHSE that induces localization on both sides of the system.

2.3 Emergent Hatano-Nelson model

Let us consider the model depicted in Fig. 2.2(a). Taking the unit cell as indicated in the figure, the Bloch Hamiltonian of this lattice is given by

$$H(k) = \begin{pmatrix} \mathrm{i}\varepsilon_a - 2t_2 \sin k & t_1 + t_2 e^{-\mathrm{i}k} & t_2 + t_1 e^{-\mathrm{i}k} \\ t_1 + t_2 e^{\mathrm{i}k} & \mathrm{i}\varepsilon_b & \mathrm{i}t_3 \\ t_2 + t_1 e^{\mathrm{i}k} & -\mathrm{i}t_3 & \mathrm{i}\varepsilon_b \end{pmatrix}. \tag{2.4}$$

Here t_1, t_2, and t_3 are real-valued hopping parameters, ε_a and ε_b are on-site gains or losses, and k is the wave vector. Furthermore, we have set the lattice spacing to be equal to unity.

We note at this point that the spectrum has a mirror symmetry with respect to the $\mathrm{Re}(E) = 0$ line; cf. Figs. 2.2(b) to 2.2(d). The mirror-symmetric spectrum stems from the fact that

$$\begin{aligned} \mathcal{S}H(k)\mathcal{S}^{-1} &= -H^*(-k), \\ \mathcal{S} &= (-\sigma_z) \oplus 1, \end{aligned} \tag{2.5}$$

where σ_z acts on the two sites of the unit cell. In the literature, this symmetry is better known as $PHS^\dagger$ [27], which is one of the two non-equivalent realizations of particle-hole symmetry in a non-Hermitian system.

If we simultaneously perform an ISR to all red sites of the full lattice and take the Bloch-Hamiltonian of the resulting effective model, we obtain

$$H_R(k, E) = A(E) + T_+(E)e^{\mathrm{i}k} + T_-(E)e^{-\mathrm{i}k}, \tag{2.6}$$

in which we recognize the Hatano-Nelson model with energy-dependent on-site term $A(E)$, and hopping parameters $T_\pm(E) \equiv v(E) \pm g(E)$ [2]. Here

$$\begin{aligned} A(E) &= \mathrm{i}\left[\varepsilon_a + \frac{2\left(\varepsilon_b + \mathrm{i}E\right)\left(t_1^2 + t_2^2\right)}{\left(\varepsilon_b + \mathrm{i}E\right)^2 + t_3^2}\right], \\ v(E) &= 2\mathrm{i}\frac{\left(\varepsilon_b + \mathrm{i}E\right)t_1 t_2}{\left(\varepsilon_b + iE\right)^2 + t_3^2} \\ g(E) &= \mathrm{i}\frac{t_2 t_3\left(t_3 - t_2\right) + t_2\left(\varepsilon_b + \mathrm{i}E\right)^2 + t_1^2 t_3}{\left(\varepsilon_b + \mathrm{i}E\right)^2 + t_3^2}. \end{aligned} \tag{2.7}$$

For the ordinary Hatano-Nelson model, i.e., no energy-dependent parameters, it is well-known that the NHSE is present when $|T_+| \neq |T_-|$ [92, 115]. This condition still holds for our effective Hamiltonian. After some algebraic manipulations, it can be expressed as

$$v_R(E)g_R(E) + v_I(E)g_I(E) \neq 0. \tag{2.8}$$

[2] Unlike the original HN model, the model presented here lacks PT symmetry due to the presence of different gains and losses. Consequently, imaginary gauge transformations into Hermitian models, as presented in Ref. [95], cannot be applied.

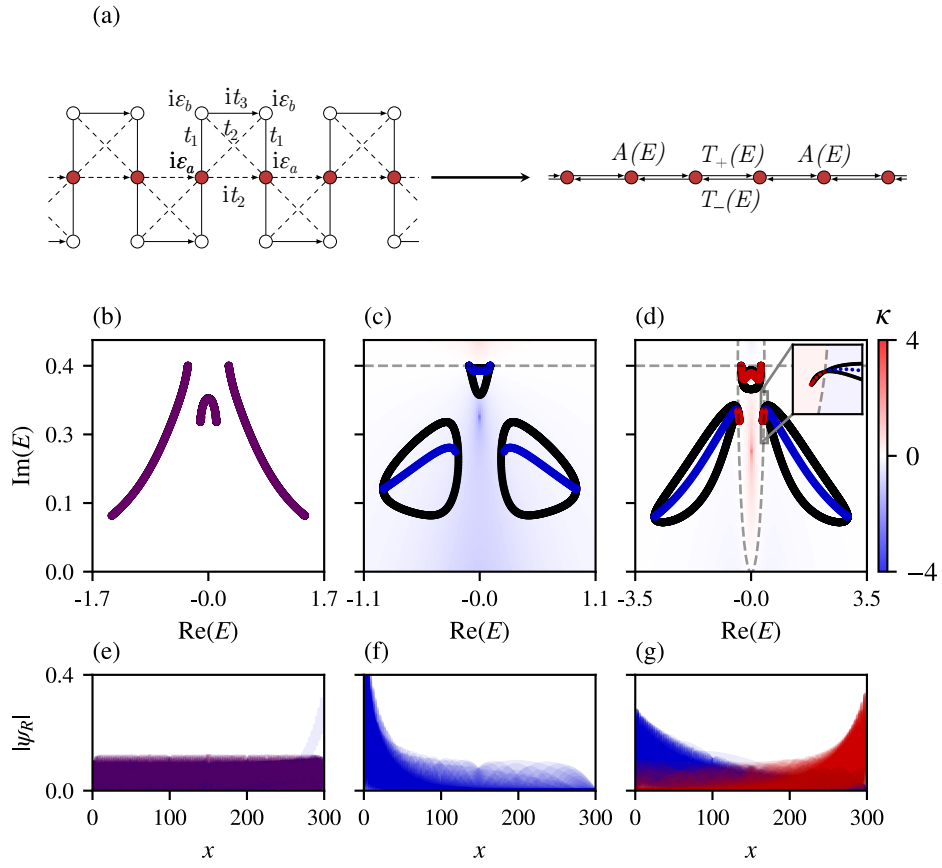

Figure 2.2: Emergent Hatano-Nelson model from ISR. (a) Lattice corresponding to the Bloch Hamiltonian given in Eq. (2.4) and its ISR to the Hatano-Nelson model with energy-dependent hopping and an energy-dependent on-site term. The gray dashed lines indicate the unit cell of the left chain, and the sites are labeled. (b-d) The complex energy spectra are presented for the system described in (a) using different parameter values: (b) $(\varepsilon_a, \varepsilon_b, t_1, t_2, t_3) = (0, 0.4, 0, 0.5, 0.3)$; (c) $(\varepsilon_a, \varepsilon_b, t_1, t_2, t_3) = (0, 0.4, 0.4, 0.2, 0.1)$; and (d) $(\varepsilon_a, \varepsilon_b, t_1, t_2, t_3) = (0, 0.4, 0.4, 1, 0.3)$. The dots are color-coded, representing left-localized (blue), right-localized (red), or bulk-like (purple) modes, with black and colored lines indicating PBC and OBC, respectively. The background displays $\kappa(E)$, where larger absolute values of κ indicate stronger localization of the corresponding skin mode. Dashed grey lines correspond to $\kappa(E) = 0$. (e-g) Right eigenstates are shown for the same parameter choices as the above panels, using the same coloring conventions.

The subscripts R and I represent real and imaginary parts, respectively. By substituting Eq. (2.7) into Eq. (2.8), it follows that the NHSE is present when t_1, t_2 and ε_b are all non-zero (see Section 2.A).

Let us now visualize the above statements in terms of the eigenvalues and eigenstates. We start by inspecting a setup with $t_1 = 0$ and show its eigenvalue spectrum in Fig. 2.2(b). The spectrum (denoted by a solid purple line) is the same for open boundary conditions (OBC) and periodic boundary conditions (PBC). The (right) eigenvectors are depicted in Fig. 2.2(e) and show, as expected, no NHSE. However, upon close inspection of Fig. 2.2(e), one can see a mode sitting at the right boundary. This is a consequence of lattice termination and is elaborated upon in Section 2.5.1.

Leaving the trivial case behind us, we investigate a setup where t_1, t_2, and ε_b are all non-zero. Specifically, we choose $(\varepsilon_a, \varepsilon_b, t_1, t_2, t_3) = (0, 0.4, 0.4, 0.2, 0.1)$. For this choice of parameters, the eigenvalue spectrum is shown in Fig. 2.2(c). The black line represents the PBC eigenvalue spectrum, which forms three simple loops in the complex energy plane. Importantly, the PBC spectrum no longer coincides with the OBC spectrum (shown in blue). The background color in this figure represents a contour plot of the skin length scale [92]

$$\kappa(E) \equiv \log \sqrt{\left| \frac{T_-(E)}{T_+(E)} \right|}. \tag{2.9}$$

We note that κ is energy-dependent, which is a consequence of the energy-dependence of the system's hopping parameters. This energy dependence is an essential difference from the ordinary Hatano-Nelson model. There, κ is constant, such that all skin modes show the same length scale. In an emergent Hatano-Nelson model, however, each mode has its skin length given by Eq. (2.9). In particular, a (right) PBC-eigenstate whose energy E lies in a region with $\kappa < 0$ ($\kappa > 0$) will be localized at the system's left (right) boundary. Since all of the system's OBC eigenvalues correspond to $\kappa < 0$, we expect all of the eigenstates to be left-localized. This is indeed the case, as can be seen from Fig. 2.2(f).

Let us now modify the parameters to realize the so-called bipolar NHSE [178]. A system with a bipolar NHSE features two classes of right eigenstates: One localized at the left boundary and the other localized at the right boundary. To find this phenomenon in our setup, we choose $(\varepsilon_a, \varepsilon_b, t_1, t_2, t_3) = (0, 0.4, 0.4, 1, 0.3)$. The system's eigenvalues are depicted in Fig. 2.2(d), which has an insect-like shape. Again, PBC (black) and OBC (blue/red) spectra do not coincide, as expected from the fact that all t_1, t_2, and ϵ_b are non-vanishing. Interestingly, $\kappa(E)$ can now take both positive and negative values. In particular, we see that Fig. 2.2(d) splits into two regions: An outer, blue area, where $\kappa < 0$, and an inner, red region, where $\kappa > 0$. These two regions are separated by the dashed-grey line representing $\kappa(E) = 0$. Since the OBC spectrum lies both in the inner and outer regions, our system features a bipolar NHSE: (Right) eigenstates whose energy E lies in the blue region are left-localized, while eigenstates with E lying in the red region are right-localized. This is demonstrated in Fig. 2.2(g), where we show the system's right eigenstates, with blue/red color corresponding to the region where the respective eigenvalue lies.

ISR does not limit itself to making predictions on the NHSE. On the contrary, it may also be used to explore the topological properties of a given system. To illustrate this feature, we focus on a different but related model in the next section.

2.4 Emergent non-Hermitian SSH Model

In this section, we study the system depicted in Fig. 2.3(a), which is a modified version of the Creutz ladder [179]. Each square forms a unit cell, interconnected by a real hopping parameter w, making this a four-band model. The momentum space Hamiltonian for this system is given by

$$H(k) = \begin{pmatrix} \mathrm{i}\varepsilon_a & t_1 & t_2 & \mathrm{i}t_2 + we^{-\mathrm{i}k} \\ t_1 & \mathrm{i}\varepsilon_b & -\mathrm{i}t_3 & t_2 \\ t_2 & \mathrm{i}t_3 & \mathrm{i}\varepsilon_b & t_1 \\ -\mathrm{i}t_2 + we^{\mathrm{i}k} & t_2 & t_1 & \mathrm{i}\varepsilon_a \end{pmatrix}, \tag{2.10}$$

where all parameters are real-valued. The setup is similar to the one used by Lee [93] to show the existence of an anomalous edge state. Our model was chosen such that its ISR to the red sites in Fig. 2.3(a) results in an energy-dependent NH SSH model [41, 117], described by the following Bloch Hamiltonian:

$$H_R(k, E) = \begin{pmatrix} A(E) & T_+(E) + we^{-\mathrm{i}k} \\ T_-(E) + we^{\mathrm{i}k} & A(E) \end{pmatrix}. \tag{2.11}$$

Here

$$A(E) = \mathrm{i}\left[\varepsilon_a + \frac{(\varepsilon_b + \mathrm{i}E)\left(t_1^2 + t_2^2\right)}{(\varepsilon_b + \mathrm{i}E)^2 + t_3^2}\right] \tag{2.12}$$

and $T_\pm(E)$ are the same as given in Eqs. (2.6) and (2.7). This reduction is graphically depicted in Fig. 2.3(a). Our model features various phases, from the NHSE to topological edge modes. This model enjoys the same $PHS^\dagger$ symmetry as the previous three-band model Eq. (2.5). However, $\mathcal{S}$ now must be built from a different partitioning and is given by $\mathcal{S} = (-\sigma_z) \oplus \mathbb{1}_{2\times 2}$.

2.4.1 Onset of the NHSE

Like the Hatano-Nelson model, the NHSE is present in the NH SSH model whenever $|T_+| \neq |T_-|$. By analogy, for our emergent NH SSH model, this results in the constraint equation $v_R(E)g_R(E) + v_I(E)g_I(E) \neq 0$. In terms of the model parameters, this leads to the condition that the NHSE is present when t_1, t_2, and ε_b are not equal to zero. This is illustrated in Fig. 2.3, where the three possible scenarios are depicted. First, Fig. 2.3(b) shows the case without skin effect, clearly indicated by similar band structures for OBC and PBC, and the corresponding right eigenstate in Fig. 2.3(e). Fig. 2.3(c) shows the band structure when the NHSE is present, but only in one direction, as indicated by $\kappa(E) > 0$. The modes localize on the right-hand side, as shown in Fig. 2.3(f). Finally, Fig. 2.3(d) shows the band structure when the bipolar NHSE is present, which can be understood from the

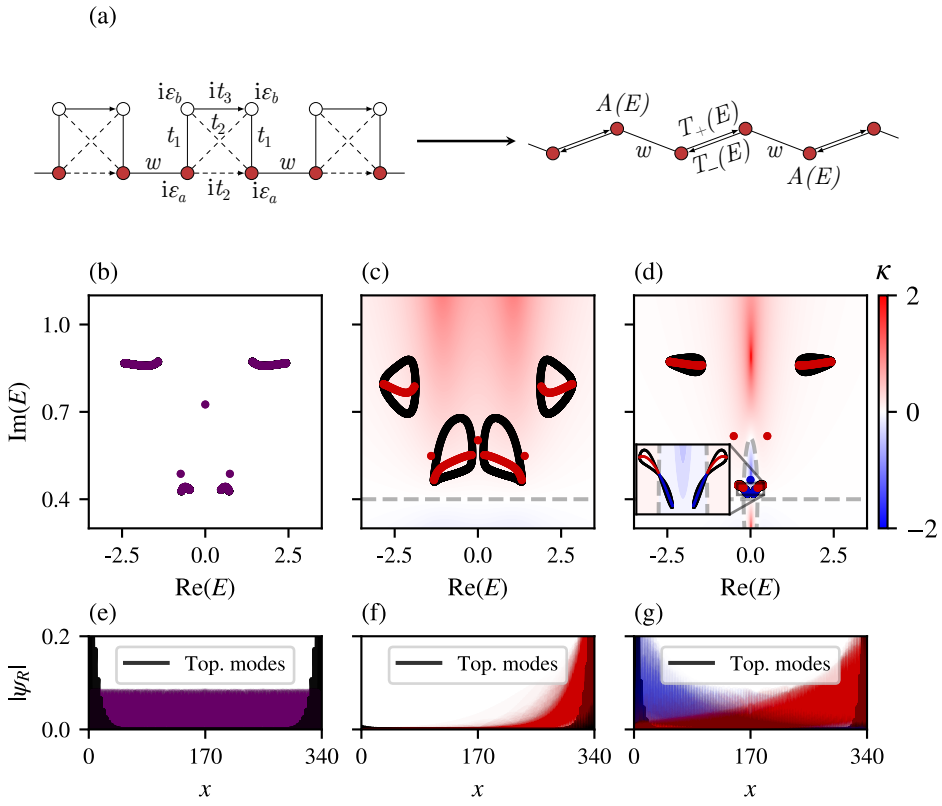

Figure 2.3: Emergent NH SSH model from ISR. (a) Lattice corresponding to the Bloch Hamiltonian given in Eq. (2.10) and its ISR to the NH SSH model with energy-dependent hopping and an energy-dependent on-site term. (b-d) The complex energy spectra are presented for the system described in (a) using different parameter values: (b) $(\varepsilon_a, \varepsilon_b, t_1, t_2, t_3) = (0.9, 0.4, 0, 0.5, 0.6)$; (c) $(\varepsilon_a, \varepsilon_b, t_1, t_2, t_3) = (0.9, 0.4, 1, 0.5, 0.9)$; and (d) $(\varepsilon_a, \varepsilon_b, t_1, t_2, t_3) = (0.9, 0.4, 0.2, 0.5, 0.2)$. In all figures, we take $w = 1.8$. The dots are color-coded, representing left-localized (blue), right-localized (red), or bulk-like (purple) modes, with black and colored lines indicating PBC and OBC, respectively. The background displays $\kappa(E)$, where larger absolute values of κ indicate stronger localization of the corresponding skin mode. Dashed grey lines correspond to $\kappa(E) = 0$. (e-g) Right eigenstates are shown for the same parameter choices as the above panels, using the same coloring conventions. We also plot the isolated topological modes in black.

contour plot of $\kappa(E)$, showing both regions of $\kappa > 0$ (red) and $\kappa < 0$ in blue. In all three situations, one can observe the presence of six topological edge modes, coming in three pairs of two degenerate modes pinned at the same energy. These are shown in black in Figs. 2.3(e)-2.3(g). We will now investigate the properties of these topological modes.

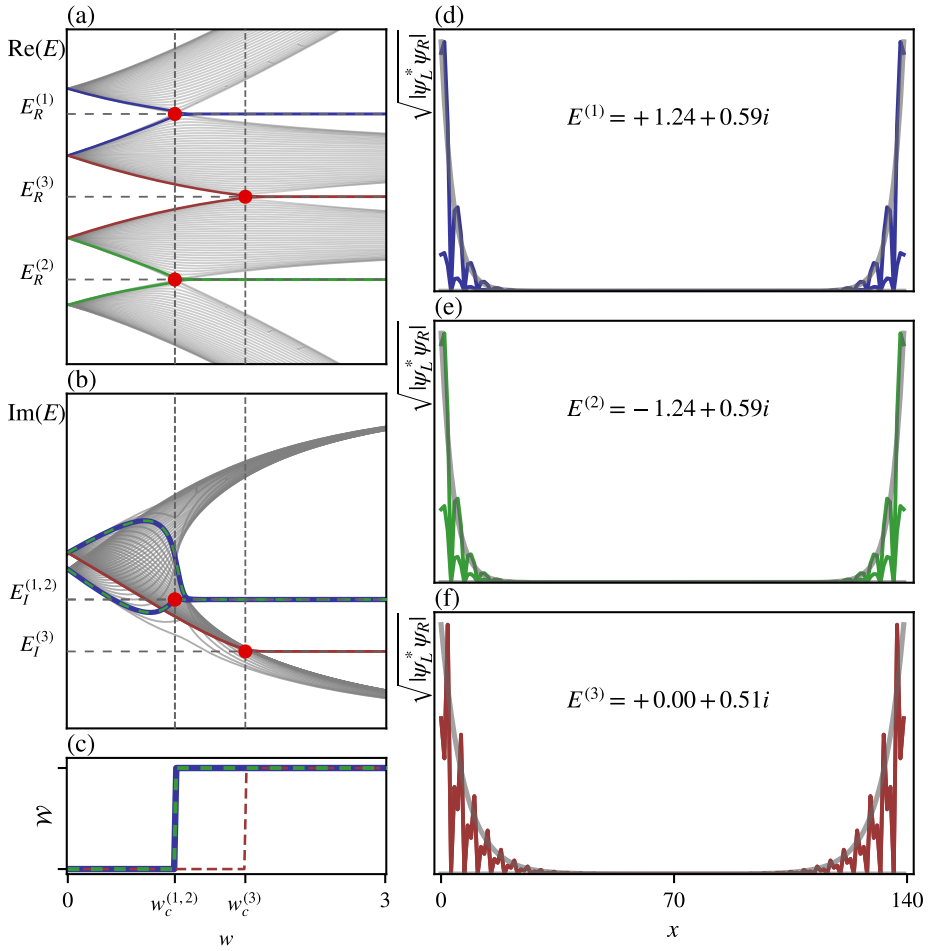

Figure 2.4: Topological phase transitions of the emergent NH SSH model as a function of w. (a) Real and (b) imaginary parts of the energy spectrum for an open chain of $N_c = 35$ unit cells. The spectra are taken for the parameter choice $(\varepsilon_a, \varepsilon_b, t_1, t_2, t_3) = (0.9, 0.4, 1, 0.5, 0.6)$.(c) The winding number given by Eq. (2.13), calculated at the three special energies E_t, clearly shows its quantization and the critical points w. (d-f) Corresponding topological edge modes, at $w = 3$, plotted together with the calculated exponential envelope in gray, with penetration depth given by Eq. (2.17). The three different colors, blue, green, and red are used consistently to mark the different edge modes [(d) to (f)], the behavior of their energies [(a) and (b)], and the values of the corresponding winding number (c).

2.4.2 Topological Edge Modes

Interestingly, we can also predict the existence of topological edge modes in the four-band model using the reduced NH SSH chain. The winding number that determines

the topological phase transition for a sublattice-symmetric 1D Hamiltonian (of which the NH SSH is an example) is given by [27]

$$\mathcal{W} = \int_{-\pi}^{\pi} \frac{dk}{4\pi i} \operatorname{Tr}\left[\sigma_z H^{-1}(k) \frac{dH(k)}{dk}\right]. \tag{2.13}$$

In our case, this expression becomes energy-dependent and is only applicable when

$$A(E) = E, \tag{2.14}$$

where $A(E)$ is defined in Eq. (2.12). This is because Eq. (2.13) is only well-defined for sublattice-symmetric systems, which in our case is a latent symmetry appearing at energies satisfying Eq. (2.14). This means that we must consider a Hamiltonian $\tilde{H}(k) \equiv H(k, E_t) - E_t \mathbb{1}_{2\times 2}$, where E_t is a solution of Eq. (2.14). For every energy satisfying this constraint, in the topological phase, there is a degenerate pair of edge states pinned at that energy. In fact, the pair is quasi-degenerate as a consequence of the finite size of the lattice. For the model at hand, there are three energies at which the transition takes place because Eq. (2.14) has three solutions. Explicit calculations of this winding number (see Section 2.A for an analytic derivation) lead to

$$\mathcal{W}(E_t) = \begin{cases} 0, & \text{if } |w| < \sqrt{|v^2(E_t) - g^2(E_t)|} \\ 1, & \text{if } |w| > \sqrt{|v^2(E_t) - g^2(E_t)|} \end{cases}. \tag{2.15}$$

Substituting the solutions E_t into Eq. (2.15) yields the three critical values w_c at which pairs of topological edge modes appear. Figs. 2.4(a) and 2.4(b) show the real and imaginary parts of the energy spectrum, respectively. The horizontal dashed lines show the calculated absolute values of the complex transition energies $E_t^{(j)} = E_R^{(j)} + E_I^{(j)}$. In contrast, the vertical dashed lines indicate the value of the predicted critical hopping parameter w_c. Robust boundary modes that persist beyond the transition point are visible in red, green, and blue. The presence of these modes can be quantified by calculating the winding number given by Eq. (2.15), as shown in Fig. 2.4(c). There is a clear jump to $\mathcal{W}(E_t) = 1$ when the critical hopping w_c is reached. Figs. 2.4(d)-2.4(f) show the corresponding edge states, with the same color coding, at $w = 3$. The values of the calculated transition energies E_t are indicated in the middle of each figure. Notice that to properly visualize the edge modes in the presence of the NHSE, $\sqrt{|\psi_L^* \psi_R|}$ is plotted rather than $|\psi_R|$. Moreover, it is important to highlight that, for each transition energy, the emergent sublattice symmetry of the reduced model ensures that the edge modes appear in pairs. This is visible in Figs. 2.4(d)-2.4(f), where a pair of edge states is shown for each energy E_t. For a further investigation of the line-gap closings of the emergent NH SSH model, we refer the reader to Section 2.B. As a final note, we see that the penetration depth of these edge states is also energy-dependent and is given by [91, 92]

$$\begin{aligned} \xi_L(E) &= \frac{1}{\log\left|\frac{v(E)-g(E)}{w}\right|}, \\ \xi_R(E) &= \frac{1}{\log\left|\frac{v(E)+g(E)}{w}\right|}, \end{aligned} \tag{2.16}$$

where the subscript L (R) stands for left (right) eigenvectors. This explains the different localization lengths observed in Figs. 2.4(d)-2.4(f). In the biorthogonal formulation the exponential envelope follows $\exp\{-x_j/2\xi_{LR}\}$, where $x_j = ja$ and

$$\xi_{LR} = \frac{\xi_L + \xi_R}{\xi_R \xi_L}. \tag{2.17}$$

This envelope is plotted in grey alongside the edge states in Figs. 2.4(d)-2.4(f).

An energy-dependent localization length is an interesting phenomenon known to occur in disordered models. However, in our case, it happens as a result of the non-Hermiticity and of the topological properties, which inherit an energy dependence from the parameters of the effective model obtained through the ISR.

2.5 Generalized construction principles

The models treated in the previous sections are individual examples of setups whose ISR has the form of an effective Hatano-Nelson or NH SSH model. In the following, we will show that one can systematically construct large families of such systems. The procedure will always be the same: an individual unit cell is built, such that its ISR to two specific sites yields equal on-site potentials, and nonreciprocal hoppings between them. Subsequently, these unit cells are connected such that either (i) a Hatano-Nelson or (ii) a NH SSH model is obtained.

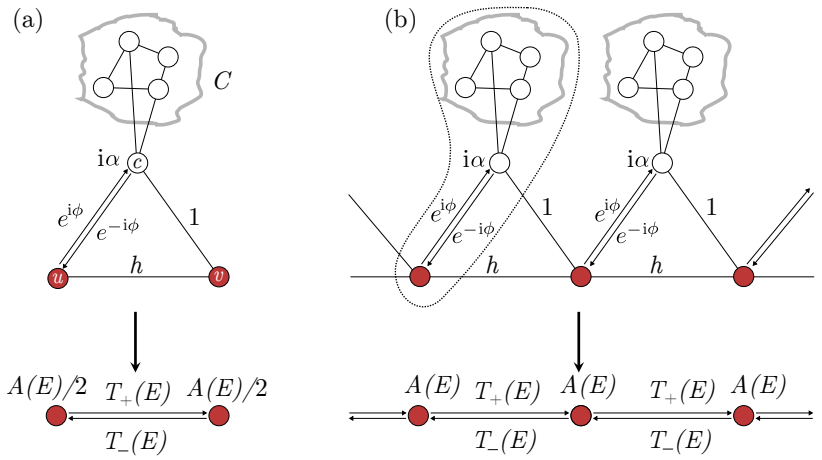

Figure 2.5: (a) ISR of the lossy, complex hopping model above onto the red sites yields the non-reciprocal effective model below. (b) Lattice realization of (a). A dashed line marks the unit cell.

2.5.1 Emergent Hatano-Nelson models

Construction principle A

The starting point for the first construction principle is a finite structure with a non-reciprocal ISR. The graphical representation of the model is sketched in Fig. 2.5(a).

The system consists of two lower sites u and v (marked in red), connected to a third site c via Hermitian couplings $\exp(i\phi)$ and 1. The site c has complex on-site potential $i\alpha$ and is further coupled to a (possibly very large) network C. For simplicity, we demand that the couplings in the network C and the couplings between this network and the site c are real-valued. However, the sites in C could have complex on-site potentials. Denoting the Hamiltonian of the resulting total system by H, its ISR to the two sites u and v yields (see Section 2.C)

$$\mathcal{R}_S(E,H) = \begin{pmatrix} A(E)/2 & T_+(E) \\ T_-(E) & A(E)/2 \end{pmatrix} .$$

Note that the exact form of $A(E)$ depends on the details of the network C.

This finite building block is now used to construct a lattice, as shown in Fig. 2.5(b), with the unit cell comprised of one site c, one network C, and *one of the two* red sites. Applying the ISR to all red sites, a Hatano-Nelson model emerges, as depicted in the lower part of Fig. 2.5(b). Importantly, since each red site of the lattice is coupled to two clouds, its on-site potential after the ISR now reads $2 \cdot A(E)/2 = A(E)$. In an open chain, the sites on the left and right end, however, will have an on-site potential of $A(E)/2$ [3].

Construction principle B

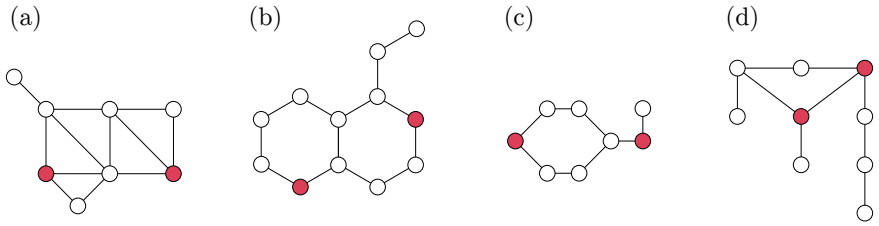

Figure 2.6: Different systems with latently symmetric sites (marked in red). In all four systems, each line corresponds to a coupling of strength one (see Refs. [167, 180] for more details regarding the design of latently symmetric setups).

The second construction principle of emergent Hatano-Nelson models relies on the concept of latent symmetry [163]. Given a system G, two sites $S = \{u, v\}$ are latently reflection symmetric if the ISR over them has the form

$$\mathcal{R}_S(E,G) = \begin{pmatrix} \mathcal{A}(E) & \mathcal{B}(E) \\ \mathcal{B}(E) & \mathcal{A}(E) \end{pmatrix} , \tag{2.18}$$

that is, if $\mathcal{R}_S(E,H)$ commutes with the permutation matrix $P := \sigma_x$. In Fig. 2.6, several setups with latently symmetric sites (marked in red) are shown. A broader overview of this topic is given in Ref. [181].

The construction scheme is sketched in Figs. 2.7(a) to 2.7(c). Fig. 2.7(a) depicts a real-symmetric subsystem G (marked by a cloud) in which two sites u and v

[3] We note that this is the reason why the non-topological edge states, as seen in Fig. 2.2(e), appear.

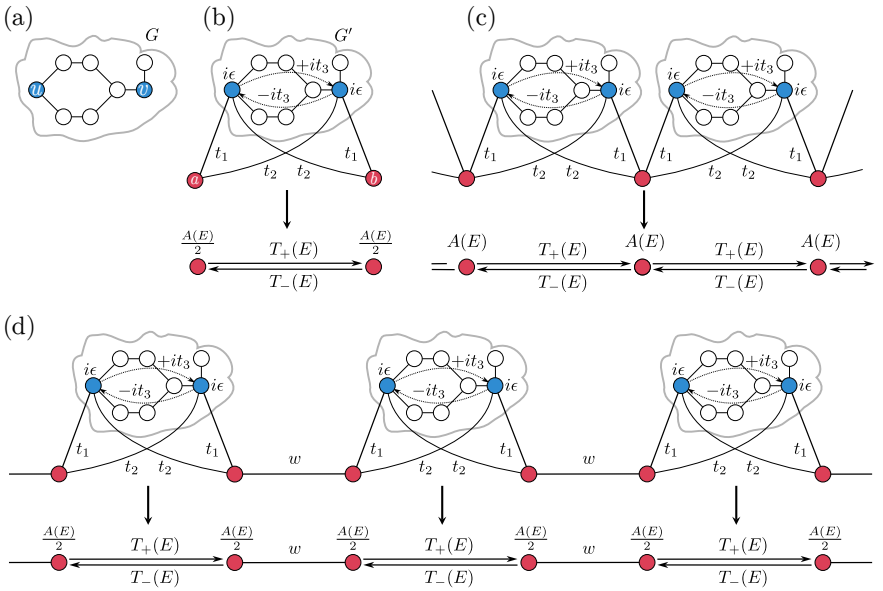

Figure 2.7: Construction scheme for the emergent Hatano-Nelson and NH SSH models. (a) The starting point: A simple setup with latently symmetric sites u, v. (b-d) ISR of the lossy, complex hopping model above onto the red sites yields the non-reciprocal effective model below.

(marked in blue) are latently symmetric. In other words, if one would perform the ISR over u, v, one would obtain Eq. (2.18). The key here is that the latent symmetry guarantees the existence of a matrix Q that commutes with the subsystem, i.e. $QG = GQ$, and which (i) permutes the sites u and v, (ii) is block-diagonal, and (iii) fulfills $Q^{-1} = Q^T = Q$ [169]. In the following, we shall use this matrix extensively.

In the next step, this subsystem is modified by adding complex on-site potentials $i\epsilon$ to u and v, which are then connected via Hermitian hoppings it_3. Note that this breaks the latent symmetry: If we denote the resulting modified subsystem by G', then the isospectral reduction of G' over u, v would read

$$\mathcal{R}_S(E, G') = \begin{pmatrix} \mathcal{A}(E) + \mathrm{i}\epsilon & \mathcal{B}(E) + \mathrm{i}t_3 \\ \mathcal{B}(E) - \mathrm{i}t_3 & \mathcal{A}(E) + \mathrm{i}\epsilon \end{pmatrix},$$

which does not commute with P. However, we have $\mathcal{R}_S(E, H)\, P = P\, \mathcal{R}_S(E, H)^T$. Due to the favorable properties of Q—in particular, its block-diagonal form—, it can be shown that $QG' = G'^T Q$.

At this point, two additional sites a and b (marked in red) are coupled to the subsystem G' with hoppings t_1 and t_2. Again employing the favorable properties of Q, it can be easily shown that the Hamiltonian H, describing the total system depicted in Fig. 2.7(b), obeys $Q'H = H^T Q'$. Here, the matrix $Q' = P \oplus Q$, with the permutation matrix P acting on the two red sites a and b. Analogously, it can

be shown that the ISR has the form

$$\mathcal{R}_S(E,H) = \begin{pmatrix} A(E)/2 & T_+(E) \\ T_-(E) & A(E)/2 \end{pmatrix}.$$

Note that one can relate $\mathcal{A}(E), \mathcal{B}(E)$ to $A(E), T_\pm(E)$, though we omit the exact relation here.

Again, a lattice can be built by taking one red site and one subsystem G' as a unit cell, see Fig. 2.7(c). Taking the ISR to all red sites of this lattice doubles the on-site potential, which then becomes $A(E)$ instead of $A(E)/2$.

2.5.2 Emergent NH SSH model

In the previous Section 2.5.1, lattices were built by taking one red site and one subsystem G' as a unit cell, which resulted in emergent Hatano-Nelson models. One could, however, also build a lattice by taking one subsystem G' and *two* red sites as a unit cell and then connect neighboring unit cells via an additional coupling w, as shown in the upper part of Fig. 2.7(d). This results in an emergent NH SSH model, which is depicted in the lower part of Fig. 2.7(d). Note that removing all complex couplings and on-site potentials would result in an effective version of the conventional SSH model. Such emergent SSH models have been recently investigated in Ref. [175].

Before concluding this work, we investigate a specific realization of the above procedure that results in an emergent NH SSH model. The setup and its ISR are depicted in Fig. 2.8(a). The resulting OBC (red and blue) and PBC (black) spectra are shown in Fig. 2.8(b) and 2.8(c), where the intercell hopping parameter is $w = 2.5$ in (b) and $w = 6.5$ in (c). This leads to the appearance of six topological edge states in (b) and eighteen in (c) (two doubly degenerate modes per energy). The overlaid transparent green circles indicate the presence of these edge modes in the OBC spectrum. The right eigenstates corresponding to the parameter choice in (b) are shown in Fig. 2.8(d). There, one can again observe the energy-dependent skin effect. Figs. 2.8(e)-2.8(g) show all six edge states that exist in (b) and their corresponding energies. Note that since there are nine solutions to the equation $A(E) - E = 0$, the total amount of possible edge states is eighteen. The double degeneracy of each energy solution is, once again, a result of the emergent sublattice symmetry.

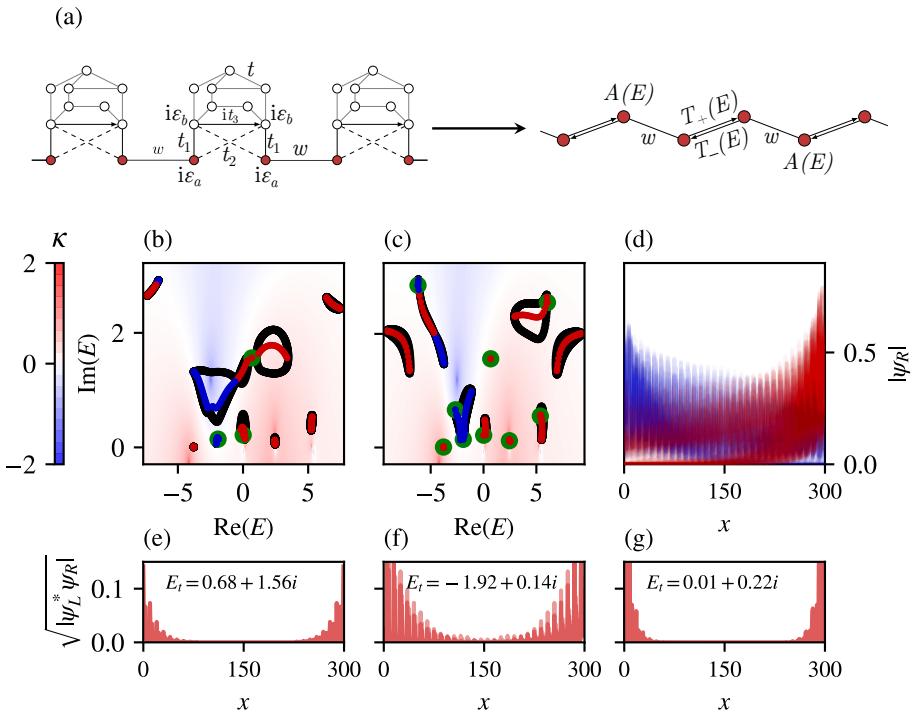

Figure 2.8: Example of a generalized construction, with a network of eight sites connected to the two sites to which the ISR is applied. (a) The model and its ISR. (b) PBC (black) and OBC (right NHSE in red, left NHSE in blue) spectra of a system with the following parameters $(a, b, t_1, t_2, t_3, t, w) = (1.19, 3.74, 1.18, 2.97, 4.24, 2.03, 2.5)$, together with the three predicted edge mode energies (with double degeneracy) shown with green circles at this particular w value. Once again, the contour plot shows the skin depth $\kappa(E)$, with its values on the color bar on the left. (c) Same as (b), but with $w = 6.5$, we now see all possible edge modes appear at nine different energies, giving a total of eighteen edge modes. (d) Right-eigenstate amplitudes corresponding to the parameter choice given in (a). (e-g) Amplitudes of all six eigenstates (two in each figure) that appear in (a), and their corresponding energies, shown in the biorthogonal basis.

2.6 Conclusion

Across many branches of physics, toy models are essential tools for understanding the key features of a given theory. In non-Hermitian physics, two such models are the Hatano-Nelson and the non-Hermitian Su-Schrieffer-Heeger (NH SSH) model. Despite their simple structure—their unit cells comprise only a single or two sites, respectively—these one-dimensional models host non-trivial boundary phenomena. In this work, we have used recent graph-theoretical insights to design systems whose so-called isospectral reduction—akin to an effective Hamiltonian—takes the form of either of these models. This procedure keeps the structure of the toy model while simultaneously enriching it by making the couplings and on-site potentials energy-dependent. Specifically, we have shown that this leads to *emergent Hatano-Nelson* or *emergent NH SSH models* featuring a two-sided non-Hermitian skin effect caused by an energy dependence of the skin localization length $\kappa(E)$. This energy dependence allows different states to be localized on different ends of the system and to have different localization strengths. For the emergent NH SSH models, we observed topological edge modes, which we could link further to a quantization of the winding number. In all cases, the original system—whose isospectral reduction becomes a Hatano-Nelson or NH SSH model—features only reciprocal (though complex-valued) couplings, with non-Hermiticity entering through complex on-site potentials (gain/loss).

We emphasize that the methods and ideas presented in this work are not limited to one-dimensional non-Hermitian Hamiltonians but are rather generic. For example, they can be applied to higher-dimensional setups, which reduce under the isospectral reduction to paradigmatic models.

Another interesting avenue to explore would be the experimental realization of the models discussed in this work. For this endeavor, the experimental setup should be able to realize (i) gain or loss, (ii) complex-valued couplings, and (iii) different network topologies. A promising platform would be electric circuit networks, which have recently been used to implement a variety of different models, including parity-time symmetric [182] or topological systems [86, 175, 183–185]. Other possible candidates for experimental realizations are photonic or acoustic waveguides and mechanical metamaterials.

2.A Detailed calculations for the NHSE and topology

2.A.1 Constraints on the NHSE

As stated in the main text, the NHSE appears whenever $|T_+(E)| \neq |T_-(E)|$, where $T_\pm(E)$ is given by Eq. (2.7). From Eqs. (2.6) and (2.7), we derive the following constraint equation

$$\frac{2t_1t_2(\varepsilon_b - E_I)\left[t_1^2t_3 + t_2\left[-t_2t_3 + t_3^2 + (\varepsilon_b - E_I)^2 + E_R^2\right]\right]}{\left[(\varepsilon_b - E_I)^2 + (t_3 - E_R)^2\right]\left[(\varepsilon_b - E_I)^2 + (t_3 + E_R)^2\right]} = 0. \tag{2.19}$$

From this constraint equation, we can easily see that the NHSE disappears whenever $t_1 = 0$, $t_2 = 0$ or $\varepsilon_b = 0$. Eq. (2.19) also allows us to determine the contour

curves of $\kappa(E) = 0$, which were plotted in Fig. 2.2(d) and Fig. 2.3(d). These are given by

$$\begin{aligned} E_I &= \varepsilon_b, \\ E_I &= \varepsilon_b \pm \frac{\sqrt{-t_2\left[E_R^2 t_2 + t_3\left(t_1^2 + -t_2^2 + t_2 t_3\right)\right]}}{t_2}. \end{aligned} \tag{2.20}$$

2.A.2 Determining the topological transition energies of the four-band model

The constraint equation that allows us to find the topological phase transition energies is $A(E) - E = 0$. This condition yields the cubic equation

$$E^3 - \mathrm{i}(\varepsilon_a + 2\varepsilon_b)E^2 - \left(t_1^2 + t_2^2 + t_3^2 + 2\varepsilon_a\varepsilon_b + \varepsilon_b^2\right)E + \mathrm{i}\left[\varepsilon_a t_3^2 + \varepsilon_b\left(t_1^2 + t_2^2\right) + \varepsilon_a\varepsilon_b^2\right] = 0. \tag{2.21}$$

This equation can be solved exactly and the solutions are used to determine the transition energies. These are given by

$$\begin{aligned} E_1 &= -\frac{1}{3}\left[A - 2^{\frac{1}{3}}\mathcal{F}_1 - 2^{-\frac{1}{3}}\mathcal{F}_2\right], \\ E_2 &= -\frac{1}{3}\left[A + (-2)^{\frac{1}{3}}\mathcal{F}_1 - \frac{1}{2}(-2)^{\frac{2}{3}}\mathcal{F}_2\right], \\ E_3 &= -\frac{1}{3}\left[A + (-1)^{\frac{2}{3}}2^{\frac{1}{3}}\mathcal{F}_1 - (-2)^{-\frac{1}{3}}\mathcal{F}_2\right], \end{aligned} \tag{2.22}$$

where we have defined the following expressions

$$\begin{aligned} \mathcal{F}_1 &= \frac{A^2 - 3B}{\left[-2A^3 + 9AB - 18C + 3\sqrt{3(4B - A^2)B^2 + 6A(2A^2 - 9B)C + 81C^2}\right]^{\frac{1}{3}}}, \\ \mathcal{F}_2 &= \left[-2A^3 + 9AB - 18C + 3\sqrt{3(4B - A^2)B^2 + 6A(2A^2 - 9B)C + 81C^2}\right]^{\frac{1}{3}}, \end{aligned}$$

with

$$\begin{aligned} A &= -\mathrm{i}\varepsilon_a + 2\mathrm{i}\varepsilon_b, \\ B &= -t_1^2 - t_2^2 - t_3^2 - 2\varepsilon_a\varepsilon_b - \varepsilon_b^2, \\ C &= \mathrm{i}\varepsilon_a t_3^2 + \mathrm{i}\varepsilon_b\left(t_1^2 + t_2^2\right) + \mathrm{i}\varepsilon_a\varepsilon_b^2. \end{aligned}$$

2.A.3 The 10-band model

The Bloch Hamiltonian for the 10-band model shown in Fig. 2.8 is given by

$$H(k) = \begin{pmatrix} \mathrm{i}\varepsilon_a & 0 & 0 & t_1 & t_2 & 0 & 0 & 0 & 0 & we^{-\mathrm{i}k} \\ 0 & 0 & 0 & 0 & t & 0 & t & 0 & 0 & 0 \\ 0 & 0 & 0 & 0 & 0 & t & t & t & 0 & 0 \\ t_1 & 0 & 0 & \mathrm{i}\varepsilon_b & -\mathrm{i}t_3 & 0 & t & 0 & t & t_2 \\ t_2 & t & 0 & \mathrm{i}t_3 & \mathrm{i}\varepsilon_b & 0 & 0 & t & 0 & t_1 \\ 0 & 0 & t & 0 & 0 & 0 & 0 & t & t & 0 \\ 0 & t & t & t & 0 & 0 & 0 & 0 & 0 & 0 \\ 0 & 0 & t & 0 & t & t & 0 & 0 & t & 0 \\ 0 & 0 & 0 & t & 0 & t & 0 & t & 0 & 0 \\ we^{\mathrm{i}k} & 0 & 0 & t_2 & t_1 & 0 & 0 & 0 & 0 & \mathrm{i}\varepsilon_a \end{pmatrix}.$$

Upon performing the ISR, the energy-dependent on-site term $A(E)$ and hopping parameters $T_\pm(E) \equiv v(E) \pm g(E)$ are given by

$$\begin{aligned} A(E) &= \mathrm{i}\varepsilon_a + \frac{\sum_{n=0}^{7} c_n E^n}{\sum_{m=1}^{8} d_m E^m} \\ v(E) &= \frac{\sum_{n=0}^{7} p_n E^n}{\sum_{m=1}^{8} d_m E^m}, \\ g(E) &= \frac{\sum_{n=0}^{7} q_n E^n}{\sum_{m=1}^{8} d_m E^m}. \end{aligned} \tag{2.23}$$

The coefficients of the polynomials can be found in Table I. They provide all the necessary ingredients to numerically solve for the nine energies that satisfy the equation $A(E) - E = 0$, and at which the topological edge modes appear.

Table 2.1: Polynomial coefficients for c_n and p_n.

n	c_n	p_n
0	$-2t^7(t_1 - t_2)^2$	$2t^7(t_1 - t_2)^2$
1	$-2t^5\left[4t\left(t_1^2 + t_1t_2 + t_2^2\right) + 3\mathrm{i}\varepsilon_b\left(t_1^2 + t_2^2\right)\right]$	$-4t^5\left[t\left(t_1^2 + 4t_1t_2 + t_2^2\right) + 3\mathrm{i}\varepsilon_b t_1 t_2\right]$
2	$4t^4\left[t\left(2t_1^2 - 3t_1t_2 + 2t_2^2\right) - 2\mathrm{i}\varepsilon_b\left(t_1^2 + t_2^2\right)\right]$	$-2t^4\left[t\left(3t_1^2 - 8t_1t_2 + 3t_2^2\right) + 8\mathrm{i}\varepsilon_b t_1 t_2\right]$
3	$2t^3\left[t\left(9t_1^2 + 2t_1t_2 + 9t_2^2\right) + 2\mathrm{i}\varepsilon_b\left(t_1^2 + t_2^2\right)\right]$	$2t^3\left[t\left(t_1^2 + 18t_1t_2 + t_2^2\right) + 4\mathrm{i}\varepsilon_b t_1 t_2\right]$
4	$t^2\left[-4t\left(t_1^2 - t_1t_2 + t_2^2\right) + 7\mathrm{i}\varepsilon_b\left(t_1^2 + t_2^2\right)\right]$	$2t^2\left[t\left(t_1^2 - 4t_1t_2 + t_2^2\right) + 7\mathrm{i}\varepsilon_b t_1 t_2\right]$
5	$-9t^2\left(t_1^2 + t_2^2\right)$	$-18t^2 t_1 t_2$
6	$-\mathrm{i}\varepsilon_b\left(t_1^2 + t_2^2\right)$	$-2\mathrm{i}\varepsilon_b t_1 t_2$
7	$t_1^2 + t_2^2$	$2t_1t_2$
8	0	0

2.A.4 Quantization of the winding number

The winding number for the reduced model in Section 2.4 is given by Eq. (2.13). Working out the trace of the product of matrices yields the following equation

Table 2.2: Polynomial coefficients for q_n and d_n.

n	q_n	d_n
0	0	$4t^7(2t+\mathrm{i}\varepsilon_b)$
1	$-6\mathrm{i}t^5t_3(t_1^2-t_2^2)$	$-2t^5\left(3\varepsilon_b^2-8\mathrm{i}\varepsilon_b t+2t^2+3t_3^2\right)$
2	$-8\mathrm{i}t^4t_3(t_1^2-t_2^2)$	$-8t^4\left(\varepsilon_b^2+2\mathrm{i}\varepsilon_b t+4t^2+t_3^2\right)$
3	$4\mathrm{i}t^3t_3(t_1^2-t_2^2)$	$2t^3\left(2\varepsilon_b^2-18\mathrm{i}\varepsilon_b t+5t^2+2t_3^2\right)$
4	$7\mathrm{i}t^2t_3(t_1^2-t_2^2)$	$t^2\left(7\varepsilon_b^2+8\mathrm{i}\varepsilon_b t+32t^2+7t_3^2\right)$
5	0	$2t^2(-2t+9\mathrm{i}\varepsilon_b)$
6	$-\mathrm{i}t_3(t_1^2-t_2^2)$	$-\varepsilon_b^2-11t^2-t_3^2$
7	0	$-2\mathrm{i}\varepsilon_b$
8	0	1

$$\mathcal{W}(E_t)=\int_{-\pi}^{\pi}\frac{dk}{2\pi\mathrm{i}}\frac{\mathrm{i}e^{\mathrm{i}k}w\left[w+a(E_t)\cos k\right]}{\left[e^{\mathrm{i}k}a(E_t)+w\right]\left[(a(E_t)+e^{\mathrm{i}k}w\right]},$$

where $a(E_t)=\sqrt{v^2(E_t)-g^2(E_t)}$. We can turn this into a contour integral on the unit circle S^1 by letting $z=e^{ik}$. This gives

$$\begin{aligned}\mathcal{W}(E_t)&=\oint_{S^1}\frac{dz}{2\pi\mathrm{i}}\frac{1}{2}\frac{w\left[2w+a\left(z+\frac{1}{z}\right)\right]}{(za+w)(a+zw)},\\&=\oint_{S^1}\frac{dz}{2\pi\mathrm{i}}\frac{1}{2a}\frac{2wz+a\left(z^2+1\right)}{z\left(z+\frac{a}{w}\right)\left(z+\frac{w}{a}\right)},\\&\equiv\oint_{S^1}\frac{dz}{2\pi\mathrm{i}}f(z),\end{aligned}$$

where we omitted the argument E_t in a, for brevity. The function $f(z)$ has two poles inside the unit circle and one outside. The pole $z_0=0$ is always inside, while $z_1=w/a$ is inside if $|w|<|a|$ (making $z_2=a/w$ outside). Using the residue theorem, we then have the following conditions

$$\mathcal{W}(E_t)=\begin{cases}\mathrm{Res}(f,z_0)+\mathrm{Res}(f,z_1), & \text{if } |w|<|a(E_t)|\\ \mathrm{Res}(f,z_0)+\mathrm{Res}(f,z_2), & \text{if } |w|>|a(E_t)|\end{cases}.$$

Since the poles are of order 1, the residues are simply given by

$$\begin{aligned}\mathrm{Res}(f,z_0)&=\lim_{z\to z_0}(z-z_0)f(z)=\frac{1}{2},\\ \mathrm{Res}(f,z_1)&=\lim_{z\to z_1}(z-z_1)f(z)=-\frac{1}{2},\\ \mathrm{Res}(f,z_2)&=\lim_{z\to z_2}(z-z_2)f(z)=\frac{1}{2},\end{aligned}$$

which finishes the proof of the quantization of the winding number,

$$\mathcal{W}(E_t)=\begin{cases}0, & \text{if } |w|<\sqrt{|v^2(E_t)-g^2(E_t)|}\\ 1, & \text{if } |w|>\sqrt{|v^2(E_t)-g^2(E_t)|}\end{cases}.$$

2.B Topological Phase Transitions in the Emergent NH SSH Model

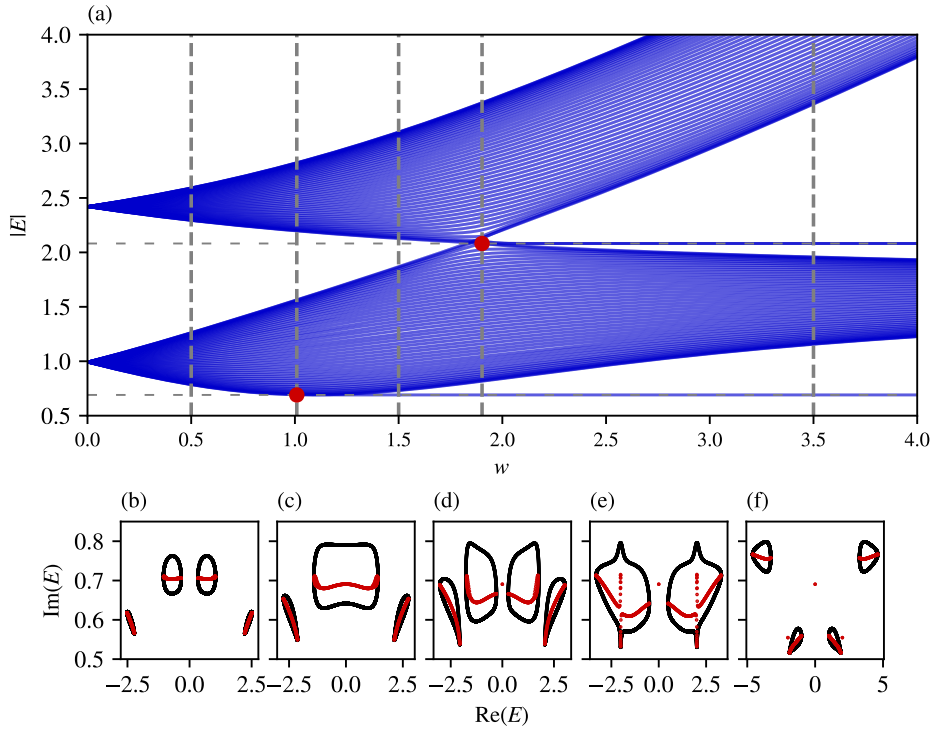

Figure 2.9: Behavior of the band structure (absolute value) of the emergent NH SSH model as described in Section 2.4. (a) Absolute value of the spectrum for $(\varepsilon_a, \varepsilon_b, t_1, t_2, t_3) = (0.8, 0.5, 1, 0.7, 1.6)$ as a function of w, for OBC with $N = 50$ unit cells. There are three topologically distinct phases. The transitions are denoted by a red dot, sitting at the intersection between the edge modes' energies (horizontal dashed gray line) and the critical w values. (b-f) The spectrum in the complex plane for fixed w corresponding to the vertical dashed gray lines in (a). Red and black points denote the OBC and PBC spectra, respectively. (b) Trivial phase, (c) first line-gap closing, (d) topological phase with one (degenerate) pair of edge modes, (e) second line-gap closing, (f) topological phase with three (degenerate) pairs of edge modes.

In this section, we analyze the different topological phases of the model described by Eq. (2.10), which reduces to the NH SSH model. Fig. 2.9(a) shows the absolute value of the spectrum as a function of w for OBC. Here, one can observe the emergence of edge modes for different values of w. The topological nature of these modes is further elaborated upon in the main text. We then take 'slices' of Fig. 2.9(a) at fixed w to obtain Figs. 2.9(b)-2.9(f), where both OBC (red) and

PBC (black) spectra are shown in the complex plane. The chosen values of w correspond to the vertical dashed lines in Fig. 2.9(a). Figs. 2.9(b), 2.9(d), and 2.9(f) show a trivial phase and two distinct topological phases, respectively. Figs. 2.9(c) and 2.9(e) show the two (OBC) line-gap closings. It should be noted that, due to the breakdown of the bulk boundary correspondence for non-Hermitian systems, the line-gap closings for OBC and PBC do not take place at the same point in parameter space.

2.C Additional information for construction principles

In the following, we show why the ISR of the structure depicted in Fig. 2.5(a) has the structure

$$\mathcal{R}_S(E,H) = \begin{pmatrix} A(E)/2 & T_+(E) \\ T_-(E) & A(E)/2 \end{pmatrix} .$$

To show this statement, we note that there exists a block-diagonal matrix Q such that $HQ = QH^T$, with

$$Q = \begin{pmatrix} 0 & e^{\mathrm{i}\phi} \\ e^{\mathrm{i}\phi} & 0 \end{pmatrix} \oplus I \equiv X \oplus I \,,$$

where we have enumerated the sites such that the two red sites u, v are sites 1 and 2. Writing $HQ = QH^T$ in block-form gives us the important relations

$$XH_{S,S} = \left(H_{S,S}\right)^T X \tag{2.24}$$

$$XH_{S,\overline{S}} = \left(H_{\overline{S},S}\right)^T \tag{2.25}$$

$$H_{\overline{S},S} = \left(H_{S,\overline{S}}\right)^T X \tag{2.26}$$

$$H_{\overline{S},\overline{S}} = \left(H_{\overline{S},\overline{S}}\right)^T . \tag{2.27}$$

Equipped with these insights, we proceed by noting that the ISR over S can be written as (see Lemma 4 in the Supplemental Material of Ref. [169])

$$\mathcal{R}_S(E,H) = H_{S,S} + \sum_{k=0}^{|\overline{S}|-1} a_k H_{S,\overline{S}} \left(H_{\overline{S},\overline{S}} - EI\right)^{k-1} H_{\overline{S},S} \tag{2.28}$$

where $|\overline{S}|$ denotes the number of sites in $\overline{S}$, and with E-dependent coefficients a_k that are obtained from the characteristic polynomial of $H_{\overline{S},\overline{S}} - EI$. Now, using

Eqs. (2.24) to (2.27) and defining $Y \equiv H_{\overline{S},\overline{S}} - EI$, we obtain

$$X\,\mathcal{R}_S(E,H)\,X^{-1} \tag{2.29}$$

$$= X H_{S,S} X^{-1} + \sum_{k=0}^{|\overline{S}|} a_k X H_{S,\overline{S}} Y^{k-1} H_{\overline{S},S} X^{-1} \tag{2.30}$$

$$= (H_{S,S})^T + \sum_{k=0}^{|\overline{S}|} a_k \left(H_{\overline{S},S}\right)^T \left(Y^{k-1}\right)^T \left(H_{S,\overline{S}}\right)^T \tag{2.31}$$

$$= \left[\mathcal{R}_S(E,H)\right]^T , \tag{2.32}$$

where we have used that $H_{\overline{S},\overline{S}}$ is symmetric. From comparing the first and last equations, it follows that the two sites of the effective Hamiltonian must have the same energy-dependent on-site potential $A(E)/2$, while the couplings $T_\pm$ between them are, in general, different from each other.

Chapter 3

Non-Hermitian Field Theory

Commonly used symbols and acronyms

Symbol/Acronym	Meaning
NH	Non-Hermitian
SSH	Su–Schrieffer–Heeger
SCBA	Self-Consistent Born Approximation
$\mathcal{H}$	Second-quantized Hamiltonian
$H(k)$	Bloch Hamiltonian
G	Green's function
$F_E(\cdots)$	Function evaluated at energy E
$\mathcal{W}(E)$	Continuum energy vorticity around base energy E
δV	Disorder fluctuations
U_0	Impurity potential strength
n_i	Impurity number density
v, w	Hopping parameters of the NH SSH model
μ	Chemical potential in the NH superconductor
Δ	Pairing strength in the NH superconductor
g	Non-reciprocity parameter

3.1 Introduction

Systems described by non-Hermitian (NH) Hamiltonians have attracted great interest in the last few years. Usually, any observable has to be represented by a Hermitian operator, such that its eigenvalues are real. However, when one considers more complicated systems, an effective description using NH Hamiltonians might be useful. A typical example arises when studying transport phenomena [186]. In this case, the effective description of an open system results in an NH Hamiltonian, giving rise to states with finite lifetimes and complex energies. More generally, while an isolated system provides an ideal platform to understand its main characteristics, a more realistic description should include coupling to its environment. Many realizations of NH models find place in mechanical, atomic, and optical systems, in which gain and loss can be controlled [111, 187–189]. This provides a solid experimental ground for theoretical studies on which the predictions can be tested.

The recent spark of interest for NH Hamiltonians arose when it was realized that a class of models allowed for an extension of the topological classification based on protecting symmetries, which exists in the Hermitian case [18, 26, 94, 118, 190–192]. There exist several differences between the Hermitian and NH classifications. For example, the bulk-boundary correspondence usually breaks down for NH topological phases and has to be replaced by a more appropriate measure of boundary phenomena, such as biorthogonal polarization [91], or through a non-Bloch bulk-boundary correspondence [92, 193, 194]. Furthermore, many models exhibit the NH skin effect [95, 195]. In addition, a recent study of the critical behavior of topological phase transitions in NH models has revealed unconventional scaling exponents, suggesting that these systems lie in different universality classes than their Hermitian counterparts [120].

In this chapter, we provide a method to study the effect of disorder on the strictly NH topological characterizations of these systems. Our framework is valid for systems that exhibit a band closing that changes the topology from a line gap to a point gap. We develop a systematic method to implement disorder by extending the discrete system to its continuous description around the band-closing point characterizing the topological phase transitions. We start our study by considering a general, discrete two-band model around the critical point, and write its continuous version. This provides us with a (1+1) dimensional field theory, which only behaves properly after selecting a single frequency component of the temporal part, as proposed by Kawabata et al. [196]. The effective (1+0) dimensional theory turns out to be topological when coupled to a gauge field. We then introduce disorder and investigate it perturbatively. The procedure is applied to the NH Su–Schrieffer–Heeger SSH model and an NH s-wave superconductor. The results are compared with numerical calculations of the discrete models. We find that strong disorder drives the system from a topological to a trivial phase in the same way.

3.2 Topological Field Theory of Two-Band Models

We consider Hamiltonians of the form

$$\mathcal{H} = \sum_k \hat{\mathbf{c}}_k^\dagger \big[\mathbf{f}(k)\cdot\boldsymbol{\sigma}\big]\hat{\mathbf{c}}_k, \tag{3.1}$$

where $\boldsymbol{\sigma} = (\sigma_1, \sigma_2, \sigma_3)$ is a vector of Pauli matrices, and the complex-valued function $\mathbf{f}(k)$ depends on the microscopic properties of the system. The annihilation operators $\mathbf{c}_k = (c_{k,A}, c_{k,B})$ are bipartite, and reflect the two-band structure of the system. An important assumption about the Hamiltonian in Eq. (3.1) is that it has at least one line-gap closing that changes the gap topology from a line-gap to a point-gap. The resulting continuum Hamiltonian is given in momentum space by

$$\mathcal{H} = \int \frac{\mathrm{d}k}{2\pi} \hat{\boldsymbol{\Psi}}^\dagger(k) \left[(\boldsymbol{\alpha}\cdot\boldsymbol{\sigma})k + \boldsymbol{\beta}\cdot\boldsymbol{\sigma}\right] \hat{\boldsymbol{\Psi}}(k), \tag{3.2}$$

where $\boldsymbol{\alpha}$ and $\boldsymbol{\beta}$ result from the linear expansion of $\mathbf{f}(k)$ around the line-gap closing and the field operator $\boldsymbol{\Psi}(x) = (\psi_A(x), \psi_B(x))^T$ obeys anticommutation relations $\{\psi_A(x_i), \psi_B(x_j)\} = \delta_{AB}\delta(x_i - x_j)$. The action associated with this Hamiltonian is given by

$$S = \int \mathrm{d}t\mathrm{d}x \boldsymbol{\Psi}^\dagger(x) \left[\mathrm{i}\partial_t + \mathrm{i}(\boldsymbol{\alpha}\cdot\boldsymbol{\sigma})\partial_x - \boldsymbol{\beta}\cdot\boldsymbol{\sigma}\right] \boldsymbol{\Psi}(x),$$

where we have set $\hbar = 1$.

Following Kawabata et al. [196], we consider a field theory in (1+1) dimensions and discard the temporal degree of freedom, which makes the theory ill-defined. The corresponding action is

$$S^{(E)} = \int \mathrm{d}x \boldsymbol{\Psi}_E^\dagger(x) \left[E + \mathrm{i}(\boldsymbol{\alpha}\cdot\boldsymbol{\sigma})\partial_x - \boldsymbol{\beta}\cdot\boldsymbol{\sigma}\right] \boldsymbol{\Psi}_E(x),$$

where the index E denotes a fixed energy. The NH topological character of the system naturally arises by coupling the matter fields to a background $U(1)$ gauge field A by virtue of minimal substitution: $\partial_x \to \partial_x - \mathrm{i}A$,

$$S^{(E)}[A] = \int \mathrm{d}x \boldsymbol{\Psi}_E^\dagger(x) \Big[G_{0,E}^{-1} + (\boldsymbol{\alpha}\cdot\boldsymbol{\sigma})A\Big] \boldsymbol{\Psi}_E(x),$$

where we introduced the (inverse) bare Green's function $G_{0,E}^{-1}$. The vacuum-to-vacuum transition amplitude is then given by

$$Z_E[A] = \int \mathcal{D}\boldsymbol{\Psi}_E^\dagger \mathcal{D}\boldsymbol{\Psi}_E e^{\mathrm{i}S^{(E)}} = \mathrm{Det}\Big[-\mathrm{i}G_{0,E}^{-1} - \mathrm{i}(\boldsymbol{\alpha}\cdot\boldsymbol{\sigma})A\Big].$$

Here, Det[...] denotes a determinant over both coordinate and spinor spaces, while det[...] only accounts for spinor space. The same convention holds for taking traces. We now shift our attention to the effective action, defined through $\exp\{\mathrm{i}S_{\mathrm{eff}}\} = Z_E[A]/Z_E[0]$. The gauge field A is assumed to be small in magnitude, such that

we can probe the system in linear response. We then have

$$\begin{aligned} S_{\text{eff}} &= -\mathrm{i}\log\{Z_E[A]/Z_E[0]\} \\ &= -\mathrm{i}\log\{Z_E[A]\} + i\log\{Z_E[0]\} \\ &= -\mathrm{i}\log\left\{\mathrm{Det}\left[-\mathrm{i}G_{0,E}^{-1} - i(\boldsymbol{\alpha}\cdot\boldsymbol{\sigma})A\right]\right\} + \mathrm{i}\log\left\{\mathrm{Det}\left[-\mathrm{i}G_{0,E}^{-1}\right]\right\} \\ &= -\mathrm{i}\,\mathrm{Tr}\left\{\log\left[-\mathrm{i}G_{0,E}^{-1} - i(\boldsymbol{\alpha}\cdot\boldsymbol{\sigma})A\right]\right\} + \mathrm{i}\,\mathrm{Tr}\left\{\log\left[-\mathrm{i}G_{0,E}^{-1}\right]\right\}, \end{aligned}$$

where in the last line we invoked the identity $\mathrm{Tr}\{\log[\dots]\} = \log\{\mathrm{Det}[\dots]\}$. The first term in the effective action can be expanded up to linear order in A

$$\begin{aligned} S_{\text{eff}} &= -\mathrm{i}\,\mathrm{Tr}\left\{\log\left[-\mathrm{i}G_{0,E}^{-1}\left(\mathbb{1} + G_{0,E}(\boldsymbol{\alpha}\cdot\boldsymbol{\sigma})A\right)\right]\right\} + \mathrm{i}\,\mathrm{Tr}\left\{\log\left[-\mathrm{i}G_{0,E}^{-1}\right]\right\} \\ &= -\mathrm{i}\,\mathrm{Tr}\left\{\log\left[\mathbb{1} + G_{0,E}(\boldsymbol{\alpha}\cdot\boldsymbol{\sigma})A\right]\right\} \\ &= -\mathrm{i}\,\mathrm{Tr}\left[G_{0,E}(\boldsymbol{\alpha}\cdot\boldsymbol{\sigma})A\right] + \mathcal{O}(A^2). \end{aligned}$$

In real space, we can write

$$G_{0,E}(x,y) = \int \frac{\mathrm{d}k}{2\pi} G_{0,E}(k) e^{\mathrm{i}k(x-y)},$$

allowing us to perform the partial trace over coordinate space

$$\begin{aligned} S_{\text{eff}} &= -\mathrm{i}\int \mathrm{d}x\mathrm{d}y\,\mathrm{tr}\left[G_{0,E}(x,y)(\boldsymbol{\alpha}\cdot\boldsymbol{\sigma})\right] A(y)\delta(x-y) \\ &= \int \frac{\mathrm{d}k}{2\pi\mathrm{i}}\,\mathrm{tr}\left[G_{0,E}(k)(\boldsymbol{\alpha}\cdot\boldsymbol{\sigma})\right]\int \mathrm{d}x A(x) \\ &\equiv \mathcal{W}(E)\int \mathrm{d}x A(x), \end{aligned} \tag{3.3}$$

where in the third line we introduced the 'energy vorticity' $\mathcal{W}(E)$ for a Hamiltonian of the form of Eq. (3.1) (A derivation of this result can be found in Appendix 3.A). Since $G_{0,E}(k)$ is diagonal in momentum space and is written in a basis of Pauli matrices, it is easily found to be

$$\begin{aligned} G_{0,E}(k) &= \left[E - (\boldsymbol{\alpha}\cdot\boldsymbol{\sigma})k - \boldsymbol{\beta}\cdot\boldsymbol{\sigma}\right]^{-1} \\ &= \frac{E + (\boldsymbol{\alpha}\cdot\boldsymbol{\sigma})k + \boldsymbol{\beta}\cdot\boldsymbol{\sigma}}{\det\left[E - (\boldsymbol{\alpha}\cdot\boldsymbol{\sigma})k - \boldsymbol{\beta}\cdot\boldsymbol{\sigma}\right]}. \end{aligned} \tag{3.4}$$

Combining Eq. Eq. (3.3) and Eq. (3.4) together with $\mathrm{tr}[\sigma_i] = 0$ and $\mathrm{tr}[\sigma_i\sigma_j] = 2\delta_{ij}$ then yields

$$\begin{aligned} \mathcal{W}(E) &= 2\int \frac{\mathrm{d}k}{2\pi\mathrm{i}} \frac{(\boldsymbol{\alpha}\cdot\boldsymbol{\alpha})k + \boldsymbol{\alpha}\cdot\boldsymbol{\beta}}{\det\left[E - (\boldsymbol{\alpha}\cdot\boldsymbol{\sigma})k - \boldsymbol{\beta}\cdot\boldsymbol{\sigma}\right]}. \\ &= 2\int \frac{\mathrm{d}k}{2\pi\mathrm{i}} \frac{||\boldsymbol{\alpha}||^2 k + \boldsymbol{\alpha}\cdot\boldsymbol{\beta}}{E^2 - ||\boldsymbol{\alpha}k + \boldsymbol{\beta}||^2}, \end{aligned} \tag{3.5}$$

where $||\boldsymbol{\alpha}||$ denotes the complex valued vector norm of $\boldsymbol{\alpha}$.

The energy vorticity captures the response of the system to the applied gauge field. It turns out that it is exactly equal to the winding of the complex energy spectrum around the point E, making it a topological invariant. Furthermore, $\mathcal{W}(E)$ appears as the current that results from the coupling to the gauge field [196]. This generically gives a proper physical interpretation of this purely NH winding number, and in the case of open boundary conditions, is an indicator of the appearance of the NH skin-effect [26, 95, 118, 193, 195, 197, 198].

3.3 Effect of Disorder

We now introduce an averaged disorder to the model to see how it affects the NH topological phases. From Eq. (3.3), we see that this means that a modification will take place in the bare Green's function through the introduction of disorder in the single particle Hamiltonian $H = H_0 + V$, where H_0 is an unperturbed Hamiltonian, and V incorporates disorder into the system. Here, we will consider the disorder to be a deviation from a zero-average configuration. We replace $V(x)$ with $\delta V(x) = V(x) - \overline{V(x)}$, with $V(x)$ a disorder potential, assumed to be of the form $V(x) = \sum_{i=1}^{N_{imp}} U(x - x_i)$, where N_{imp} is the number of impurities and $U(x)$ is an arbitrary function capturing the nature of the disorder. Thus, the spatially averaged disorder $\overline{V(x)}$ is defined as an average procedure over all x_j. The (spatial) action in the presence of disorder then reads

$$S^{(E)} = \int \mathrm{d}x \boldsymbol{\Psi}_E^\dagger(x) \left[E - H_0 - \delta V\right] \boldsymbol{\Psi}_E(x).$$

The Green's function can be expressed as a functional integral over fermionic fields

$$G_E(x,y) = -\frac{1}{Z_E} \int \mathcal{D}\boldsymbol{\Psi}_E^\dagger \mathcal{D}\boldsymbol{\Psi}_E \boldsymbol{\Psi}_E(x) \boldsymbol{\Psi}_E^\dagger(y) e^{\mathrm{i}S^{(E)}}. \tag{3.6}$$

The disorder contribution in the exponential of Eq. (3.6) is expanded, and then a disorder average is taken [199]. This procedure eliminates all terms odd in $\overline{\delta V(x)}$, and the result is the Dyson equation for the disorder averaged Green's function:

$$\begin{aligned} \overline{G_E(x,y)} &= G_{0,E}(x,y) \\ &\quad + \int \mathrm{d}x' \mathrm{d}x'' G_{0,E}(x,x') \Sigma_E(x',x'') \overline{G_E(x'',y)}, \end{aligned} \tag{3.7}$$

where the "self-energy", at a Born-approximation level, is given by

$$\Sigma_E(x,y) = -G_{0,E}(x,y) \overline{\delta V(x) \delta V(y)}. \tag{3.8}$$

For this approximation to be valid, we require the disorder potential to be weak with respect to the eigenvalues of the unperturbed system. This will then be used as the starting point in the iterative calculation of the self-consistent Born approximation (SCBA) in Section 3.4. Note that disorder averaging reinstates translational invariance, $\Sigma_E(x,y) = \Sigma_E(x-y)$. Solving the Dyson equation in momentum space yields the modified Green's function

$$\overline{G_E(k)} = \left[1 - \Sigma_E(k)\right]^{-1} G_{0,E}(k). \tag{3.9}$$

In the presence of weak disorder Eq. (3.3) and Eq. (3.9) can be combined such that the disorder averaged winding number takes the form

$$\overline{\mathcal{W}(E)} = \int \frac{\mathrm{d}k}{2\pi \mathrm{i}} \operatorname{tr}\left[(1-\Sigma_E(k))^{-1} G_{0,E}(k)(\boldsymbol{\alpha}\cdot\boldsymbol{\sigma})\right]. \tag{3.10}$$

We consider a delta-function disorder $U(x-x_j) = U_0\delta(x-x_j)$, where U_0 represents the disorder strength (scaled with units of length). This results in $\overline{\delta V(x)\delta V(y)} \approx U_0^2 n_i \delta(x-y)$, where the impurity density $n_i = N_{imp}/L$ was introduced, with L the size of the system (see Appendix Section 3.B for more details on disorder averaging). Combining this with Eq. (3.8) yields the self-energy for the delta-function disorder averaged system in momentum space

$$\Sigma_E(k) = -U_0^2 n_i \int \frac{\mathrm{d}q}{2\pi} G_0(q). \tag{3.11}$$

From Eq. (3.11), we observe that the self-energy is momentum-independent, which makes it possible to evaluate the energy vorticity analytically.

3.4 NH SSH model

A paradigmatic model to study NH topological matter in one dimension is the NH SSH model for fermions. The SSH model describes a bipartite one-dimensional chain with A and B sites obeying a sub-lattice symmetry. Here, we consider the NH SSH model with non-reciprocal intracell hopping (see fig. 1.8 in the chapter "Preliminaries"). The corresponding Hamiltonian reads

$$\mathcal{H} = (v-g)\sum_{j=1}^{N} c_{A,j}^\dagger c_{B,j} + (v+g)\sum_{j=1}^{N} c_{B,j}^\dagger c_{A,j} + w\sum_{j=1}^{N}\left(c_{B,j}^\dagger c_{A,j+1} + c_{A,j+1}^\dagger c_{B,j}\right),$$

where the intra- and inter-cell hopping are denoted by v and w, respectively. Moreover, the parameter g introduces non-reciprocity in the intracell hopping. N denotes the number of unit cells. The dispersion relation follows from diagonalizing the Hamiltonian in momentum space, yielding

$$E_\pm(k) = \pm\sqrt{w^2+v^2-g^2+2wv\cos k - 2\mathrm{i}wg\sin k}.$$

This Hamiltonian has phase transitions changing the gap topology from a line gap to a point gap and vice versa at $k = 0, \pi$. This is illustrated in Fig. 3.1. Expanding the Hamiltonian around these points then gives $\boldsymbol{\alpha} = (0, \pm w, 0)$ and $\boldsymbol{\beta} = (v \pm w, -\mathrm{i}g, 0)$, where the $\pm$ denotes the expansions around $k = 0$ and $k = \pi$, respectively. Evaluating the energy vorticity for the NH SSH model yields

$$\mathcal{W}_\pm(E) = \mp\frac{1}{2}\left[\operatorname{sgn}(\gamma-\eta) + \operatorname{sgn}(\gamma+\eta)\right], \tag{3.12}$$

with $\gamma = g/w$, $\eta = \operatorname{Re}\sqrt{M_\pm^2 - \mathcal{E}^2}$, $M_\pm = (v \pm w)/w$ and $\mathcal{E} = E/w$. The full model is described by the combination of these two Dirac models. The components

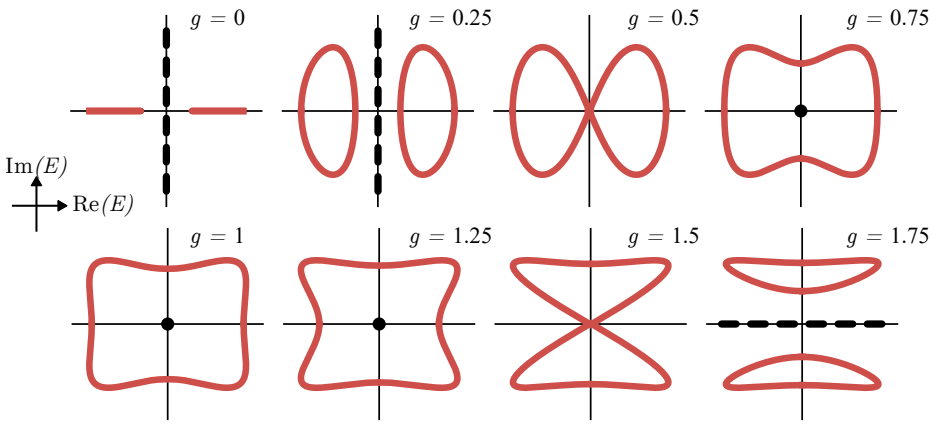

Figure 3.1: Gap structure of the non-Hermitian SSH model with parameter choices $w = 1$ and $v = 1/2$. For these values, the gap structure changes at $g = 0.5$ and $g = 1.5$. The thick dotted lines represent a line gap, while the black dot at the origin represents the point gap.

$\mathcal{W}_\pm(E)$ relate to the full invariant as $\mathcal{W}(E) = \mathcal{W}_+(E) + \mathcal{W}_-(E)$. We remark that the vorticity is equal to the difference of the two half-integer windings around the exceptional points [118], $\mathcal{W}(0) = \nu_1 - \nu_2$. These windings are defined through

$$\nu_j = \int \frac{\mathrm{d}k}{2\pi} \frac{d}{dk} \arctan\left[\frac{\mathrm{Re}\, f_2 - (-1)^j \,\mathrm{Im}\, f_1}{\mathrm{Re}\, f_1 + (-1)^j \,\mathrm{Im}\, f_2}\right],$$

where the functions $f_{1,2}$ are introduced in Eq. (3.1). The phase diagram obtained from (ν_1, ν_2) was shown in the preliminaries chapter, in Fig. 1.10 (a). Note that $\mathcal{W}(E)$ is evaluated at $E = 0$ because the NH SSH model possesses sublattice symmetry. Fig. 3.2 shows the phase diagram of the NH SSH model. This invariant renders all phases that are adiabatically connected to the Hermitian model ($g = 0$) indistinguishable from each other, which is a result of the purely NH nature of the energy vorticity $\mathcal{W}_\pm(E)$.

Upon including disorder in the NH SSH model, the self-energy, defined through Eq. (3.11), reads

$$\Sigma_E(k) = -\frac{U_0^2 n_i}{2w} \begin{pmatrix} 0 & -\mathrm{sgn}(\gamma + M_\pm) \\ \mathrm{sgn}(\gamma - M_\pm) & 0 \end{pmatrix},$$

from which the corrected Green's function readily follows through Eq. (3.9). Evaluating Eq. (3.3) using the corrected Green's function then yields the energy vorticity for the disorder averaged NH SSH model within the Born approximation (see Appendix Section 3.C for a full derivation),

$$\overline{\mathcal{W}_\pm(0)} = \frac{\mathcal{W}_\pm(0)}{1 + \left(\frac{U_0^2 n_i}{2w}\right)^2 \mathrm{sgn}(\gamma - M_\pm)\mathrm{sgn}(\gamma + M_\pm)}. \tag{3.13}$$

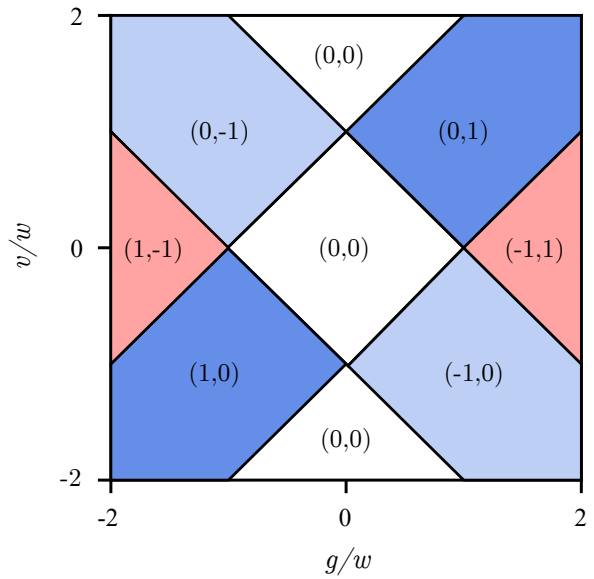

Figure 3.2: Phase diagram for the NH SSH model, obtained from the NH winding numbers $(\mathcal{W}_+(0), \mathcal{W}_-(0))$. The invariants come in pairs, where the first one is calculated around the gap closing point $k = 0$ and the second one around the point $k = \pi/a$.

Starting from this expression, we can initiate the calculation of the SCBA. We can solve it in an iterative way through

$$\Sigma_E^{(n)}(k) = -U_0^2 n_i \int \frac{\mathrm{d}q}{2\pi} \overline{G_E^{(n-1)}(q)},$$

$$\overline{G_E^{(n)}(k)} = \left[1 - \Sigma_E^{(n)}(k)\right]^{-1} \overline{G_E^{(n-1)}(k)},$$

with $\overline{G_E^{(0)}(k)} = \overline{G_E(k)}$ and $\Sigma_E^{(0)}(k)$ corresponding to the Born approximation. From this, we calculate the SCBA winding number to order n:

$$\overline{\mathcal{W}_\pm^{(n)}(0)} = \int \frac{dq}{2\pi i} \mathrm{tr} \left\{ \left[\prod_{j=1}^{n} \left(1 - \Sigma_0^{(n-j+1)}\right)^{-1} \right] G_0(q)(\boldsymbol{\alpha} \cdot \boldsymbol{\sigma}) \right\}.$$

It is found that the general expression for the n^{th} order winding number is given by that of the zeroth order one, modulated by a rational function of U_0^2,

$$\overline{\mathcal{W}_\pm^{(n)}(0)} = \frac{\sum_{j=0}^{n} a_j^{(n)} \left(\frac{U_0^2 n_i}{2w} \mathrm{sgn}(\gamma + M_\pm)\mathrm{sgn}(\gamma - M_\pm) \right)^j}{\sum_{j=0}^{n+2} b_j^{(n)} \left(\frac{U_0^2 n_i}{2w} \mathrm{sgn}(\gamma + M_\pm)\mathrm{sgn}(\gamma - M_\pm) \right)^j} \mathcal{W}_\pm(0), \tag{3.14}$$

where the coefficients $a_j^{(n)}$ and $b_j^{(n)}$ are renormalized at each iteration. We have added the analytic expressions of the first four corrections in Table 3.1.

Table 3.1: First four corrections to the winding number, as given by the SCBA. Notice that the expressions follow the general formula given by Eq.(3.14).

Order	Value	Additional expressions
$\mathcal{W}_\pm^{(0)}$	$\mp\frac{1}{2}\left[\mathrm{sgn}\left(\gamma - M_\pm\right) + \mathrm{sgn}\left(\gamma + M_\pm\right)\right]$	
$\mathcal{W}_\pm^{(1)}$	$\frac{1}{1+\mathcal{U}^2 S}\mathcal{W}_\pm^{(0)}$	$S \equiv \mathrm{sgn}(\gamma - M_\pm)\mathrm{sgn}(\gamma + M_\pm)$ $\mathcal{U} \equiv \left(\frac{U_0^2 n_i}{2w}\right)$
$\mathcal{W}_\pm^{(2)}$	$\frac{1+\mathcal{U}^2 S}{\left(1+2\mathcal{U}^2 S\right)^2 + \mathcal{U}^2 S}\mathcal{W}_\pm^{(0)}$	
$\mathcal{W}_\pm^{(3)}$	$\frac{\xi}{\left(\xi+2\mathcal{U}^2 S\right)^2 + \mathcal{U}^2 S}\mathcal{W}_\pm^{(0)},$	$\xi = \frac{\left(1+2\mathcal{U}^2 S\right)^2 + \mathcal{U}^2 S}{1+\mathcal{U}^2 S}$
$\mathcal{W}_\pm^{(4)}$	$\frac{\xi\Omega}{\left(\Omega+\varphi\mathcal{U}^2 S\right)^2 + \xi^2\mathcal{U}^2 S}\mathcal{W}_\pm^{(0)}$	$\Omega \equiv \left(\xi+2\mathcal{U}^2 S\right)^2 + \mathcal{U}^2 S$ $\varphi \equiv 2\xi + 4\mathcal{U}^2 S + 1$

Several iterations of the SCBA, corresponding to different regions in Fig. 3.2, are plotted in Fig. 3.3, indicating that the curve converges to a sharper transition as the number of iterations grows. We observe that $\mathcal{W}_+(0)$ ($\mathcal{W}_-(0)$) is driven from minus (plus) one to zero [Fig. 3.3(a)]. For phases where either $\mathcal{W}_\pm(0)$ is already zero in the unperturbed system, they remain zero [Fig. 3.3(b,c)], as can be inferred from Eq. (3.13). The disorder implementations in the continuum and discrete models are different in nature. It is, therefore, sensible to make a comparison between the models based on the spatial two-point correlations of the disorder potential. In the continuous model, it takes the form $\overline{\delta V(x)\delta V(y)} = U_0^2 n_i \delta(x-y)$, while in the discrete model, it is $\overline{V_i V_j} = (V_0^2/3)\delta_{ij}$. We used $n_i = 0.025$ to compare the transitions in Fig. 3.3, but one should be aware that the impurity density n_i influences the location and sharpness of the transition.

To study the influence of impurity density, we also computed the averaged energy vorticity in the SCBA as a function of impurity density and plotted the results in Fig. 3.4. One observes that higher impurity density leads to an earlier onset of the phase transition. This behavior is to be expected because a higher impurity density yields a more disordered system.

3.5 NH s-wave Superconducting Chain

Now, consider a spinful ($S = 1/2$) superconducting chain given by the following Hamiltonian:

$$\begin{aligned}\mathcal{H} = & \, w\sum_{j,s}(c_{j,s}^\dagger c_{j+1,s} + \text{h.c.}) - \mu\sum_{j,s}(c_{js}^\dagger c_{js} - 1) \\ & + \Delta\sum_j (c_{j,\uparrow}^\dagger c_{j+1,\downarrow}^\dagger + \text{h.c.}) + g\sum_j (c_{j,\uparrow}^\dagger c_{j,\downarrow}^\dagger - c_{j,\downarrow}c_{j,\uparrow}),\end{aligned}$$

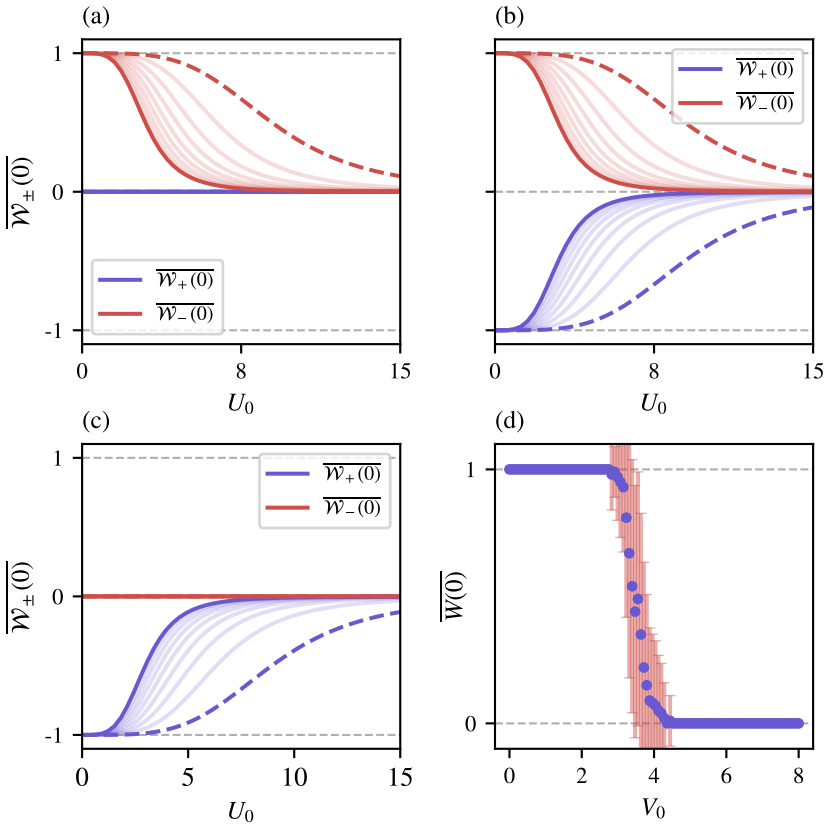

Figure 3.3: Disorder-driven topological to trivial phase transition in the NH SSH model. (a-c) Average energy vorticity $\mathcal{W}_+(0)$ and $\mathcal{W}_-(0)$ as a function of U_0 starting from the clean phase, with parameters (a) $(v, w, g, n_i) = (0.5, 1, 2, 0.025)$, (b) $(v, w, g, n_i) = (1, 1, 1, 0.025)$ and (c) $(v, w, g, n_i) = (-1, 1, 1, 0.025)$, corresponding to three NH topologically distinct phases. A transition from the topological to the trivial phase is clearly observed. The dashed line corresponds to the Born approximation calculation, while the consecutive lines correspond to the multiple iterations of the SCBA. Note that the energy vorticity shows non-integer values around the critical point because it is an averaged quantity. (d) Numerically calculated average energy vorticity for the discrete NH SSH model upon inclusion of on-site disorder. The calculations are done for $N = 100$ cells, $(v, w, g) = (1, 1, 1)$, and averages were taken over 100 disorder realizations.

where $s = \uparrow, \downarrow$ represents spin, w is the hopping parameter, μ the chemical potential, Δ the nearest-neighbor superconducting pairing strength, and the non-Hermiticity is introduced through the parameter g, representing an imbalance in the on-site superconducting pairing. The Hermitian model exhibits nontrivial topological phases, manifested through the presence of Majorana modes at the boundaries of the open

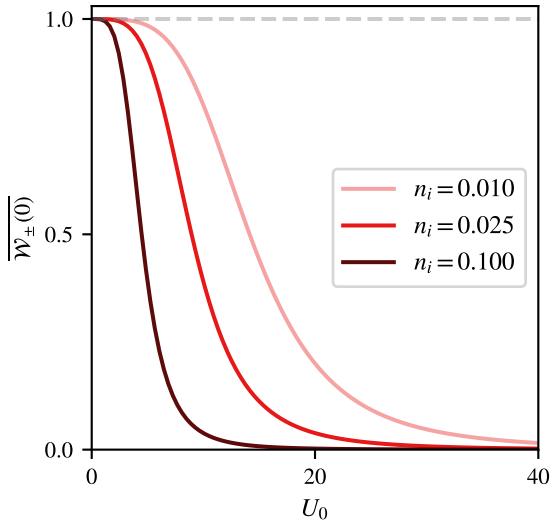

Figure 3.4: Dependence of $\overline{\mathcal{W}_{-}(0)}$ on the impurity density n_i in the SCBA for parameters $(v, w, g) = (0.5, 1, 1)$.

system [200]. Here, we include an NH term to extend the topological phase diagram and study its purely NH part. For simplicity, we set $\Delta = w$. Diagonalizing the Hamiltonian in momentum space results in two bands $E_{\pm}(k)$,

$$E_{\pm}(k) = \pm\sqrt{w^2 + \mu^2 - g^2 - 2w\mu\cos k - 2\mathrm{i}wg\sin k},$$

for which a line-gap closing occurs at $k = 0, \pi$. The field theory around those points is then readily obtained from the coefficients in Eq. (3.2), $\boldsymbol{\alpha} = (0, \mp w, 0)$ and $\boldsymbol{\beta} = (0, -\mathrm{i}g, \pm w - \mu)$. The winding number takes exactly the same form as for the SSH model. It is given by Eq. (3.12), but with $M_{\pm} \equiv (\pm w - \mu)/w$. The inclusion of disorder gives a similar result as obtained for the SSH model.

3.6 Comparison to Numerical Calculations of Disorder in the discrete case

We are interested in evaluating the robustness of the energy vorticity when disorder is introduced in the system. For the lattice model, we have [26, 27]

$$\mathcal{W}(E) = -\int_{\mathrm{BZ}} \frac{\mathrm{d}k}{2\pi\mathrm{i}} \frac{d}{dk} \log\left\{\det\left[H(k) - E\right]\right\}. \tag{3.15}$$

Introducing disorder often leads to a loss of translational invariance. As a result, it is no longer possible to obtain the Bloch Hamiltonian $H(k)$, rendering Eq. (3.15) useless. This problem is solved by introducing a Peierls-like phase in the intercell

hopping [26], yielding (for the NH SSH model)

$$\mathcal{H}(\Phi) = (v-g)\sum_{j=1}^{N} c_{A,j}^{\dagger} c_{B,j} + (v+g)\sum_{j=1}^{N} c_{B,j}^{\dagger} c_{A,j} + w\sum_{j=1}^{N}\left(e^{+i(\Phi/N)} c_{B,j}^{\dagger} c_{A,j+1} + \text{h.c.}\right),$$

The Hamiltonian $H(\Phi)$ itself is not periodic upon increasing the flux Φ by 2π, but the quantity $\text{Det}\left[H(\Phi)\right]$ is [26]. This allows us to define

$$\mathcal{W}(E) = -\int_0^{2\pi} \frac{\mathrm{d}\Phi}{2\pi \mathrm{i}} \frac{d}{d\Phi} \log\left\{\det\left[\mathcal{H}(\Phi) - E\right]\right\}. \tag{3.16}$$

While the two expressions for $\mathcal{W}(E)$ look very similar, it is important to realize that the latter is a function of the real-space Hamiltonian. This has the important consequence that we no longer require translational invariance to calculate $\mathcal{W}(E)$. We consider the disorder potential $V = \sum_{j=1}^{N} V_j \left(c_{j,A}^{\dagger} c_{j,A} + c_{j,B}^{\dagger} c_{j,B}\right)$. The values of V_j are sampled from a uniform distribution $[-V_0, V_0]$, where V_0 is the disorder strength. In Fig. 3.3(d), we plot the results obtained by averaging over 100 realizations of disorder for the same parameter values used for the continuum model shown in Fig. 3.3(b). We observe that as the disorder strength increases, the system is driven towards a trivial state, in which the energy vorticity winding number is zero, which agrees with the general features observed from the analytic derivations. Note that this kind of disorder breaks the sublattice symmetry of the system and leads to an earlier onset of the phase transition. If, instead, one would implement disorder in the hopping amplitudes in a uniform way, the symmetry would be preserved, and the phase transition would occur for higher values of V_0. However, the averaging procedure in the continuum model does not distinguish between these two forms of lattice disorder. To see this, consider adding a random variable to the amplitudes v and w. In the continuum model, this amounts to adding a disorder potential that couples to the fermion field components $\psi_A(x)$ and $\psi_B(x)$,

$$H_d = \int dx \mathbf{\Psi}^{\dagger} \delta V(x) \sigma_1 \mathbf{\Psi}.$$

Upon taking the disorder average, the terms with odd powers of disorder fluctuations vanish and we are left with the nearest-order contribution of the self-energy given by

$$\Sigma_E(x,y) = -G_{0,E}(x,y)\overline{\delta V(x)\sigma_1 \delta V(y)\sigma_1}. \tag{3.17}$$

From Eq. (3.17), we see that since $\sigma_1^2 = \mathbb{1}$, we end up with the same contribution as Eq. (3.8). This means that the continuum model cannot distinguish between a sublattice-symmetry preserving hopping disorder and the symmetry-breaking on-site disorder of the lattice model. This sets up a boundary in the current approach, limiting the application of the field theory description. Similar results were obtained in the context of Anderson localization using the replica method [201].

3.7 Conclusions

We introduced a generic field-theoretical method to analytically study the effect of disorder in one-dimensional two-band NH models that feature one or more band closing points. We have shown how the intrinsically NH topological phases of these systems are affected by disorder within the SCBA. A NH topological invariant naturally arises when coupling the continuum field theory to a background gauge field, and is expressed in terms of a trace over the momentum-space Green's function. The resulting change in Green's function can then be tracked when we apply averaging procedures in the perturbative expansion. We apply these ideas to the paradigmatic NH SSH model and a model featuring NH s-wave superconductivity. The two models exhibit very similar dispersion relations and are, therefore, equally influenced by the disorder. One would expect these transitions to be extremely sharp, as they are represented by a topological quantity. However, the computations represent averages over disorder realizations, which smooths out the transitions. This feature is even more prominent in the analytic model. Nonetheless, the results still allow us to capture the fact that a topological phase transition occurs upon the introduction of sufficiently strong disorder, which is expressed by a change in the averaged energy vorticity.

One might also wonder how disorder affects the skin modes. This has been studied previously using numerical approaches [26, 197, 202], but it would be interesting to investigate whether the current framework provides analytic tools to understand this effect. In addition, one could use the replica method to obtain further insight into the effects of disorder, as done in a study of disordered topological semimetals [203]. The use of the replica method may produce a richer phenomenology and new insights.

Finally, it would be interesting to investigate the effect of interactions in these NH topological models. We can apply the same techniques to study their effects on the winding number by simply replacing the bare Green's function with an interacting one. We are confident that the methodology developed here will stimulate further research in this direction.

3.A Energy vorticity in the continuum limit

Starting from Eq. (13) of the main text,

$$\mathcal{W}(E) = -\int_{\mathrm{BZ}} \frac{\mathrm{d}k}{2\pi\mathrm{i}} \frac{d}{dk} \log\left\{\det\left[H(k) - E\right]\right\},$$

and taking the continuum limit stretches the integration bounds to encompass the whole real line. Furthermore, we should substitute $H(k) = (\boldsymbol{\alpha}\cdot\boldsymbol{\sigma})k + \boldsymbol{\beta}\cdot\boldsymbol{\sigma}$,

$$\begin{aligned}
\mathcal{W}(E) &= -\int_{-\infty}^{\infty} \frac{\mathrm{d}k}{2\pi\mathrm{i}} \frac{d}{dk} \log\left\{\det\left[(\boldsymbol{\alpha}\cdot\boldsymbol{\sigma})k + \boldsymbol{\beta}\cdot\boldsymbol{\sigma} - E\right]\right\} \\
&= -\int_{-\infty}^{\infty} \frac{\mathrm{d}k}{2\pi\mathrm{i}} \frac{d}{dk} \mathrm{tr}\left\{\log\left[(\boldsymbol{\alpha}\cdot\boldsymbol{\sigma})k + \boldsymbol{\beta}\cdot\boldsymbol{\sigma} - E\right]\right\} \\
&= -\int_{-\infty}^{\infty} \frac{\mathrm{d}k}{2\pi\mathrm{i}} \mathrm{tr}\left\{\frac{d}{dk} \log\left[(\boldsymbol{\alpha}\cdot\boldsymbol{\sigma})k + \boldsymbol{\beta}\cdot\boldsymbol{\sigma} - E\right]\right\}.
\end{aligned}$$

Performing the derivative yields

$$\mathcal{W}(E) = -\int_{-\infty}^{\infty} \frac{\mathrm{d}k}{2\pi\mathrm{i}} \mathrm{tr}\left\{\left[(\boldsymbol{\alpha}\cdot\boldsymbol{\sigma})k + \boldsymbol{\beta}\cdot\boldsymbol{\sigma} - E\right]^{-1} (\boldsymbol{\alpha}\cdot\boldsymbol{\sigma})\right\}.$$

Using $G_{0,E}^{-1}(k) = E - (\boldsymbol{\alpha}\cdot\boldsymbol{\sigma})k - \boldsymbol{\beta}\cdot\boldsymbol{\sigma}$, we can write

$$\mathcal{W}(E) = \int_{-\infty}^{\infty} \frac{\mathrm{d}k}{2\pi\mathrm{i}} \mathrm{tr}\left[G_{0,E}(k)(\boldsymbol{\alpha}\cdot\boldsymbol{\sigma})\right],$$

which is equal to Eq. (3.3) of the main text.

3.B Derivation of the disorder averaged Green's function

In this section, we will show the derivation leading to the disorder averaged Green's function. All sub-scripted E's will be dropped in this section for notational convenience. Let us start from the definition of the Green function

$$G(x, x') = -\frac{1}{Z}\int \mathcal{D}\psi^\dagger \mathcal{D}\psi\, \psi(x)\psi^\dagger(x') e^{\mathrm{i}S}, \tag{3.18}$$

where the action S is given by

$$S = \int \mathrm{d}x \psi^\dagger(x)\left[E - H_0 - \delta V\right]\psi(x).$$

Here, H_0 is some one-particle quadratic Hamiltonian, and δV is the disorder potential, which is zero on average. For weak disorder strength, this action can be

treated perturbatively,

$$\begin{aligned} Z &= \int \mathcal{D}\psi^\dagger \mathcal{D}\psi e^{\mathrm{i}S} \\ &= \int \mathcal{D}\psi^\dagger \mathcal{D}\psi \Big[1 + \mathrm{i}\int \mathrm{d}y \psi^\dagger(y)\delta V(y)\psi(y) + \frac{\mathrm{i}^2}{2}\int \mathrm{d}y\mathrm{d}z \psi^\dagger(y)\delta V(y)\psi(y) \\ &\qquad \times \psi^\dagger(z)\delta V(z)\psi(z) + \dots\Big] e^{\mathrm{i}S_0} \\ &= Z_0\Big[1 + \mathrm{i}\int \mathrm{d}y G_0(y,y)\delta V(y) + \frac{\mathrm{i}^2}{2}\int \mathrm{d}y\mathrm{d}z\Big(G_0(y,y)G_0(z,z) - \\ &\qquad G_0(z,y)G_0(y,z)\Big)\delta V(y)\delta V(z)\Big], \end{aligned} \tag{3.19}$$

and

$$\begin{aligned} ZG(x,x') = &-\int \mathcal{D}\psi^\dagger\mathcal{D}\psi\, \psi(x)\psi^\dagger(x')\left(1 + \mathrm{i}\int \mathrm{d}y\psi^\dagger(y)\delta V(y)\psi(y) + \right. \\ &\left. \frac{\mathrm{i}^2}{2}\int \mathrm{d}y\mathrm{d}z\psi^\dagger(y)\delta V(y)\psi(y)\psi^\dagger(z)\delta V(z)\psi(z) + \dots\right) e^{\mathrm{i}S_0} \\ = Z_0 &\Big[G_0(x,x') + \mathrm{i}\int \mathrm{d}y\Big(G_0(x,x')G_0(y,y) - G_0(x,y)G_0(y,x')\Big)\delta V(y) + \\ &\frac{\mathrm{i}^2}{2}\int \mathrm{d}y\mathrm{d}z\Big(G_0(x,x')G_0(y,y)G_0(z,z) + G_0(x,x')G_0(y,z)G_0(z,y) - \\ &2G_0(x,y)G_0(x',y)G_0(z,z) + 2G_0(x,z)G_0(y,x')G_0(z,y)\Big)\delta V(y)\delta V(z)\Big] \end{aligned} \tag{3.20}$$

where S_0, G_0 and Z_0 denote the unperturbed action, Green's function and vacuum-to-vacuum transition amplitude, respectively. Wick's theorem has been used extensively in the above. Substituting Eq. (3.19) and Eq. (3.20) in Eq. (3.18) then yields, to second order, in $V(x)$

$$\begin{aligned} G(x,x') = G_0(x,x') - \mathrm{i}\int \mathrm{d}y G_0(x,y)\delta V(y)G_0(y,x') + \\ \mathrm{i}^2\int \mathrm{d}y\mathrm{d}z G_0(x,y)\delta V(y)G_0(y,z)\delta V(z)G_0(z,x'), \end{aligned}$$

or, up to any order in $V(x)$

$$G(x,x') = G_0(x,x') + \int \mathrm{d}y\mathrm{d}z G_0(x,y)\Sigma(y,z)G(y,x'), \tag{3.21}$$

where $\Sigma(y,z) = -i\delta V(y)\delta(y-z)$. This follows from the fact that any disconnected Green's function contribution from the numerator gets canceled by the denominator contribution at any order, and we can extend the derivation to all orders. Recall that $\delta V(x)$ is defined as

$$\delta V(x) = V(x) - \overline{V(x)},$$

with $V(x) = \sum_{i=1}^{N_{imp}} U(x - x_i)$. The disorder average was then defined in the main text as

$$\overline{V(x)} = \frac{1}{L^{N_{imp}}} \int \mathrm{d}x_1 \mathrm{d}x_2 \cdots \mathrm{d}x_{N_{imp}} V(x).$$

By definition, we have $\overline{\delta V(x)} = 0$, such that the terms linear in $\delta V(x)$ in Eq. (3.21) vanish upon taking the disorder average. This then yields

$$\overline{G(x,x')} = G_0(x,x') + \mathrm{i}^2 \int \mathrm{d}y \mathrm{d}z G_0(x,y) G_0(y,z) \overline{\delta V(y) \delta V(z)}\, \overline{G(y,x')},$$

in which we recognize the self-energy

$$\Sigma(y,z) = -G_0(y,z) \overline{\delta V(y) \delta V(z)}. \tag{3.22}$$

The average of the product of potential terms simplifies to

$$\overline{\delta V(y) \delta V(z)} = \overline{V(y) V(z)} - \overline{V(y)}\, \overline{V(z)}.$$

Taking delta-peaked disorder, i.e. $U(x - x_i) = U_0 \delta(x - x_i)$, we find $\overline{V(y)} = U_0 n_i$ and

$$\begin{aligned}
\overline{V(y)V(z)} &= \frac{1}{L^{N_{imp}}} \int \mathrm{d}x_1 \mathrm{d}x_2 \cdots \mathrm{d}x_{N_{imp}} U_0^2 \sum_{i=1}^{N_{imp}} \sum_{j=1}^{N_{imp}} \delta(y - x_i) \delta(z - x_j) \\
&= \frac{U_0^2}{L^{N_{imp}}} \left(L^{N_{imp}-1} N_{imp} \delta(y - z) + L^{N_{imp}-2} N_{imp} (N_{imp} - 1) \right) \\
&\approx U_0^2 n_i^2 + U_0^2 n_i \delta(y - z),
\end{aligned} \tag{3.23}$$

for $N_{imp} \gg 1$. This leads to

$$\Sigma(y,z) = -U_0^2 n_i G_0(y,z) \delta(y - z),$$

with constant Fourier components, given by

$$\Sigma(k) = -U_0^2 n_i \int \frac{\mathrm{d}q}{2\pi} G_0(q).$$

3.C Calculations for the non-Hermitian SSH model

The SSH Hamiltonian reads

$$\mathcal{H} = \sum_k \mathbf{c}_k^\dagger \begin{pmatrix} 0 & v - g + we^{-\mathrm{i}k} \\ v + g + we^{\mathrm{i}k} & 0 \end{pmatrix} \mathbf{c}_k.$$

Expanding the exponential up to linear order allows one to write the matrix as $(\boldsymbol{\alpha} \cdot \boldsymbol{\sigma})k + \boldsymbol{\beta} \cdot \boldsymbol{\sigma}$, with the coefficients

$$\boldsymbol{\alpha} = \begin{pmatrix} 0 \\ \pm w \\ 0 \end{pmatrix}, \qquad \boldsymbol{\beta} = \begin{pmatrix} v \pm w \\ -\mathrm{i}g \\ 0 \end{pmatrix}.$$

Substituting these coefficients in Eq.(3.5) yields

$$\begin{aligned}\mathcal{W}_{\pm}(E) &= 2\int \frac{\mathrm{d}k}{2\pi\mathrm{i}} \frac{w^2 k \mp \mathrm{i}wg}{E^2 + g^2 - w^2k^2 \pm 2\mathrm{i}wgk - (v \pm w)^2} \\ &= 2\int \frac{\mathrm{d}k}{2\pi\mathrm{i}} \frac{k \mp \mathrm{i}\gamma}{\mathcal{E}^2 + \gamma^2 - k^2 \pm 2\mathrm{i}\gamma k - M_{\pm}^2},\end{aligned}$$

where we introduced the scaled parameters $\gamma = g/w$, $\mathcal{E} = E/w$ and $M_{\pm} = (v \pm w)/w$. Upon rewriting the denominator, this turns into

$$\begin{aligned}\mathcal{W}_{\pm}(E) &= -2\int \frac{\mathrm{d}k}{2\pi\mathrm{i}} \frac{k \mp \mathrm{i}\gamma}{\left[k \mp \mathrm{i}\left(\gamma + \sqrt{M_{\pm}^2 - \mathcal{E}^2}\right)\right]\left[k \mp \mathrm{i}\left(\gamma - \sqrt{M_{\pm}^2 - \mathcal{E}^2}\right)\right]} \\ &= -\int \frac{\mathrm{d}k}{2\pi\mathrm{i}} \frac{k \mp \mathrm{i}\left(\gamma + \sqrt{M_{\pm}^2 - \mathcal{E}^2}\right) + k \mp \mathrm{i}\left(\gamma - \sqrt{M_{\pm}^2 - \mathcal{E}^2}\right)}{\left[k \mp \mathrm{i}\left(\gamma + \sqrt{M_{\pm}^2 - \mathcal{E}^2}\right)\right]\left[k \mp \mathrm{i}\left(\gamma - \sqrt{M_{\pm}^2 - \mathcal{E}^2}\right)\right]} \\ &= -\int \frac{\mathrm{d}k}{2\pi\mathrm{i}} \left[\frac{1}{k \mp \mathrm{i}\left(\gamma - \sqrt{M_{\pm}^2 - \mathcal{E}^2}\right)} + \frac{1}{k \mp \mathrm{i}\left(\gamma + \sqrt{M_{\pm}^2 - \mathcal{E}^2}\right)}\right] \\ &= -\int \frac{\mathrm{d}k}{2\pi\mathrm{i}} \left[\frac{\left(k \mp \mathrm{Im}\sqrt{M_{\pm}^2 - \mathcal{E}^2}\right) \pm \mathrm{i}\left(\gamma - \mathrm{Re}\sqrt{M_{\pm}^2 - \mathcal{E}^2}\right)}{\left(k \mp \mathrm{Im}\sqrt{M_{\pm}^2 - \mathcal{E}^2}\right)^2 + \left(\gamma - \mathrm{Re}\sqrt{M_{\pm}^2 - \mathcal{E}^2}\right)^2} + \right. \\ &\qquad \left. \frac{\left(k \pm \mathrm{Im}\sqrt{M_{\pm}^2 - \mathcal{E}^2}\right) \pm \mathrm{i}\left(\gamma + \mathrm{Re}\sqrt{M_{\pm}^2 - \mathcal{E}^2}\right)}{\left(k \pm \mathrm{Im}\sqrt{M_{\pm}^2 - \mathcal{E}^2}\right)^2 + \left(\gamma + \mathrm{Re}\sqrt{M_{\pm}^2 - \mathcal{E}^2}\right)^2}\right] \\ &= \mp\frac{1}{2}\left[\mathrm{sgn}\left(\gamma - \mathrm{Re}\sqrt{M_{\pm}^2 - \mathcal{E}^2}\right) + \mathrm{sgn}\left(\gamma + \mathrm{Re}\sqrt{M_{\pm}^2 - \mathcal{E}^2}\right)\right],\end{aligned}$$

where in the last line, we used the integral

$$\int \frac{\mathrm{d}k}{2\pi\mathrm{i}} \frac{k + \mathrm{i}\alpha}{k^2 + \alpha^2} = \frac{1}{2}\mathrm{sgn}\left(\mathrm{Re}\,\alpha\right).$$

In the remainder of this section, we will set $E = 0$, which we argued to be the correct choice in the main text. The phase diagram corresponding to Eq. (3.24) is shown in Fig. 1. Notably, this invariant renders all phases adiabatically connected to the Hermitian model ($g = 0$) indistinguishable from each other. This results from the purely non-Hermitian nature of the energy vorticity $\mathcal{W}_{\pm}(E)$. To find the

self-energy for a delta-peaked disorder, we first evaluate

$$\begin{aligned}
\int \frac{\mathrm{d}q}{2\pi} G_0(q) &= -\frac{1}{w}\int \frac{\mathrm{d}q}{2\pi} \frac{1}{q^2 + M_\pm^2 - \gamma^2 \mp 2\mathrm{i}\gamma q} \begin{pmatrix} 0 & \mp \mathrm{i}q + M_\pm - \gamma \\ \pm \mathrm{i}q + M_\pm + \gamma & 0 \end{pmatrix} \\
&= -\frac{1}{w}\int \frac{\mathrm{d}q}{2\pi} \frac{\mp i}{[(q \mp \mathrm{i}(\gamma - M_\pm)]\,[(q \mp \mathrm{i}(\gamma + M_\pm)]} \\
&\qquad \times \begin{pmatrix} 0 & q \mp \mathrm{i}(\gamma - M_\pm) \\ -q \pm \mathrm{i}(\gamma + M_\pm) & 0 \end{pmatrix} \\
&= \frac{1}{w}\int \frac{\mathrm{d}q}{2\pi\mathrm{i}} \begin{pmatrix} 0 & \mp \frac{1}{q \mp \mathrm{i}(\gamma + M_\pm)} \\ \pm \frac{1}{q \mp \mathrm{i}(\gamma - M_\pm)} & 0 \end{pmatrix} \\
&= \frac{1}{2w} \begin{pmatrix} 0 & -\mathrm{sgn}\,(\gamma + M_\pm) \\ \mathrm{sgn}\,(\gamma - M_\pm) & 0 \end{pmatrix}.
\end{aligned} \tag{3.24}$$

Substituting this in the expression for the disorder averaged energy vorticity, we obtain

$$\begin{aligned}
\overline{\mathcal{W}_\pm(0)} &= \int \frac{\mathrm{d}k}{2\pi\mathrm{i}}\, \mathrm{tr}\left[(1 - \Sigma_E(k))^{-1} G_{0,0}(k)(\boldsymbol{\alpha}\cdot\boldsymbol{\sigma})\right] \\
&= \int \frac{\mathrm{d}k}{2\pi\mathrm{i}} \frac{1}{1 + (U_0^2 n_i/2w)^2 \mathrm{sgn}(\gamma - M_\pm)\mathrm{sgn}(\gamma + M_\pm)} \\
&\times \mathrm{tr}\left[\begin{pmatrix} 1 & \frac{U_0^2 n_i}{2w}\mathrm{sgn}(\gamma + M_\pm) \\ -\frac{U_0^2 n_i}{2w}\mathrm{sgn}(\gamma - M_\pm) & 1 \end{pmatrix} G_{0,0}(k)\,(\boldsymbol{\alpha}\cdot\boldsymbol{\sigma}) \right] \\
&= \frac{1}{1 + \left(\frac{U_0^2 n_i}{2w}\right)^2 \mathrm{sgn}(\gamma - M_\pm)\mathrm{sgn}(\gamma + M_\pm)} \int \frac{\mathrm{d}k}{2\pi\mathrm{i}}\, \mathrm{tr}\left[G_{0,0}(k)\,(\boldsymbol{\alpha}\cdot\boldsymbol{\sigma})\right] \\
&= \frac{\mathcal{W}_\pm(0)}{1 + \left(\frac{U_0^2 n_i}{2w}\right)^2 \mathrm{sgn}(\gamma - M_\pm)\mathrm{sgn}(\gamma + M_\pm)},
\end{aligned} \tag{3.25}$$

where, in lines 2 to 3, we used the fact that the Green function is diagonal in the sublattice sector, such that the off-diagonal contributions to the self-energy vanish upon taking the trace.

Chapter 4

Topological phases of the interacting SSH model: an analytical study

Commonly used symbols and acronyms

Symbol/Acronym	Meaning
SSH	Su–Schrieffer–Heeger
IR	Infrared
UV	Ultraviolet
RG	Renormalization Group
CFT	Conformal Field Theory
$\mathcal{H}$	Second-quantized Hamiltonian
$H(k)$	First-quantized Bloch Hamiltonian
$\mathcal{L}$	Lagrangian density
m	Fermion mass
v_F	Fermi velocity
V_0	Lattice interaction strength
$g = \lim_{a\to 0} \frac{V_0 a}{2}$	Field-theory coupling strength
G	Green's function
$\mathcal{P}$	Polarization density response

In the past two decades, noninteracting topological phases, traditionally analyzed through electronic band theory, have garnered significant attention due to the discovery of materials exhibiting unconventional electronic properties [16, 204]. Most notably, the prediction of the quantum spin Hall effect in graphene by Kane and Mele [68, 205] initiated intense research in the field of topological insulators, which are materials with insulating bulk and conducting boundaries. Since then, the theoretical understanding of these systems reached a high level of sophistication. For example, the bulk-boundary correspondence for two-dimensional (2D) time-reversal symmetry broken insulators states that whenever the bulk Hall resistivity of the system is quantized, there exist gap traversing states, which are located at the boundary of the system [46]. On the other hand, a 2D topological insulator respecting time-reversal symmetry will exhibit the quantum spin Hall effect, where the boundary states carry spin currents instead of charge currents. This type of behavior does not only exist in 2D but also in 3D and in 1D, albeit when subjected to different spectral and spatial symmetry constraints [20].

In 3D, for example, a strong topological insulator respects time-reversal symmetry. It has conducting surface states, which are very robust due to spin-momentum locking and cannot be destroyed by the presence of disorder or any symmetry-respecting perturbation [43, 47]. It also features a rich variety of additional possible effects, such as quantized magnetoelectric polarizability, providing a realization of axion electrodynamics in a condensed-matter setting [48, 49]. In 1D, systems possessing inversion symmetry feature a quantized polarization density. This fact can be attributed to two significant results: the formulation of the polarization as a Berry phase [50], and the fact that the Berry phase is quantized to $\phi = 0, \pi$ for inversion symmetric systems [51]. In this case, anomalous polarization corresponding to fractionalized charges on the system's two boundaries is possible. The overarching theme in all of these cases is that one can compute bulk quantities of these systems and relate them to a corresponding boundary theory.

Additionally, they are called topological insulators because these bulk quantities are often expressed as topological invariants [16, 44]. For example, if an inversion-symmetric 1D system also possesses sublattice symmetry, it is possible to define a winding number ν, directly proportional to the quantized Berry phase, $\phi = \pi\nu$. Another example would be a time-reversal symmetry broken 2D system, in which the Hall conductivity is quantized and given by a Chern number [52]. This is why physical properties related to these topological invariants are very robust, as long as one respects the symmetries of the system and its gap is preserved.

All these systems may be described by a theoretical framework based on non-interacting electrons [16, 44]. This is usually justified because many materials can be described by Fermi liquid theories in 2D and 3D at low energies. However, this description can break down in strongly correlated systems. Furthermore, in 1D, no such description is possible, and one cannot ignore the effects of electron-electron interactions. This means that the most natural state in 1D is a strongly correlated non-Fermi liquid, an example of which is the Tomonaga-Luttinger liquid [206–208].

The effect of interactions in topological insulators is not a new subject, and a significant number of studies have already been conducted in this direction [32, 209–216]. For instance, many topological invariants have been generalized to expressions

that hold in the many-body case, or in weakly interacting topological insulators [210–212]. In 1D, the paradigmatic model for a topological insulator studied extensively is the SSH chain [41]. It is a tight-binding model of noninteracting fermions with nearest-neighbor alternating hopping strengths. Depending on the sign of the difference between the two hopping parameters, both a trivial phase and a topological phase can arise. In the topological phase, two degenerate edge modes exist at $E = 0$ due to sublattice symmetry.

The inclusion of interactions has been explored in various works [32, 212–216], relying on numerical or perturbative approaches. Some other works have explored extensions of the model to longer range hoppings [217] or to ladder systems [218]. The general result is that the topological phase usually survives the presence of interactions up to some threshold value of the interaction strength, after which the system transitions to a charge-density wave state. Another noteworthy study of the SSH model was conducted in Ref. [71], where they experimentally realized a many-body topological phase of interacting hard-core bosons. Unlike their fermionic counterparts, the many-body bosonic representation of the protecting symmetry permits next-nearest neighbor couplings, which break sublattice symmetry in the single-particle picture. Remarkably, this implies that the many-body topological phase remains intact despite the addition of such perturbations.

The study of the topological invariant in the presence of interactions in the integer quantum Hall effect is somewhat similar to the situation we are treating in our manuscript. In this case, it has been shown that it does not drive a topological phase transition [65].

In this work, we explore the polarization density as a topological invariant and provide an analytic treatment of its behavior in the low-energy sector of the interacting fermionic SSH model, with symmetry-preserving interactions. Studying the polarization density under interactions is meaningful because it is a physical observable. We achieve this by formulating the polarization density in terms of Green's functions, which are suitable for a many-body approach in the interacting case. This method is similar to the quantum Hall effect, where the transverse conductivity is quantized and proportional to the filling fraction, identifiable as a topological invariant. This identification justifies extending the study of topological invariants to interacting cases as long as the related physical observable is well-defined and measurable. Additionally, using a field theory formalism at low energy leverages many exact results in 1D for integrable models, contrasting with higher-dimensional cases. A similar study was done for the non-Hermitian SSH model with random disorder [2].

By combining various arguments, we derive an exact expression of the polarization density and provide a physical interpretation of the results, consistent with previous studies. This chapter's main result is that the continuum theory's polarization density describes the same two topologically distinct insulating phases as for the non-interacting case. Still, it now contains an extra factor from the fields' scaling dimensions in the low-energy quantum field theory. The interpretation is that this measures the altered nature of the excitations in the system. There are two contributions: the renormalization of the electronic charge due to quasiparticle smearing and an additional contribution from the soliton's topological charge. The

latter cannot be explained within the Fermi liquid framework and highlights the difference between the effects of interactions in 1D systems compared to higher dimensions [208].

This chapter is structured as follows. In Section 4.1, we describe the noninteracting SSH model, its topological invariant, and the type of interactions that we will be considering. In Section 4.2, we formulate the polarization density as a response to an external electric field. In Section 4.3, we explore the effect of interactions on the polarization density. We also provide an intuitive understanding of the result, stating that an adiabatic charge pumping procedure from a trivial to a topological phase would pump one quantum of the renormalized charge, which we have calculated exactly. Finally, in Section 4.4, we present our concluding remarks and give an outlook to additional extensions of our results beyond the regimes considered in this work.

4.1 Lattice SSH model

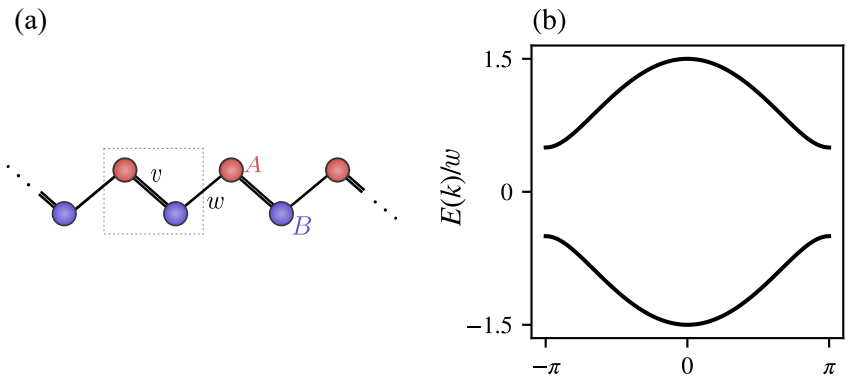

Figure 4.1: (a) The SSH chain, with sublattice A (top) and B (bottom) colored in red and blue, respectively. The dotted box shows a choice of unit cell. The intracell hopping is v and the intercell hopping is w. (b) The energy spectrum of the SSH model's Bloch Hamiltonian

The SSH model was originally introduced to describe the behavior of electrons and the emergence of solitonic defects in a polyacetylene molecule [41]. It is a nearest-neighbor tight-binding model for spinless fermions hopping on a 1D chain with two alternating bond strengths [see Fig. 4.1 (a)]. The Hamiltonian of the SSH model is given by

$$\begin{aligned}\hat{\mathcal{H}} &= v\sum_{j=1}^{N} c_{A,j}^{\dagger}c_{B,j} + w\sum_{j=1}^{N} c_{B,j}^{\dagger}c_{A,j+1} + \text{h.c.},\\ &= \int_{-\pi/a}^{\pi/a} \frac{\mathrm{d}k}{2\pi} \begin{pmatrix} c_{A,k}^{\dagger}, & c_{B,k}^{\dagger}\end{pmatrix} H(k) \begin{pmatrix} c_{A,k} \\ c_{B,k}\end{pmatrix},\end{aligned}$$

where v and w are intracell and intercell hopping, respectively. The sum in the first line runs over cell indices, and A, B refers to the two sites inside a unit cell with a lattice constant a and periodic boundary conditions at the ends of the chain. The momentum space formulation is shown in the second line, where we have taken the limit $N \to \infty$. The main object of interest is the single-particle Bloch Hamiltonian

$$H(k) = d_x(k)\sigma_x + d_y(k)\sigma_y, \tag{4.1}$$

where $d_x(k) = v + w\cos ka$, $d_y(k) = -w\sin ka$ and σ_i are Pauli matrices acting in the A, B space. The two energy bands are given by

$$\begin{aligned} E_\pm &= \pm\sqrt{d_x^2 + d_y^2}, \\ &= \pm\sqrt{v^2 + w^2 + 2vw\cos ka}\ . \end{aligned}$$

They are depicted in Fig. 4.1 (b). The two bands can touch and close the gap when $v = \pm w$, at $ka = 0$ ($v = -w$) and $ka = \pi$ ($v = w$). This signals a change between topologically distinct phases [219].

4.1.1 Symmetries and Topology

The SSH model possesses two symmetries: sublattice symmetry $A \leftrightarrow B$, characterized by

$$\sigma_z H(k)\sigma_z = -H(k),$$

and inversion symmetry $j \to N - j + 1$, characterized by

$$\sigma_x H(k)\sigma_x = H(-k)\ .$$

The former allows for the definition of a winding number invariant [16], while the latter forces the quantization of this winding number to just two values [51]. For a sublattice symmetric gapped Hamiltonian, the following equation defines a winding number [16]

$$\nu = \int_{-\pi/a}^{\pi/a} \frac{\mathrm{d}k}{4\pi i}\,\mathrm{tr}\left[\sigma_z H^{-1}(k)\partial_k H(k)\right]. \tag{4.2}$$

This formulation allows one to write Eq. (4.2) in terms of Green's functions [210]. This will be used later to investigate the invariant's fate in the interacting system. For the SSH chain, we show in Appendix 4.A that this invariant yields

$$\nu = \begin{cases} 0, & \text{if } |v| > |w|\ , \\ 1, & \text{if } |v| < |w|\ . \end{cases} \tag{4.3}$$

We can relate the winding number ν to the Berry phase ϕ of the system at half-filling,

$$\phi = \int_{-\pi/a}^{\pi/a} \mathrm{d}k\,\langle u_-(k)|\, i\partial_k\, |u_-(k)\rangle\,,$$

where $|u_-(k)\rangle$ is the lower band's Bloch state. It is quantized by virtue of inversion symmetry to $\phi = 0$ for $|v| > |w|$ and $\phi = \pi$ for $|v| < |w|$.

According to the modern theory of polarization [50], the Berry phase is closely related to the position of Wannier centers inside unit cells and, as such, indicates the presence/absence of a "topological" polarization,

$$P = \frac{e\phi}{2\pi} \mod e = \begin{cases} 0, & \text{if } \nu = 0, \\ \frac{1}{2}, & \text{if } \nu = 1. \end{cases} \tag{4.4}$$

The $\mod e$ always appears in the definition of absolute polarization. It accounts for the 2π ambiguity of the Berry phase and physically for the choice of a unit cell [50]. This polarization manifests itself as a bulk-boundary correspondence: if the system has open boundaries, there will be half-quantized charges sitting at the boundary of the system. This, in turn, means that there will be an anomalous response to an external electromagnetic field [7, 220].

4.1.2 Interactions and the continuum limit

As we will be interested in the low-energy physics of the topological phases, we shall first derive the continuum limit of the noninteracting model at low energies. Since these transitions happen at $ka = 0$ and $ka = \pi$, for the sake of simplicity, we take all parameters to be positive and expand the Bloch Hamiltonian around $ka = \pi$ to linear order in ka,

$$\begin{aligned} H(\pi + ka) &= \begin{pmatrix} 0 & v - w - iwka \\ v - w + iwka & 0 \end{pmatrix} \\ &= m_0\sigma_x + wka\sigma_y, \end{aligned} \tag{4.5}$$

where $m_0 = v - w$ will serve as a bare mass parameter in the field theory description. Note that for the transition at $k = 0$, we need to replace $w \to -w$. The real space Hamiltonian is obtained by replacing $k \to -i\partial_x$ (we set $\hbar = 1$),

$$\mathcal{H} = \int \mathrm{d}\tau \Psi^\dagger(x) \left[m_0\sigma_x - iv_\mathrm{F}\sigma_y\partial_x \right] \Psi(x), \tag{4.6}$$

where we introduced the Dirac spinor

$$\hat{\Psi}(x_j) = \frac{1}{\sqrt{a}} \begin{bmatrix} c_{A,j} \\ c_{B,j} \end{bmatrix}, \tag{4.7}$$

and dropped the j index when taking the limit $a \to 0$. We have also introduced the Fermi velocity $v_F = wa$. This leads to the interpretation of the sublattice structure as a pseudospin degree of freedom. Using the gamma matrix representation $\gamma_0 = \sigma_x$, $\gamma_1 = i\sigma_z$, and $\bar{\Psi} \equiv \Psi^\dagger\gamma_0$ together with the slash notation $\not{\partial} = \gamma_0\partial_t - \gamma_1\partial_x$, we have the usual free Hamiltonian and Lagrangian densities of a Dirac fermion,

$$\begin{aligned} \mathcal{H}_0(x) &= \bar{\Psi}(x) \left(iv_\mathrm{F}\gamma_1\partial_x + m_0 \right) \Psi(x), \\ \mathcal{L}_0(x) &= \bar{\Psi}(x) \left(iv_\mathrm{F}\not{\partial} - m_0 \right) \Psi(x). \end{aligned}$$

Because of the constrained spatial degrees of freedom, 1D systems are generically strongly interacting – fermions cannot move past each other without interacting [208]. To incorporate this effect, we consider the simplest interaction term that respects the symmetries of the system: a nearest-neighbor repulsion between spinless fermions placed in the same cell (intercell coupling would also break sublattice symmetry),

$$\mathcal{H}_{\mathrm{I}} = V_0 \sum_{j=1}^{N} n_{A,j} n_{B,j}, \tag{4.8}$$

where $n_{\alpha,j} = c^{\dagger}_{\alpha,j} c_{\alpha,j}$, with $\alpha = A, B$. Usually, the densities are shifted by half to ensure half-filling and to respect particle-hole symmetry. This can also be accommodated by adding a chemical potential term in the free Hamiltonian. However, these terms do not matter in the continuum theory that we will be considering and will usually be treated using typical prescriptions such as normal ordering. Using the Dirac spinor Eq. (4.7), the continuum version of the interaction can be written as

$$\mathcal{H}_I = \frac{g}{2} \int \mathrm{d}x \left[\bar{\Psi}(x)\gamma_\mu \Psi(x)\right]^2,$$

where

$$g = \lim_{a\to 0} \frac{V_0 a}{2}.$$

Combining all terms, the Lagrangian density for the continuum limit of the interacting SSH model is given by

$$\mathcal{L} = \bar{\Psi}(x)\left(i v_F \partial\!\!\!/ - m_0\right)\Psi(x) - \frac{g}{2}\left[\bar{\Psi}(x)\gamma_\mu \Psi(x)\right]^2, \tag{4.9}$$

which is the Thirring model [221, 222].

4.1.3 Generalization: extended SSH model

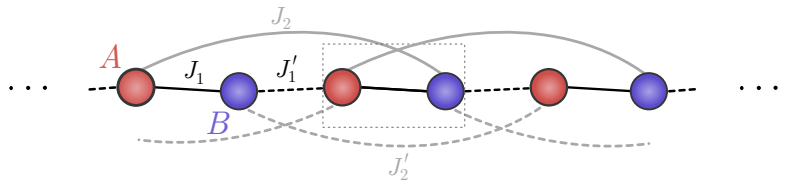

Figure 4.2: Extended SSH chain. Only the simplest extension has been considered in this figure, namely, the inclusion of J_2 and J_2'.

The SSH model can be generalized simply by including longer-range hoppings that respect all previously discussed symmetries. This model was studied in previous works to understand the interplay between long-range hoppings and disorder [223] and, more recently, the effect of interactions on the topological phases [224].

An example of this extension to a next-next-nearest neighbor is shown in Fig. 4.2. More generally, one can keep adding these hoppings by skipping $2n$ sites each time, resulting in the following Bloch Hamiltonian

$$H(k) = \sum_{n=1}^{l} \begin{pmatrix} 0 & h_n(k) \\ h_n^*(k) & 0 \end{pmatrix}, \tag{4.10}$$

with $h_n(k) = J_n e^{-i(n-1)k} + J_n' e^{ink}$. When $l = 1$, this reduces to the regular SSH model with $J_1 = v$ and $J_1' = w$. Because of its extended nature, higher winding numbers are possible, resulting in multiple edge state pairs. However, because the system still obeys inversion symmetry, the polarization Eq. (4.4) is still quantized to 0 (even winding numbers) or 1/2 (odd winding numbers).

Consequently, this system has more possibilities for gap closings and transitions between two phases with different winding numbers. Nevertheless, as long as the interaction term (4.8) is still the same, the Thirring model is still the low-energy theory that describes the physics near the transition point, but with modified Fermi velocities and bare masses. For example, we consider the model near the $k = \pi$ transition again. The bare mass and Fermi velocities are then given by

$$\begin{aligned} m_0 &= \sum_{n=1}^{l} \left[(-1)^{n-1} J_n + (-1)^n J_n'\right], \\ v_{\mathrm{F}} &= a \sum_{n=1}^{l} \left[(-1)^{n-1}(n-1) J_n + (-1)^n J_n'\right]. \end{aligned} \tag{4.11}$$

4.2 Polarization as a response to an external field: non-interacting case

This section aims to show that we can formulate the electronic system's response to an external electric field by considering the effective action for a pure background gauge field using statistical field theory. The polarization density can be obtained by taking the derivative of the free energy with respect to an external electric field,

$$\mathbf{P} = \frac{1}{V} \frac{\partial F}{\partial \mathbf{E}}, \tag{4.12}$$

where V is the volume of the system. We will focus on the one-dimensional case and derive formulae for the lattice and continuum versions of the SSH model.

4.2.1 Lattice Model

Let us start by considering the general expression of a non-interacting Hamiltonian on a lattice,

$$\mathcal{H} = \sum_{ij} \sum_{\mu,\nu} c_{i,\mu}^\dagger h_{ij}^{\mu\nu} c_{j,\nu} = \sum_{k} \sum_{\mu\nu} c_{k,\mu}^\dagger h_k^{\mu\nu} c_{k,\nu}.$$

The indices i, j refer to unit-cell, while μ, ν refer to internal degrees of freedom, such as sublattice, orbitals, spins, etc. In a tight-binding formulation, the coupling to an

external gauge field is achieved by performing a Peierls substitution, which stems from the principle of minimal coupling. That is, one replaces $h_{ij}^{\mu\nu} \to h_{ij}^{\mu\nu} e^{iA_{ij}}$, where $A_{ij} = \int_{x_i}^{x_j} A(x)\mathrm{d}x$ is the integral of the gauge field from unit cell i to j. Approximating the field to be constant on the scale of the unit cell and assuming weak coupling, we can linearize the exponential with respect to A. Subsequently, rewriting everything in momentum space yields

$$\mathcal{H} = \sum_k \sum_{\mu\nu} c_{k,\mu}^\dagger h_k^{\mu\nu} c_{k,\nu} + \sum_{kq} \sum_{\mu\nu} c_{k+q/2,\mu}^\dagger \frac{\partial h_k^{\mu\nu}}{\partial k} c_{k-q/2,\nu} A_{-q},$$

where we used

$$A_{ij} = \frac{1}{\sqrt{N}} \sum_q e^{i(x_i - x_j)q} A_q \ .$$

We are also neglecting the diamagnetic contribution, proportional to A^2. This approximation is justified when probing the polarization response of the system using a weak electric pulse. With the full matrix Bloch Hamiltonian as $H(k) = \sum_{\mu,\nu} h_k^{\mu\nu} |\mu\rangle \langle\nu|$, we can write down the imaginary time action as follows

$$\begin{aligned} S[A] = \int_0^{1/T} \mathrm{d}\tau \sum_{kq} \Psi^*(k,\tau) \Bigg\{ \left[\partial_\tau - H\left(\frac{k+q}{2}\right) \right] \delta_{k,q} \\ - \partial_k H\left(\frac{k+q}{2}\right) A(q-k; \tau - \tau') \Bigg\} \Psi(q,\tau), \end{aligned}$$

where the field $\Psi(k,\tau)$ is a Grassmann-valued field obtained by considering coherent states of the annihilation field operator in the second-quantization language. The integral over imaginary time τ runs from 0 to the inverse temperature $1/T$ (with units $\hbar = k_\mathrm{B} = 1$). The partition function for this system is then conveniently written as a path integral over the fields Ψ and Ψ^*, and has a formal solution

$$\begin{aligned} Z[A] &= \int \mathcal{D}\Psi^* \mathcal{D}\Psi \exp\left(-S[A]\right) \\ &= \exp\left[\mathrm{Tr}\log\left(-G^{-1}\right)\right], \end{aligned}$$

where we wrote $G^{-1} = G_0^{-1} + \mathcal{A}$, representing the Green's function as a formal operator, and Tr is a general trace operation over discrete and continuous indices. We have split the contributions into a "bare" one and one coming from the gauge field. The matrix $\mathcal{A}$ is the additional contribution from the derivative of the Hamiltonian. The "bare" Green's function (in Fourier space) can be obtained by finding the inverse of the following matrix

$$G_0(k, i\omega_n) = \left[i\omega_n + H(k)\right]^{-1},$$

with fermionic Matsubara frequencies $\omega_n = \pi(2n+1)T$. We now expand the matrix logarithm to linear order in A,

$$Z[A] \equiv Z[0] \exp\left(-S_\mathrm{eff}[A]\right),$$

where the effective action is given by $S_{\text{eff}}[A] = \text{Tr}\,(G_0\mathcal{A})$. Working out the generalized trace yields

$$\text{Tr}\,(G_0\mathcal{A}) = \sum_n \sum_q \tilde{P}(q, i\omega_n) A(q, i\omega_n),$$
$$\tilde{P}(q, i\omega_n) = \sum_k \text{tr}\left[G_0(k, i\omega_n)\partial_k H\,(k)\right]\delta_{q,0},$$

where tr is the trace over internal degrees of freedom. Therefore, we can express the free energy as

$$F[A] = -T\log(Z) = -T\log(Z_0) + TS_{\text{eff}}[A].$$

Using Eq. (4.12) for the polarization density, we see that the functional derivative with respect to the electric field will only pick up the effective action contribution:

$$P(q, i\omega_n) = \frac{T}{V}\frac{\delta S_{\text{eff}}}{\delta E(q, i\omega_n)}.$$

We now choose a specific gauge where the applied electric field is constant and corresponds to a pulse. For this, we use a gauge potential A_x such that $E_x = -\partial_\tau A_x = E_0\delta(\tau)$. This is given by

$$A_x(x, \tau) = E_0 T \sum_n \frac{e^{-i\omega_n\tau}}{i\omega_n}. \tag{4.13}$$

Hence, the electric polarization density becomes

$$P(q, i\omega_n) = \frac{1}{\pi(2n+1)}\int_{-\pi}^{\pi}\frac{\mathrm{d}k}{2\pi i}\text{tr}\left[G_0(k, i\omega_n)\partial_k H(k)\right], \tag{4.14}$$

where we have turned the sum into an integral over the Brillouin zone. The "static" version thereof, at zero temperature, is given by

$$\mathcal{P}_{\text{tot},0} \equiv \pi P(0,0) = \int_{-\pi}^{\pi}\frac{\mathrm{d}k}{2\pi i}\,\text{tr}\left[G_0(k,0)\partial_k G_0^{-1}(k,0)\right], \tag{4.15}$$

where we included the subscript 0 in $\mathcal{P}_{\text{tot},0}$ to indicate the non-interacting case. We could write Eq. (4.15) because the Green's function at zero temperature is equivalent to the inverse of the Bloch Hamiltonian. Note that this type of polarization is not well defined for crystalline insulators, which is why the modern theory of polarization was developed in the first place [50]. This occurs because there is a gauge degree of freedom in the choice of unit cells to define the dipole moment. However, the formulation of Green's functions is still beneficial. For a sublattice symmetric Hamiltonian, the relative polarization between sublattices $\mathcal{P}_0$ is a well-defined and gauge-invariant quantity, which we can obtain simply by multiplying the expression inside the trace by $\sigma_z/2$. Eq. (4.15) then becomes

$$\mathcal{P}_0 = \int_{-\pi}^{\pi}\frac{\mathrm{d}k}{4\pi i}\text{tr}\left[\sigma_z G_0(k,0)\partial_k G_0^{-1}(k,0)\right], \tag{4.16}$$

which is equivalent to the winding number, Eq. (4.2). Similar expressions have been discussed in Refs. [210, 225], but we derive ours in a different context here. We further note that there is a factor two difference with the Berry phase definition of polarization and that this formulation does not take into account the $\mod e$ ambiguity. Since we are mainly interested in the continuum formulation, this should not be a problem as it still indicates the two topologically distinct phases, as we will see shortly.

4.2.2 Continuum polarization of the SSH model

From this point onward, we shall set $v_F = 1$. From the continuum Hamiltonian of the SSH model Eq. (4.6), we can infer what the action functional of this system will be in the imaginary time formulation:

$$\begin{aligned} S &= \int \mathrm{d}x\mathrm{d}\tau \Psi^*(x,\tau)\left[\partial_\tau - i\sigma_y\partial_x - m_0\sigma_x\right]\Psi(x,\tau) \\ &= -\int \mathrm{d}x\mathrm{d}\tau \int \mathrm{d}x'\mathrm{d}\tau' \Psi^*(x,\tau) G_0^{-1}(x,\tau;x',\tau')\Psi(x',\tau'), \end{aligned}$$

where we introduced the Green's function G_0, whose momentum representation is

$$G_0(k,i\omega_n) = \frac{-i\omega_n + k\sigma_y + m_0\sigma_x}{\omega_n^2 + m_0^2 + k^2}.$$

Instead of the Peierls substitution used in the lattice formulation, we will directly introduce a background gauge field through minimal coupling. That is, we replace $\partial_j \to \partial_j + iA_j$, where $A_\tau(x,\tau) = -i\phi(x,\tau)$, with $\phi(x,\tau)$ the electric potential, and $A_x(x,\tau)$ is the magnetic potential. This modifies the Green's function to $G^{-1} = G_0^{-1} - \mathcal{A}$, where

$$\mathcal{A} = -A_\tau + \sigma_y A_x.$$

Note that we are omitting coordinates for simplicity. We now integrate out the fermionic degrees of freedom in the partition function to obtain an effective action, which, to linear order, is given by $S_{\text{eff}}[\mathcal{A}] = \mathrm{Tr}\,(G_0\mathcal{A})$. The generalized trace operation is given by

$$\begin{aligned} \mathrm{Tr}\,(G_0\mathcal{A}) &= \int \mathrm{d}x\mathrm{d}\tau \int \mathrm{d}x'\mathrm{d}\tau' \,\mathrm{tr}\left[G_0(x-x',\tau-\tau')\mathcal{A}(x',\tau'-\tau)\delta(x-x')\right] \\ &= \int \mathrm{d}\tau\mathrm{d}\tau' \,\mathrm{tr}\left[G_0(0,\tau-\tau')\int \mathrm{d}x\mathcal{A}(x,\tau'-\tau)\right]. \end{aligned} \tag{4.17}$$

We choose a gauge potential in Eq. (4.13) that yields an electric pulse at time τ. We can then write Eq. (4.17) as

$$\mathrm{Tr}\,(G_0\mathcal{A}) = T\sum_n \int \frac{\mathrm{d}k}{2\pi}\,\mathrm{tr}\left[G_0(k,i\omega_n)i\sigma_y\right]A(0,i\omega_n),$$

Noting that $\partial_k G_0^{-1}(k,i\omega_n) = -\sigma_y$, we have

$$\mathrm{Tr}\,(G_0\mathcal{A}) = T\sum_n \int \frac{\mathrm{d}k}{2\pi i}\,\mathrm{tr}\left[G_0\partial_k G_0^{-1}\right]A(0,i\omega_n).$$

This means we have the same expression for the polarization as in the lattice model, Eq. (4.14). A direct calculation of the relative polarization, with $\sigma_z/2$ inside the trace, yields (see Appendix 4.A),

$$\mathcal{P}_0 = \frac{1}{2}\text{sign}\,(m_0)\,. \tag{4.18}$$

The half-quantization condition above arises due to the integration over momentum space covering the entire real line. Consequently, it is no longer a winding number, and there is no reason for it to be an integer. Nonetheless, it remains valuable in identifying the topological phase transition. Additionally, the continuum polarization can effectively capture the integer change in polarization across the transition, specifically $\Delta\mathcal{P}_0 = 1$ (in units of the free electron charge).

4.3 Effects of Interactions

We have so far seen that the polarization density for a non-interacting system can be expressed, in the lattice and continuum theories, in terms of the noninteracting Green's function. We have used an imaginary time formulation to derive those expressions. Still, since we are interested in the static polarization, which does not contain any Matsubara frequency, we might as well consider a generic field theory instead of an Euclidean one. Equipped with this knowledge, we will now explore the effects of interactions in a more general setting.

4.3.1 Expectations from scaling properties

Before we compute the polarization explicitly, here we present arguments as to its expected behavior in the case of the Thirring model Eq. (4.9), which is an integrable massive quantum field theory (discussed in more detail in Appendix 4.B).

Consider the full Green's function (including non-symmetry-breaking interactions that only contribute to the off-diagonal matrix elements) in its most general form,

$$G(k,0) = \begin{pmatrix} 0 & f(k) \\ f^*(k) & 0 \end{pmatrix}, \tag{4.19}$$

where

$$f(k) = |f(k)|e^{i\varphi(k)}.$$

By substituting Eq. (4.19) into Eq. (4.16), we obtain the polarization

$$\mathcal{P} = \lim_{\Lambda\to\infty} \frac{1}{2\pi}\int_{-\Lambda}^{\Lambda} \mathrm{d}k\partial_k\varphi(k), \tag{4.20}$$

where we have introduced a cutoff Λ, which we will come back to later. In other words, the polarization is a winding of the Green's function's complex phase φ from $k = -\infty$ to $k = \infty$. As such, its contributions can only come from zeros or poles. Since the massive Thirring model, given by Eq. (4.9), is integrable, we can safely assume that it is continuous and differentiable everywhere on the real axis, except possibly at $|k| = 0, \infty$ (see Appendix 4.B). Moreover, we also know from

the Lehmann representation that the poles of the Green's function still correspond to excitation energies, even in the interacting case where they are renormalized. Assuming that these are nonzero (since the theory is massive), the only contribution to the winding number would come from possible zeros at the infrared (IR) and ultraviolet (UV) points $|k| = 0, \infty$. It is thus sufficient to study the behavior of the Green's function at the fixed points of the renormalization group (RG) flow (IR and UV regions). The UV behavior of any theory can be accessed from the conformal field theory (CFT) at the UV point. If this theory is connected to a massive IR fixed point through the RG flow, then the Green's function behaves as follows:

$$g(r) \sim \begin{cases} r^{-y}, & \text{if } r \to 0 \ , \\ e^{-mr}, & \text{if } r \to \infty \ , \end{cases} \tag{4.21}$$

where y is the CFT scaling dimension of the field and m is the mass of the lightest particle. In momentum space (see Appendix 4.C for a derivation), this becomes

$$g(k) \sim \begin{cases} k^{y-2}, & \text{if } k \to \infty \ , \\ \dfrac{1}{m}, & \text{if } k \to 0 \ . \end{cases} \tag{4.22}$$

Because of the mass gap, the topological invariant is well defined, as the integral Eq. (4.20) does not contain any divergence and can be written as

$$\mathcal{P} = \frac{1}{2\pi} \lim_{\Lambda \to \infty} \left[\varphi(\Lambda) - \varphi(-\Lambda) \right] .$$

The only relevant contribution will be from negative large momenta, since then an extra phase $e^{\pm i\pi y}$ arises, as can be inferred from Eq. (4.22). Hence, the polarization must be of the form $\mathcal{P} = \pm y/2$, for $y < 1$.

The main conclusion is that y, the *scaling dimension* of the field, redefines the amplitude of the continuum polarization. As for the sign, which determines the topological phase transition, it is still fully determined by the mass parameter,

$$\mathcal{P} = \frac{1}{2} \text{sign}\,(m)\, y = y\mathcal{P}_0 \ , \tag{4.23}$$

where $\mathcal{P}_0$ is the non-interacting polarization density from Eq. (4.18). The reason for this is the following [see Fig. 4.3]: the integration runs along the real axis, and the winding function has a branch cut parallel to it, with branching points at infinity and at the Green's function's zero. The choice of Riemann sheet for either $e^{i\pi}$ or $e^{-i\pi}$ is crucial and is enforced by the mass parameter. It dictates the direction from which the branch cut is approached, i.e., the Riemann sheet of the winding function over which the integration runs. If the mass gap vanishes, the integration runs precisely over the branch cut and does not produce a well-defined result. This is consistent with the fact that the polarization is not defined for a gapless system.

These assumptions can be explicitly verified in the free case, when $g(k) = e^{i\varphi(k)}$, with

$$\varphi(k) = \arctan\left(\frac{-k}{m}\right) .$$

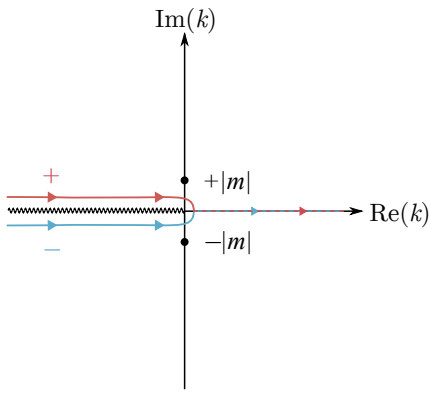

Figure 4.3: Different integration paths: above (red) or below (blue) the branch cut, depending on the sign of the mass.

Since $\varphi(k)$ has a logarithmic branch cut, the Riemann surface contains an infinite number of different sheets. However, physically, only the difference between two adjacent sheets is relevant. This result holds for any chiral invariant model, emphasizing the importance of a mass gap to protect the topological phase.

4.3.2 Polarization for the Thirring model

Our next goal is to use insights about the Thirring model to derive exact results for the polarization Eq. (4.16), using the interacting Green's function. As shown in the previous section, one may expect to find all the information in the scaling dimension of the fermionic field, provided that the system is gapped. The Thirring Lagrangian, given by Eq. (4.9), has two parameters: a bare mass m_0 (which is just the dimerization of the chain) and the local self-interaction coupling strength g, considered strictly positive in our analysis. However, since this is a quantum field theory, the physical mass m and *effective coupling* β are not equal to the respective bare quantities from the Lagrangian. To extract non-perturbatively the relations between physical and bare parameters of the field theory, we can exploit the mapping between the Thirring and the sine-Gordon model [226] (for more details, see Appendix 4.B). The Lagrangian of the latter is

$$\mathcal{L}_{\mathrm{SG}} = \frac{v_{\mathrm{F}}^2}{16\pi} \left(\partial_\mu \Phi\right)^2 + \frac{m_0^2}{\beta^2} \left(\cos \beta\Phi - 1\right) \ ,$$

where $\Phi(x,t)$ is a bosonic scalar field, and the effective coupling is

$$\beta^2 = \frac{1}{2} \frac{1}{1 - g/\pi} \ .$$

The sine-Gordon model describes a theory of stable solitonic excitations, which interpolate between different classical vacua of the theory $\Phi_{0,n} = 2n\pi/\beta$. This correspondence allows one to link the fermionic fields Ψ of the Thirring model to the operators in the sine-Gordon model that create or annihilate solitons, $e^{i\beta\Phi/2}\mathcal{O}^1_{\beta/2}$.

Here, $\mathcal{O}^1_{\beta/2}$ is a string operator, which accounts for the symmetry among the classical vacua $\Phi \to \Phi + 2n\pi/\beta$. This symmetry is also present in the quantum theory.

As an example of this mapping, it was shown [227] that the physical mass of Thirring fermions and sine-Gordon solitons scales as a power law of the bare mass

$$m^2(m_0, g) = C(g) \left(m_0^2\right)^{\frac{1}{2-2\beta^2}}, \tag{4.24}$$

where $C(g)$ is a function of the bare Thirring coupling g. This exact result was obtained by using non-perturbative bosonization methods in Ref. [227] (see Appendix 4.B for explanations). Additionally, the repulsive regime of the Thirring model, $\pi/2 > g > 0$, corresponds to the regime $1/2 < \beta^2 < 1$ in the sine-Gordon model. In this case, Thirring fermions and antifermions, carrying a renormalized electronic charge e^*, are mapped into solitons and antisolitons, carrying a topological charge. The latter is defined as

$$Q_t = \frac{\beta}{2\pi} \int_{-\infty}^{+\infty} \mathrm{d}x \partial_x \Phi(x,t). \tag{4.25}$$

Note that, in this case, the term topological refers to how the field $\Phi(x,t)$ interpolates between the different minima of the sine-Gordon potential, i.e., the symmetry between different ground states of the model, and not to the topological phase.

Exploiting this mapping even further, the zero frequency Green's function of the Thirring model, defined as

$$G(k) = \int_{-\infty}^{+\infty} \frac{\mathrm{d}x}{2\pi} e^{ikx} \langle \Psi(x) \bar{\Psi}(0) \rangle, \tag{4.26}$$

can be computed in terms of the form factors of the soliton-creating operator of the sine-Gordon model, $\tilde{\mathcal{O}} = e^{i\beta\Phi/2}\mathcal{O}^1_{\beta/2}$,

$$F_n^{\tilde{\mathcal{O}}}(\theta_1, \cdots, \theta_n) \equiv \langle 0 | \, \tilde{\mathcal{O}} \, | \theta_1, \cdots, \theta_n \rangle \,,$$

where θ_i are the rapidities of particles related to their momenta via $p_i = m \sinh \theta_i$ (see Appendix 4.B for more details and the soliton-creating operator's exact form). The Green's function then takes the form

$$G(k) = \sum_{n=0}^{\infty} \int_{-\infty}^{+\infty} \frac{\mathrm{d}x}{2\pi} \frac{\mathrm{d}\theta_1}{2\pi} \cdots \frac{\mathrm{d}\theta_n}{2\pi} e^{ikx} |F_n^{\tilde{\mathcal{O}}}(\theta_1, \ldots, \theta_n)|^2 \delta \left(k - m \sum_{j=1}^{n} \sinh \theta_j \right). \tag{4.27}$$

Using the UV-normalization proposed in Ref. [228], the scaling dimension of the Thirring fermionic field (which is the exponent of the power-like scaling at large momenta, discussed in Section 4.3.1) is found to be

$$y = \frac{1}{2} \left(\frac{1}{1 - g/\pi} + 1 - \frac{g}{\pi} \right). \tag{4.28}$$

This result can be numerically verified from Eq. (4.27) using the Feynman gas method [229]. The scaling of Eq. (4.26) in the UV region is also consistent with

conformal perturbation theory [230]. The exponent y can be identified as the scaling dimension of the field in the related CFT (more details are available in Appendix 4.D).

Therefore, the polarization density of the interacting SSH model in the continuum limit may be readily computed using Eq. (4.23) and Eq. (4.28),

$$\mathcal{P} = \frac{1}{4}\left(\frac{1}{1-g/\pi} + 1 - \frac{g}{\pi}\right)\mathrm{sign}(m)\ . \tag{4.29}$$

This is the main result of this chapter. However, there are limitations.

It is known that when the interaction is strong enough (i.e., $g > \pi/2$), the system becomes gapless [226]. In this case, the interaction makes the massive term irrelevant in the RG sense. It does not drive the system out of the critical region but explores it, as the Hamiltonian is neither gapped nor conformal. The physics of this scaling region is closer to the Luttinger liquid and is not captured by the behavior of the polarization, which is well defined for gapped systems as insulators. Additionally, an important property of the physical mass is that the gap is closed when the effective coupling B reaches an essential singularity (i.e., $\beta^2 = 1$ or $g = \pi/2$) of Eq. (4.24). Otherwise, the sign of the mass never changes. This means that the polarization jumps along the same line $m_0 = 0$ of the free case, and the effect of interactions does not change the shape of the phase diagram in this massive regime.

The polarization of the continuum limit of the interacting SSH model and the corresponding phase diagram are shown in Figs. 4.4(a) and 4.4(b), respectively. We note that the phase diagram in the continuum limit is different from that of the lattice model. This is because we are considering different approaches: we are studying the polarization in the continuum limit using field theoretical tools, while most numerical studies consider the behavior of different order parameters on the lattice. This means the continuum limit does not capture boundaries, finite-size effects, and excited state properties of lattice models, such as band curvature. It might fail to determine what other order parameters can be captured , such as the different shapes of critical lines in the original lattice model. For instance, the *gapless* straight line in Fig. 4.4(b) is different from the one obtained in the literature, where numerical schemes were used to compute similar phase diagrams [217, 218].

One of the main interpretations of these results is that the polarization is only modified to account for the fractionalized charge of the excitations of the theory. Indeed, the term $(1 - g/\pi)^{-1}$ and its inverse, appearing in Eq. (4.29), come from two contributions: the renormalized electronic charge of the Thirring fermion and a second term that is a consequence of the degeneracy of the ground state, carried by the string operator accompanying the soliton creation operators, respectively. Thus, electron-electron interactions do not change the qualitative description of the topological phases but do quantitatively modify it to account for the renormalization of the polarization. Moreover, if one were to construct an adiabatic charge pump, such as the Rice-Mele charge pump [219], the quantized charge transferred after one cycle would now be fractionalized to this new value. Indeed, the induced current results from a change in polarization, driven by a change in configuration in the insulator's bound charges. The Rice-Mele pump is known to adiabatically

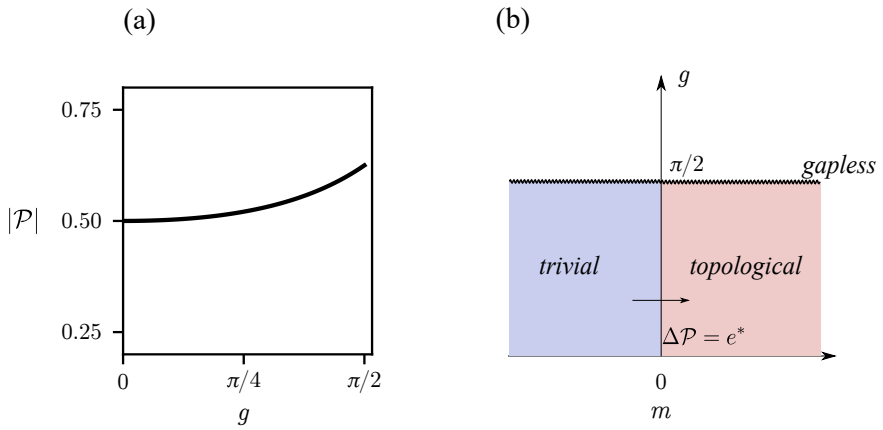

Figure 4.4: (a) Continuum polarization as a function of the interaction strength of the Thirring model. The deviation from the noninteracting value is relatively small in the region where the interaction strength allows for a well-defined polarization, i.e., $0 \leq g < \pi/2$. (b) Phase diagram for the low-energy sector of the repulsive interacting SSH chain in the region where the polarization is well defined. We identify trivial and topological regions from the exact mapping established at the level of the free theory (i.e., along the m-axis). The introduction of interaction in the system does not spoil the topology of the chain until the interaction overcomes the threshold (represented by the wiggling line) and the system undergoes a phase transition. The jump in the polarization, here represented by a change of color from blue to red, along the g-axis, signals the passage from a trivial into a topological phase, accompanied by a change in polarization $\Delta\mathcal{P} = e^*$, where e^* is the charge carried by the excitations of the theory.

modulate a 1D chain, such that it is tuned from the trivial to the topological phase of the SSH model and back again to its trivial phase [231]. As a result, the change in polarization is $\Delta P = 1$ (recall that we are working with units where $e = 1$). This picture is still valid in the continuum model, with $\Delta\mathcal{P} = 1$. As such, we can interpret the modification of the amplitude of the polarization in Eq. (4.29) as a result of the modification of the charge of the elementary excitations of the theory, i.e., $\Delta\mathcal{P} = e^*$, as sketched in Fig. 4.4.

Finally, we would like to point out that all the results derived in the last section also hold when one considers the generalization to the extended SSH model Eq. (4.10). Even though the winding number of the lattice theory might take higher values, signaling multiple topologically distinct phases, the polarization itself is only nontrivial whenever the winding number is an odd integer [see Eq. (4.4), which is defined modulo the uncertainty quantum e]. The general case contains infinitely many topologically distinct atomic limits, half of which are of the obstructed nature [20]. When taking the continuum limit near a phase transition, the Thirring model describes two topologically distinct phases corresponding to neighboring winding numbers. In other words, it models the transition between a phase with nontrivial polarization and one with zero polarization. The only change

occurs in different definitions of the Fermi velocities v_F and mass parameters m_0, which are given in Eq. (4.11).

To gain a deeper understanding of these results, we will employ perturbation theory, the renormalization group, and terminology from Fermi liquid theory to provide additional physical insights and interpretations.

4.3.3 Perturbation theory

Perturbation theory requires regularization schemes, such as introducing a cutoff Λ in momentum space, which we can consider proportional to the inverse of the lattice spacing in the related fermionic chain problem. Such a cutoff Λ is needed when the interaction parameter g is considered because perturbation theory produces divergent contributions. These are resolved either by considering counterterms in the Lagrangian or are regularized by the presence of the cutoff Λ and eliminated by a convenient redefinition. In practice, an infinitesimal redefinition of the cutoff $\Lambda \to \Lambda + \delta\Lambda$ can be performed, leading to a shift in all other parameters of the theory subject to a renormalization, i.e., the coupling constants and the field prefactors,

$$\begin{aligned} g_i &\to g_i + \delta g_i \ , \\ \Psi &\to (1 + \delta\eta)\Psi \ , \\ \beta^{(i)}_{\mathrm{RG}} &\equiv -\Lambda \tfrac{\delta g_i}{\delta \Lambda} \simeq -\tfrac{\partial g_i}{\partial \log \Lambda} \ , \\ \gamma &= -\Lambda \tfrac{\delta \eta}{\delta \Lambda} \simeq -\tfrac{\partial \eta}{\partial \log \Lambda} \ , \end{aligned}$$

where $i = 1, 2$, with $g_1 = m$ and $g_2 = g$. We have also defined the RG beta functions β_{RG} of the parameters g_i and implied a change in the scaling dimension γ because of the redefinition of the field through η. Additionally, the correlation functions containing n fields transform as

$$G^{(n)}(\Lambda, g_i) \to (1 + n\delta\eta) G^{(n)}(g_i) \ .$$

Requiring that their form must be independent of the value of the cutoff Λ leads to the so-called Callan-Symanzik equation:

$$\begin{aligned} \frac{\mathrm{d}}{\mathrm{d}\log\Lambda} G^{(n)}(k_1, \ldots, k_n; \Lambda, g) &= 0 \\ \left[\Lambda \frac{\partial}{\partial \Lambda} + \sum_i \beta_{\mathrm{RG}}(g_i) \frac{\partial}{\partial g_i} + n\gamma \right] G^{(n)}(k_1, \ldots, k_n; \Lambda, g) &= 0. \end{aligned} \tag{4.30}$$

Using the fact that $\beta_{\mathrm{RG}} \to 0$ in the UV limit, Eq. (4.30) results in $\log G \sim 2\gamma \log(k/\Lambda)$. Therefore, we find that the argument of the two-point function is

$$\varphi(k) \sim -i \log G = -2i\gamma \log\left(\frac{k}{\Lambda}\right),$$

which corroborates the dependence of the polarization on the scaling dimension of the fermionic field. Taking $k \to \Lambda$ and then $\Lambda \to \infty$ also confirms that the polarization is independent of regularization schemes and the form of the cutoff.

Although perturbation theory in 1D systems differs significantly from higher-dimensional cases [208], it can provide valuable insights for interpreting results. For instance, Eq. (4.23), derived non-perturbatively, can be analyzed using Fermi liquid terminology. This approach paves the way for potential generalizations of our arguments to interacting topological fermionic systems in 2D or 3D. This can be shown by associating the renormalization group procedure with Fermi liquid theory. The simplest way to do so is by considering the many-body Green's function close to its poles, which takes the form

$$G(k,\omega) = \frac{Z}{\omega - \epsilon(k)} \ , \tag{4.31}$$

where $\epsilon(k)$ is the energy of the excitations with momentum k. The shift $\delta\eta$, dictated by the scaling dimension of the fermion field, induces a shift of the quasiparticle weight Z. In the Fermi liquid framework, this quantity measures Fermi-liquid behavior: as long as $Z \simeq 1$, excitations behave as free electrons with dressed mass and electric charge, i.e., they are the system's quasiparticles. When this is the case, we do not expect the polarization to be affected by interactions, except for the "trivial" renormalization of the electronic charge. However, our result Eq. (4.29) contains an additional contribution related to the degeneracy of the ground state of the dual bosonic model, breaking the Fermi liquid picture and signaling the fact that the fermionic excitations are not reducible to dressed electrons but are entirely different.

Let us now compute the lowest order corrections to the polarization given by Eq. (4.16), but with the full interacting Green's function. The polarization can be expanded as

$$\mathcal{P} = \mathcal{P}^{(0)} + g\mathcal{P}^{(1)} + \frac{g^2}{2}\mathcal{P}^{(2)} + \dots$$

The lowest order expansion of the exact solution of the polarization Eq. (4.29) is of order g^2. Thus, we expect that perturbation theory reproduces this functional relationship, i.e., $\mathcal{P}^{(1)} = 0$ and $\mathcal{P}^{(2)} \neq 0$.

To perform the calculations, we first recall that the fully interacting Green's function obeys the self-consistent Dyson equation, which is formally given by

$$\begin{aligned} \hat{G} &= \hat{G}_0 + \hat{G}_0 * \hat{\Sigma} * \hat{G} \\ &= \hat{G}_0 + \hat{G}_0 * \hat{\Sigma} * \hat{G}_0 + \hat{G}_0 * \hat{\Sigma} * \hat{G}_0 * \hat{\Sigma} * \hat{G}_0 + \cdots \ , \end{aligned} \tag{4.32}$$

where the hat is used to denote the formal operators and the stars denote their multiplication. The self-energy $\hat{\Sigma}$ represents all the one-particle irreducible diagrams in the expansion of the two-point correlation function (i.e., the Green's function). The inverse of the Green's function is simply

$$\hat{G}^{-1} = \hat{G}_0^{-1} - \hat{\Sigma} \ . \tag{4.33}$$

Substituting Eq. (4.32) and Eq. (4.33) into Eq. (4.16), one obtains two terms, which will be considered separately,

$$\mathrm{Tr}\left[\sigma_z G \partial_k G_0^{-1}\right], \tag{4.34}$$

and

$$\mathrm{Tr}\left[\sigma_z G \partial_k \Sigma\right]. \tag{4.35}$$

To first order, the self-energy $\hat{\Sigma}$ does not depend on momentum (see the Feynman diagram in Fig. 4.5).

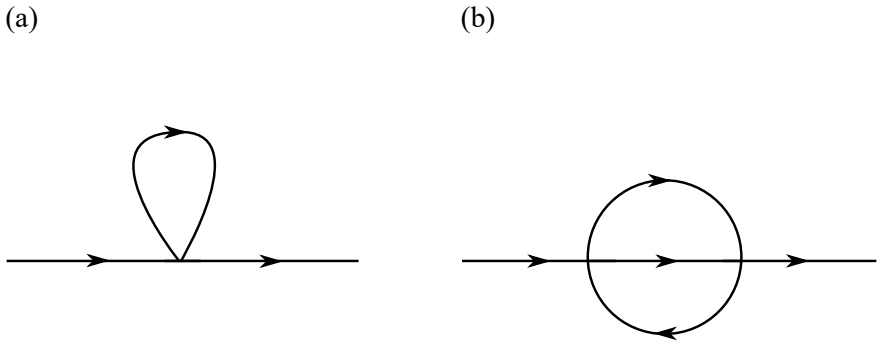

Figure 4.5: The two relevant corrections to the Green's function. (a) The self-energy is momentum-independent in this case. (b) The lowest correction to the self-energy acquires a linear momentum dependence, resulting in a g^2 correction to the polarization.

Thus, only the first term Eq. (4.34) contributes to the first-order correction to the self-energy, i.e.

$$g\mathcal{P}^{(1)} = \int_{-\infty}^{+\infty} \frac{\mathrm{d}k}{4\pi i}\, \mathrm{Tr}\left[\sigma_z G_0 \Sigma G_0 \partial_k G_0^{-1}\right]. \tag{4.36}$$

To compute Σ, we will use the fully relativistic propagators, vertex functions, and the Feynman rules depicted in Fig. 4.6. The self-energy depicted in Fig. 4.5(a) then reads

$$\begin{aligned}\Sigma^{(1)} &= g \int \frac{\mathrm{d}^2 q}{(2\pi)^2} \gamma_\mu G_0(k,\omega)\gamma^\mu \\ &= 2mg\mathbb{1} \int \frac{\mathrm{d}^2 q}{(2\pi)^2} \frac{1}{\omega^2 - k^2 - m^2}\ .\end{aligned}$$

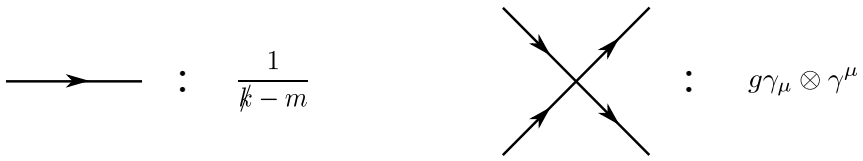

Figure 4.6: Feynman rules for the propagator in momentum space and the interaction vertex. The relation to the initially used propagator is obtained by multiplying it from the left by $-\sigma_x$.

Without proceeding with the calculation of this divergent integral (which requires a careful renormalization with a counterterm in the Lagrangian), we can nevertheless see, after multiplying by $-\sigma_x$ [see Fig. 4.5], that

$$\Sigma^{(1)} = \alpha g \sigma_x \ , \tag{4.37}$$

where α is the constant obtained by carrying out the integral. Substituting Eq. (4.37) into Eq. (4.36), we obtain

$$g\mathcal{P}^{(1)} = -g\alpha \int_{-\infty}^{+\infty} \frac{\mathrm{d}k}{2\pi} \frac{(k^2 - m^2)k}{(k^2 + m^2)^2} \ ,$$

which is zero because the integrand is an odd function of k, confirming that there are no corrections to the free theory at first order in g.

The second-order contribution to the polarization comes from a term of the second type of first order contributions Eq. (4.35). This means that we require a momentum-dependent self-energy correction, for which the simplest example is shown in Fig. 4.5(b) and given by

$$\Sigma^{(2)} = g^2 \int \frac{\mathrm{d}^2 q \mathrm{d}^2 q'}{(2\pi)^4} \gamma^\mu G_0(k + q - q') \gamma_\mu G_0(q) \gamma^\nu G_0(q') \gamma_\nu .$$

This expression is rather lengthy and leads to divergences if evaluated without proper regularization. For the sake of simplicity, we assume a linear dependence on momentum. In some limiting cases, this linear dependence can be derived explicitly (see Ref. [228] for a specific example). Then, we take

$$\Sigma^{(2)} = \frac{g^2}{2} \sum_{\mu=0}^{3} \alpha_\mu \sigma_\mu k \ ,$$

where now $\sigma_0 = \mathbb{1}$, and σ_i, with $i = 1, 2, 3$, are the usual Pauli matrices. The simplest term that can contribute to the polarization to second order is then

$$\begin{aligned} \frac{g^2}{2}\mathcal{P}^{(2)} &= -\frac{g^2}{2} \int \frac{\mathrm{d}k}{4\pi i} \operatorname{Tr}\left[\sigma_z G_0 \partial_k \Sigma^{(2)}\right] \\ &= \frac{g^2}{2} \int \frac{\mathrm{d}k}{2\pi} \frac{\alpha_1 k - \alpha_2 m}{k^2 + m^2} \ . \end{aligned}$$

We can calculate the integral explicitly and obtain

$$\mathcal{P}^{(2)} = -\frac{\alpha_2}{2} \ , \tag{4.38}$$

confirming our expectations that the first correction in perturbation theory to the polarization should be of order g^2.

The absence of a first-order contribution also highlights that charge renormalization is not the only process contributing to the polarization response in the Thirring model [232]. If it were, a term proportional to g/π would be present. This supports the mathematical assumptions made using non-perturbative arguments and the renormalization group. From a physical perspective, it confirms that the breakdown of the Fermi liquid paradigm in one-dimensional models also affects the topological properties related to their linear response.

4.4 Conclusion

An analytic determination of topological properties of interacting fermionic systems has always proven to be a daunting task; so far, numerical results have been widely used in the field, but in this work, we have explicitly evaluated the topological invariant Eq. (4.16) in the low-energy regime of the interacting SSH chain with nearest-neighbour density-density coupling. The physical interpretation of this quantity was given in the free case as the relative polarization between sublattices. The interaction term that we considered respects the symmetries of the non-interacting system, and its continuum limit yields the Thirring model, which enabled the formulation of the problem using this framework and allowed us to obtain exact analytic results. We find that the IR and UV regions play a prominent role in the continuum theory. Namely, the presence of a mass gap in the infrared regime protects the result obtained by the characterization of the ultraviolet regime in terms of the scaling dimension of the fermionic field. The role of the mass parameter in determining the topological phase transitions of the lattice model is akin to how the interplay between the Semenoff mass and the Haldane mass dictates topological phase transitions in the Chern insulator [56]. Our result can be readily generalized to cases where longer-range hoppings are included. Such models allow for more topological phase transitions. Still, in the vicinity of each of them, they can all be modeled by Thirring field theories where the details of different transitions are encoded by the various masses and the Fermi velocities Eq. (4.11). The jump in the relative polarization is then computed in the same way as for the interacting SSH.

Moreover, its interpretation in terms of polarization and a quantized charge-pumping argument facilitates the description of topological phases through the bulk-boundary correspondence. This enables the construction of a phase diagram within the applicable regime. The modification of the polarization amplitude can be understood as coming from the renormalized charge, together with a quantity that weighs the degeneracy of the ground state carried by the excitations of the interacting theory. Although our results only apply to a family of 1D lattice models described by integrable interacting field theories in the continuum limit, they provide numerous insights regarding the nature of topological phase transitions in interacting models. For instance, the most relevant effects of interactions are the renormalization of the charge and, in this case, the degeneracy of the ground state. Additionally, most of the topological properties in the low-energy regime are determined by the scaling regions of the RG flow, where the UV regime influences the magnitude of the polarization Eq. (4.23) and the IR protects it via the presence of a gap. Finally, the non-Fermi liquid behavior leads to a simple redefinition of the polarization jump from integers to reals but does not affect the shape of the phase diagram.

As an outlook, it would be valuable to investigate whether this picture still holds when considering different types of interactions. The resulting low-energy effective field theories would vary, and some may not be integrable. Nevertheless, perturbative methods can always be used to compute the scaling dimensions of the fields and study the modification of the polarization. modification of the polarization.

4.A Quantization of the winding number

4.A.1 Lattice model

The Green's function for the Hamiltonian given by Eq. (1.3) is

$$G_0(k,0) = \frac{1}{(v^2+w^2+2vw\cos k)} \begin{pmatrix} 0 & v+we^{-ik} \\ v+we^{ik} & 0 \end{pmatrix}. \tag{4.39}$$

Working out the trace in Eq. (4.16) yields

$$\nu = \int_{-\pi}^{\pi} \frac{\mathrm{d}k}{4\pi i} \frac{2iw\,(w+v\cos k)}{v^2+w^2+2vw\cos k}.$$

We will solve this using contour integration. Before we do that, we shall rewrite the equation as

$$\nu = \int_{-\pi}^{\pi} \frac{\mathrm{d}k}{4\pi} \frac{2+Ve^{ik}+Ve^{-ik}}{(1+Ve^{ik})(1+Ve^{-ik})},$$

where we have introduced the parameter $V = v/w$. This integral can be rewritten as an integral over the unit circle S^1 in the complex plane by defining $z = e^{ik}$,

$$\begin{aligned} \nu &= \oint_{S^1} \frac{dz}{2\pi i} \frac{1}{2V} \frac{Vz^2+2z+V}{z(z+V^{-1})(z+V)}, \\ &\equiv \oint_{S^1} \frac{dz}{2\pi i} f(z). \end{aligned}$$

The function $f(z)$ has two poles inside the unit circle and one outside. The pole $z_0 = 0$ is always inside, while $z_1 = -V^{-1}$ is inside if $|w| < |v|$ (making $z_2 = -V$ outside). Using the residue theorem, we then have the following conditions

$$\nu = \begin{cases} \mathrm{Res}(f,z_0) + \mathrm{Res}(f,z_1), & \text{if } |w| < |v|, \\ \mathrm{Res}(f,z_0) + \mathrm{Res}(f,z_2), & \text{if } |w| > |v|. \end{cases}$$

Since the poles are of order 1, the residues are simply given by

$$\begin{aligned} \mathrm{Res}(f,z_0) &= \lim_{z\to z_0} (z-z_0) f(z) = \frac{1}{2}, \\ \mathrm{Res}(f,z_1) &= \lim_{z\to z_1} (z-z_1) f(z) = -\frac{1}{2}, \\ \mathrm{Res}(f,z_2) &= \lim_{z\to z_2} (z-z_2) f(z) = \frac{1}{2}, \end{aligned}$$

which finishes the proof of the quantization of the winding number,

$$\nu = \begin{cases} 0, & \text{if } |w| < |v|, \\ 1, & \text{if } |w| > |v|. \end{cases}$$

4.A.2 Continuum model

In this case, we start from Eq. (4.5) and write down the Green's function as

$$G_0(k,0) = \frac{1}{m^2 + w^2k^2}\begin{pmatrix} 0 & m+iwk \\ -m-iwk & \end{pmatrix}, \tag{4.40}$$

where we recovered the parameter w to compute the integral in the general case. Working out the trace in Eq. (4.16) yields

$$\begin{aligned}\nu &= \int_{-\infty}^{\infty} \frac{\mathrm{d}k}{4\pi i} \frac{2imw}{m^2 + w^2k^2} \\ &= \int_{-\infty}^{\infty} \frac{\mathrm{d}k}{2\pi} \frac{\mathcal{M}}{\mathcal{M}^2 + k^2} \\ &= \frac{\mathcal{M}}{2\pi} \int_{-\infty}^{\infty} \mathrm{d}k \frac{1}{\mathcal{M}^2} \frac{1}{1 + (k/\mathcal{M})^2},\end{aligned}$$

where we introduced the scaled mass parameter $\mathcal{M} = m/w$. Now we use the fact that $a/a^2 = 1/|a|$, and substitute $k = \mathcal{M}x$ to get

$$\nu = \frac{\mathcal{M}}{2\pi|\mathcal{M}|} \int_{-\infty}^{\infty} \mathrm{d}x \frac{1}{1+x^2} = \frac{1}{2}\mathrm{sign}(\mathcal{M}).$$

The last equality results from $a/|a| = \mathrm{sign}(a)$ and the integral evaluating to π.

4.B Thirring and sine-Gordon models

In this section, we list some properties of the Thirring model. Most of them are obtained using its bosonic dual, the sine-Gordon model. Both are instances of integrable field theories, which are (1+1)-dimensional field theories that have an infinite number of local conserved charges. Such operators commute with the respective Hamiltonian and will strongly constrain the scattering between particles and, in general, the dynamics in the model. Scattering between particles is elastic and factorizes into subsequent two-particle scatterings. These requirements are strict enough to analytically fix the form of the scattering matrix via bootstrap methods [233], which is why these theories are analytically solvable. In particular, the Green's functions and the operator's matrix elements can be derived analytically.

Starting from the Lagrangians of the Thirring and sine-Gordon models (for simplicity, we consider $v_\mathrm{F} = 1$)

$$\begin{aligned}\mathcal{L}_\mathrm{Th} &= \bar{\Psi}(x)\left(i\partial\!\!\!/ - m_0\right)\Psi(x) - \frac{g}{2}\left[\bar{\Psi}(x)\gamma_\mu\Psi(x)\right]^2, \\ \mathcal{L}_\mathrm{SG} &= \frac{1}{16\pi}\left(\partial_\mu\Phi\right)^2 + \frac{m_0^2}{\beta^2}\left(\cos\beta\Phi - 1\right),\end{aligned}$$

the scattering matrix of Thirring fermionic excitations, labeled by $i = \pm$ when fermions (+) or antifermions (−) are considered, can be fully specified using inverse scattering methods. It is given by [222, 232]

$$S_{ij}(\theta) = -e^{8i/\beta^2}\frac{e^\theta - e^{-8i/\beta^2}}{e^\theta - e^{8i/\beta^2}}\delta_{ij} + (1-\delta_{ij}), \tag{4.41}$$

where the argument θ is the difference between two rapidities θ_1 and θ_2, related to the momenta p_1 and p_2 through $p_i = m\cosh\theta_i$. The scattering matrix has the following action on a two-particle state

$$S_{i_1 i_2}(\theta)|\theta_1,\theta_2\rangle_{i_1,i_2} = |\theta_2,\theta_1\rangle_{i_2,i_1}.$$

Moreover, given its action on states, we can infer that $S(-\theta) = S^\dagger(\theta) = S^{-1}(\theta)$, which holds for Eq. (4.41). This expression depends also on the parameter β^2, which is just the coupling of the sine-Gordon model. Moreover, we take the mass of the Thirring fermion m to be a renormalized version of the mass parameter m_0, given by Eq. (4.24) and obtained by studying the sine-Gordon theory. Before turning to the latter, we briefly introduce how correlation functions are evaluated in the Thirring model: once the following matrix elements of a certain operator V are known,

$$F^V_{n;i_1\dots i_n}(\theta_1,\dots,\theta_n) = \langle 0|V|\theta_1,\dots,\theta_n\rangle_{i_1\dots i_n}, \tag{4.42}$$

the Lehmann representation is fully described as an absolutely convergent series (after Wick rotating to Euclidean spacetime)

$$\begin{aligned} G^V(x,t) &= \langle 0|V(x,t)V^\dagger(0,0)|0\rangle \\ &= \sum_{n=0}^{\infty}\int_{-\infty}^{+\infty} \mathrm{d}\theta_1\dots\mathrm{d}\theta_n |F^V_n(\theta_1,\dots,\theta_n)|^2 e^{i(kx+\Omega t)}, \end{aligned} \tag{4.43}$$

where $k = m\sum_{j=1}^n \sinh\theta_j$ and $\Omega = m\sum_{j=1}^n\cosh\theta_j$. Because of their importance, the matrix elements of Eq. (4.42) are dubbed form factors, and self-consistency arguments constrain their analytic form [234]. One can also infer from the representation Eq. (4.43) that two-point functions in momentum space do not contain zeroes on the real axis, except for $k\to 0,\infty$. Moreover, Eq. (4.43) is crucial to verify scaling properties of Green's function in the UV and IR regions in Eq. (4.21): the first can be studied using the Feynman gas method, and one can numerically check that predictions from CFTs are consistent with form factor computations, while the second is straightforward since, by performing a Wick rotation, one can show that every two-point function scales as e^{-mL} in this regime, where L is the system size.

Now, to unveil the relations between the bare and the physical quantities of the Thirring model, we turn to the sine-Gordon model. Moreover, the bosonization procedure naturally lends itself to a more straightforward computation of the Green's function of the Thirring model, compared to the direct method. We start by the bosonisation relations between the fermionic fields Ψ and $\bar\Psi$ and the bosonic ones Φ and Θ, where Θ is the dual field given by $-\partial_x\Theta(x,t) = \partial_t\Phi(x,t)$,

$$\begin{aligned} \Psi(x,t) &= \exp\left\{\frac{i}{2}\left[\beta\Phi(x,t) + \frac{1}{\beta}\Theta(x,t)\right]\right\}, \\ \bar\Psi(x,t) &= \exp\left\{-\frac{i}{2}\left[\beta\Phi(x,t) - \frac{1}{\beta}\Theta(x,t)\right]\right\}. \end{aligned} \tag{4.44}$$

In the main text, we employ then the following notation, borrowed from Ref. [228]:

$$\begin{aligned}\Psi(x,t) &= e^{i\beta\Phi(x,t)/2}\mathcal{O}^1_{\beta/2}(x,t),\\ \bar{\Psi}(x,t) &= e^{-i\beta\Phi(x,t)/2}\mathcal{O}^1_{-\beta/2}(x,t),\end{aligned} \tag{4.45}$$

where the operator $\mathcal{O}^1_{\pm\beta/2}$ contains an infinite product given by the Baker-Campbell-Hausdorff factorisation of the exponential in Eq. (4.44), and depends on the phase field Θ and all its commutators with Φ. Moreover, the origin of a string-like term in the fermionic creation/annihilation operators is given by the relation between the bosonic field and its dual,

$$\Theta(x,t) = -\int_{-\infty}^{x} \mathrm{d}s\partial_t\Phi(s,t). \tag{4.46}$$

Such an operator appears in the exponent of Eq. (4.44) and weights the configuration of the field from the point x where it is placed, to $-\infty$. We proceed finally by plugging in the definition Eq. (4.44) into the Thirring Lagrangian in Eq. (4.9) to obtain

$$\mathcal{L}_{\mathrm{SG}} = \frac{1}{2}\left[(\partial_x\Phi)^2 + (\partial_x\Theta)^2\right] + \frac{m_0^2}{\beta^2}\left(\cos\beta\Phi - 1\right), \tag{4.47}$$

Provided the following identity holds:

$$\beta^2 = \frac{1}{2}\frac{1}{1-g/\pi}, \tag{4.48}$$

that allows us to relate the coupling constants from the two models.

The sine-Gordon model has another peculiarity, namely, it can be understood as the integrable deformation of a coset CFT $(\mathrm{G}_1 \times \mathrm{G}_1)/\mathrm{G}_2$ [235, 236]. This piece of information, joined with the study of the thermodynamics of the model using the thermodynamics Bethe Ansatz, allows one to compute the relation between mass and coupling constant. Fateev developed the original argument for a broad class of models, which were refined by Zamolodchikov in the sine-Gordon case [237]. Here, we briefly follow Mussardo [238] for a simple review of the main argument. The main idea lies in computing the free energy of an integrable model both using the thermodynamics Bethe Ansatz and conformal perturbation theory (see Section 4.D for an introduction): in the first case, we can expand for small values of the mass m, while in the second we will expand in the coupling constant g. We are then able to match the two series, getting the expression:

$$\beta = \mathcal{D}m^{2-2\Delta},$$

which is expected from dimensional analysis (the conformal weight Δ belongs to the relevant deforming operator, i.e. $\cos\beta\Phi$ in the sine-Gordon case and $\Delta_{\mathrm{SG}} = \beta^2$), but the meaningful prefactor $\mathcal{D}$ can be directly computed. We stress that such a result cannot be obtained directly from the Thirring model itself and proves once more the power of bosonization methods.

4.C Derivation of the scaling behavior of Green's function in momentum space

We start by considering the Fourier transform of the Green's function, i.e., Green's function in momentum space,

$$G(\mathbf{k}) = \int_{\mathbb{R}^2} \frac{\mathrm{d}\mathbf{k}}{(2\pi)^2} G(\mathbf{x}) e^{-i\mathbf{k}\cdot\mathbf{x}},$$

where spacetime is equipped with a Euclidean signature. We now split the integration region into three different ones:

1. The UV region $|x| < a$,
2. The regular region $a < |x| < R$,
3. The IR region $|x| > R$.

From Eq. (4.21), we know the behavior in the scaling regions, and by redefining the integration variables $\mathbf{k}\cdot\mathbf{x} = kr\cos\theta$, with $kr = s$, we obtain in the UV region

$$G_{\mathrm{UV}}(\mathbf{k}) = k^{y_{\mathrm{uv}}-2} \int_0^{+ka} \frac{\mathrm{d}s}{2\pi} \int_0^{2\pi} \frac{\mathrm{d}\theta}{2\pi} s^{y_{\mathrm{uv}}-1} e^{-is\cos\theta},$$

where y_{uv} is the scaling dimension in the UV regime. The only momentum dependence left in the integral is in the extremes of integration. When the system approaches the critical phase, it is only determined by its UV completion. As such, we can consider the limit $a \to \infty$, and the only dependence is power-law-like (as we would be expecting from a simple scaling argument [239]). For the same reason, this expression is also a pure power-law when the momentum is large.

When the IR region is considered, the same considerations occur, except for the presence of different integrands depending on whether we consider massive or massless theories. For a massive theory, the result would read

$$G_{\mathrm{IR}}(k) = e^{-mR}\left(\frac{e^{ikR}}{k+im} - \frac{e^{-ikR}}{k-im}\right),$$

and the region for $k \to 0$ is fully described by the constant result proportional to $1/m$. For gapless systems, this result is just

$$G_{\mathrm{IR}}(k) = k^{y_{\mathrm{ir}}-2} \int_{kR}^{+\infty} \frac{\mathrm{d}s}{2\pi} s^{y_{\mathrm{ir}}-1} e^{-is},$$

and it ensures again a power-law behavior. For pure CFTs, $y_{\mathrm{uv}} = y_{\mathrm{ir}}$.

Our treatment does not affect the regular region; the only requirement that it must fulfill is the absence of zeroes or singularities, which is ensured in integrable models.

4.D Scaling dimension in quantum field theory

An unexpected outcome of the renormalization procedure in quantum field theories is the presence of anomalous dimensions of local fields. This effect can be understood from two different points of view: at the level of a lattice, in which the rescaling of the lattice spacing induces a change in the theory's parameters, or at the level of the field theory, where the couplings run under rescaling of the momentum space.

Even though the relation between the two is, at first sight, straightforward (the lattice spacing and the momentum cutoff of a theory are reciprocal to each other), it is highly relevant to the understanding of our results: the invariance from lattice spacing and momentum cutoff informs us about the necessity of describing our topological invariant/polarization only in terms of scale-invariant quantities, i.e. quantities that are defined in scaling invariant regions of the theory. In addition, the realization of the quantum field theory on a lattice and the insertion of a momentum cutoff are both instances of a regularization procedure needed when interactions are relevant in a quantum field theory. We shall now outline why and how scale-invariant regimes are present in lattice and continuum theories [240].

Lattice. Consider a lattice of length $L = Na$, where N is the number of sites and a is the lattice spacing. Imposing that the universal properties of the physical system contained in its partition function are invariant under rescaling, we can perform a change of the lattice spacing $a \to a' = ba$ and the number of sites $N \to N'$. This procedure is called a real-space renormalization group. To keep the partition function of the system unchanged, all the parameters describing the Hamiltonian of the theory will change accordingly in a generally complicated and nonlinear transformation $g_i \to g_i' = f_i(\{g_k\}, b)$. The iteration of this procedure leads to a family of points in the coupling constant manifold representing the same system, observed with different values of the parameters a and N. Since the correlation length of the system is simply rescaled,

$$\xi(g') = b^{-1}\xi(g),$$

the fixed points of the RG, $g_i^* = f_i(\{g_k^*\}, b)$, imply that the correlation length vanishes (trivial points) or diverges (critical points) across them. This, in turn, implies that the physical dimension of operators on the lattice changes along the renormalization group flow. An operator on the trivial point has a dimension equal to its physical dimension, established by means of usual dimensional counting, while one at the critical dimension is determined by critical exponents. These two values are usually different, and this difference is accounted for by the anomalous dimension. The reason for this phenomenon is better understood in continuum theories.

Continuum. In a field theory, performing the renormalization procedure in momentum space is simpler. Here, divergences in Feynman diagrams must be accounted for by introducing counterterms in the Lagrangian, resulting in a shift of the couplings and leading to similar conclusions. These divergences in Feynman diagrams parts – usually at high momenta – require a regularization procedure,

typically achieved by imposing a momentum cutoff Λ. Following this procedure, the sources of singular behavior can be safely removed at the price of introducing a dependence between the couplings – and the fields – on the cutoff via counterterms, i.e., $g_i \to g_i' = f_i(\{g_k\}, \Lambda)$. Adding new counterterms at higher orders of the coupling constants is equivalent to shifting the cutoff value toward infinity (which is the point where it is formally removed). On the other hand, we can also squeeze our momentum space by rescaling the cutoff $\Lambda \to \Lambda' = \Lambda/b$; we would get the same picture of the lattice procedure, and we could study the relation between couplings and cutoff in detail without the need to compute more counterterms. Expanding the knowledge of the UV-region $k \in (\Lambda, +\infty)$ with this procedure allows studying the properties of the model close to the critical fixed point; it is then simple to draw the picture we used in Section 4.C of the whole momentum space split into regular part (determined by the massive interacting theory), IR-region (ruled by the trivial fixed point as a massive free theory) and the UV-region (described by the critical fixed point as a massless interacting theory). Moreover, as elucidated in the main text, imposing the invariance of expectation values (namely correlation functions) leads to a set of equations [see Eq. (4.30)] that rule the renormalization group flow in the momentum space; among these, the presence of counterterms for fields induces a non-trivial anomalous dimension, especially at the fixed point where $f_i(g^*) = 0$. Now, we can understand the presence of an anomalous dimension as the effect of mixing between the original free field with others needed to remove singularities arising from turning on the interaction; in other words, the dressing of the free field induces the anomalous dimension.

It is then clear why taking the continuum limit of the interacting SSH model would not spoil its topology. Since the polarization is a scale-invariant quantity, it is customary to consider the limit for $a \to 0$, where the Thirring model is retrieved. More than that, the polarization must retain scale-independent properties from fixed points related to the Thirring model, i.e., its massive free fermionic theory in the IR regime and the massless Thirring model at the UV point.

In addition, one can check the scaling properties of Green's functions along the RG trajectory that connects the two fixed points, as in Eq. (4.21), where the scaling dimension of fermionic creation and annihilation operators enters. The form factor expansion fully controls the IR point, so we just check the UV, which is the one depending on the anomalous dimension. The idea lies in considering the fixed point (which, for simplicity, we consider described by a CFT and not just critical; this is the case for Thirring and the sine-Gordon model) and a perturbation that drives the system away from it by opening a gap in the spectrum. Note that the above-mentioned integrable theories can also be expressed close to their critical fixed points as gap-opening perturbations of conformal field theories. CFTs are fully solvable, and the perturbation we add,

$$\mathcal{L} = \mathcal{L}_{\mathrm{CFT}} + \lambda V(r),$$

can be treated perturbatively for arbitrary small values of λ. Hence, one can reconstruct exactly the terms of the series for expectation values of local operators

A_k:

$$\langle A_k \rangle_\lambda = \frac{1}{Z_\lambda} \sum_{n=0}^{\infty} \frac{(-\lambda)^n}{n!} \int \mathrm{d}r_1 \dots \mathrm{d}r_n \langle A_k V(r_1) \dots V(r_n) \rangle_0.$$

Then, we can extract the most diverging term of the Green's function in the limit $r \to 0$, studying the operator product expansion in the off-critical region,

$$\Psi(z, \bar{z}) \bar{\Psi}(0) = \sum_k C^k_{\Psi \bar{\Psi}}(z, \bar{z}) A_k(0).$$

We then obtain, based on dimensional analysis,

$$C^k_{\Psi \bar{\Psi}}(z, \bar{z}) = z^{\gamma_k - 2\gamma_\Psi} \bar{z}^{\gamma_k - 2\bar{\gamma}_\Psi} \sum_{n=0}^{\infty} D^{k,n}_{\Psi \bar{\Psi}} (\lambda r^{2 - \gamma_\Psi - \bar{\gamma}_\Psi})^n,$$

where $r = (z\bar{z})^{1/2}$. Then, the most diverging term occurs for $n = 0$ and $\gamma_k = 0$, which involves the identity operator $A_0 = \mathbf{1}$. We have shown that in the limit $r \to 0$, the dominant contribution is still given by a power-law determined by the CFT that describes the fixed point. Such a statement is valid at any level of perturbation theory and directly leads to Eq. (4.21).

Part II

Aperiodic Systems

Chapter 5

Impurities in Quasicrystals

Commonly used symbols and acronyms

Symbol/Acronym	Meaning
IPR	Inverse Participation ratio
W_n	Aperiodic word of generation n
F_n	Fibonacci number of generation n
T_n	Tribonacci number of generation n
$\phi = (1+\sqrt{5})/2$	Golden ratio
$\beta \approx 1.8393$	Tribonacci constant
H	Hamiltonian
H_n	Hamiltonian of the n^{th} generation chain
v_i	Potential at site i
t_i	Hopping amplitude between site i and site $i+1$
t_w, t_s	Weak and strong hopping amplitudes, respectively
D_q	Multifractal dimension
$\langle O \rangle_X$	Average overlap integral of cluster X
$\langle I \rangle$	Average IPR

5.1 Introduction

Since their discovery by Dan Shechtman [121], quasicrystals have attracted much attention. Their unusual properties, such as low thermal conductivity, low friction coefficients, high hardness, corrosion resistance, and superplasticity, have made them attractive for applications. Their utility ranges from heat-insulating materials, through coating that increases hardness, all the way to medical implants, where prosthetics made from quasicrystalline material have shown minimal cytotoxicity effects [122–125]. Many studies have been conducted on the nature and properties of quasicrystals. Not being identified as classical crystals, they are characterized by forbidden discrete symmetries, such as the fivefold rotation group, with the archetypal example being AlMg [121]. One way to understand the emergence of this symmetry is by tiling a 2D plane [241]. On the other hand, a more structural way of understanding all quasiperiodic arrangements is to view them as projections from higher dimensional lattice spaces, which have a perfectly periodic structure [242, 243]. Although mainly manufactured in laboratories, quasicrystals have also been observed to occur in nature, where the structure was found to exist in a Siberian meteorite sample [244]. A mechanism for forming artificial and natural quasicrystalline phases has recently been proposed. It consists of the superposition of two 1D periodic subsystems with incommensurate periods, where charge-density waves favor the emergence of a quasiperiodic tiling of the atomic lattice [245].

The fact that quasicrystals are not periodic in their microscopic structure makes them a more complicated problem to study than their periodic counterpart. One way to simplify the problem and obtain relevant results is to study a 1D abstraction of the natural system. In that case, the most popular toy model is given by the 1D Fibonacci quasicrystal [136], described by a tight-binding model for a particle subject to a lattice potential. Depending on the chosen model, the Fibonacci sequence modulates the on-site potential or the hopping parameter. It takes on two discrete values, which will be explained in more detail later. This model exhibits peculiar properties: its energy spectrum is singular-continuous and self-similar, and its wavefunctions possess multifractal properties [246]. A renormalization scheme was introduced to explain the features of the spectrum and its scaling symmetries [136]. This scheme was subsequently used to understand the gap labeling theorem [149], applied to the purely hopping Fibonacci chain. Together with the conumbering scheme [135], it offered an insightful way to characterize the wavefunctions in terms of their renormalization paths [247]. Nowadays, new insights are still being provided. These range from the topological character of the system to superconductivity [137, 139, 152, 247–250].

In this chapter, we aim to understand how impurities disrupt the quasiperiodic order. We start by investigating the effect of a single impurity on the wavefunction canvas using the wavefunction renormalization mentioned above. We find that a transition regime exists for weak impurities in which the quasiperiodic order remains intact in parts of the system. This is manifested by preserving symmetry in the wavefunction amplitude as a function of conumbered sites and can be quantified by calculating cluster-averaged overlap integrals. As the strength of the impurity is raised, a disordered phase appears, characterized by the wavefunctions' localization, compatible with previous results in Ref. [251], where "resonant states" were

identified in the presence of an impurity.

Moreover, the transition regime can be labeled by the renormalization path of the site where the impurity has been placed. This behavior is also visible in the state-averaged inverse participation ratio (IPR) as a function of the impurity strength. The different types of IPR can be grouped in terms of the renormalization path of the site where the impurity is placed. Some impurity realizations lead to the surprising delocalization-relocalization phenomena for a range of impurity strengths. This observation is very similar to one found in a recent study, where random disorder was introduced in the hopping parameters and was shown to lead to a regime of delocalization before a "reentrant localization" takes place [252, 253]. This also applies to some extent when multiple weak impurities are added, where the individual contributions can be superposed to produce the full disruptive pattern. Since the quasiperiodic order is gradually lost, the transition regime can be characterized by a classification of the kind of disorder induced, and we find that the disorder develops in an organized way.

The paper is structured as follows. In Section 5.2, we briefly describe the Fibonacci chain in a tight-binding approximation. We then provide an overview of the understanding of its spectrum through a renormalization procedure. In Section 5.3, we generalize this construction to the Tribonacci chain and the Rauzy fractal. In Section 5.4, we introduce disorder by adding one impurity to the system. We show that we can classify disorder by the renormalization path label of the site where the impurity is placed. Finally, in Section 5.5, we present our conclusions and outlook.

5.2 The Model

We start by briefly recalling how to generate the Fibonacci sequence. We then explain how it can be understood as a quasicrystal arising from a cut-and-project scheme from a two-dimensional square lattice. We then construct the Fibonacci chain by encoding the sequence in a tight-binding Hamiltonian and analyzing its properties through a renormalization procedure.

5.2.1 Fibonacci Tight-Binding Model

Inflation Method The Fibonacci sequence, represented by a binary alphabet $\{A, B\}$, can be generated iteratively through the inflation rule

$$\begin{aligned} A &\to AB, \\ B &\to A, \end{aligned}$$

starting with the "zeroth" letter S. The n^{th} iteration, W_n, will be referred to as the n^{th} approximant of the Fibonacci word, the size of which will be denoted by $|W_n| = F_n$. This sequence has the property

$$\lim_{N\to\infty} \frac{F_{n+1}}{F_n} = \frac{1+\sqrt{5}}{2} \equiv \phi, \tag{5.1}$$

where ϕ is called the *golden ratio*. The Fibonacci sequence is often represented in terms of word size and takes the form $\{F_n\}_{n=0}^{\infty} = \{1, 1, 2, 3, 5, 8, 13, \dots\}$. Another property is that each term can be generated recursively through:

$$F_{n+2} = F_{n+1} + F_n, \tag{5.2}$$

with $F_0 = F_1 = 1$. In terms of Fibonacci words, the recursion relation can be written as

$$W_{n+2} = W_{n+1} W_n.$$

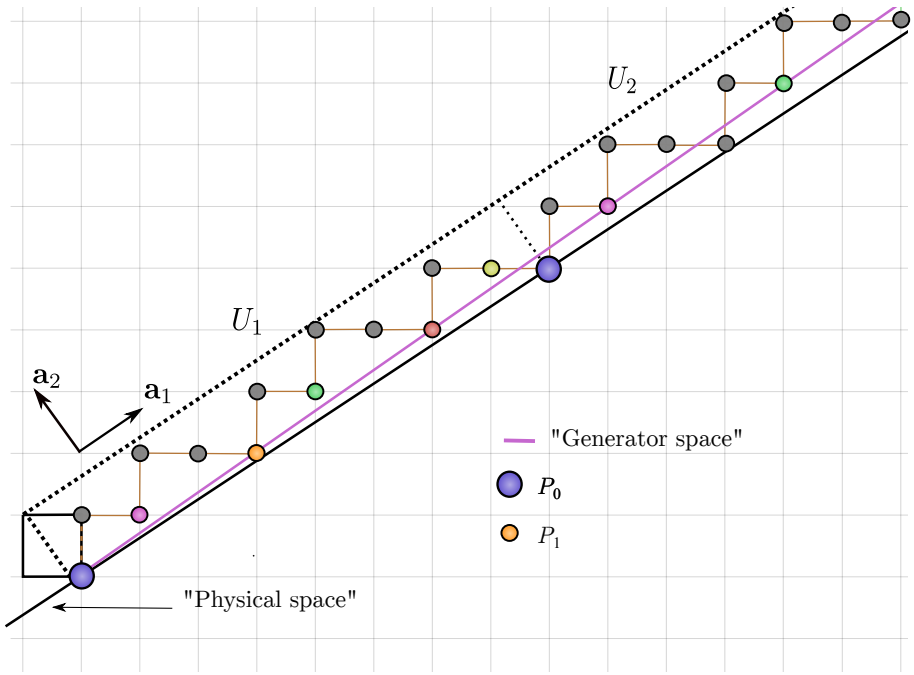

Figure 5.1: $\mathbb{Z}^2$ space, with a Fibonacci quasicrystal approximant cell containing 13 sites ($\phi_6 = 8/5$). The vectors $\mathbf{a}_1$ and $\mathbf{a}_2$ are also shown for reference. The strip containing the sites to be projected is defined by translating the red square along the physical space. The repeating unit cells are denoted by U_i. The purple line is the generator space Span$\{\mathbf{h}\}$, with $\mathbf{h} = (3, 2)$. The points on the generator are marked with different colors. Notice that points in unit cell U_2 below the generator line are repetitions of the points marked in orange and red in the first unit cell U_1. Conversely, the points above the generator in the first unit cell U_1 marked in purple and green are repetitions of points on the generator in unit cell U_2.

Cut and Project Methods and Conumbers The Fibonacci sequence is known to be quasiperiodic, i.e., it can be obtained as a projection of a higher-dimensional periodic sequence. This method is the so-called cut-and-project scheme of generating quasiperiodic lattices. In this case, points on $\mathbb{Z}^2$ are projected onto a line

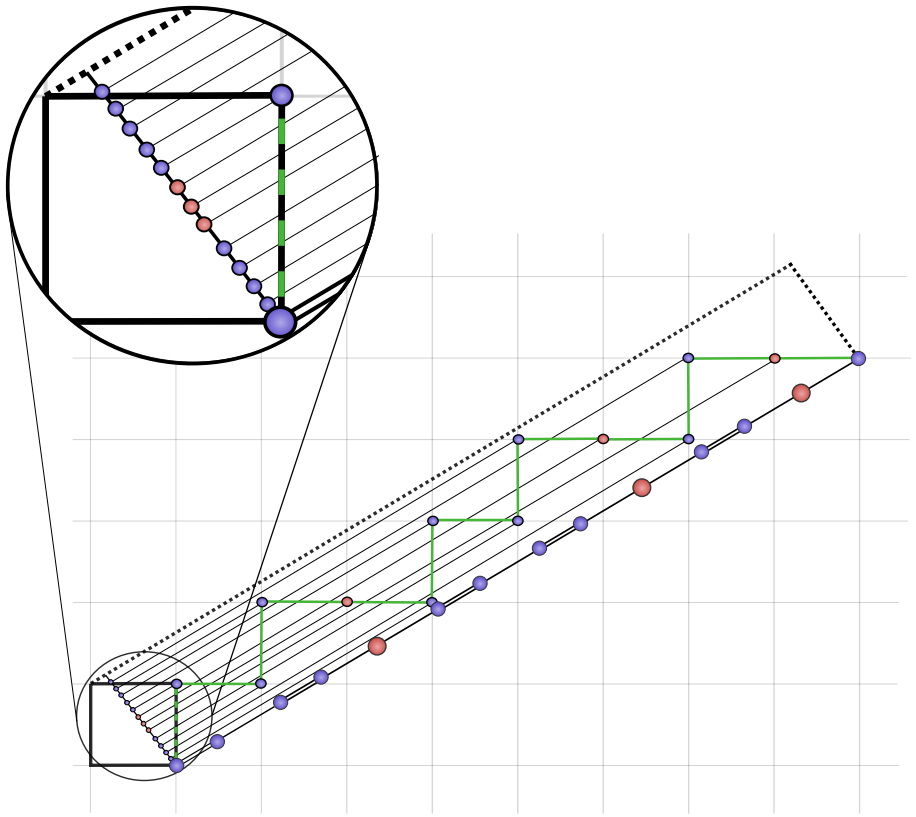

Figure 5.2: Both projections are shown here, with a zoom-in on the orthogonal space to show how the conumbered sites are organized. The real space chain has also been adorned with the different hoppings corresponding to the two distances (L and S).

of slope $1/\phi$ (see Fig. 5.1, where the line represented in black is called the "physical space"). To construct the n^{th} periodic (rational) approximant of the infinite chain, we define the vector $\mathbf{a}_1 = (F_{n-1}, F_{n-2})$, which points along the line of slope $1/\phi_n = F_{n-2}/F_{n-1}$ (with $\phi_{N\to\infty} = \phi$). We then consider a unit square, the lower left vertex of which lies at the origin of the chain [see the black square in Fig. 5.1], which is then translated in the direction of $\mathbf{a}_1$. All the points within the strip traced by the square are then projected onto the physical line. The result is a chain where the nearest neighbors have relative distances A (long) and B (short), arranged in a Fibonacci sequence. We will also consider the projection in the orthogonal space, spanned by the vector $\mathbf{a}_2 = (-F_{n-2}, F_{n-1})$. When the same selection of points within the strip is projected along the line spanned by $\mathbf{a}_2$, an interesting arrangement of the sites is obtained. Indeed, in Fig. 5.1, we see that the projection along $\mathbf{a}_2$ amounts to an ordering of the sites in terms of their distance from the physical line. The shortest distance corresponds to the orange point, followed by the red, purple, and green points. We observe that they all lie on the line called

"generator space" (the origin of the name will become clear later). The Fibonacci chain allows for two types of sites: the ones surrounded by two A bonds, which we shall call "atomic" and represented by a red dot in Fig. 5.2, and those separated by an S bond, henceforth called "molecular" and represented by a blue dot. In Fig. 5.2, we see that on top of rearranging the points according to their distance from the physical line, the orthogonal projection also rearranges them in terms of their type: the atomic sites are placed in the middle, while the molecular ones are at the sides of the newly arranged chain. This scheme is called "conumbering", as the rearrangement of the sites is achieved by attaching a "conumber" to each site of the original Fibonacci chain. The scheme is constructed as follows: we define a "generator", $\mathbf{h} = \overrightarrow{P_0P_1}$, where P_0 and P_1 are the origin and the point with the smallest distance to the physical line. As stated, all subsequent points of shortest distances will lie on the line generated by $\mathbf{h}$. However, these points will not all lie within the first unit cell [denoted U_1 in Fig. 5.1], and the primary function of the conumbering scheme is to identify the points that lie outside of the first unit cell with the points that lie in it. The scheme thus performs a modulo operation on those points. The generator $\mathbf{h}$ will always generate the nearest previous rational approximant line within the strip traced by the unit square. Thus, conumbered points, before projection, are given by

$$\begin{aligned}\mathbf{x}_j &= j\mathbf{h}\mathrm{mod}[\mathbf{a_1}] \\ &= j\Big(a\mathrm{mod}(F_{n-1}), b\mathrm{mod}(F_{n-2})\Big)\end{aligned}$$

where a and b are two Fibonacci numbers that identify the nearest point and $j \in \{0, \ldots, F_n - 1\}$ is the "conumber". There is a periodicity in the difference between consecutive rational approximants of ϕ:

$$\mathrm{sign}(\phi_{n+1} - \phi_n) = (-1)^{n+1}, \quad n = \{0, 1, 2, ...\}.$$

This means that the slope that determines the generator is either the previous approximant or the one before it, depending on whether this slope is higher or lower than the actual approximant. After projection, this yields the usual formula used in recent literature [135, 247],

$$j = x_j F_{n-1}\mathrm{mod}(F_n), \tag{5.3}$$

where $x_j \in \{0, \ldots, F_n - 1\}$ denotes the sites in increasing order on the real lattice. The conumbered sites are very convenient because they organize the real lattice sites by their local environment. The other advantage is that one can observe the symmetry between the energy levels and the amplitude localization (see Section 5.4).

Tight-Binding Hamiltonians

The Fibonacci chain is constructed by considering the nearest-neighbor tight-binding Hamiltonian

$$H = \sum_{i=1}^{\infty} \Big[v_i \left|i\right\rangle \left\langle i\right| + t_i \left|i\right\rangle \left\langle i+1\right| + \mathrm{h.c.} \Big]. \tag{5.4}$$

We can either modulate the on-site potential v_i or the hopping parameter t_i. We shall refer to the two cases as the "on-site model" and the "hopping model". The modulation is applied as follows:

$$v_i = \begin{cases} v_w, & \text{if } i^{\text{th}} \text{ letter is } A, \\ v_s, & \text{if } i^{\text{th}} \text{ letter is } B, \end{cases} \tag{5.5}$$

for the on-site model and

$$t_i = \begin{cases} t_w, & \text{if } i^{\text{th}} \text{ letter is } A, \\ t_s, & \text{if } i^{\text{th}} \text{ letter is } B, \end{cases} \tag{5.6}$$

for the hopping model. The subscripts w and s have been chosen to reflect that A represents a longer distance and would correspond to a weak bond (hopping strength), while B is a short distance and thus a stronger bond. The two models have been studied extensively in Refs. [136, 139, 254], where the renormalization scheme [136] was used to reveal the multifractal properties of the model [247, 254]. The on-site model was also studied in Ref. [139] through the perspective of local symmetries, where a systematic way to control the edge modes of a finite chain was devised.

In the remainder of this paper, we focus on the hopping model, to which we apply periodic boundary conditions to renormalize it properly. The resulting spectrum has many interesting properties characteristic of quasiperiodic systems. The infinite chain has a singular-continuous spectrum, which is also self-similar [247, 255]. An example of the spectrum of a $n = 16$ chain is shown in Fig. 5.3. There, we observe a structure exhibiting trifurcation, which is self-similar. A renormalization procedure was devised by Nori et al. [136] to explain these features. There is also a direct mapping between the on-site and hopping models under the perturbative renormalization scheme (see Ref. [136]).

5.2.2 Renormalization of the Chains

The spectrum of the Fibonacci chain can be understood by performing a perturbative renormalization procedure to the hopping model, which is exact in the limit $\rho \equiv t_w/t_s \to 0$. Note that this can also be applied to the on-site Fibonacci chain, which, after one renormalization step, becomes a hopping Fibonacci chain. We start from the original Hamiltonian and, without loss of generality, set the on-site energy to be a constant, $V_i \equiv V = 0$. Then, we split it into an unperturbed part H_0 and a perturbation H_1, with

$$\begin{aligned} H_0 &= \sum_j t_s \left|j\right\rangle \left\langle j+1\right| + \text{h.c}, \quad \text{if} \quad j \bmod(\phi) < \phi^{-1}, \\ H_1 &= \sum_j t_w \left|j\right\rangle \left\langle j+1\right| + \text{h.c}, \quad \text{if} \quad j \bmod(\phi) \geq \phi^{-1}. \end{aligned} \tag{5.7}$$

The conditions imposed rely on the quasiperiodicity of $\text{sign}\left[(j+1)\text{mod}(\phi) - j\text{mod}(\phi)\right]$, which corresponds to the Fibonacci sequence in terms of $\{-1, 1\}$.

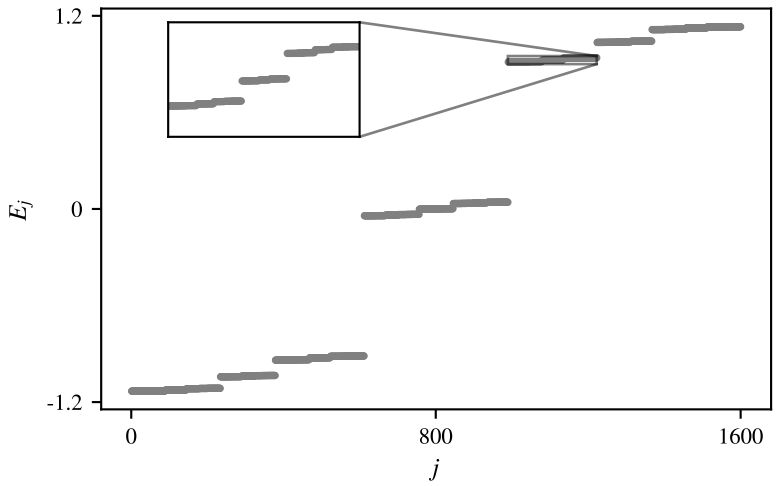

Figure 5.3: Energy spectrum of the $n = 16$ approximant Fibonacci chain, with 1597 sites, in the hopping model. The trifurcating structure can be seen at different energy scales. Self-similarity is also visible when looking at the inset of the upper cluster's lowest quasi-band. The modulation strength has been set to $\rho \equiv t_w/t_s = 0.2$.

The unperturbed Hamiltonian has three levels with a very large degeneracy, namely $E = 0, \pm t_s$. This sets the starting point of the renormalization procedure, which is applied to each of the three unperturbed levels independently. Following the nomenclature proposed by Macé et al. [247], we have one atomic deflation, corresponding to the atomic level ($E = 0$) and two molecular deflations corresponding to the bonding and anti-bonding molecular levels ($E = \pm t_s$). The atomic deflation takes the original chain of size F_n to a smaller Fibonacci chain of size F_{n-3}, while the molecular deflations map the original chain to one of size F_{n-2}. The renormalized hopping strengths, in each case, are given by:

$$\{t'_w, t'_s\} = \begin{cases} \left\{\dfrac{t_w^2}{2t_s}, \dfrac{t_w}{2}\right\} = \dfrac{\rho}{2}\{t_w, t_s\}, & \text{(bonding)} \\ \left\{\dfrac{t_w^3}{t_s^2}, -\dfrac{t_w^2}{t_s}\right\} = \rho^2\{t_w, -t_s\}, & \text{(atomic)} \\ \left\{\dfrac{t_w^2}{2t_s}, -\dfrac{t_w}{2}\right\} = \dfrac{\rho}{2}\{t_w, -t_s\}, & \text{(anti-bonding).} \end{cases}$$

We can thus write the original n^{th} approximant Hamiltonian, H_n, as a direct sum of three sub-Hamiltonians up to and including $\mathcal{O}(\rho^3)$ [254]:

$$H_n = \left(\frac{\rho}{2}H_{n-2} + t_s\right) \oplus \rho^2 H_{n-3} \oplus \left(\frac{\rho}{2}H_{n-2} - t_s\right). \tag{5.8}$$

Since each chain is a Fibonacci approximant, we can apply this procedure iteratively until one cannot further decimate any generation. The procedure for each

cluster type is depicted in Figs. 5.4 and 5.5. To be more precise, the atomic deci-

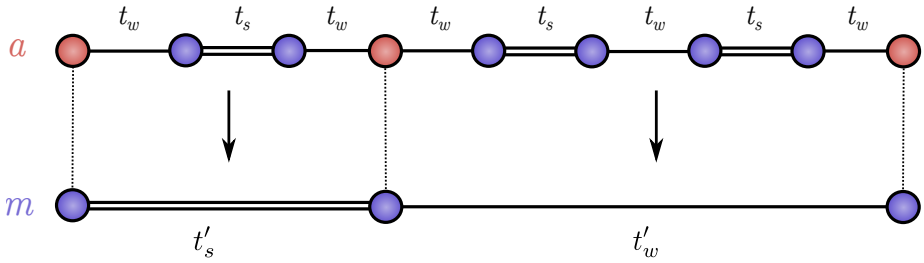

Figure 5.4: Decimation of the atomic-leveled chain. We have also colored the sites consistently with our previous definition for atomic and molecular sites. This figure gives a simple example of a renormalization path of a site in the n^{th} approximant chain. In this case, a chain of length $F_5 = 8$ is renormalized to a chain of length $F_2 = 2$. The renormalization path is just 'am'. This figure was inspired by those made in Refs. [136, 247].

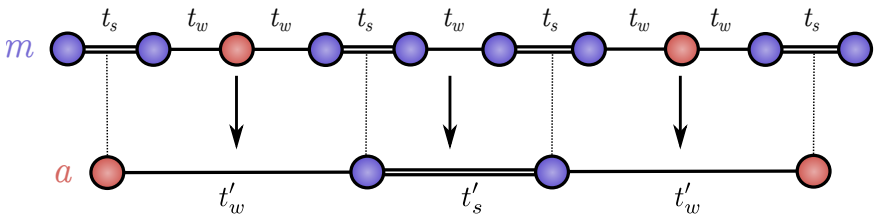

Figure 5.5: Decimation of the molecular-leveled chain. The same coloring scheme has been used to label the sites. Here, we have another simple example of renormalization paths: ' ma' on the left and 'mm' in the middle. The chain of length $F_5 = 8$ is changed to a chain of length of $F_3 = 3$. This figure was inspired by those made in Refs. [136, 247].

mation takes every atomic site of the chain (F_{n-3} of them). It connects every pair with a renormalized hopping strength that is strong when they are close to each other and weak when longer distances separate them (see Fig. 5.4). The molecular decimation, on the other hand, takes every superposition of two molecular sites (eigenstate of energy $\pm t_s$, each of which has a F_{n-2} degeneracy), connected by t_s in the original Fibonacci chain, and creates a new chain made up by these superpositions. The hoppings are connected similarly as in the atomic deflation, i.e., a strong hopping whenever these two renormalized sites are separated by a short distance in the original chain and a weak hopping when the distance is larger (see Fig. 5.5).

The renormalization path will play an important role when we study the effect of impurities in a Fibonacci chain. The renormalization path is defined in two ways. The first is a string of letters 'a' and 'm', which stand for the nature of the site at each renormalization step. Starting from an n^{th} approximant chain, two paths appear: 'amma...' for an atomic site at the top of the renormalization process or

'mmam...' for a molecular one. The other definition pertains to energy eigenstates and the cluster to which they belong. Since there are three distinct clusters, we define the eigenstate renormalization path by a string of letters 't', 'c' and 'b', describing the top cluster (bonding molecular), the central cluster (atomic), and the bottom cluster (anti-bonding molecular), respectively. For example, a particular level can then be encoded by the symbolic string sequence 'tctbt...c'. A particular symmetry exists between the two renormalization paths in the perturbative limit ($\rho \ll 1$), which has been made evident by the graphical representation given in Ref. [247]. This symmetry manifests itself when we rearrange the chain sites in terms of the conumber defined in Section 5.2.1 $C_N(j) = jF_{n-1} \mathrm{mod}(F_n)$ [see Fig. 5.2]. The fractal nature of the eigenstates becomes manifest in this representation, which is used in Section 5.4.1 to show how impurities disrupt this order.

5.3 The Tribonacci chain

A direct generalization of the Fibonacci sequence is obtained when enlarging the binary alphabet from which the words are constructed to one containing k letters. Changing the notation for convenience to numbers, the alphabet is $\mathcal{A} = \{0, 1, 2 \cdots, k-2, k-1\}$ and we impose the substitution rule

$$\begin{aligned} &0 \to 01, \\ &1 \to 02, \\ &2 \to 03, \\ &\vdots \\ &k-2 \to 0(k-1), \\ &k-1 \to 0. \end{aligned}$$

The infinite words constructed from these rules still satisfy the Pisot substitution conjecture and are, therefore, quasicrystals, as they have a pure-point Fourier spectrum [256]. The generalized picture of the cut-and-project scheme is that of increasing codimension: the projection occurs from a k-dimensional hypercubic lattice to a one-dimensional line. The word size $|W_n|$ is also subject to the recursion relations

$$|W_n| = \sum_{i=n-k}^{n-1} |W_i|.$$

Thus, the next step towards a generalization of the Fibonacci chain is obtained by a ternary alphabet. That is, $\mathcal{A} = \{A, B, C\}$, and the substitution rule is the *Tribonacci* substitution

$$\begin{aligned} &A \to AB, \\ &B \to AC, \\ &C \to A. \end{aligned} \tag{5.9}$$

The Tribonacci word starts with $ABACABAA\cdots$, and the Tribonacci constant, similar to the Fibonacci constant, is the dominant eigenvalue of the substitution

matrix associated with the symbolic dynamical system of the Tribonacci substitution. That is, the real root of the cubic equation $x^3 - x^2 - x - 1 = 0$, given by

$$\beta = (1 + \sqrt[3]{19 + 3\sqrt{33}} + \sqrt[3]{19 - 3\sqrt{33}})/3 \approx 1.8393, \tag{5.10}$$

This constant also appears in the ratio between the two subsequent Tribonacci numbers, satisfying

$$\begin{aligned} T_{N-3} + T_{N-2} + T_{N-1} &= T_N, \quad N > 3, \\ \lim_{N\to\infty} \frac{T_N}{T_{N-1}} &= \beta, \end{aligned} \tag{5.11}$$

with $T_0 = 1$, $T_1 = 1$, and $T_2 = 2$. The first few Tribonacci numbers are 1, 1, 2, 4, 7, 13, $\cdots$

5.3.1 The Tribonacci Hamiltonian

Some results obtained for the Fibonacci chain can be generalized to a Tribonacci chain, yielding additional insights and connections to mathematical objects such as the Rauzy fractal [257]. By modulating the tight-binding hopping parameter, $t_i \in \{t_1, t_2, t_3\}$, with the Tribonacci sequence Eq. (5.9), one obtains the Tribonacci chain [1], whose Hamiltonian is

$$H = \sum_{i=1}^{T_N} t_i \left|i\right\rangle \left\langle i+1\right| + \text{h.c.},$$

where T_N is the n^{th} Tribonacci number. This chain still features all the characteristics of the Fibonacci chain, with a singular-continuous and self-similar energy spectrum and multifractal eigenstates. An example of the spectrum is plotted in Fig. 5.6, where we chose only one modulation strength for simplicity, i.e., $\rho \equiv t_1/t_2 = t_0/t_1$. In this case, we see five pieces of self-similar quasi-bands. These clusters are also amenable to a perturbative renormalization procedure, for which the Hamiltonian of the n^{th} generation word takes the following form

$$\begin{aligned} H_n \approx (z_2 H_{n-3}^{(p_2,q_2)} - t_2) \oplus (z_1 H_{n-2}^{(p_1,q_1)} - t_1) \oplus z_0 H_{n-4}^{(p_0,q_0)} \\ \oplus (z_1 H_{n-2}^{(p_1,q_1)} + t_1) \oplus (z_2 H_{n-3}^{(p_2,q_2)} + t_2), \end{aligned} \tag{5.12}$$

where z_i, p_i and q_i, for $i = 0, 1, 2$, can be determined from perturbation theory [5]. The superscripts correspond to exponents in the modulation ratio ρ of the n^{th} approximant. A typical renormalized hopping t_i' takes the form

$$t_i' \sim \rho^{ap+bq} t_i,$$

where, once again, a and b also depend on the details of perturbation theory. The corrections to this Hamiltonian are of order $\mathcal{O}(\rho^{2+p+q})$.

[1] We have studied this chain in great detail during the master thesis of Julius Krebbekx, which led to the publication of Ref. [5].

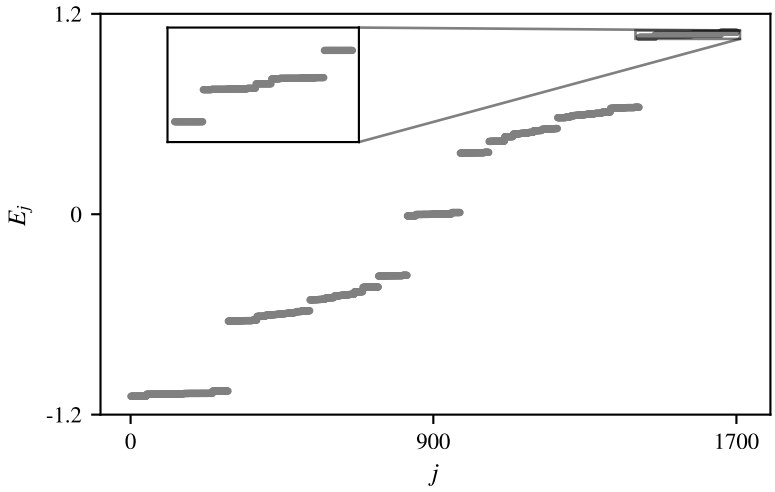

Figure 5.6: Energy spectrum of the $n = 13$ approximant hopping Tribonacci chain, with 1705 sites. The "quinfurcating" structure can be seen at different energy scales. Self-similarity is also apparent when looking at the inset of the upper cluster's highest quasi-band. The modulation strength has been set to $\rho = 0.5$.

5.3.2 The Rauzy fractal

Using the cut-and-project scheme, we can obtain a generalization of the conumbers to higher dimensions. The projection onto the space orthogonal to the physical space rearranges sites in terms of their local environments. However, in this case, there are three different local environments, and the orthogonal space is two-dimensional. The resulting "acceptance set", the set of points within the unit cube mapped to the orthogonal space, constitutes a Rauzy fractal [257], depicted in Fig. 5.7(a). The three possible regions, just like in the Fibonacci case, depend on what type of bonds the sites are connected to. Five possible neighborhoods exist, but two pairs are equivalent if one does not distinguish the left and right bonds. These are

1. Region 0: sites connected by t_0 bonds on both sides.
2. Region 1: sites connected by a t_0 bond on one side and a t_1 bond on the other.
3. Region 2: sites connected by a t_0 bond on one side and a t_2 bond on the other.

These regions are scaled versions of themselves, with a scaling factor given by the Tribonacci constant β given in Eq. (5.10).

One can use the Rauzy fractal to plot the wavefunctions and see that eigenstates belonging to a particular quasi-band have primarily support on one region of the Rauzy fractal, as exemplified in Fig. 5.7(b). There, we distinguish between the left

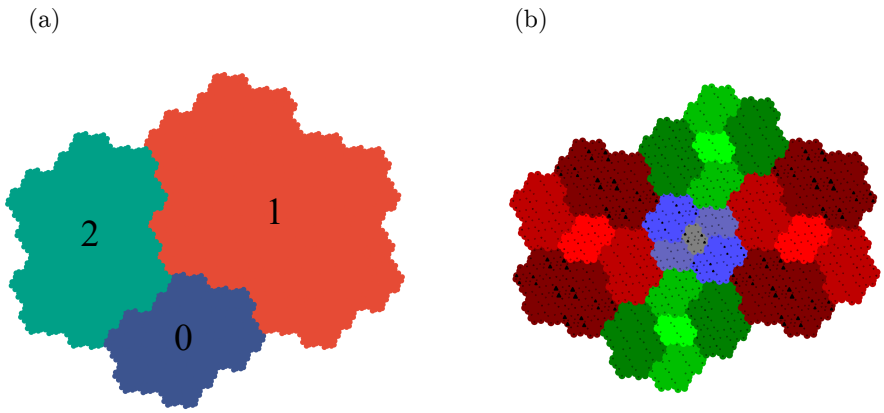

Figure 5.7: (a) The Rauzy fractal, where each region represents an area to which a site belonging to one of the three possible environments is mapped. (b) The symmetric Rauzy fractal now distinguishes between the left and right environment. The self-similar structure of the Rauzy fractal and the amplitudes of an example wavefunction are also shown. The size of each triangle represents the amplitude of the wavefunction on that particular site. The primary support in this case is in the red region for a state whose energy lies in the quasi-band corresponding to the H_{n-3}. These figures were created by master student Julius Krebbekx.

and right bonds and observe the self-similarity of the eigenstates on a symmetric version of the Rauzy-fractal. The support is primarily in the red region for a state whose energy lies in the quasi-band corresponding to H_{n-2}. This generalizes the self-similar symmetry between energy eigenstates and their spatial distributions, observed in the eigenstates map of the Fibonacci chain in Fig. 5.9(a).

5.3.3 Multifractal properties

Finally, we study the multifractal properties of the energy spectrum and eigenstates of the Tribonacci chain. Eigenstates with multifractal characteristics are typical of systems undergoing a localization phase transition [258]. These states are dubbed critical, and multifractal dimensions are associated with them [255, 259].

We will briefly review how multifractal dimensions arise in studying strange sets, such as those arising in dynamical systems [259]. We consider a bounded set S with a measure $\mu(S) = 1$, which we partition into finitely many hypercubes K_i of side length l. Applying the measure μ to K_i, denoted $\mu(K_i)$, is akin to asking what is the probability that a point x lies within the hypercube K_i. When we change the length scales of the hypercubes, multifractals have the local scaling behavior [255]

$$\mu(K_i) \propto l^{\alpha(x)}.$$

Consider now the number N of hypercubes for which the scaling exponent lies

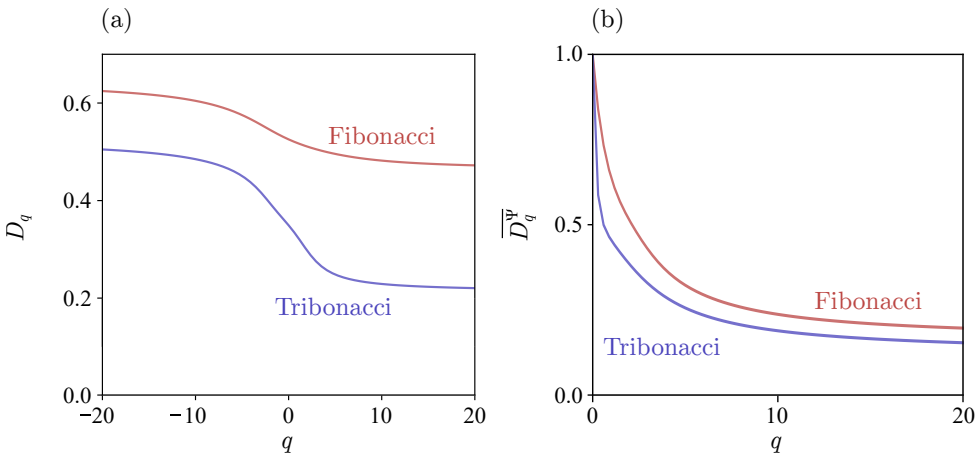

Figure 5.8: (a) Multifractal dimensions of the Fibonacci (red) and Tribonacci (blue) energy spectra. (b) Average multifractal dimensions of the eigenstates of the Fibonacci (red) and Tribonacci (blue) chains.

within $[\alpha, \alpha + \mathrm{d}\alpha)$. This number is given by

$$N \propto \tilde{\rho}(\alpha)\mathrm{d}\alpha,$$

where $\tilde{\rho}(\alpha)$ is a sort of local density of hypercubes. For fractal sets, we typically have a generic behavior given by [255]

$$\tilde{\rho}(\alpha) \propto l^{-f(\alpha)}. \tag{5.13}$$

The function $f(\alpha)$, typically continuous on a bounded interval, is called the local dimension of a subset $S_\alpha \subset S$ with local scaling exponent α.

Hentschel et al., in earlier work, gave another general definition for a continuous dimension function [259]

$$D_q = \lim_{l \to 0^+} \frac{1}{q-1} \frac{\log\left[\sum_i \mu(K_i)^q\right]}{\log l}. \tag{5.14}$$

This is a generalization of the box-counting dimension obtained when $q = 0$, the information dimension when $q = 1$ and the correlation dimension when $q = 2$ [260]. To evaluate D_q, one defines the following partition function for balls $S_i \subset S$, whose radius $l_i < l$,

$$\mathcal{Z}(q, \tau, l, S) = \sum_{i=1}^{N} \frac{\mu(S_i)^q}{l^\tau} \tag{5.15}$$

Taking the limit $l \to 0^+$, the partition function can only be of order 1 if $\tau(q) = (q-1)D_q$. Moreover, the local dimension $f(\alpha)$ and the multifractal dimension D_q

are conjugate functions, related through a Legendre transform

$$\alpha(q) = \frac{\mathrm{d}}{\mathrm{d}q}\tau(q),$$
$$f(\alpha(q)) = q\alpha(q) - \tau(q).$$

The curve D_q is constant and equal to the box-counting dimension for a single fractal or a regular set such as $\mathbb{R}^n$. Conversely, in that case, the local dimension $f(\alpha)$ is only defined for one point α. The telltale signs that the sets are multifractal objects are the nontrivial curves D_q or $f(\alpha)$.

In Fig. 5.8(a) and (b), we plot the multifractal dimensions of the energy spectrum and the average multifractal dimension of eigenstates for both the Fibonacci (red) and Tribonacci (blue) chains. Indeed, we see that both feature multifractality characteristics, as they show a continuous curve of D_q.

5.4 Introducing Disorder in the Fibonacci chain

There are multiple ways of introducing disorder by adding impurities. It was already shown [251] that even the introduction of one impurity in a relatively long chain has a drastic effect on the spectrum. In particular, it reduces the fractal dimension of the global density of states while increasing that of the local wavefunctions. Moreover, since the spectrum of the Fibonacci chain is singular-continuous [255], i.e., it has an infinite number of gaps, every state is affected by the presence of this impurity. The extent to which they are affected will, however, depend on the strength of the impurity. We will see that, for weak impurity strengths, a departure from criticality can be characterized using the renormalization path formulation described before. To this end, we first show that we can organize the impurity-induced disorder using the conumbering scheme. We then quantify this more thoroughly by studying the localization properties of the states through their inverse participation ratios. For the rest of the paper, we consider impurities by adding an extra term to the Hamiltonian:

$$H = H_F + \sum_{m \in S_I} V_I \left|m\right\rangle \left\langle m\right|, \tag{5.16}$$

where H_F is the pure Fibonacci Hamiltonian, and the impurities lie on a set of sites $m \in S_I$, with V_I denoting the impurity strength. We mainly focus on the single impurity case but extend the discussion later on to multiple impurities of the same strength.

5.4.1 Organizing Disorder: Renormalization Path

Before one departs completely from criticality, observing a structure in how disorder sets in is possible. We found that it can be organized according to the renormalization path that the site at which the impurity has been placed follows. For example, let us place a weak impurity (at 10% hopping strength) in a generation 9 chain with 55 sites. In that case, a total of 9 renormalization paths exist. Each generates one disordered graph, as shown in Fig. 5.9 and Fig. 5.10. From now on, we

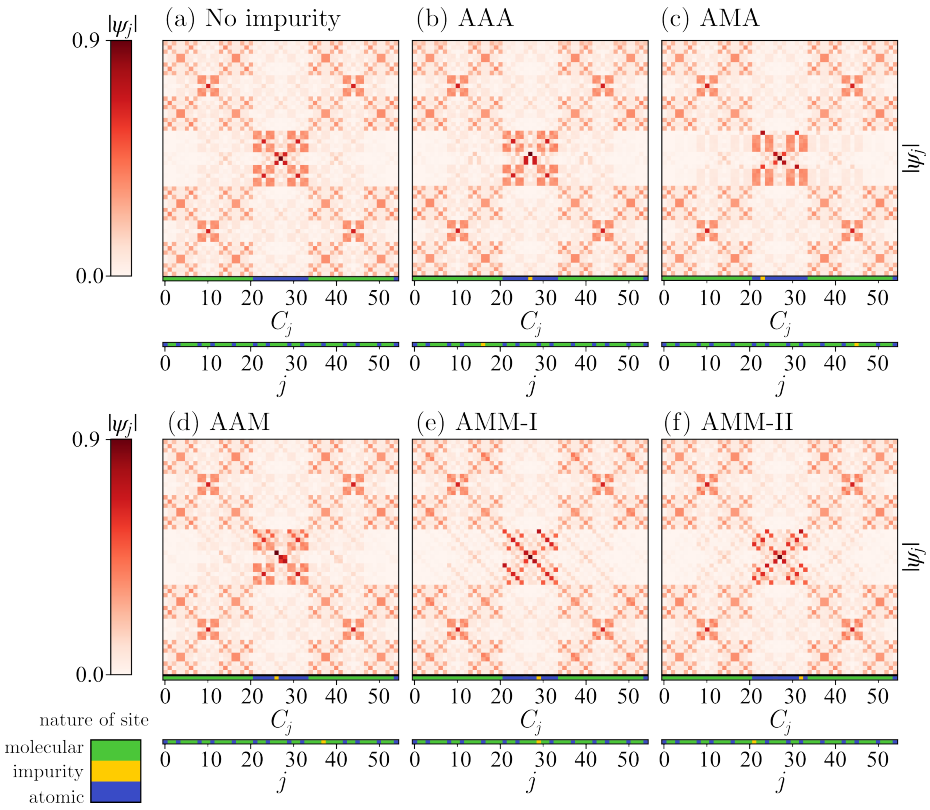

Figure 5.9: Atomic disorder classes listed in table 5.1. On the left side, we have two color codes: first, the local wavefunction modulus is plotted in shades of red; on the lower part, we have represented the lattice sites by their nature. Each site is either molecular (green), atomic (blue), or has an impurity (yellow). The parameters chosen for the numerical calculation are $\rho = 0.2$ and $V_I = 0.1t_w$. Note that because the impurity is weak, it mainly affects the atomic cluster and leaves the molecular cluster almost intact. (a) No impurity; (b-d) impurity on an AAA, AMA, and AAM site, respectively; (e) and (f) impurity on an AMM site,

will position the impurities at random sites in the Fibonacci chain. Then, we will identify the corresponding impurity positions in terms of conumbers. This allows us to identify which positions affect the eigenstate map the least. In Fig. 5.9(a), we present the unperturbed fractal pattern, as obtained in Ref. [247]. Its central part results mainly from the atomic sites, while the four surrounding structures result from molecular sites. Then, we successively position an impurity at various atomic sites in Figs. 5.9(b-f) The resulting patterns correspond almost one-to-one with the renormalization paths of the sites where the impurities are placed. Every site belonging to one path gives rise to the same disruption pattern [except the last two Figs. 5.9(e),(f)]. The same applies to impurities placed on molecular sites, as shown in Figs. 5.10(a-f). There is again a one-to-one correspondence

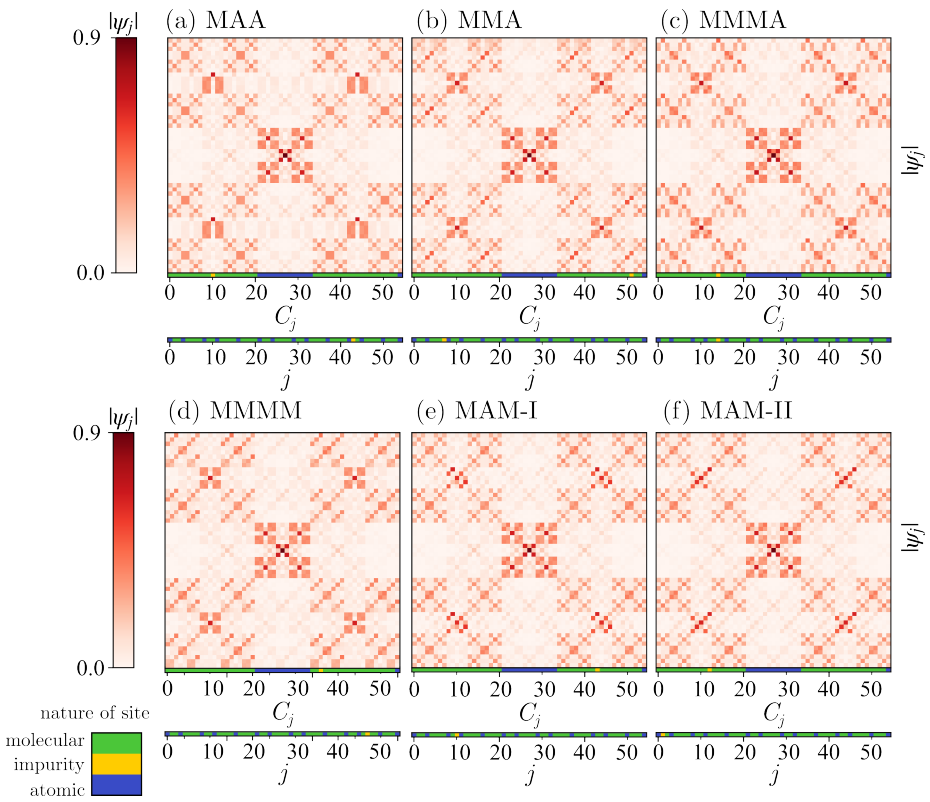

Figure 5.10: Molecular disorder classes listed in table 5.1. The color coding and parameters are the same as above. In this case, we find disorder mostly in the molecular cluster while the atomic one is almost intact. (a-f) Impurities on sites belonging to classes MAA, MMA, MMMA, MMMM and MAM (I and II), respectively.

between the pattern and the renormalization path, except for the last two cases, Figs. 5.10(e) and (f). Starting from an atomic impurity at the carefully selected AAA site, as shown in Fig. 5.9(b), it mainly affects one eigenstate. Noting that the eigenstates are ordered in terms of increasing energy, we see that the slight increase from the impurity potential shifts this state's energy (which is the closest to the unperturbed atomic energy $E = 0$) upwards. Since the renormalized chains correspond to atomic subclusters, the molecular clusters are left completely intact. Even the molecular subclusters of the original atomic cluster are relatively well preserved. In Fig. 5.9(c), the impurity is placed at an AMA site. We now have two states that are mostly affected by the presence of the impurity. These are the atomic states of the two F_4 chains resulting from the decimation procedure (one atomic site per chain, with atomic energies $E = \pm t'_s = \pm(\rho/2)t_s$, respectively). The previous two examples were the ones that disturbed the spatial distribution of the wavefunctions the least. The next three (AAM, AMM I, and AMM II) show a higher level of disorder in the structure. However, we still see that this disorder is

Table 5.1: List of renormalization paths and the number of distinct graphs it generates. We included the number of sites belonging to a particular renormalization path for reference. Note the almost one-to-one correspondence between the number of graphs and the renormalization paths.

Renormalization Path	Number of sites	Number of distinct graphs
MMMM	16	1
MMMA	8	1
MMA	8	1
MAM	8	2
MAA	2	1
AMM	8	2
AMA	2	1
AAM	2	1
AAA	1	1

mainly confined to the atomic cluster in the weak impurity regime.

When placing an impurity on molecular sites, all resulting possibilities are shown in Fig. 5.10(a)-(f). In Fig. 5.10(a), we see the least amount of disorder, which can easily be explained, just as in the atomic case, by disrupting two particular states. These are the atomic sites of two F_4 chains (one per chain, of energy $E = \pm t_s$, respectively), resulting from an MAA decimation procedure. This is qualitatively very similar to the AMA case, except that the atomic subclusters are different and are centered around the unperturbed molecular energy states. The following five graphs show the same behavior in the weak impurity regime as in the atomic case. We mostly see a disruption of the symmetric patterns within the molecular clusters, while the atomic cluster is mainly left intact.

In table 5.1 we have listed all the renormalization paths and the number of graphs they generate. The observation is that there is an almost one-to-one correspondence between the amount of renormalization paths and the possible type of disorder the system is subjected to. It is not exact, as there are two renormalization paths that each give rise to two distinct graphs, namely AMM in the atomic case and MAM in the molecular case [see Figs. 5.9 and 5.10 (e) and (f)]. Therefore, we can predict how many disordered graphs can be obtained by calculating the number of distinct renormalization paths.

Based on our numerical implementations, a breakdown of this behavior is observed for strong impurity strengths. This is illustrated in Figs. 5.11(a) and (b), where we plot two graphs with a strong on-site impurity placed on an atomic and a molecular site, respectively. These observations can be quantitatively substantiated by calculating overlap integrals. For this reason, we will show that in the presence of a weak atomic (molecular) impurity, the atomic (molecular) cluster is mostly affected. In contrast, the molecular (atomic) cluster is left intact. To see that, we need to calculate cluster-averaged overlap integrals, i.e., the average

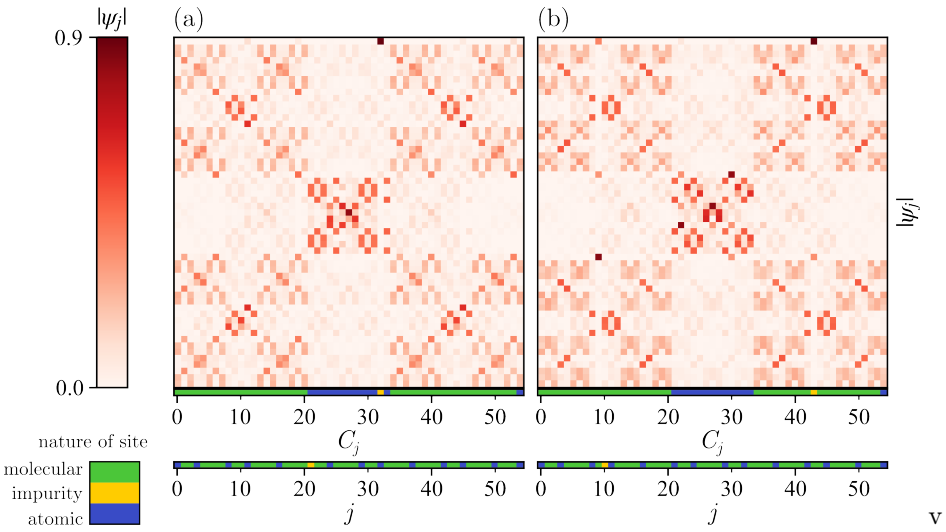

Figure 5.11: Disorder induced by a strong impurity of order $V_I = 10t_w$. (a) Atomic impurity. (b) Molecular impurity. In both cases, all clusters are affected by its presence.

overlap integrals between the clean Fibonacci chain and the one with an impurity. These are given by

$$\langle O \rangle_A = \frac{1}{F_{n-3}} \sum_{i=1}^{F_{n-3}} \left(\sum_{j=1}^{F_n} \left| \langle \psi^0_{i,A}(x_j) | \psi^I_{i,A}(x_j) \rangle \right| \right), \tag{5.17}$$

$$\langle O \rangle_M = \frac{1}{2F_{n-2}} \sum_{i=1}^{2F_{n-2}} \left(\sum_{j=1}^{F_n} \left| \langle \psi^0_{i,M}(x_j) | \psi^I_{i,M}(x_j) \rangle \right| \right). \tag{5.18}$$

with $|\psi^0_{i,X}(x_j)\rangle$ and $|\psi^I_{i,X}(x_j)\rangle$ the clean and perturbed eigenstates, respectively, of the atomic/molecular cluster (for $X = A, M$). The results are shown in Fig. 5.12(a-d), where we see that for the weak impurity strengths considered, the overlaps stay very close to 1 when the type of the site does not belong to the cluster considered, while it decreases more steeply when the impurity site does belong to the cluster. We have also verified whether these observations are size-dependent features, but it is not the case, as shown in Appendix 5.A. Another interesting property is the additivity of the disrupted patterns when one adds several weak impurities. One can superpose the eigenstate maps of the individual impurity disruptions to obtain the total disordered pattern. The simple examples in Fig. 5.13 illustrate this: there are two atomic impurities in Fig. 5.13(a), characterized by the renormalization paths AAA+AMA, and in Fig. 5.13(b), we add a molecular impurity to the previous two, such that the total disruption is characterized by the paths AAA+AMA+MMMA. It looks like the graphs have been superimposed on top of one another, as seen from the graphs in Figs. 5.9(b,c) and Fig. 5.10(c). Naturally, there is a limitation to these observations, as the amount of paths grows substantially with the size of

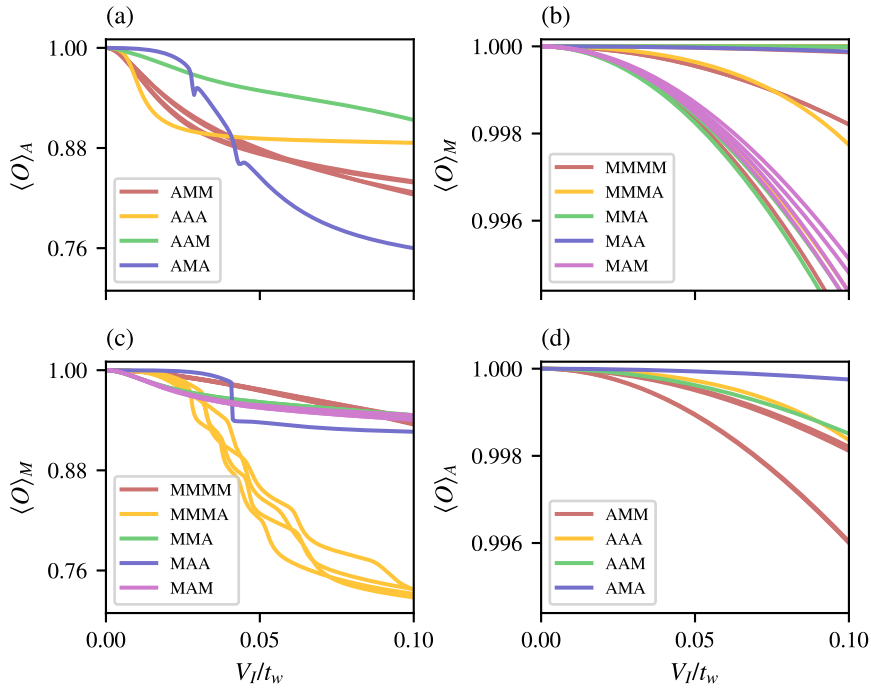

Figure 5.12: cluster averaged overlap integrals in the presence of (a,b) an atomic impurity and (c,d) a molecular impurity, for all possible impurities that result in different realizations and which are labeled by the renormalization path of the site at which they are placed. The atomic (molecular) cluster is left mostly intact by a molecular (atomic) impurity for the strengths considered. The parameters considered are still the same as the previous figures, with $\rho = 0.2$ and the number of sites $N = 55$.

the chain. Moreover, as the impurities grow stronger, the additivity of the graphs breaks down, and the impurities start to influence each other, an effect easily visible in the eigenstate map in Fig. 5.14. There, we added an impurity ten times the previous strength on an AAA site and another on an MA site. We can see that the two individual graphs are not superimposed. Additionally, this superposition is not exact, even for weak impurities. Indeed, since the eigenstate map represents probability densities, we know that in the case of multiple weak impurities, we can write down the amplitudes to first order in perturbation theory as

$$\psi_\alpha(x_i) = \alpha(x_i) + V_I \sum_{\beta \neq \alpha} \frac{\beta(x_i)}{E_0^{(\alpha)} - E_0^{(\beta)}} \sum_m \alpha(x_m)\beta^*(x_m) \tag{5.19}$$

where α and β denote eigenstates of the pure Fibonacci chain (without impurities). Since we are depicting a conumbered version of $|\psi_\alpha(x_i)|^2$, we also have nonlinearities entering the picture. In the case of very weak impurities, they are overshadowed

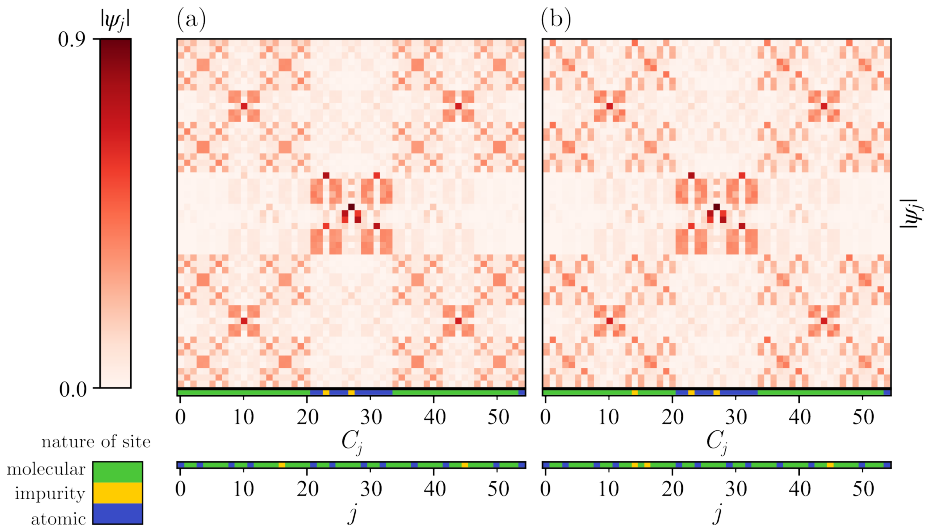

Figure 5.13: Example of multiple weak impurities ($V_I = 0.1t_w$) placed on the Fibonacci chain. (a) AAA-AMA pattern. (b) AAA-AMA-MMMA pattern. Remarkably, one can add the individual contributions from each class to generate the (weak) multi-impurity classes.

by the linear term, which is why we observe this additive feature. The nonlinearities are more pronounced in Fig. 5.15, where we plot the impurity-averaged inverse participation ratio (IPR, introduced in Sec. IIIB) of the single impurity realizations and compare it to the IPR of the system containing all the impurities. We see that they have the same behavior regarding how they depend on the strength of impurity, but they are not equal. Moreover, the similarities quickly disappear with increasing impurity strength, rendering the classification of multiple impurities more complicated than for the single impurity case. The nonlinearities are also more strongly pronounced in this case, which is expected because we are looking at the fourth moment of probability density.

At this point, we note that the existence of resonant states [251], especially in the case of weak impurities (of order $0.1t_w$), allows for what can be called a "transition regime", in which some level of quasiperiodic order is still present in parts of the system. We shall see in the next section that this can also be characterized by studying the localization properties of the system.

5.4.2 Localization Properties

We begin by making the general observation that introducing a strong impurity generally leads to the localization of one or several states. This is promptly visualized when one inspects the numerically obtained eigenstate map in Fig. 5.16, where the localization can be visualized for one of the eigenstates (white stripe, extending over several sites below the center of the figure). This behavior marks a departure from criticality, i.e., the wavefunctions of quasiperiodic systems are neither ex-

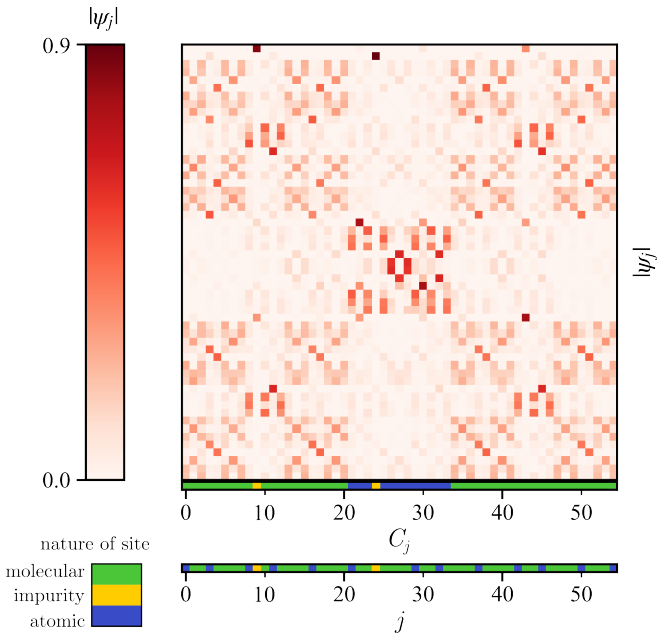

Figure 5.14: Two relatively strong impurities placed on an MAM site and an AMM site. Their strength is set at $V_I = 10t_w$. The result is not a superposition of the individual MAM and AMM graphs (see Fig. 5.11 for comparison).

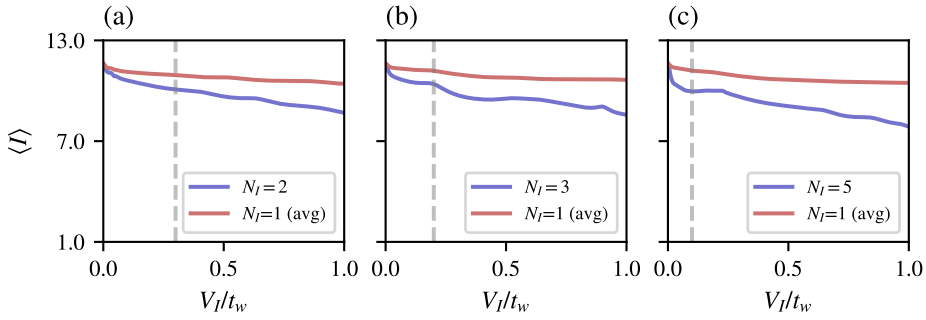

Figure 5.15: Comparisons between the impurity averaged IPRs of single-impurity realizations and the IPR of the multi-impurity system. (a) Two impurities, (b) three impurities, and (c) five impurities. We see that they approximately follow a similar evolution until an arbitrarily set threshold (red dashed line), after which the variations are not correlated.

tended nor localized. In Fig. 5.16, we see the localization around the site where the impurity was placed (site number 11 on the figure, where the darkest square marks the strongest amplitude). To properly determine the localization behavior of the system, we will calculate the IPR. For a particular eigenstate $|\alpha\rangle = \sum_i \psi_\alpha^m(x_i)\,|i\rangle$,

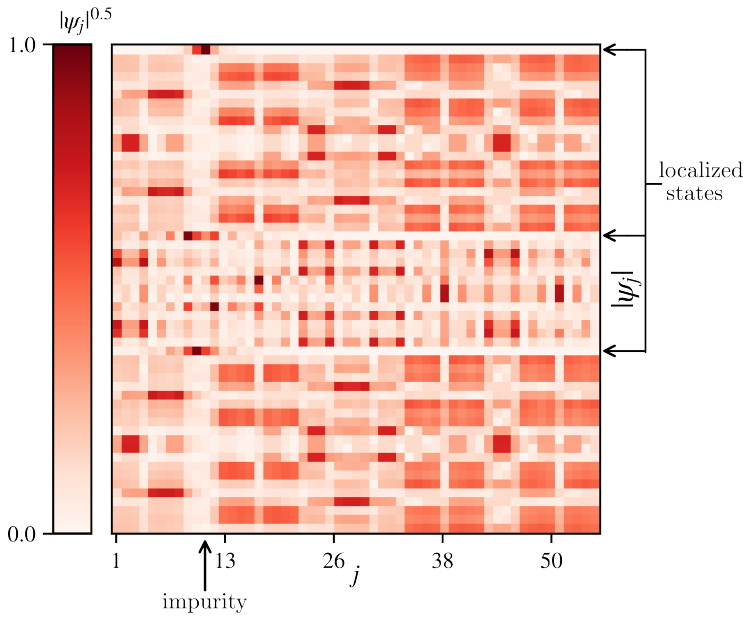

Figure 5.16: Impurity placed on a generation 9 chain (55 sites) at site number 11. The localized states are visible, with a white stripe extending over a wide range of sites, as indicated by the black arrow on the right. We used a strong impurity of order $10t_w$, with the ratio ρ=0.2 for clarity. A black arrow shows the impurity location

where proper normalization is imposed ($\sum_i |\psi_\alpha^m(x_i)|^2 = 1$), it is defined as

$$I_\alpha = \left(\sum_{j=1}^{F_n} |\psi_\alpha(x_j)|^4 \right)^{-1} . \tag{5.20}$$

This quantity gives a good measure of localization: in the fully localized limit, where we have $|\psi(x_m)|^2 = 1$ for some site x_m and zero otherwise, $I_\alpha = 1$. In the fully delocalized limit, where the probability density is uniform ($|\psi(x_i)|^2 = 1/N$ for all sites x_i), $I_\alpha = N$. The symmetry between the renormalization paths of energy levels and the sites is lost by introducing an impurity. However, we still want to be able to characterize the localization properties using the renormalization path of the sites. Therefore, instead of looking at each state's IPR, we look at the average IPR over all states. Thus, we define the state-averaged IPR as

$$\langle I \rangle = \frac{1}{F_n} \sum_{\alpha=1}^{F_n} I_\alpha = \frac{1}{F_n} \sum_{\alpha=1}^{F_n} \left(\sum_{j=1}^{F_n} |\psi_\alpha(x_j)|^4 \right)^{-1} . \tag{5.21}$$

We have plotted various $\langle I \rangle$ results in Fig. 5.17. We observe that, as hinted in the previous section, the behavior of the IPR can be grouped in terms of the renormalization path that a site belongs to. For the atomic case, all distinct representatives

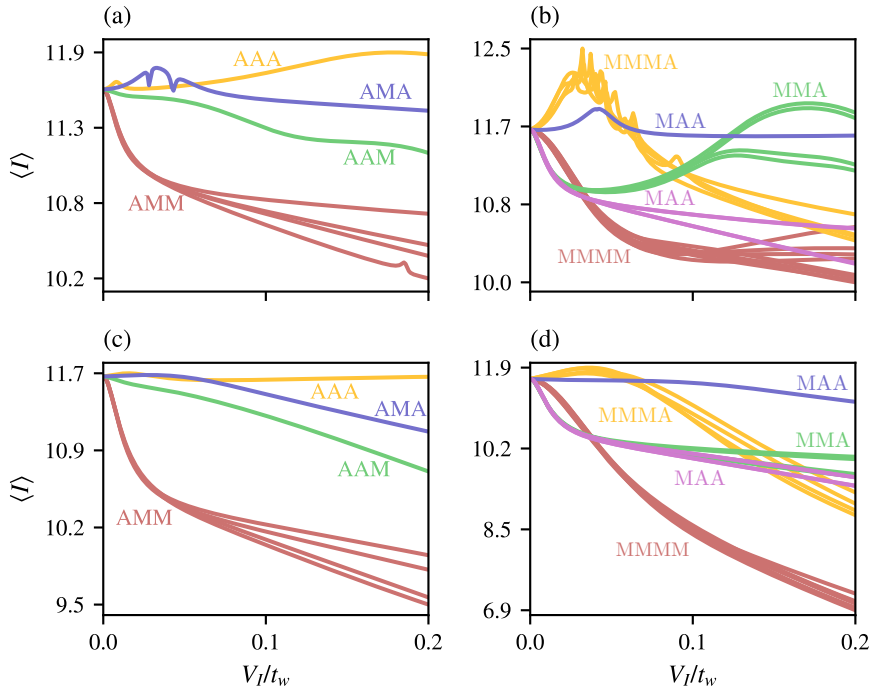

Figure 5.17: (a) Average IPR for the various realizations of atomic impurity placements. (b) Average IPR for the various realizations of molecular impurity placements. (c,d) show the same quantity as approximated using nondegenerate perturbation theory. It is clear that for weak impurity strengths up to at least $V_I \approx 0.1t_w$, the behaviors are grouped in terms of the nature of the site at which the impurities have been placed. Naturally, we label them by the renormalization paths that they belong to. The system size is again $N = 55$ and the modulation strength $\rho = 0.2$. We also note that the discrepancies between the approximated and the exact IPRs can be resolved by adding higher-order terms in the perturbation theory.

of the four renormalization paths of the $N = 55$ chain are plotted (seven distinct curves). There is one curve for AAA, AAM, and AMA, while there are four for AMM. Up to $V_I \approx 0.1t_w$, one observes that curves belonging to the same renormalization path follow the same evolution as a function of impurity strength. In the molecular case, we have again plotted all distinct representatives (19 curves). There are eight curves for MMMM, four for MMMA, four for MMA, two for MAM and one for MAA. They are also relatively well grouped up by renormalization path, up to a strength $V_I = 0.1t_w$. We can understand why this grouping happens by using first-order nondegenerate perturbation theory. The IPR, in this case, is given by (see Appendix 5.B)

$$I_\alpha^m = \frac{\sum_i |\psi_\alpha^m(x_i)|^2}{\sum_i |\psi_\alpha^m(x_i)|^4}, \tag{5.22}$$

where the non-normalized amplitudes, to first order in perturbation theory, are given by

$$\psi_\alpha^m(x_i) = \alpha(x_i) + V_I \sum_{\beta\neq\alpha} \frac{\alpha(x_m)\beta^*(x_m)\beta(x_i)}{E_0^{(\alpha)} - E_0^{(\beta)}}. \tag{5.23}$$

Here $|\alpha\rangle = \sum_i \alpha(x_i)\,|i\rangle$ (same for β) denote the pure, nondegenerate, Fibonacci energy eigenstates, with $E_0^{(\alpha)}$ their energies. From this expression, we can see why the grouping in terms of renormalization paths takes place: the amplitudes $\alpha(x_m)$ and $\beta(x_m)$ will be very similar when the site x_m belong to the same renormalization path. We can understand this from the perturbative treatment of the clean Fibonacci chain, where it is known that to zeroth order, the amplitudes are strictly localized on sites belonging to the same renormalization path [136, 247]. The next orders correct for this strict localization, but the highest weight remains on the sites with the same renormalization path. This also explains the origin of the symmetric fractal picture we observed in Sec. II. For comparison, we plotted the IPR calculated perturbatively in Fig. 5.17 (c) and (d). We see that globally, it provides an excellent approximation of the behavior, and the grouping is more pronounced. Another feature that we can observe from the IPRs is that some impurity configurations lead to an average delocalization of the states for a range of impurity strengths, as can be seen, for example, in Fig. 5.17 (b), where the blue curve shows an increase in IPR before it decreases. This comes as a surprise, as one expects that the introduction of disorder leads to more localization. Similar results were recently obtained in Ref. [253] for a system in which random disorder was introduced in the hopping parameters.

5.5 Conclusion

In this chapter, we studied the effect of disorder by introducing impurities in the Fibonacci chain. We first introduced the 1D model in the tight-binding approximation and briefly explained how to understand the spectrum through a deflation procedure. This was then followed by the introduction of an impurity in the quasiperiodic lattice, which leads to the appearance of at least one localized state. We have then shown that in the weak impurity regime, disorder is introduced in a very structured manner, following labeling provided by the renormalization path of the sites where the impurities have been placed. The disorder is restricted to subclusters of the system. This indicates a transition regime between a more insulating state where disorder is dominant and the typical critical states in a quasiperiodic lattice. We emphasize that our viewpoint stems from the essential notion of conumbers. They are crucial in revealing the structure with which disorder sets in and makes our observations intuitive. They were further substantiated by studying the behavior of overlap integrals and localization properties through the IPR.

Although the renormalization scheme is only exact in the limit $\rho \ll 1$, even $\rho = 0.5$ is sufficiently small for the results to hold, and any $\rho \leq 0.2$ leads to well-separated energy clusters [136]. In this sense, the results of our analysis are not exact but provide a qualitative understanding of the role played by impurities in a Fibonacci hopping model. Furthermore, the weak impurity regime was studied

perturbatively, yielding good results. This seems to work well as long $V_I < \rho$, which mainly forces the impurity to disrupt a particular cluster.

Finally, we generalized the construction of a Fibonacci tight-binding Hamiltonian to a Tribonacci sequence. We saw that a similar renormalization procedure can be applied, yielding a "quinfurcarting" energy splitting. It was shown that the concept of conumbers generalizes to the Rauzy fractal and that there is a symmetry between the ordering of energy eigenstates and wavefunctions on the Rauzy fractal. Finally, we showed that both the energy spectrum and eigenstates have typical behaviors expected of multifractal sets, proving that this system also possesses critical eigenstates.

As an outlook, it would be interesting to study the effect that disorder has in disrupting the local symmetry structure of the system. This is partly because we initially believed that it could play a role in inhibiting the effect of impurities, as was observed in the case of the AAA graph in Fig. 5.9(b). Indeed, this site is the center of a vast region of palindromic symmetry. However, this naive interpretation was quickly ruled out as the MMA graph in Fig. 5.10(a) offered minimal disruption, even though it had no locally symmetric region surrounding it. In recent work, the on-site model of the Fibonacci chain has been studied using a *local resonator mode* framework [139]. It would be interesting to find an analog version of this framework in the hopping model, which offers an intuitive understanding of the effect of impurities on local symmetries. This could help further understand the topological features of the Fibonacci chain. Indeed, it is possible to study the robustness of a topological phase by subjecting the system to impurities. Since the gap-labeling theorem has been reinterpreted in terms of renormalization paths [247], the presence of stable gap states can be analyzed by the amount of disorder in the graphs. This, in turn, should be related to how the impurity breaks the (local) palindromic symmetry or preserves it. Hence, one can evaluate whether this symmetry protects the topological phase or if it is different.

5.A Finite-size Scaling of IPR and Size Dependence of Overlap Integrals

In this section, we provide a finite size scaling analysis plot in Fig. 5.18 to show that an impurity induces localization. Since the IPR grows with size as $I_\alpha \propto L^\nu$, with $\nu \to 0$ meaning complete localization and $\nu \to 1$ full delocalization, as $N \to \infty$, the finite-size scaling analysis is done by numerically calculating the ratio $\langle I(V)\rangle/\langle I(0)\rangle \propto L^\gamma$. If the log-log plot has a positive slope ($\gamma > 0$), it means the state became more delocalized, and if the slope is negative ($\gamma < 0$), it became more localized in the presence of an impurity. We observe a negative slope in both Figs. 5.18 (a) and (b), which means that the impurity induces localization of states, on average.

Furthermore, we show that the general features of the cluster-averaged overlap integrals are not size-dependent. In other words, if an impurity has been placed on an atomic site, then the molecular cluster is less affected by its presence than the atomic cluster (vice-versa for a molecular impurity). To this end, we computed the cluster-averaged overlap integral for different Fibonacci approximant chain sizes,

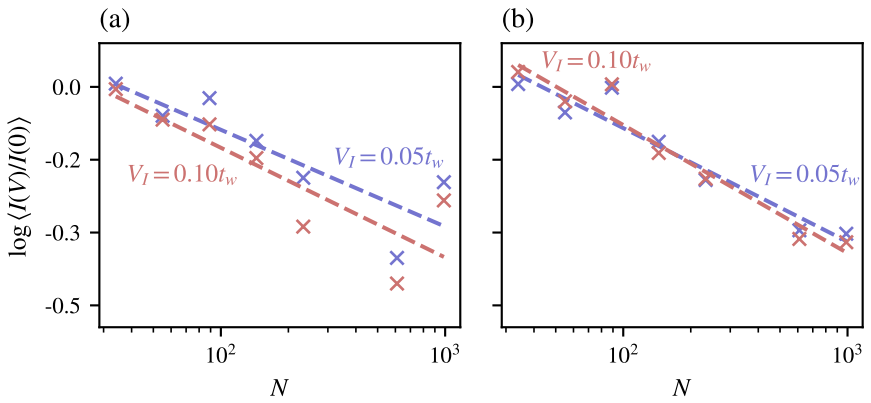

Figure 5.18: Finite size scaling of the averaged IPR in the presence of (a) an atomic impurity and (b) a molecular impurity. In both cases, we have a negative slope in the log-log line, meaning we are witnessing more localization when an impurity is introduced in the system.

choosing just one impurity to represent the general features. The results are plotted in Fig. 5.19. The behavior described in the bulk of the text is still observed for both atomic and molecular impurities cases. When an impurity is placed in an atomic (molecular) site, the cluster-averaged overlap integral is larger for the molecular (atomic) cluster, even though in both cases, the overlap globally decreases for increasing sizes. These features get washed off as the impurity strength decreases and the size increases. Therefore, a crossover size $M(V)$ must exist that increases with decreasing impurity strength. This size yields a threshold to the relevance of the results presented in this paper. Given an arbitrary threshold of similarity $\langle O \rangle_X = 0.9$ for a cluster of type X, we observe the following: In Fig. 5.19 (a), for an atomic impurity, the crossover size for the molecular cluster is reached at $N = 4181$ starting at impurity strength $V_I = 0.15t_w$. In Fig. 5.19 (d), for a molecular impurity, we do not reach the crossover size for the atomic cluster for any of the strengths considered, and $\langle O \rangle_A > 0.95$ for all sizes considered. In Figs. 5.19 (b) and (c), when the cluster type is the same as the impurity type, the threshold is reached very quickly, as expected.

5.B Perturbative calculation of the IPR

Let us consider a system described by the Hamiltonian $H = H_0 + V$, where H_0 is the usual Fibonacci Hamiltonian and V is the perturbation containing the impurity of strength V_I, placed at some site m. An eigenstate $|\psi\rangle$ of the Hamiltonian H can be written, to first order in perturbation theory, as

$$|\psi\rangle = |\alpha\rangle + \sum_{\beta \neq \alpha} \frac{\langle \beta | V | \alpha \rangle}{E_0^{(\alpha)} - E_0^{(\beta)}} |\beta\rangle \,, \tag{5.24}$$

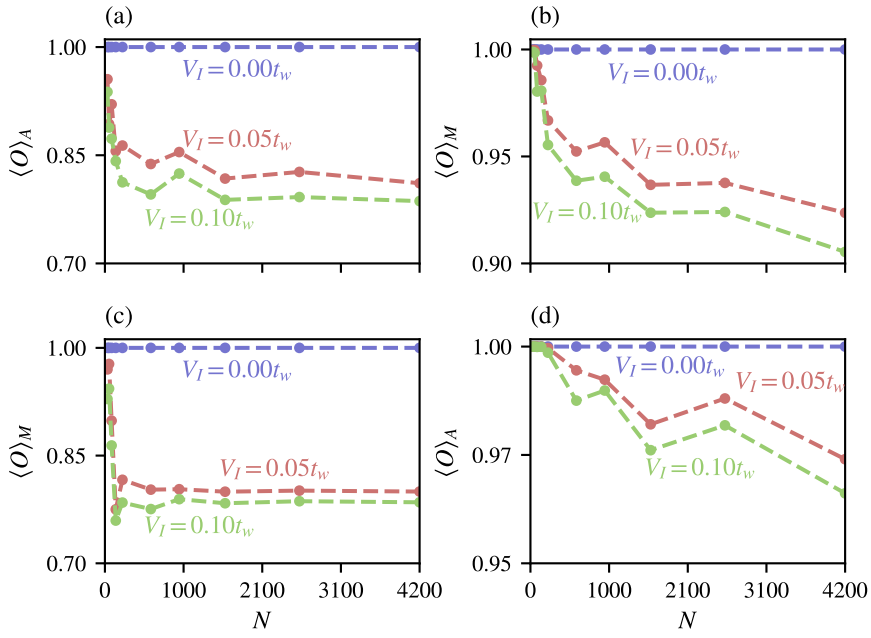

Figure 5.19: Cluster-averaged overlap integral versus system size for eight different system sizes, corresponding to Fibonacci chain approximants ranging from generation 8 to 17. (a,b) Overlap integrals in the presence of an atomic impurity. (c,d) Overlap integrals in the presence of a molecular impurity. In both of them, the cluster that is least disturbed is the one belonging to sites of a different nature than the one on which the impurity has been placed.

where $|\alpha\rangle$ and $|\beta\rangle$ are eigenstates of the Fibonacci Hamiltonian H_0, and the E_0's are eigenvalues. We expand these states in the position basis, $|\alpha\rangle = \sum_i \alpha(x_i)\,|i\rangle$, and obtain (omitting normalization for now)

$$
\begin{aligned}
|\psi\rangle &= \sum_{i=1}^{N} \alpha(x_i)\,|i\rangle + \sum_{\beta\neq\alpha}\sum_{i,j,k} \frac{\beta^*(x_i)\alpha(x_j)\beta(x_k)\,\langle i|\,V\,|j\rangle}{E_0^{(\alpha)} - E_0^{(\beta)}}\,|k\rangle \\
&= \sum_{i=1}^{N} \alpha(x_i)\,|i\rangle + V_I \sum_{\beta\neq\alpha}\sum_{k=1}^{N} \frac{\beta^*(x_m)\alpha(x_m)\beta(x_k)}{E_0^{(\alpha)} - E_0^{(\beta)}}\,|k\rangle \\
&= \sum_{i=1}^{N} \left(\alpha(x_i) + V_I \sum_{\beta\neq\alpha} \frac{\beta^*(x_m)\alpha(x_m)\beta(x_i)}{E_0^{(\alpha)} - E_0^{(\beta)}} \right) |i\rangle \\
&\equiv \sum_{i=1}^{N} \psi_\alpha^m(x_i)\,|i\rangle\,.
\end{aligned}
$$

The second line results from the matrix elements of the perturbation V only having one element V_I on the diagonal, corresponding to site m. In the last line, we defined our quantity of interest $\psi_\alpha^m(x_i)$, the amplitude of the states at sites x_i. The subscript α is a reminder that its zeroth order state is $|\alpha\rangle$, and the superscript m indicates that the impurity has been placed at the site x_m. We also need to know the norm of the state to normalize it properly. At this order of perturbation theory, it is given by

$$\begin{aligned}\langle\psi|\psi\rangle &= 1 + \sum_{\substack{\beta\neq\alpha\\ \beta'\neq\alpha}} \frac{\langle\alpha|\,V\,|\beta\rangle\,\langle\beta'|\,V\,|\alpha\rangle}{(E_0^\alpha - E_0^\beta)(E_0^\alpha - E_0^{\beta'})}\,\langle\beta|\beta'\rangle \\ &= 1 + \sum_{\beta\neq\alpha} \frac{|\,\langle\alpha|\,V\,|\beta\rangle\,|^2}{(E_0^{(\alpha)} - E_0^{(\beta)})^2} \\ &= 1 + V_I \sum_{\beta\neq\alpha} \frac{\left|\alpha^*(x_m)\beta(x_m)\right|^2}{(E_0^{(\alpha)} - E_0^{(\beta)})^2}.\end{aligned}$$

With the state and its norm, we can write down an approximate expression for the IPR

$$I_\alpha = \frac{\sum_{i=1}^N |\psi_\alpha^m(x_i)|^2}{\sum_{i=1}^N |\psi_\alpha^m(x_i)|^4}, \tag{5.25}$$

where we assume proper normalization of the state $|\psi\rangle$. We start by working out the expression for $|\psi_\alpha^m(x_i)|^4$ to 2^{nd} order in V_I,

$$\begin{aligned}|\psi_\alpha^m(x_i)|^4 = &\left[\left(\alpha(x_i) + V_I \sum_{\beta\neq\alpha} \frac{\beta^*(x_m)\alpha(x_m)\beta(x_i)}{E_0^{(\alpha)} - E_0^{(\beta)}}\right)\left(\alpha^*(x_i)\right.\right. \\ &\left.\left. + V_I \sum_{\beta\neq\alpha} \frac{\beta(x_m)\alpha^*(x_m)\beta^*(x_i)}{E_0^{(\alpha)} - E_0^{(\beta)}}\right)\right]^2 \\ = &\,|\alpha(x_i)|^4 + 4|\alpha(x_i)|^2 \mathrm{Re}\big[f_\alpha^m(x_i)\big] V_I \\ &+ \left[4\big|f_\alpha^m(x_i)\big|^2 + 2\mathrm{Re}\big[(f_\alpha^m(x_i))^2\big]\right] V_I^2 + \mathcal{O}(V_I^3).\end{aligned} \tag{5.26}$$

where we defined the function

$$f_\alpha^m(x_i) \equiv \alpha^*(x_i) \sum_{\beta\neq\alpha} \frac{\alpha(x_m)\beta^*(x_m)\beta(x_i)}{E_0^{(\alpha)} - E_0^{(\beta)}}. \tag{5.27}$$

This function is the quantity that explains why the grouping happens in terms of the renormalization path of the sites. As mentioned previously in the main text, the amplitudes $\alpha_(x_m)$ and $\beta(x_m)$ have most of their support on the sites belonging to the same renormalization path. With this, we have an analytic expression for the IPR of state $|\psi_\alpha\rangle$,

$$I_\alpha = \frac{1 + \sum_i \left(\mathrm{Re}\big[f_\alpha^m(x_i)\big] V_I + \frac{|f_\alpha^m(x_i)|f_\alpha^m(x_i)|^2}{|\alpha(x_i)|^2} V_I^2\right)}{\mathcal{I}_\alpha^{-1} + \zeta_\alpha^m V_I + \gamma_\alpha^m V_I^2}, \tag{5.28}$$

where we defined three other expressions for the coefficients in front of the impurity strengths for the $|\psi_\alpha^m(x_i)|^4$ expression:

$$\begin{aligned}
\mathcal{I}_\alpha^{-1} &\equiv \sum_i |\alpha(x_i)|^4, \\
\zeta_\alpha^m &\equiv \sum_i 4|\alpha(x_i)|^2 \mathrm{Re}\big[f_\alpha^m(x_i)\big], \\
\gamma_\alpha^m &\equiv \sum_i \Big[4\big|f_\alpha^m(x_i)\big|^2 + 2\mathrm{Re}\big[(f_\alpha^m(x_i))^2\big]\Big].
\end{aligned}$$

Chapter 6

Spectral Properties of Coupled Fibonacci Chains

Commonly used symbols and acronyms

Symbol/Acronym	Meaning
CLS	Compact Localized State
H	Hamiltonian
v_j	Potential on site j
h	Hopping amplitude of the on-site Fibonacci chain
t_j	Hopping amplitudes of the hopping Fibonacci chain
$c = \lvert h/(v_A - v_B)\rvert$	Contrast parameter
W_n	Fibonacci word of generation n
F_n	Fibonacci number of generation n
$\phi = (1+\sqrt{5})/2$	Golden ratio

6.1 Introduction

Although the behavior of aperiodic chains has been investigated extensively and in great detail, comparatively little work has been dedicated to the case where two or more chains are coupled to each other, forming an *aperiodic ladder* [261–265]. In this chapter, we take a step into this realm by analyzing a range of different coupling schemes between two identical one-dimensional Fibonacci chains. Specifically, we study cases where the two chains are directly coupled in a uniform, non-uniform, or quasiperiodic manner and evaluate the resulting spectral properties, namely the energy eigenvalues and eigenstates. Additionally, we study a special case of an indirect coupling, that is, two chains coupled to each other through some intermediate sites. These cases are easily tractable, since they possess a reflection symmetry that allows the block-diagonalization of the Hamiltonian.

We find different spectra depending on the setup. In the case of uniform coupling, the eigenvalue spectrum is identical to that of two uncoupled Fibonacci chains, but with shifted energy eigenvalues. On the other hand, if the two chains are coupled only through a single site, the spectrum consists of two Fibonacci chains with an on-site defect. The structure of the eigenvalue spectrum becomes more complex in the case of quasiperiodic coupling, for which a richer hierarchical structure reveals itself through a perturbative renormalization approach. If only the sites of one specific type (A or B) are coupled to each other, we show that, for a specific value of the interchain coupling, half of the eigenstates are critical, while the others are extended. Interestingly, these two different classes of eigenstates possess different parity with respect to a corresponding reflection operation and can thus be selectively excited by incoming waves of negative or positive parity. This could be used to control the transport properties of this system. Finally, we also realize couplings between the chains through some intermediate sites, which leads to the appearance of flat bands in a quasiperiodic lattice.

This chapter is organized as follows. To be self-contained, we start by briefly reviewing the properties of the Fibonacci chain in Section 6.2, followed by an overview of the methods used to generate our results in Section 6.3. In Section 6.4, we analyze the simplest way of coupling two Fibonacci chains, namely a uniform one. In Section 6.5, we investigate different cases of non-uniform coupling. We start by connecting only sites of a specific type to each other in Section 6.5.1. Then, in Section 6.5.2, we analyze the case where only two sites are coupled. In Section 6.6, we couple the two chains in a quasiperiodic fashion and analyze the resulting eigenvalue spectrum in terms of a renormalization scheme. Finally, in Section 6.7, we consider the scenario where the two chains are not directly coupled to each other, but through intermediate sites. Our conclusions are presented in Section 6.8.

6.2 A single Fibonacci chain

We consider a general Fibonacci chain model, namely a nearest-neighbor tight-binding chain with periodic boundary conditions. The on-site potential and hopping amplitudes are both modulated by the Fibonacci sequence, and the corre-

sponding Hamiltonian is given by

$$H = \sum_{j=1}^{N} v_j \left|j\right\rangle \left\langle j\right| + \sum_{\langle i,j\rangle} t_i \left|i\right\rangle \left\langle j\right| \tag{6.1}$$

where $|j\rangle$ denotes a basis state fully localized on the j-th site and $\langle i,j\rangle$ denotes nearest-neighbors. The on-site potential v_j and the hopping amplitude t_j are both binary and follow the sequence of a Fibonacci word W_n of generation n. The latter is defined by the recursion relation

$$W_n = W_{n-1}W_{n-2}, \quad n \geq 2,$$

which is a binary representation of the Fibonacci sequence. This inductive recursion formula is expressed as a string concatenation instead of a number addition. It can be generated through repeated application of the substitution rule $A \to AB$ and $B \to A$, with the initial two words being $W_0 = B$, $W_1 = A$. We note that the Fibonacci sequence is most commonly represented in numeric form through the recursion formula

$$F_n = F_{n-1} + F_{n-2}, \quad n \geq 2,$$

where $F_0 = F_1 = 1$ and F_n is the n^{th} Fibonacci number, which is equal to the word length $|W_n| = F_n$. The ratio between the number of letters A and B is equal to the golden ratio ϕ in the $n \to \infty$ limit [266],

$$\lim_{N\to\infty} \frac{F_n}{F_{n-1}} = \frac{1+\sqrt{5}}{2} \equiv \phi\,.$$

The Hamiltonian Eq. (6.1) can be studied in its general form or reduced to a purely on-site or hopping Fibonacci model, where the parameters $t_j = h$ or $v_j = v$ are uniform. These have been termed diagonal and off-diagonal models in the literature, while Eq. (6.1) is referred to as the mixed model. All these models have been studied previously in their various forms [131, 134, 136, 246]. Still, one crucial aspect is the equivalence between the on-site and hopping models under a perturbative renormalization scheme [136]. This means that we can uncover all essential features by studying the unmixed models. For this reason, we will focus on the on-site model for our analysis. In this case, the on-site potential v_j of the j-th site is equal to either v_A or to v_B, depending on whether the j-th character of W_n is equal to A or to B, and the hopping parameter is constant and equal to h. We note that the number of sites in the chain is then equal to $|W_n| = F_n$.

Fig. 6.1 (a) shows a graphical representation of such a Fibonacci chain. Due to the periodic boundary conditions, the depicted system constitutes the unit cell of a periodic approximant of the quasicrystal (if $n \to \infty$, it becomes a proper quasicrystal). This is a system that has long-range order without being periodic. Its eigenstates form a set of critical states, which have atypical localization properties. This means that they are neither extended nor localized [125]. The eigenvalues have a spectral measure that is singular-continuous and forms a fractal set (a Cantor set of measure zero). This feature is also observed in the eigenstates,

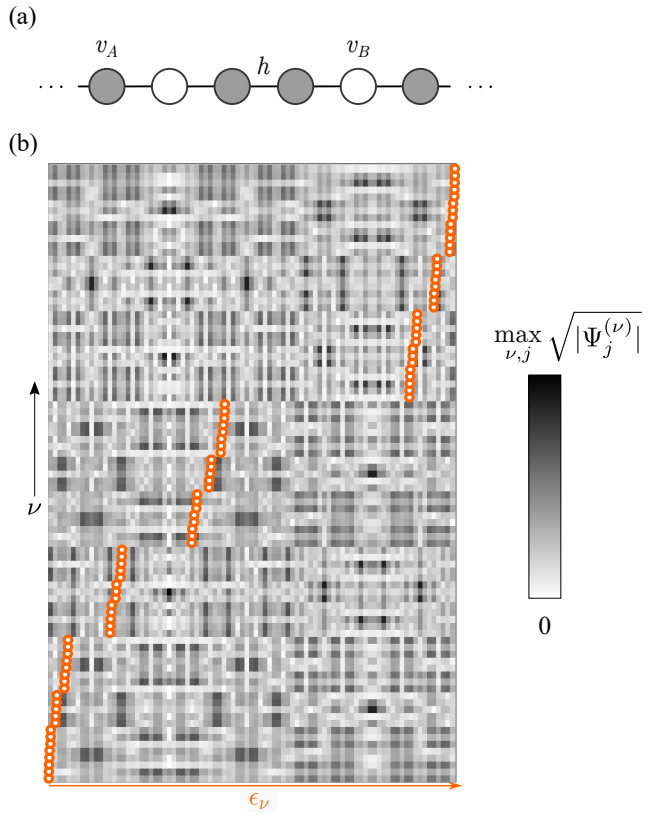

Figure 6.1: (a) Graphical representation of a Fibonacci chain with periodic boundary conditions (see text for details). (b) Eigenstate map for such a Fibonacci chain of $F_{10} = 89$ sites. Each of the F_{10} rows of the gray scale image shows the value of $|\Psi^{(\nu)}(j)|^{1/2}$ (with each eigenstate normalized), where j is a site index, ν is an energy index, and with each square pixel corresponding to one of the F_n sites. The orange dots denote the eigenenergy ϵ_ν of the eigenstates. The eigenvalues and eigenstates were obtained for $h = -1$, $v_A = 0$ and $v_B = 3$.

with wavefunctions that show multifractal properties [247]. In Fig. 6.1 (b), the eigenstates of a Fibonacci chain with $F_{10} = 89$ are graphically depicted.

The properties of quasicrystals have been studied in a multitude of ways, ranging from perturbative methods based on a renormalization formalism [129, 136] to exact results using a transfer matrix approach [267] or a symmetry perspective, which offers insights on the fragmentation of states in terms of local spatial structures of the chain [139].

Before we continue, let us briefly comment on possible realizations of the Hamiltonian Eq. (6.1). We note that the following statements also hold for the more complex models that we will present later in this manuscript. Since we treat the matrix eigenvalue problem $H|\Psi\rangle = E|\Psi\rangle$, the setups proposed in this work are well

suited for a realization in various systems modeled by such a problem, as long as the relevant matrix elements that correspond to couplings and on-site potentials of our Hamiltonian can be controlled. An immediate candidate, for instance, is a system of evanescently coupled optical waveguides [110]. Here, each site corresponds to a monomodal waveguide. By suitably tuning quantities such as waveguide shape and spacing, the on-site potentials v_j and couplings $h_{i,j}$ are tunable in a wide range.

We remark that the propagation of light in such arrays of evanescently coupled photonic waveguides can be described by a discrete, time-dependent Schrödinger equation, which would also allow us to probe the dynamics of the setups proposed in this work. Another realization that is directly feasible is in terms of electric circuits, where the sites are nodes of the circuit, and with on-site potentials and couplings being determined by how the nodes are grounded and interconnected to each other [86, 183].

6.3 Methods

In this section, we will provide a comprehensive description of the methods employed to calculate and illustrate the relevant quantities before delving into the obtained results. We will begin by explaining the numerical methods utilized in this study, which encompass the creation of all eigenstate maps. Subsequently, we will outline the analytic methods employed to describe the section concerning quasiperiodic coupling.

6.3.1 Numerical methods

Unless mentioned otherwise, all eigenvalues and eigenvectors were obtained by numerically diagonalizing the corresponding Hamiltonian. In the case of two coupled Fibonacci chains, we individually diagonalized the two Hamiltonians $H_{\pm}$ (see Section 6.4) and then constructed the total eigenstates by symmetrizing/antisymmetrizing these states. We note that this procedure automatically provides an assignment of the eigenvalues of the total Hamiltonian to negative/positive parity. The eigenstate maps (as in Fig. 6.1) and energy plots (as in Fig. 6.3) were produced with Mathematica.

6.3.2 Analytical methods

Hierarchical splitting and renormalization The main analytic tool used in this work is a perturbative renormalization procedure based on the degenerate Brillouin-Wigner perturbation theory, described in the works of Niu and Nori [129, 136].

Consider a one-dimensional chain described by a tight-binding Hamiltonian that incorporates a set of hierarchical hoppings, where the hopping strengths follow the relation $T_j \ll T_{j-1} \ll \cdots T_2 \ll T_1$ (as depicted in the topmost chain of Fig. 6.2). In this scenario, we can employ a perturbative renormalization approach to calculate the energy levels of the topmost chain.

This perturbative renormalization approach treats the weaker hoppings (T_j with higher indices) as perturbations to the dominant hopping term (T_1). This allows

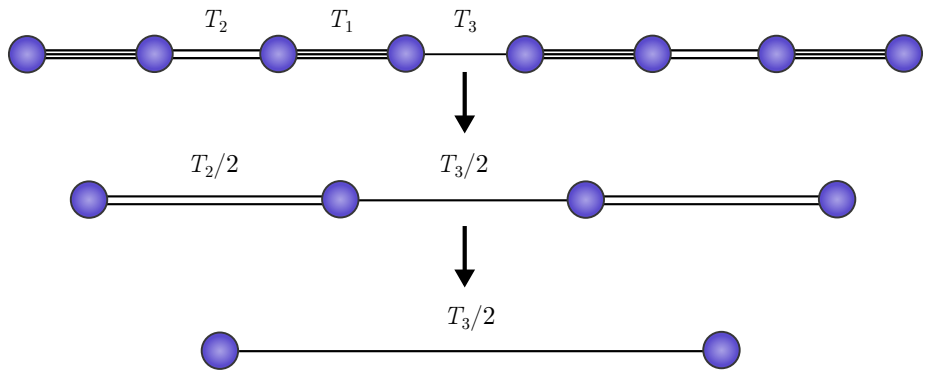

Figure 6.2: Graphical representation of the renormalization procedure. The topmost chain has a hierarchical distribution of hoppings, with $T_3 \ll T_2 \ll T_1$. The sites in the middle chain represent the (anti)bonding states of the unperturbed Hamiltonian of the topmost chain, which have effective couplings $T_2/2$ and $T_3/2$. In its turn, the lowermost chain represents the (anti)bonding states of the middle chain, with its effective coupling given by $T_3/2^2$. Figure inspired from [129].

us to systematically incorporate the effects of the weaker hoppings and compute the resulting energy levels of the topmost chain. We do this by using the subset of unperturbed degenerate eigenstates as the basis set for the perturbed Hamiltonian. We then apply the Brillouin-Wigner perturbation theory to calculate the effective couplings between these states.

In Fig. 6.2, this process is visually represented by the middle chain, where each blue site represents a (anti)bonding degenerate eigenstate of the T_1 molecule. By considering these (anti)bonding states as the basis, we can determine the effective couplings induced by the weaker hoppings (T_j) and calculate the resulting energy levels of the topmost chain. In principle, this process is repeated indefinitely, but in practice, one takes a chain of finite size and imposes periodic boundary conditions to perform the calculations. The energy levels form a cluster of 2^j values around the base energy E_0

$$E = E_0 \pm T_1 \pm \frac{T_2}{2} \pm \cdots \pm \frac{T_j}{2^{j-1}} \,. \tag{6.2}$$

Brillouin-Wigner perturbation theory We shall now give a brief overview of Brillouin-Wigner perturbation theory. Consider a Hamiltonian $H = H_0 + H_1$, with H_1 acting as a perturbation to H_0. Let E_0 be a degenerate energy eigenvalue, and Q denote the projection operator onto the corresponding degenerate subspace. We also denote the complementary projection operator $P = \mathbb{1} - Q$. The eigenvalue equation $H|\psi\rangle = E|\psi\rangle$ can be rewritten such that

$$P|\psi\rangle = P\frac{1}{E - H_0}H_1|\psi\rangle = P\frac{1}{E - H_0}PH_1|\psi\rangle \tag{6.3}$$

where the last equality follows from $P^2 = P$ and $PH_0 = H_0P$. We now write

$$\begin{aligned}
|\psi\rangle &= (Q+P)\,|\psi\rangle \\
&= Q\,|\psi\rangle + P\frac{1}{E-H_0}PH_1\,|\psi\rangle \\
&= Q\,|\psi\rangle + P\frac{1}{E-H_0}PH_1(Q+P)\,|\psi\rangle \\
&\;\;\vdots \\
&= \sum_{n=0}^{\infty}\left(P\frac{1}{E-H_0}H_1\right)^n Q\,|\psi\rangle\,,
\end{aligned}$$

where we have just consistently used Eq. (6.3). With the above equation, we can now easily obtain an effective Hamiltonian for the degenerate subspace with eigenvalue E_0 through a left multiplication by QH,

$$\begin{aligned}
QH\,|\psi\rangle = EQ\,|\psi\rangle &= \left[QH_0Q + QH_1\sum_{n=0}^{\infty}\left(P\frac{1}{E-H_0}H_1\right)^n Q\right]Q\,|\psi\rangle \\
&\equiv H_{\text{eff}}Q\,|\psi\rangle
\end{aligned} \tag{6.4}$$

Using this effective Hamiltonian, it will be possible to understand the structure of the spectrum in the case of quasiperiodic coupling, which is treated in Section 6.6.

6.4 Uniform coupling

Let us investigate the setups where two such chains—each consisting of F_n sites and with periodic boundary conditions—are coupled to each other in different ways. We will focus on the impact of these different coupling schemes on the corresponding spectral properties.

The first and simplest scenario occurs when the two chains are uniformly coupled to each other, as shown in Fig. 6.3 (a). The setup is then described by

$$H = H_I + h'\sum_{i=1}^{N}\Big(\,|i_u\rangle\langle i_l| + |i_l\rangle\langle i_u|\,\Big) \tag{6.5}$$

with

$$H_I = \sum_{x=u,l}\sum_{i=1}^{N} v_i\,|i_x\rangle\langle i_x| + h\sum_{x=u,l}\sum_{\langle i,j\rangle}|i_x\rangle\langle j_x| \tag{6.6}$$

where $|i_u\rangle$, $|i_l\rangle$ denote basis states fully localized on the i-th site of the upper or lower chain, respectively. We note that such a setup has been investigated in Ref.[268], though with a focus on the density of states and multifractal properties and not on the eigenvalues and eigenstates.

To understand the impact of such a uniform coupling, we employ the up/down mirror symmetry of the setup. Due to this symmetry, the eigenstates have definite parity under an exchange of the lower and upper chains. This fact can be used

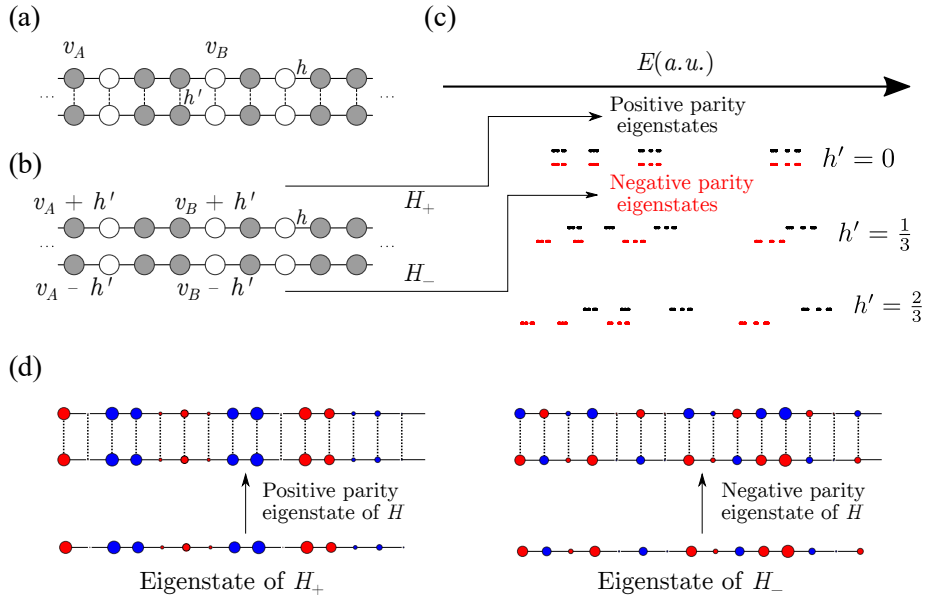

Figure 6.3: (a) Two uniformly coupled Fibonacci chains. (b) The result of writing the original system in terms of the symmetry-adapted basis Eqs. (6.7) and (6.8). In this basis, the setup decomposes into the two disconnected chains H_+ and H_-. (c) A sketch of the shifting spectra for different coupling strengths h' (see text for details). The eigenstates of H_+ and H_- correspond to eigenstates of the total Hamiltonian H with positive and negative parity, respectively, represented in (d). Here, specific eigenstates of H_+ and H_- are shown. At each site, the sign of the eigenstate is represented by a red/blue color, while the amplitude is depicted by the radius of the circle.

to construct a symmetry-adapted basis $\mathcal{S}$, consisting of $N = F_n$ states of positive parity

$$|1_u\rangle + |1_l\rangle, \ldots, |N_u\rangle + |N_l\rangle \tag{6.7}$$

and N states with negative parity

$$|1_u\rangle - |1_l\rangle, \ldots, |N_u\rangle - |N_l\rangle \ . \tag{6.8}$$

Written in this basis, $H' = \mathcal{S}^{-1} H \mathcal{S}$ consists of two isolated subsystems, H_+ and H_-. These two subsystems are shown in Fig. 6.3 (b). It can be seen that each is equal to an isolated Fibonacci chain of N sites, though with on-site potentials uniformly shifted by plus or minus h'. That is, $H_\pm = H_I \pm h' I$, with I being the identity matrix.

Let us now explore the implications of the above, starting with the eigenvalues of H. Since H and H' are related by a similarity transformation, the two Hamiltonians share the same eigenvalue spectrum. Moreover, since H' consists of the two disconnected chains $H_\pm$, the eigenvalue spectrum of H', $\sigma(H') = \sigma(H)$, is

given by the combination of the eigenvalue spectra of these chains [1]. Now, because $H_\pm = H_I \pm h'I$, we see that the eigenvalue spectrum of H_+ (H_-) is that of H_I shifted upwards (downwards) by h', respectively. In other words, the inter-chain coupling strength h' plays the role of an "energy shift parameter" [see Fig. 6.3 (c)]. Before we continue, we remark that the eigenstates of H can be simply constructed from those of H_+ and H_- by symmetrizing or anti-symmetrizing these states; this is demonstrated in Fig. 6.3 (d).

6.5 Non-uniform coupling

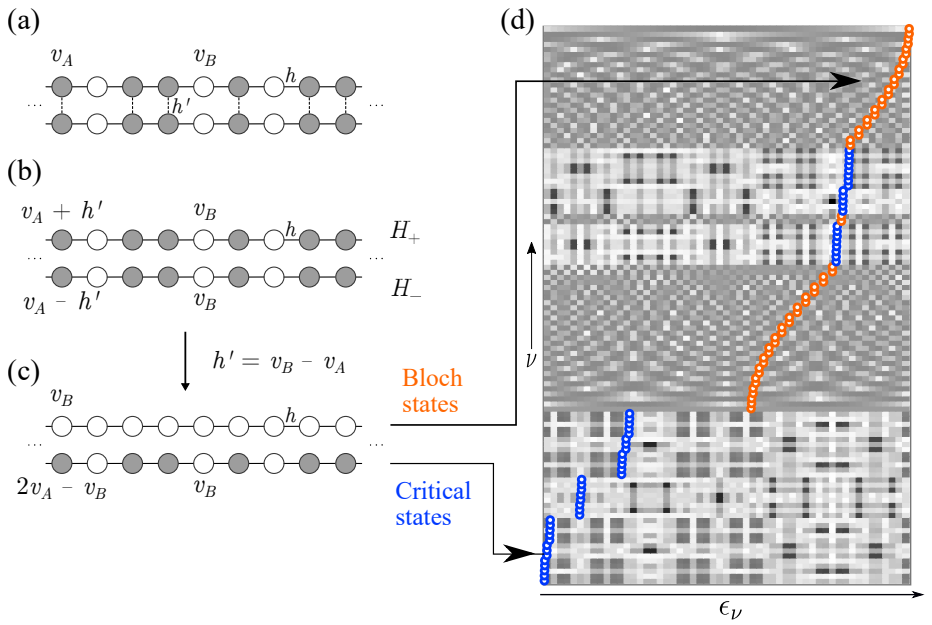

Figure 6.4: (a) Two Fibonacci chains that are coupled by connecting their A-sites to each other through couplings with strength h'. (b) The decomposition into H_+ and H_-. (c) When choosing $h' = v_B - v_A$, H_+ becomes periodic, while H_- remains a Fibonacci chain. Thus, the positive parity eigenstates of H (which correspond to symmetrized eigenstates of H_+) are of Bloch-character, while the negative parity eigenstates of H (which correspond to anti-symmetrized eigenstates of H_-) are critical states. (d) The eigenstate map of the setup for this particular choice of h'. Since the eigenstates $\Psi^{(\nu)}$ of H are either symmetric (orange dots; Bloch-states) or anti-symmetric (blue dots; critical states), each of the $2F_n$ rows in this eigenstate map only shows the amplitudes on half of the sites of the total system; the total eigenstate could be obtained through symmetrization or anti-symmetrization. The eigenvalues and eigenstates were obtained for $h = -1$, $v_a = 0$, and $v_B = 3$. The color map is the same as in Fig. 6.1, with black pixels corresponding to $\max_{\nu,j} \sqrt{|\Psi_j^{(\nu)}|}$.

[1] To be precise, the spectrum of H is the multiset sum of the spectra of H_+ and H_-.

Having understood the impact of coupling the two chains uniformly, we now proceed to more complex scenarios. In all cases, we will maintain the reflection symmetry between the two chains. Thus, we can still decompose the total Hamiltonian into two smaller chains, H_+ and H_-.

6.5.1 Coupling only A or only B-sites

In the first case, we couple only the A sites to each other, as depicted in Fig. 6.4(a). Repeating the same steps as above, we obtain $H' = \mathcal{S}^{-1} H \mathcal{S} = H_+ \oplus H_-$, though now with

$$H_\pm = \sum_{i=1}^{N} v_i^\pm \left|i\right\rangle \left\langle i\right| + h \sum_{\langle i,j\rangle} \left|i\right\rangle \left\langle j\right| \tag{6.9}$$

where $v_A^\pm = v_A \pm h'$, while $v_B^\pm = v_B$ is unchanged [see Fig. 6.4(b)]. In a completely analogous manner, coupling only the B-sites to each other will result in an energy shift of the on-site potentials of the B-sites only.

A particularly interesting case occurs when coupling only the A-sites and setting $h' = v_B - v_A$. For this special choice of h', H_+ becomes a uniform chain with zero on-site potential. However, H_- is still a Fibonacci chain. Now, since the eigenstates of $H_\pm$ correspond to positive/negative parity eigenstates of the full chain, the system features an interesting combination of traits: while the positive parity eigenstates are *extended*, the negative parity eigenstates are *critical*. For a quantum system, this means that the phase diagram of such a Hamiltonian features a special point $h' = v_B - v_A$, at which the system's behavior is highly dependent on the energies of one-particle excitations. As depicted in Fig. 6.4(a), depending on the energy of these parity eigenstates, they will either form Bloch waves (orange energy levels) or critical states (blue energy levels). It is interesting to see that a specific point in parameter space shows a mixture of singular continuous and absolutely continuous spectra. This provides a platform where both properties of extended and critical states can be exploited by tuning the Fermi level. In the critical regime, for example, (thermal) conductivities are in general very low (in some cases, they are even lower than for conventional insulators) [269, 270]. On the other hand, the fully extended regime provides the possibility of having phases with high (electrical) conductivities.

Finally, let us note that the possibility of Bloch-states in coupled aperiodic setups has also been observed in Refs. [262, 263], in which more complicated coupling schemes have been used.

6.5.2 Defect-coupling

Another possibility is the selective coupling of only a small subset of sites. In the extreme case, this subset consists of one site in each chain [see Fig. 6.5 (a)]. The result of such a coupling can be easily deduced. Using the symmetry adapted basis, we see that $H_\pm$ will both be simple Fibonacci chains, with added impurities at the sites that are coupled [see Fig. 6.5 (b)]. Such systems have been analyzed previously, and it was found that a single weak impurity is sufficient to render the spectrum unstable and reduce its fractal dimension, leading to a loss of criticality

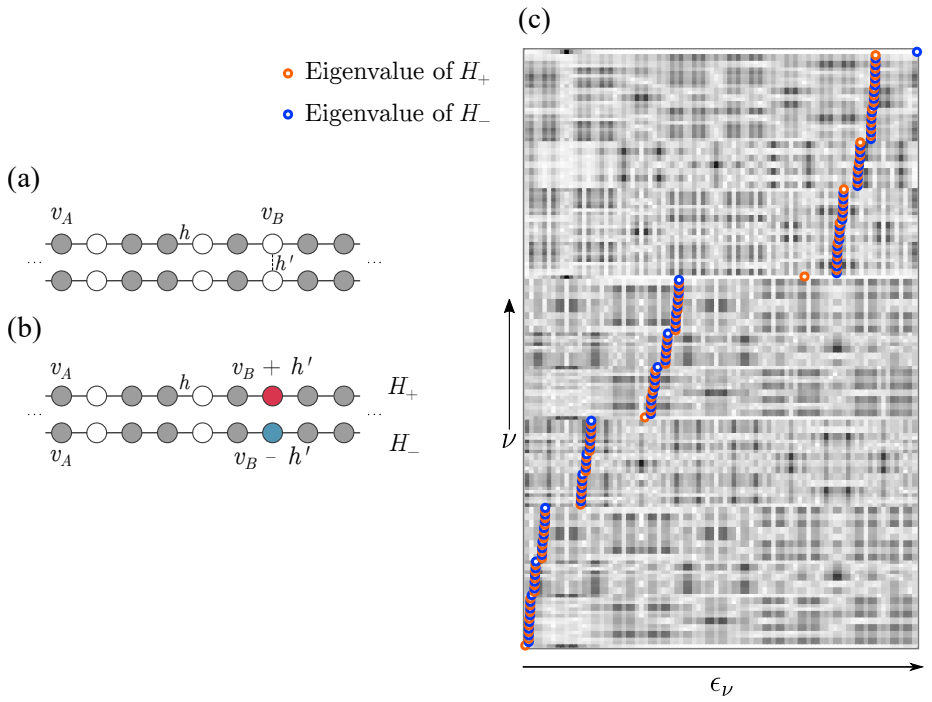

Figure 6.5: (a) Two Fibonacci chains coupled by connecting a single site of each chain to each other. (b) The decomposition into H_+ and H_-. (c) Eigenstate map for a setup of two Fibonacci chains that are coupled together at the 10-th site. As a result of this *defect-coupling* (see text for details), several eigenstates lie in gaps between quasi-bands. Orange dots correspond to eigenvalues of H_+ and blue dots to those of H_-. The eigenvalues and eigenstates were obtained with $h = -1$, $v_A = 0$, and $v_B = 3$. The color map is the same as in Fig. 6.1, with black pixels corresponding to $\max_{\nu,j} \sqrt{|\Psi_j^{(\nu)}|}$.

in all states [251]. On top of that, it was also recently found that this does not affect all states equally. Using Niu's renormalization procedure [129, 136], it was shown that the degree of criticality loss is dependent on the renormalization path of the site at which the impurity is placed [4]. This means that the location of the impurity impacts which states of the unperturbed Fibonacci chain are the most affected.

Alternatively, the impact of a single-site defect can be analyzed in a framework of local resonators [139]. These local resonators form the building blocks of the whole chain. In an unperturbed (without impurity) chain, each eigenstate is approximately symmetric with respect to a local parity operator. The sites with the highest amplitudes will be the ones corresponding to the resonator structures, which are symmetric under local parity. This approximate symmetry depends on the contrast $c = |h|/|v_A - v_B|$, and is exact in the limit $c \to 0$. By placing an impurity on a particular site, one creates a new local resonator structure in the chain,

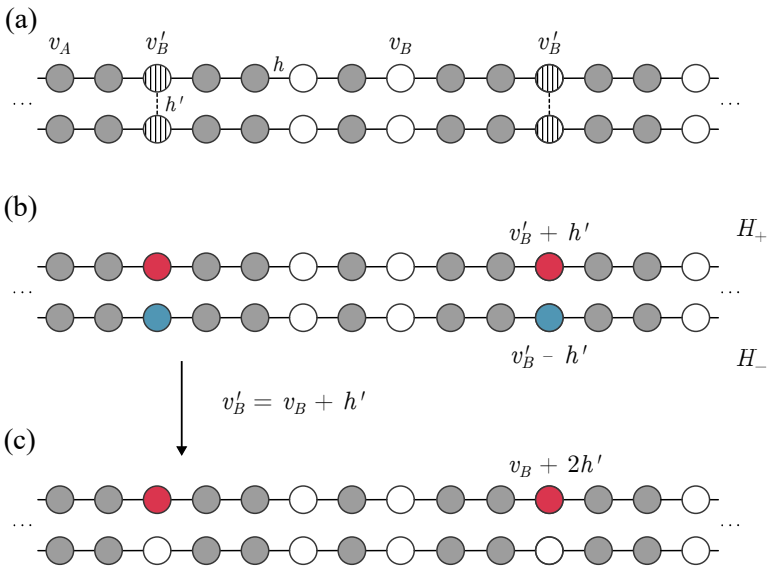

Figure 6.6: (a) An excerpt of two Fibonacci chains coupled to each other in a quasiperiodic manner, that is, by coupling the B-sites occurring in the pattern $AABAA$ together. (b) The result of the symmetry-induced decomposition into H_+ and H_-. (c) Since we know that the symmetry-induced decomposition results in a different on-site potential for $H_\pm$, we already assign a different v'_B to the coupled sites, which for ease of analysis is set to $v'_B = v_B + h$, resulting in the case we study in more detail in Section 6.6.1. In this simplified version, H_- is the standard Fibonacci chain, so we only need to analyze H_+.

and as such, new localization properties arise, yielding states with amplitude distributions that are radically different from the rest of the eigenstates. This can be seen in Fig. 6.5 (c), where the in-gap states have very strong localization, marked by the darker patches around a particular region of the chain (see the topmost level, for example, where there is a very dark patch around site $j = 10$) around this new local resonator block [139].

6.6 Quasiperiodic coupling

Yet another alternative way of coupling the two chains is in a quasiperiodic manner. Out of the many possibilities, here we illustrate an immediate and interesting one: We couple only a subset of B-sites to each other; namely, those appearing in the pattern $AABAA$, as shown in Fig. 6.6(a), where the striped B site sits in between two A sites on each side. We further set the coupling between the chains to h and choose the coupled B site energy to $v'_B = v_B + h$, such that H_- becomes a regular Fibonacci chain, with on-site energies v_A and v_B. On the other hand, H_+ now features new on-site energies: $v_B + 2h$, distributed in a quasiperiodic manner. For this choice of coupling, there are F_{n-5} such new sites (which is the number of

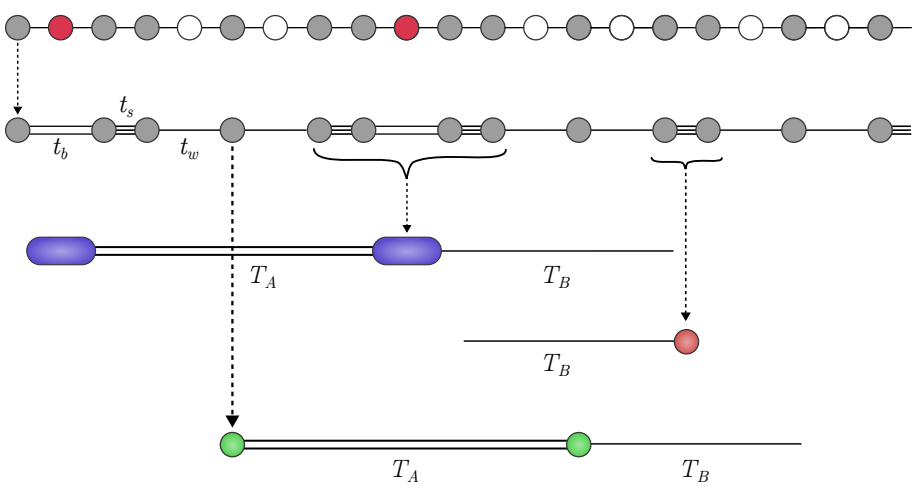

Figure 6.7: Decimation procedure for the effective chain described by H_+ in Fig. 6.6 (c). For each of the three degenerate levels, we define a decimated chain with effective new couplings. This allows us to track how the different levels structure themselves. In this example, we focus on the chain resulting from the v_A cluster. The couplings are first renormalized to three values $|t_s| > |t_b| > |t_w|$. The number of lines connecting the unperturbed eigenstates is representative of the coupling strengths. At the next order of perturbation theory, the unperturbed degenerate eigenstates are slightly more complicated and correspond to four-atom molecules, dimers, and isolated sites. These then correspond to three chains with blue, light red, and green sites, respectively. The next corrections correspond to the Fibonacci case, where the levels trifurcate at each step. The hopping parameters T_A and T_B are calculated in Appendix 6.A.

$AABAA$ blocks in a chain of length F_n).

In analyzing the effective chain using a renormalization approach, we make the assumptions that $h < 0$ and $v_A < v_B$. These assumptions are made to enforce the trifurcating structure necessary for the Fibonacci chain's renormalization group flow.

6.6.1 Decimation Procedure.

We can apply the usual decimation procedure known for hierarchical chains [136]. In this case, the novelty lies in the chain with three different on-site energies, as shown, for example, in Fig. 6.7. There are three renormalized chains that result from the first decimation step. We can analyze them separately to see how each energy level splits into different branches. A sketch of the branching structure is shown in Fig. 6.8, where one sees that there are three main clusters. The v_C cluster follows the Fibonacci trifurcarting structure from the start. The v_B cluster splits into six levels, each of which starts trifurcating according to the Fibonacci structure. Finally, the v_A cluster splits into seven levels that also trifurcate afterward. In the thermodynamic limit, these levels keep on trifurcating indefinitely,

leading to a spectrum that is a Cantor set and known to be singular continuous [271]. In Appendix 6.A, we provide a comprehensive explanation of the step-by-step renormalization process involved in handling the binary hoppings T_A and T_B for each cluster. In the next section, we show that these analytic tools lead to a good approximation and understanding of the structure of the spectrum.

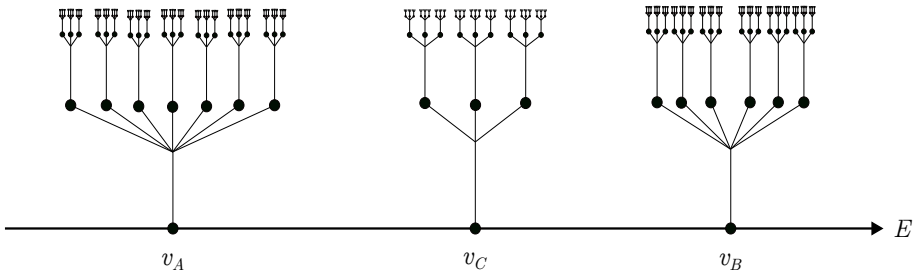

Figure 6.8: Energy splitting structure after each renormalization step. Energy scales are greatly distorted and do not represent actual gap sizes. Note that $v_C = v_B + 2h$.

6.6.2 Effective Couplings and Energy Corrections

In order to calculate the effective couplings and energy corrections at each splitting, we use the Brillouin-Wigner perturbation theory. For each cluster, we use the effective Hamiltonian Eq. (6.4)

$$H_{\text{eff}} = QH_0Q + QH_1 \sum_{n=0}^{n} \left(P \frac{1}{E - H_0} H_1 \right)^n Q,$$

where H_1 is the perturbation corresponding to the weakest coupling, Q is the projector onto the eigenspace of H_0 corresponding to the cluster of interest, while P projects out of it. At first, H_0 is just composed of on-site energies and H_1 of the coupling h between the isolated sites. This results in the three degenerate levels that form the main clusters. In the next order of perturbation theory, H_0 denotes the Hamiltonian of the corresponding renormalized chain, with the weakest coupling turned off. H_1 is then the perturbation with either t_w or t_b turned on, depending on which subchain we are dealing with (i.e. depending on whether $t_b > t_w$ or vice-versa).

With this effective Hamiltonian for each of the clusters, the renormalized couplings can be found by calculating $\langle E_j | H_{\text{eff}} | E_{j+1} \rangle$, where $|E_j\rangle$ are the zeroth order local eigenstates, which are either one atomic site, a two or a four-atom molecule, depending on the situation. We now first state the results obtained from the first-order corrections, which we shall subsequently prove. We find the first three

renormalized couplings to be given by

$$(t_b, t_s, t_w) = \begin{cases} \left(\dfrac{c}{1-2c},\ 1,\ c\right) h, & \text{(Cluster A)} \\ \left(-\dfrac{c^4}{2},\ -c,\ c^2\right) h, & \text{(Cluster B)} \\ \left(0,\ -\dfrac{1}{4}\left[\dfrac{c}{1-2c}\right]^5,\ \dfrac{1}{16}\left[\dfrac{c}{1-2c}\right]^8\right) h, & \text{(Cluster C)} \end{cases} \tag{6.10}$$

where we have defined the contrast parameter $c \equiv |h/(v_A - v_B)|$, which controls how well the perturbation theory behaves. We point out that the physics described by the theory is consistent for

$$c < \frac{1}{4^{\frac{1}{3}}(1+4^{\frac{1}{6}})} \approx 0.27875, \tag{6.11}$$

after which it fails to deliver reasonable results. This will be proven in the following paragraphs.

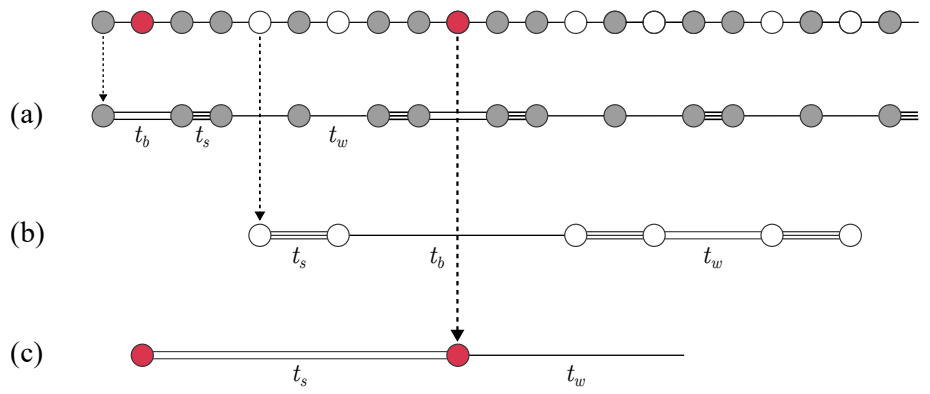

Figure 6.9: Decimation procedure. The topmost chain results from the equipartition theorem applied to the coupled Fibonacci chains we started with. It corresponds to the Hamiltonian H_+ with red sites of energies $v_C = v_B + 2h$. The grey and white sites have energies v_A and v_B, respectively. (a) The renormalized chain that was shown as an example in Section 6.6, with $|t_s| > |t_b| > |t_w|$. (b) The chain corresponds to the renormalization of the grey sites. In this case, we have $|t_s| > |t_w| > |t_b|$. (c) The chain corresponds to the renormalization of the red sites, with $|t_s| > |t_w|$. This chain is already a proper hopping Fibonacci chain.

First order renormalized hoppings Fig. 6.9 shows that one can form three effective chains (a), (b), and (c), corresponding to the clusters v_A, v_B and $v_C = v_B + 2h$ respectively. Before deriving our results, we recall that we are working in the regime of parameters where $v_A < v_B$ and $h < 0$. This is done to obtain a hierarchy of hopping strengths that will result in the infinitely trifurcating structure

after (at most) the second renormalization step. The v_C cluster is a regular hopping Fibonacci chain. In fact, if one starts from a chain of generation n, with F_n sites, one ends up with one of generation $n-5$, with F_{n-5} sites. By calculating the matrix element $\langle E_j| H_{\text{eff}} |E_{j+1}\rangle$, where H_{eff} is given by Eq. (6.4), between the nearest-neighboring eigenstates of the unperturbed Hamiltonian H_0 in the $E = v_C$ subspace, we find that this chain has effective renormalized hoppings, to nearest order in the contrast $c = |h|/|v_A - v_B|$, given by

$$\begin{aligned} t_s &= \frac{h^6}{4(v_B - v_A + 2h)^5} = -\frac{1}{4}\left[\frac{c}{1-2c}\right]^5 h, \\ t_w &= \frac{1}{16}\frac{h^9}{(v_B - v_A + 2h)^8} = \frac{1}{16}\left[\frac{c}{1-2c}\right]^8 h. \end{aligned} \tag{6.12}$$

Next, we consider the v_B chain, which contains six clusters. Two clusters correspond to the two-atom molecule bonded by t_s, while the other four correspond to the four-atom molecule (composed of two two-atom molecules bonded by $|t_w| > |t_b|$). These clusters will further start to trifurcate because they end up having the structure of a hopping Fibonacci chain after decimation. The renormalized hoppings of this chain are given by

$$\begin{aligned} t_b &= \frac{-h^5}{2(v_B - v_A)^4} = -\frac{c^4}{2}h, \\ t_s &= \frac{h^2}{v_B - v_A} = -ch, \\ t_w &= \frac{h^3}{(v_B - v_A)^2} = c^2 h. \end{aligned} \tag{6.13}$$

Finally, we consider the v_A cluster. It has seven clusters. The six clusters come from the same structures as the v_B chain, i.e., two- and four-atoms molecules, and the additional cluster comes from isolated sites. Once again, each one of these clusters will start trifurcating at the next steps of decimation, and one retrieves the hopping Fibonacci chain structure. The renormalized hoppings of this chain are

$$\begin{aligned} t_b &= \frac{h^2}{v_A - v_B - 2h} = \frac{c}{1-2c}h, \\ t_s &= h, \\ t_w &= \frac{h^2}{v_A - v_B} = ch. \end{aligned} \tag{6.14}$$

Regime of validity of the perturbation theory Let us now study the regime of validity, which results in the hopping hierarchy discussed previously. Starting with the v_B subspace, which is the simplest to deal with, we see from Eq. (6.13) that the hierarchy $|t_s| > |t_w| > |t_b|$ will always hold for $c \in (0, 1)$. This immediately results in the trifurcating structure after one iteration of the renormalization procedure. The v_A subspace, on the other hand, further restricts the range of c.

In order to have $|t_s| > |t_b| > |t_w|$, we must impose

$$1 > \left|\frac{c}{1-2c}\right| > c$$

which leads to $0 < c < 1/3$. Finally, the v_C subspace will give us the final restriction to impose the hierarchy leading to a trifurcating structure. This means we want $|t_s| > |t_w|$, leading to

$$\frac{1}{4}\left|\frac{c}{1-2c}\right|^5 > \left|\frac{c}{1-2c}\right|^8$$

Solving for $c > 0$ yields the final restriction

$$c < \frac{1}{4^{\frac{1}{3}}(1+4^{\frac{1}{6}})}. \tag{6.15}$$

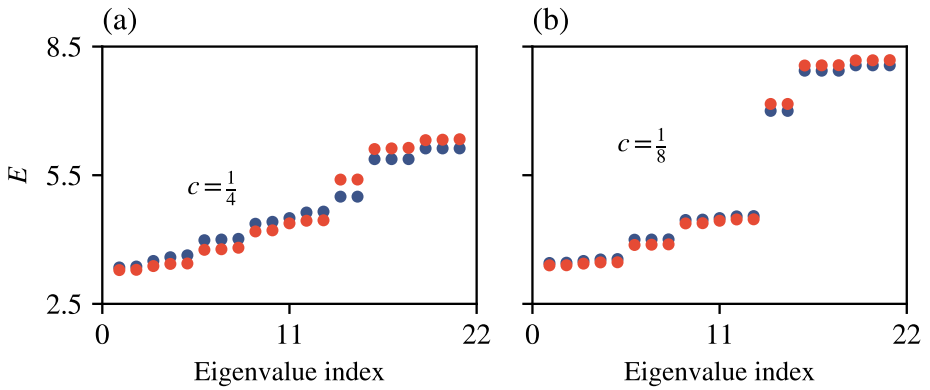

Figure 6.10: Comparison between the perturbative calculations (blue) and the direct numerical calculation (red) of the chain containing two "impurities" of strength $v_B + 2h$, at the center of the resonator structure $AABAA$. The chain's length is 21 sites. The structure is the same, and the discrepancy gets smaller as the contrast decreases. (a) Contrast $c = 1/4$, which is close to the limits of applicability of the perturbation theory. (b) Contrast $c = 1/8$. The energy is shown in arbitrary units.

Energy corrections We also determined the first-order energy corrections using the same perturbation theory and found the spectrum shown in Fig. 6.10. The energy levels calculated using perturbation theory (in blue) and those from numerical direct diagonalization (in red) have the same structure, with some discrepancies that disappear as the contrast $c \to 0$. This is illustrated in Fig. 6.10 (a) and (b) with $c = 1/4$ and $c = 1/8$, respectively. The structure of the spectrum is well approximated by the theory, even for a small chain size of 21 sites. The exact expressions for the energy levels can be found in Table 1 of Appendix 6.A.

Now, one only needs to add the spectrum of the regular chain to this "modified" chain to obtain the full spectrum of the two connected chains, as shown in Fig. 6.11.

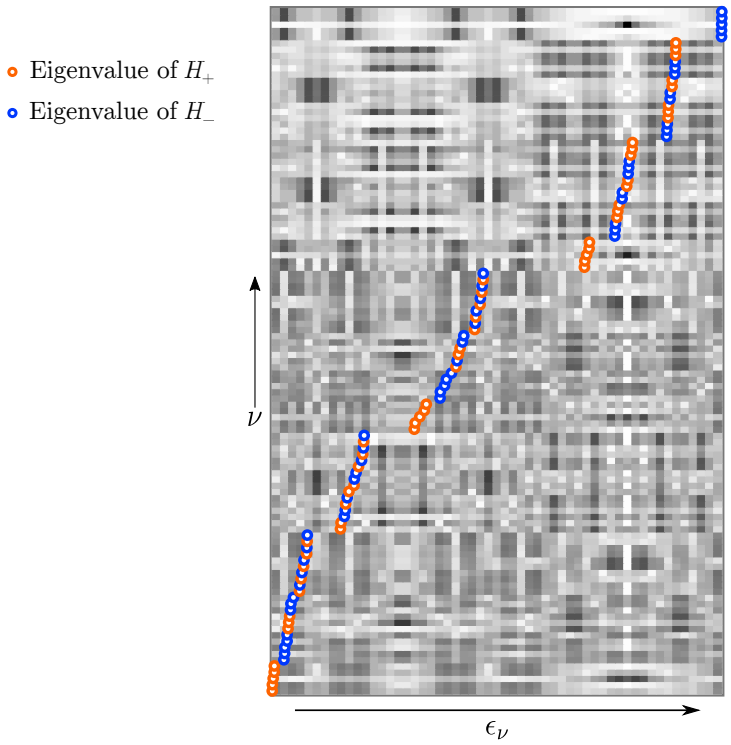

Figure 6.11: Eigenstate map for a setup consisting of two quasiperiodically coupled Fibonacci chains, each of length $F_9 = 55$ sites. Orange dots correspond to eigenvalues of H_+, and blue dots correspond to eigenvalues of H_-. The color map is the same as in Fig. 6.1, with black pixels corresponding to $\max_{\nu,j} \sqrt{|\Psi_j^{(\nu)}|}$.

6.7 Coupling through intermediate sites

In the following, we consider a case where the two Fibonacci chains are not coupled directly, but instead through intermediate sites. Before we start, let us first investigate a setup where two *periodic* chains are coupled indirectly, as shown in Fig. 6.12 (a). In Fig. 6.12 (b), we depict the band structure of this so-called "one-dimensional Lieb lattice" [272]. What makes this lattice interesting is that, among four dispersive bands, it also features one completely flat band fulfilling $E(k) =$ constant for all k. This defining feature of flat bands renders them dispersionless; they suppress wave transport [273]. On the other hand, the density of states in a flat band diverges, so that any disorder or non-linear effects may qualitatively change the transport properties [273, 274]. Moreover, in lattices where the single-particle Hamiltonian features a flat band, even arbitrarily weak interactions may act non-perturbatively. This can lead to boson pair formation [275–277] or other interesting phases, such as the Haldane insulator [278] and Wigner crystals [279].

In two dimensions, a classic example of a system with flat bands is the Lieb

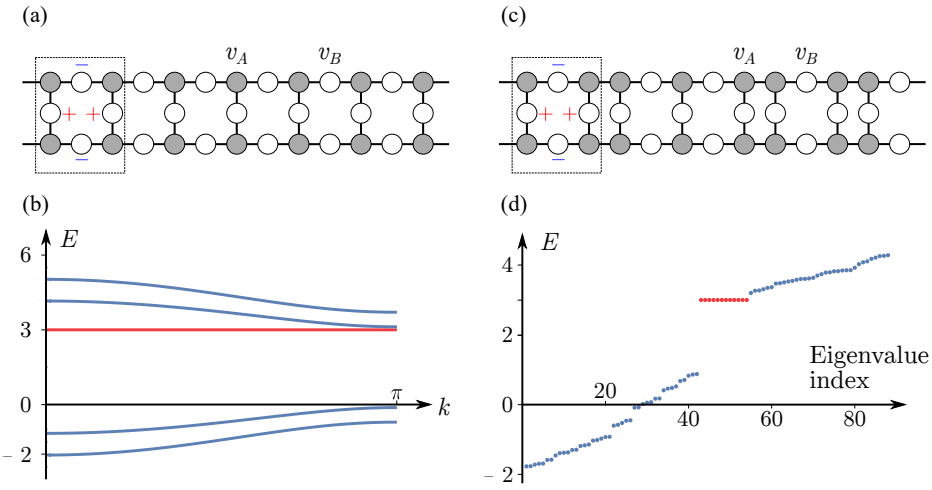

Figure 6.12: (a) The one-dimensional Lieb-lattice and its spectrum (b). (c) the quasiperiodic Lieb lattice and its spectrum (d). For the quasiperiodic Lieb lattice, the spectrum was computed for a finite setup with a total number of 88 sites (34 in the upper and lower chain and 20 B-sites in the center). For all figures, $v_A = 0$ and $v_B = h = 1$.

lattice, whose structure is very similar to the system depicted in Fig. 6.12 (a). The two-dimensional Lieb lattice has been realized in a number of different experimental platforms, such as tailored atomic structures on substrates [280, 281], evanescently coupled waveguide arrays [282, 283], terahertz spoof plasmons [284], or cold-atom setups [285, 286]. Interestingly, the CuO_2 planes in high-temperature cuprate superconductors possess a Lieb lattice structure, and it has been conjectured that flat bands might play a role in their high critical temperature [273, 287–291]

Flat bands are also interesting from another perspective, since they are tightly connected to the emergence of a special kind of eigenstates, the so-called "compact localized state" (CLS) [292–294]. For the one-dimensional Lieb lattice, a CLS is shown in Fig. 6.12 (a), consisting of an excitation of only four B sites. Thus, the CLS "lives" only on a single plaquette (marked by a dotted rectangle) and strictly vanishes outside it. In other words, it is perfectly localized on a very small part of the setup.

The defining feature of CLSs — namely, their perfect localization — renders these states very robust against perturbations: Since they vanish *exactly* outside their localization domain $\mathcal{D}$, they are not affected by any changes to the system outside $\mathcal{D}$. Due to this property, CLSs are ideal candidates for storing information [295, 296]. The perfect localization of CLSs might further be interesting in the context of photonic waveguide arrays, where it allows for diffraction-free transmission of information in the form of CLSs [282, 297].

After the above considerations, let us now couple two aperiodic Fibonacci chains in an indirect manner. Out of the many possibilities, here we choose one of the

simplest yet quite interesting setups, depicted in Fig. 6.12 (c). Each A-site of the upper chain is coupled by an intermediate B-site to its counterpart A-site on the lower chain. This setup also features a macroscopic number of CLSs, one of which is depicted in Fig. 6.12 (c).

When comparing the one-dimensional version of the Lieb lattice [298, 299]—shown in Fig. 6.12 (a)—to the coupled Fibonacci chains depicted in Fig. 6.12 (c), one sees that they are rather similar. Due to this high similarity, we call the coupled Fibonacci setup of Fig. 6.12 (c) the "quasiperiodic Lieb lattice". The similarity in the structure of the two lattices is also visible in their eigenvalue spectra, since both lattices feature a flat (quasi) band. The emergence of this flat band can easily be understood, since (for an infinite setup) there is an infinite number of plaquettes, and thus an infinite number of degenerate CLSs. In both cases, the flat bands emerge due to destructive interference [273].

6.8 Conclusions

In this work, we analyzed various ways of coupling two identical Fibonacci chains to each other. The main tool that helped us to identify the features of these systems is a symmetry-adapted block-diagonalization of the Hamiltonian H into $H_+ \oplus H_-$. Once we find the eigenstates of $H_\pm$, we can symmetrize/anti-symmetrize them, respectively, to obtain the eigenstates of the original Hamiltonian H. In addition, the eigenvalue spectrum of the system is simply given by a multiset sum of the eigenvalue spectra of the blocks $H_\pm$.

After briefly introducing the individual Fibonacci chain, we started by exploring the effects of uniformly coupling two identical chains. We then found that the resulting eigenvalue spectrum is just a sum of two shifted Fibonacci spectra, which renders the behavior of a particle in such a system identical to that in a conventional Fibonacci chain. We have subsequently explored the case of a nonuniform coupling, where we coupled only A (or only B) sites. An interesting scenario occurs when the interchain coupling is $h' = v_B - v_A$, since H_+ then becomes a periodic chain, for which the eigenstates are Bloch waves. On the other hand, H_- is still a Fibonacci chain, such that the complete spectrum offers a mixture of critical and fully extended eigenstates, identifiable by the parity of the corresponding wavefunctions.

The next type of coupling that we have analyzed is between a small subset of sites, i.e., a so-called defect coupling, leading to block Hamiltonians $H_\pm$, which are Fibonacci chains with on-site defects. This has been followed by another interesting and more complicated case of quasiperiodically coupled chains. The resulting block Hamiltonians could be thought to be like several coupled defects, but we have shown, through a perturbative renormalization analysis, that all states in this chain belong to the same family of critical states.

Finally, we explored two Fibonacci chains coupled to each other in the same manner as the nonuniform coupling of Section 6.5, but with an intermediate site in between. This offers the possibility of having a set of CLSs, leading to a flat bland in the energy spectrum. Overall, the demonstrated emergence of CLSs in

the quasiperiodic Lieb lattice represents an interesting addition to the existing literature on these phenomena in quasiperiodic setups (see, for instance, [300–302]).

Two immediate tasks for the near future would be to analyze the quasiperiodic Lieb lattice in the context of interacting electrons or to investigate the impact of (correlated) disorder on the transport properties.

6.A Determination of effective hopping amplitudes and energy corrections of the quasiperiodic coupling case

In the next subsections, we will determine the energy corrections and the renormalized Fibonacci hoppings for each cluster.

6.A.1 v_A cluster

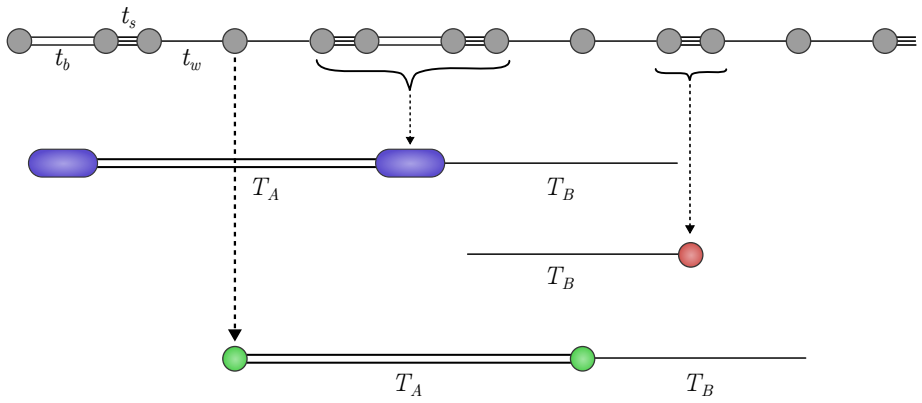

Figure 6.13: Decimation of the v_A cluster's effective chain. The blue rectangles represent the states of the four-atom molecules. They correspond to the renormalized sites of the chain and have an on-site energy given by E_{4M}. The effective hoppings T_A and T_B are Fibonacci distributed and further renormalization leads to the Fibonacci trifurcating structure. Below, we have the two-atom molecular chain, where each red site represents a dimer. In this figure, only one of them appears, but for a larger chain, there are Fibonacci distributed couplings, which is when the trifurcating structure starts after this point in the renormalization procedure. Finally, the bottom chain corresponds to isolated (green) sites, forming the last degenerate subspace of H_0^A. The effective chain for this subspace also has couplings that are Fibonacci distributed.

Starting with the v_A cluster, we can split it into the three categories depicted in Fig. 6.13. The 4-atom molecule leads to four energy eigenvalues,

$$E_{4M}^{A} = \pm\frac{1}{\sqrt{2}}\sqrt{t_b^2 + 2t_s^2 \pm \sqrt{(t_b^2 + 2t_s^2)^2 - 4t_s^4}}, \tag{6.16}$$

where the subscript $4M$ reminds us that it is for the 4-atom molecule, while the superscript A indicates that it applies to the initial level v_A. The 2-atom molecule and the isolated atom have eigenvalues, respectively, equal to

$$E^A_{2M} = \pm t_s, \tag{6.17}$$

$$E^A_A = 0. \tag{6.18}$$

In order to calculate the effective hoppings using the Brillouin-Wigner degenerate perturbation theory, we need to know the eigenstates of H^A_0, which for the $E^A_A = 0$ level are just the corresponding isolated sites. For the 2-atom molecules, these are given by $\left|E^A_{2M}\right\rangle = 2^{-1/2}(|i\rangle \pm |i+1\rangle)$ for some localized one-particle state at site number i, corresponding to the sites coupled by the strongest bond, and for the 4-atom molecules

$$\left|E^A_{4M}\right\rangle = \frac{a_0\,|i\rangle + a_1\,|i+1\rangle + a_2\,|i+2\rangle + a_3\,|i+3\rangle}{\sqrt{a_0^2 + a_1^2 + a_2^2 + a_3^2}}$$

for the relevant sites i to $i+3$, as shown in Fig. 6.13. The coefficients can be computed by solving the eigenvalue problem

$$\begin{pmatrix} 0 & t_s & 0 & 0 \\ t_s & 0 & t_b & 0 \\ 0 & t_b & 0 & t_s \\ 0 & 0 & t_s & 0 \end{pmatrix} \begin{pmatrix} a_0 \\ a_1 \\ a_2 \\ a_3 \end{pmatrix} = E_{4M} \begin{pmatrix} a_0 \\ a_1 \\ a_2 \\ a_3 \end{pmatrix}.$$

A solution to this problem is

$$\begin{aligned} a_0 &= 1, & a_1 &= \frac{E_{4M}}{t_s}, \\ a_2 &= \frac{E^2_{4M} - t_s^2}{t_b t_s}, & a_3 &= \frac{E_{4M}}{t_s}\frac{E^2_{4M} - t_s^2 - t_b^2}{t_b t_s}, \end{aligned} \tag{6.19}$$

where we ommited the superscript A for brevity. Each of the degenerate subspaces can be associated to its own chain, with its own couplings in the renormalization picture (see Fig. 6.13).

The effective Hamiltonian for the v_A cluster is found by setting the perturbation Hamiltonian H_1 to be the one with all matrix elements containing t_w. We remind the reader that the general expression was given by Section 6.6.2.

***E_{4M}* Chain (blue)** The couplings in the 4-atom molecular chain are given by the matrix element $\left\langle E^A_{4M,j}\right| H^A_{eff} \left|E^A_{4M,j+1}\right\rangle$, where j is the renormalized site index. To nearest order in t_w, they read

$$\begin{aligned} T_A &= \frac{a_3}{N}\frac{t_w^2}{E_{4M}}, \\ T_B &= \frac{a_3}{N}\frac{t_w^4 t_s}{E^2_{4M}(E^2_{4M} - t_s^2)}, \end{aligned} \tag{6.20}$$

where we defined $N \equiv a_0^2 + a_1^2 + a_2^2 + a_3^2$. Note that there are four different E_{4M}'s and hence four sets of coefficients a.

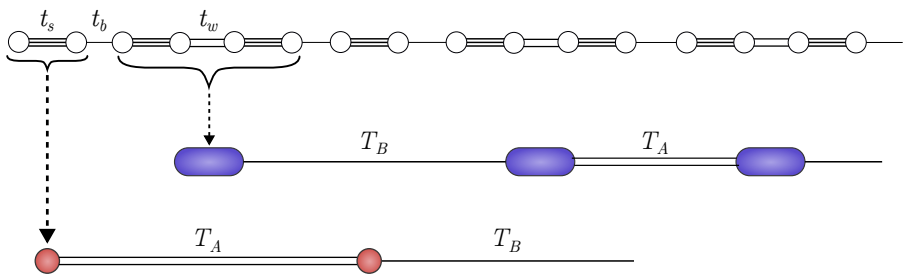

Figure 6.14: Decimation of the v_B cluster's effective chain. The blue rectangles represent the states corresponding to the four-atom molecules, like in Fig. 6.13. Below, we have the red sites representing dimers, also similar to Fig. 6.13. The couplings in both cases follow a Fibonacci sequence and will also trifurcate after this step in the renormalization procedure.

***E_{2M}* Chain (red)** The 2-atom molecular chain's couplings are obtained from the matrix elements $\langle E^A_{2M,j}| H^A_{eff} |E^A_{2M,j+1}\rangle$. The calculation yields

$$\begin{aligned} T_A &= \pm\frac{t_w^4}{2t_s^2}\sum_{j=0}^{3}\frac{a_3^{(j)}}{N_j\left(\pm t_s - E_{4M}^{(j)}\right)}, \\ T_B &= \frac{t_w^6}{2t_s^3}\left(\sum_{j=0}^{3}\frac{a_3^{(j)}}{N_j\left(\pm t_s - E_{4M}^{(j)}\right)}\right)^2, \end{aligned} \tag{6.21}$$

where we have now explicitely given a label to each of the four sets of a_j's, and by extention, N_j's as well. The $\pm$ refers to the bonding and anti-bonding energy levels.

***E_A* Chain (green)** Finally, the isolated atom chain has the following couplings

$$\begin{aligned} T_A &= -\frac{t_w^2}{2t_s}, \\ T_B &= -t_w^2\sum_{j=0}^{3}\frac{a_3^{(j)}}{N_j E_{4M}^{(j)}}. \end{aligned} \tag{6.22}$$

6.A.2 v_B cluster

For the v_B cluster's effective chains, we only have two categories, as shown in Fig. 6.14. The first (blue) corresponds to a 4-atom molecular chain, with the same energy eigenvalues and eigenstates formulae as the previous ones, but with a different set of $\{t_b, t_s, t_w\}$ [see Eq. (6.10)]. The second (red) subchain corresponds to the 2-atom molecular chain. We shall, once again, refer to them as the E_{4M} and E_{2M} chains, respectively.

***E_{4M}* Chain (blue)** The couplings in this case are given by

$$\begin{aligned} T_A &= \frac{t_w}{N} a_3, \\ T_B &= \frac{a_3}{N} \frac{t_w^2 t_s}{E_{4M}^2 - t_s^2}. \end{aligned} \tag{6.23}$$

***E_{2M}* Chain (red)** The couplings for this chain are

$$\begin{aligned} T_A &= \pm \frac{t_w^2}{2} \sum_{j=0}^{3} \frac{a_3^{(j)}}{N_j \left(\pm t_s - E_{4M}^{(j)} \right)}, \\ T_B &= \pm \frac{t_w^3}{2} \left(\sum_{j=0}^{3} \frac{a_3^{(j)}}{N_j \left(\pm t_s - E_{4M}^{(j)} \right)} \right)^2. \end{aligned} \tag{6.24}$$

6.A.3 Table of energy corrections

Table 6.1: The first order correction to the three clusters v_A, v_B and $v_B + 2h$. Any higher order correction will further split each of these energies into three, with corrections given by $\pm T_A$ and 0 (see the above sections for the values of T_A in each case). Each of the three levels again will split into three and so on, with the well known spectrum structure of the hopping Fibonacci chain.

E_0	E_1
v_A	$\frac{1}{\sqrt{2}}\sqrt{t_b^2 + 2t_s^2 + \sqrt{(t_b^2 + 2t_s^2)^2 - 4t_s^4}}$
	$\frac{1}{\sqrt{2}}\sqrt{t_b^2 + 2t_s^2 - \sqrt{(t_b^2 + 2t_s^2)^2 - 4t_s^4}}$
	t_s
	0
	$-t_s$
	$\frac{1}{\sqrt{2}}\sqrt{t_b^2 + 2t_s^2 + \sqrt{(t_b^2 + 2t_s^2)^2 - 4t_s^4}}$
	$-\frac{1}{\sqrt{2}}\sqrt{t_b^2 + 2t_s^2 - \sqrt{(t_b^2 + 2t_s^2)^2 - 4t_s^4}}$
v_B	$\frac{1}{\sqrt{2}}\sqrt{t_b^2 + 2t_s^2 + \sqrt{(t_b^2 + 2t_s^2)^2 - 4t_s^4}}$
	$-\frac{1}{\sqrt{2}}\sqrt{t_b^2 + 2t_s^2 - \sqrt{(t_b^2 + 2t_s^2)^2 - 4t_s^4}}$
	t_s
	$-t_s$
	$-\frac{1}{\sqrt{2}}\sqrt{t_b^2 + 2t_s^2 + \sqrt{(t_b^2 + 2t_s^2)^2 - 4t_s^4}}$
	$-\frac{1}{\sqrt{2}}\sqrt{t_b^2 + 2t_s^2 - \sqrt{(t_b^2 + 2t_s^2)^2 - 4t_s^4}}$
$v_B + 2h$	t_s
	0
	$-t_s$

Chapter 7

Topology in Aperiodic Systems

Commonly used symbols and acronyms

Symbol/Acronym	Meaning
SSH	Su Schrieffer Heeger
ES	Entanglement Spectrum
BZ	Brillouin Zone
OBC	Open Boundary Condition
PBC	Periodic Boundary Condition
H	Hamiltonian
$\tilde{t}$	Hopping amplitude
V_j	Potential value at site j
δ	Dimerization of the SSH model
$\phi(t)$	Time-dependent Berry phase
W_n	Aperiodic word of generation n
P	Polarization density
ξ_α	Entanglement spectrum eigenvalue

7.1 Introduction

Electronic band theory is a cornerstone of condensed-matter physics, usually grounded on the crystalline structures found in solid-state materials. The latter allows one to use crystal cells to construct Bloch Hamiltonians, which are much simpler to deal with than their real-space counterparts. By using these Bloch band structures, a well-established theoretical framework for topological insulators (TI's) and superconductors has been developed during the last decades [44, 60, 303]. However, topologically nontrivial insulating states are not restricted to periodic systems, as they have also been found in amorphous materials and disordered systems [304, 305].

One of the main properties of TI's is the bulk-boundary correspondence, which implies the existence of robust in-gap edge modes in one dimension (1D) and *gapless* boundary states in two and higher dimensions (2D and 3D). The physical response of such systems can be probed by the application of external perturbations, after which one finds either conducting channels at the boundary of an otherwise insulating bulk in 2D and 3D or an anomalous polarization response and fractional corner charges in 1D [41, 51, 220, 306]. Another class of 1D systems for which quantized boundary responses are possible are superconductors. A prime example where this happens is the Kitaev chain [40], which hosts Majorana edge states.

In the case of periodic crystals, the nontrivial topology of 2D and 3D TI's is generally attributed to the nonexistence of a complete set of exponentially localized Wannier functions, also known as an *obstruction to Wannierization* [61]. As a consequence, a topologically nontrivial state cannot be adiabatically connected to an atomic limit in which electrons occupy maximally localized Wannier states. In 1D, however, it is known that localized Wannier bases can always be constructed, such that there cannot be any topological obstruction [307]. Nevertheless, topologically nontrivial insulators, with anomalous polarization and fractional boundary charges, in fact, exist. These phases are known to be equivalent to *obstructed atomic limits*, which are not adiabatically connected with *trivial atomic limits* [20]. In order for this to happen, crystalline symmetries must be imposed on the system. The only possible such symmetry in 1D is inversion, forcing the polarization density of the system to be quantized at 0 or $1/2$ (in units where $e = 1$) [51, 220]. In turn, it is possible to relate the bulk topological invariant of a chiral-symmetric (or equivalently sublattice-symmetric) 1D system to its quantized polarization [16], and therefore understand the physical implications of the nontrivial topology of a 1D insulator. Namely, an anomalous boundary response exists in the obstructed atomic phase in the form of a quantized polarization resulting from the pile-up of fractionalized charges at the edges. The paradigmatic example of such a phase is realized in the Su-Schrieffer-Heeger (SSH) model [41].

Given that most toy models realizing such phases are typically periodic crystals, one wonders whether aperiodic 1D systems can also host obstructed atomic limits. Intense efforts have been made in the last decade to understand whether nontrivial topological phases could also exist in 1D quasicrystalline systems [137, 152, 248, 308]. It was shown that the gapped spectra of quasicrystalline Hamilto-

nians carry nontrivial signatures of topology. For example, a typical quasicrystal carries gap labels that have a topological origin and can be understood from K-theory [149]. These topological indices have also been linked with the pumping of boundary states [23, 137]. However, the question remains whether these observations constitute genuine signatures of anomalous boundary physics related to bulk properties by means of a bulk-boundary correspondence. In other words, do the topological labels observed in noncrystalline systems in 1D imply the existence of an electronically insulating topological phase, which is adiabatically connected to some type of obstructed atomic limit, and to which anomalous boundary physics can they be linked? To the best of our knowledge, this question has so far not been fully addressed, and we show in this work that it is indeed possible to find such phases for finite-size realizations of aperiodic systems. In order to reach this conclusion, we will use typical probes for anomalous edge responses, such as the Berry phases of crystalline approximants, the anomalous polarization responses to external static electric fields, and entanglement spectrum (ES) degeneracies. The systems that we will consider are the Fibonacci chain, the Tribonacci chain, and the Thue-Morse chain. By performing the adiabatic charge pumping protocol proposed in Ref. [24] for the Fibonacci chain, we show that multilevel pumping also works for at least two other aperiodic modulations: the Tribonacci sequence and the Thue-Morse sequence. We then identify the points in time where the Berry phase of these approximants is exactly 0 or π. These turn out to be the points where the boundary states of open systems are degenerate. For the Thue-Morse chain, a similar situation happens as for the SSH model. The $\phi = \pi$ point is, in fact, an inversion-symmetric realization of the system, which admits an anomalous polarization response of $P = 0.5$ due to the degeneracy of the edge modes. For the Fibonacci and Tribonacci chains, we use their palindromic factors to study their inversion-symmetric realizations and draw the same conclusions.

This chapter is structured as follows. In Section 7.2, we briefly review how signatures of nontrivial states in insulators are probed and the associated physical observables that result from the bulk-boundary correspondence in 1D. This is followed in Section 7.3 by a short overview of aperiodic systems. In Section 7.4, we present the charge-pumping protocol and the results obtained for the various aperiodic systems considered in this work. In Section 7.5, we discuss the results obtained from examining the various physical signatures of nontrivial 1D states across three distinct classes of aperiodic systems. We show that all the signatures that one should expect to see are present in these systems. Finally, in Section 7.6, we conclude with a summary and outlook.

7.2 Signatures of nontrivial states

In order to introduce our probes of nontrivial signatures, we will first consider a two-band, 1D periodic crystal, for which the insulating ground state consists of a filled valence band, separated from the conduction band by a gap. The paradigmatic model for such a system is the SSH chain [41]. It will be used as a benchmark in Section 7.5 to compare the results on aperiodic systems. The Hamiltonian is given

by

$$H_{\mathrm{SSH}} = -\tilde{t}\sum_{j=1}^{2N}\left[1-(-1)^j\delta\right]c_j^\dagger c_{j+1} + \mathrm{h.c.}, \tag{7.1}$$

where $\tilde{t}$ is the hopping amplitude, δ is the dimerization parameter, and N the amount of unit cells. The parameter space is the 1D Brillouin zone (BZ). We can define the Berry phase of the valence band eigenstate $|\psi_-(k)\rangle$ with respect to the BZ as

$$\phi = i\oint_{\mathrm{BZ}} dk\,\langle\psi_-(k)|\,\partial_k\,|\psi_-(k)\rangle\,.$$

It turns out that under the constraint of inversion symmetry in 1D, the Berry phase (also called Zak phase in this case) must be quantized to either 0 or π [51]. Additionally, since the Hamiltonian also exhibits chiral symmetry $\mathcal{S}H\mathcal{S}^{-1} = -H$, with $\mathcal{S}$ denoting the chiral symmetry operator, an additional protection of this phase takes place if the boundary modes are at $E = 0$. This spectral symmetry allows one to define the winding number [16]

$$\nu = \int \frac{dk}{4\pi i}\,\mathrm{Tr}\left[\mathcal{S}\partial_k \log H(k)\right],$$

which can be shown to be related to the quantized Berry phase of a inversion symmetric system through $\phi = \pi\nu \bmod 1$. For $\delta < 0$, the SSH chain is in the topological phase, and has two boundary zero modes. The winding number can be calculated exactly and is $\nu = 0$ ($\nu = 1$) for $\delta > 0$ ($\delta < 0$).

Bulk-Boundary Correspondence. The quantization of the winding number has an interesting physical meaning, which eventually takes the form of a bulk-boundary correspondence. The reason is that the spectrum of the Berry phase measures the average position of electrons in the ground state within a unit cell [50]. This, in turn, indicates how charge is distributed within a unit cell. In the case of an inversion symmetric insulator, $\phi = 0$ corresponds to a charge distribution around the center of a unit cell, while $\phi = \pi$ corresponds to a charge distribution at its boundaries. The polarization density is then related to the Berry phase through the following equation [50]

$$P = \frac{\phi}{2\pi} \bmod 1 = \begin{cases} 0, & \text{if } \phi = 0, \\ \dfrac{1}{2}, & \text{if } \phi = \pi. \end{cases} \tag{7.2}$$

This means that if one takes a finite system composed of an integer amount of unit cells, so as to keep the inversion symmetry intact, one finds half charges located at the boundaries of the system. The infinitesimal response to an external electric field should reflect this property. If a system does not preserve inversion symmetry, then the polarization density can take any value. This means that it is only possible to obtain quantized Berry phases, and therefore a quantized boundary response when inversion symmetry is present in 1D.

We can further understand these topological properties in terms of adiabatic deformations from trivial atomic limits to obstructed atomic limits. They are the

only two different elementary band representations possible for systems possessing inversion symmetry [20]. The half charges that result from such a situation are also intimately related to the concept of a filling anomaly, in which Wannier centers do not coincide with atomic sites [19]. Finally, this last point allows for another useful formulation of the topological phase through the ES. A robust signature of this filling anomaly is a degenerate ES of the insulator's many-body ground state [31].

Most of the theory discussed in this section relies on translational invariance and a crystalline structure for theoretical analysis. However, our focus is on understanding how these features manifest in aperiodic systems. To facilitate this exploration, we will first provide a brief overview of these systems in the following section.

7.3 Aperiodic Systems

Contrary to their periodic counterparts, these systems do not possess translation symmetry and are sometimes referred to as systems with deterministic disorder. That is, these systems show some type of long-range order even though they are not periodic [125]. For a comprehensive review and references, we refer the reader to the introduction of this thesis.

In 1D, *aperiodic* order is usually encoded in sequences of symbols that can be generated using a inflation rule. The mathematical study of such structures is called symbolic dynamics [141]. That is the study of the dynamical system formed by a set of symbols subjected to the repeated application of a function that maps the set of symbols to the set of combinations of symbols.

We consider finite-size words $W \in \mathcal{V}$, where $\mathcal{V}$ denotes the set of finite words that can be generated from an alphabet $\mathcal{A} = \{a_0,\ a_1,\ \cdots, a_m\}$ of inequivalent symbols. These words can be constructed by repeatedly applying a substitution rule $\sigma : \mathcal{A} \to \mathcal{V}$. The substitution rule imposes recurrence relations on words, which makes it easy to generate them. Suppose one starts with the "seed" letter a_0. We call the word *uniquely* generated by applying the rule σ to the seed letter n times the n^{th} approximant of the aperiodic sequence. Below, we give a few examples of aperiodic sequences that we use throughout this work.

Fibonacci sequence. The Fibonacci words can be generated from the binary alphabet $\mathcal{A} = \{A, B\}$ by applying the following recursion relation,

$$W_n = W_{n-1}W_{n-2},\ \text{for } n > 1,$$
$$W_0 = A,\ W_1 = AB,$$

In the above equation, the product of words means that they are concatenated. This is an example of a 1D quasicrystal, as it can be obtained via a cut-and-project scheme from a regular 2D square lattice [142].

Tribonacci sequence. The Tribonacci word is an extension of the Fibonacci word, and it is also a quasicrystal. However, its cut-and-project scheme results

from a 3D cubic lattice instead [5]. The alphabet generating the word is composed of three letters $\mathcal{A} = \{A, B, C\}$, and the recursive scheme to generate the word is

$$W_n = W_{n-1}W_{n-2}W_{n-3}, \text{ for } n > 2,$$
$$W_0 = A,\ W_1 = AB,\ W_2 = ABAC.$$

Thue-Morse sequence. The two previous words are examples for which the Pisot substitution conjecture holds [143, 144]. The characteristic matrix of the substitution dynamics has a polynomial of degree equal to its dimension. This makes their diffraction spectrum pure-point. It is for this reason that they can be called quasicrystals [142]. The Thue-Morse chain is not generated by a Pisot substitution and is an example of an aperiodic chain that is not a quasicrystal. It has a singular-continuous diffraction spectrum [145]. The sequence is generated by repeatedly applying the substitution rule $\sigma(A) = AB$ and $\sigma(B) = BA$ to the binary alphabet. Alternatively, it can be generated by the following recurrence relation

$$W_n = W_{n-1}\overline{W_{n-1}},\ n > 0,$$
$$W_0 = A,$$

where $\overline{W_n}$ is the bit-wise negated word: $A \to B$ and $B \to A$. That is, the n generation word is obtained by concatenating the $n-1$ generation word with its bit-wise negated version.

Rudin-Shapiro sequence. Finally, the last example of an aperiodic chain that we investigate is the Rudin-Shapiro chain [146]. This system is different from the previous three in the sense that it features an absolutely continuous diffraction spectrum. In order to generate the binary Rudin-Shapiro sequence, we use the following two-step procedure: We first impose the substitution rule on the four-letter alphabet $\mathcal{A} = \{A, B, C, D\}$:

$$\sigma : \begin{cases} A \mapsto AB, \\ B \mapsto AC, \\ C \mapsto DB, \\ D \mapsto DC. \end{cases}$$

This is then followed by the second step, which identifies $A, B \to A$, and $C, D \to B$. In this way, starting with the seed A, we obtain the Rudin-Shapiro binary sequence, which starts as $AAABAABAAAABBBAB\cdots$.

7.4 Topological Charge Pumping of Aperiodic Systems

The idea of topological charge pumping dates back to an argument made by Laughlin to explain the robustness of the quantized conductance in a two-dimensional

quantum Hall system [309]. Soon thereafter, Thouless showed, using similar arguments, that particle transport in a 1D system subjected to an adiabatic evolution will obey the same quantization condition [310]. Because charge pumping is analoguous to the Quantum Hall phase in 2D, where a quantized amount of charge is pumped on the boundary of a cylinder upon the insertion of one flux quantum [52, 309].

The topological classification enjoyed by the 1D quasicrystalline insulator is equivalent to the 2D class A of the ten-fold way [18]. It is the most robust class, as it is devoid of any symmetry. As long as the perturbations are applied adiabatically, it is guaranteed that the system stays in the same topological phase. This is the reason why quasi-crystallinity is completely irrelevant to the topological classification of a 2D time-reversal-symmetry-breaking insulator.

In fact, recent work has shown quantized topological charge transport in a periodically modulated (in time) 1D Fibonacci quasicrystal [24]. A Rice-Mele [311] pump with a Fibonacci modulation of the potentials displays the interesting possibility of multilevel pumping, a feature that is not present in equivalent crystalline systems. When the modulation is quasiperiodic, the number of pumped charges is instead characterized by a Bott index [312, 313], which, in the thermodynamic limit, is equivalent to the Chern number obtained in the periodic modulation case.

In the following, we shall briefly describe how quantized charge pumping occurs in a 1D periodic crystal, and how this quantization can be ascribed to the Chern theorem.

7.4.1 Charge transport as a polarization current

Starting from a 1D crystalline insulator, an adiabatic evolution of the system driven by a parameter λ induces a change in the polarization density

$$\Delta P = \int_{\lambda_i}^{\lambda_f} d\lambda \partial_\lambda P.$$

The modern theory of polarization [50] dictates that

$$\partial_\lambda P = \frac{1}{2\pi} \sum_n^{\text{occ}} \int_0^{2\pi} dk \ \text{Im} \langle \partial_\lambda u_n | \partial_k u_n \rangle$$

where $|u_n\rangle$ is a Bloch state corresponding to the n^{th} band of the system. If the parameter λ is periodic, i.e. the evolution is cyclic, one can identify $\text{Im} \langle \partial_\lambda u_n | \partial_k u_n \rangle = F^{(n)}(\lambda, k)$ as a Berry curvature, which means that the total change in polarization over one cyclic change of λ yields a total integral of the Berry curvature over a torus,

$$\begin{aligned} \Delta P &= \frac{1}{2\pi} \sum_n^{\text{occ}} \int_0^{2\pi} dk \oint d\lambda F^{(n)}(\lambda, k) \\ &= \sum_n^{\text{occ}} C_n \in \mathbb{Z}, \end{aligned} \tag{7.3}$$

where C_n denotes the Chern number of the n^{th} band. In the modern theory of polarization, this change in polarization can also be understood as a change in the Wannier center positions through the Berry phase formulation of the average position operator. Therefore, Eq. (7.3) predicts that there is an integer amount of charges crossing the unit cell of the 1D crystal. This means that, as a consequence of the Chern theorem, the total change in polarization is quantized to an integer number.

An intuitive example of a system that will also be discussed later is the Rice-Mele charge pump [219, 311]. This model connects the trivial phase of the SSH model to its topological phase and back to its trivial phase in an adiabatic cycle by breaking chiral symmetry. The Rice-Mele Hamiltonian is given by

$$H(t) = \sum_{j=1}^{N} \left[\Delta - (-1)^j \delta(t)\right] c_j^\dagger c_{j+1} - \sum_{j=1}^{N} (-1)^j h(t) c_j^\dagger c_j + \text{h.c.}, \tag{7.4}$$

where the first part is similar to the SSH model in Eq. (7.1), but with an independent hopping parameter Δ and a time-dependent dimerization $\delta(t)$. The second term adds a time-dependent staggered on-site potential, such that the bulk gap stays throughout the whole period. The time-modulated functions are given by

$$\begin{aligned} \delta(t) &\equiv \delta_0 \cos(2\pi t/T), \\ h(t) &\equiv h_0 \sin(2\pi t/T). \end{aligned}$$

Here, δ_0 and h_0 are constant amplitudes, and T is the modulation period. The Bloch Hamiltonian for this system is simply given by

$$H(k,t) = \begin{pmatrix} h(t) & v_+ + v_- e^{-ik} \\ v_+ + v_- e^{ik} & -h(t) \end{pmatrix},$$

where $v_\pm = \Delta \pm \delta(t)$. Then, it becomes clear that at $t = 0, T$, the system is in the trivial phase of the SSH model, with $h(0) = 0$ and $v_+ > v_-$. On the other hand, at $t = T/2$, the system is in the topological phase, with $v_+ < v_-$.

7.4.2 Bott-Index formulation of quantized charge pumping

In Ref. [24], the Bott index [312, 313] was used to demonstrate quantized charge pumping for a generalized Fibonacci chain, whose on-site and hopping parameters followed the quasiperiodic modulation. We will now summarize how the Bott index is defined for charge pumping and show that it leads to the same phase diagram as the Chern number.

In its most general form, the Bott index is a measure of the total phase picked up by a string of 2D position operators $(\hat{X}, \hat{Y})$, projected onto the insulating ground state $|\psi\rangle$, as they complete infinitesimal loops in real space. The contribution from all such loops over the whole system yields the Bott index. More concretely, let

$$\begin{aligned} \hat{U} &= \hat{\mathcal{P}} \exp\left(\frac{2\pi i \hat{X}}{L_x}\right) \hat{\mathcal{P}}, \\ \hat{V} &= \hat{\mathcal{P}} \exp\left(\frac{2\pi i \hat{Y}}{L_y}\right) \hat{\mathcal{P}}, \end{aligned} \tag{7.5}$$

where L_x and L_y are the dimensions of the system in the x and y directions, respectively. The Bott index is then defined as

$$\mathcal{B} \equiv \frac{1}{2\pi} \operatorname{Im} \operatorname{Tr} \log \left(\hat{V} \hat{U} \hat{V}^\dagger \hat{U}^\dagger \right). \tag{7.6}$$

It has been shown that $\mathcal{B} = C$ in the thermodynamic limit [312]. Still, even in the finite-size system, under periodic boundary conditions, it is a good indicator of a nontrivial topological character. Indeed, it works very well for nonperiodic 2D systems, such as disordered Chern insulators or amorphous materials [304, 305, 312]. In the case of adiabatic charge pumping, one deals with a periodic temporal parameter, which simplifies the formulation of the problem, as the Hamiltonian is in block diagonal form along the time axis and has instantaneous eigenstates $|\psi(t)\rangle$. It can be shown that the Bott index can be formulated in terms of a new set of operators $\tilde{U}, \tilde{V}$, which are obtained from Eq. (7.5) by understanding the action of the $\hat{Y}$ operator on momentum eigenstates. These operators take the form

$$\begin{aligned} [\tilde{U}_t]_{mn} &= \langle \psi_m(t) | \exp\left(\frac{2\pi i \hat{X}}{L_x} \right) | \psi_n(t) \rangle \,, \\ [\tilde{V}_{t,t+\Delta t}]_{mn} &= \langle \psi_m(t) | \psi_n(t + \Delta t) \rangle \,, \end{aligned}$$

where Δt denotes a discrete time step between adjacent times. Therefore, one can compute the Bott index as

$$\mathcal{B} = \frac{1}{2\pi} \sum_{t=0}^{T} \operatorname{Im} \operatorname{Tr} \log \left(\tilde{V}_{t,t+\Delta t} \tilde{U}_{t+\Delta t} \tilde{V}^\dagger_{t,t+\Delta t} \tilde{U}^\dagger_t \right). \tag{7.7}$$

In Fig. 7.1, one can see the equivalence of the phase diagram computed from (a) the Chern number given by Eq. (7.3) and (b) the Bott index given by Eq. (7.7).

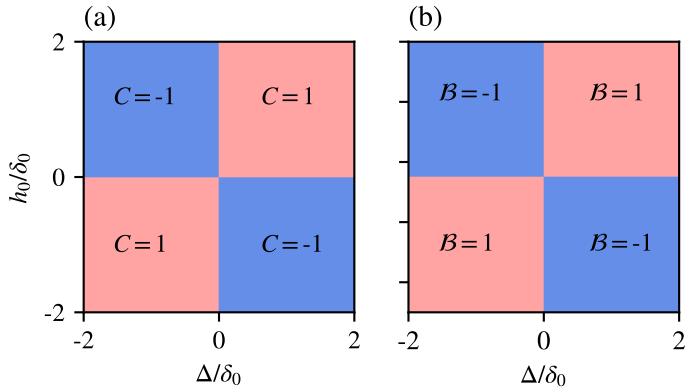

Figure 7.1: Equivalence of the topological phase diagram of the periodic Rice-Mele model, at half-filling, between (a) the Chern number formulation and (b) the Bott index formulation.

7.4.3 Aperiodic systems

Recent work has shown quantized topological charge transport in a time-periodically modulated 1D Fibonacci quasicrystal [24]. Using Eq. (7.4), but modifying the periodic modulation of the dimerization and on-site potentials to a quasiperiodic one following the Fibonacci sequence, they have been able to show the possibility of multilevel pumping, a feature that is not present in equivalent crystalline systems. Multilevel pumping entails that it is possible to pump across multiple gaps simultaneously. In the Fibonacci modulation case, this can be understood from a renormalization perspective, in which gaps of different generations can be mapped to each other [24] due to the self-similar nature of the energy spectrum. In this work, we show that multilevel pumping occurs for at least two other aperiodic modulations: a Tribonacci sequence and a Thue-Morse sequence. Each one represents a different class of aperiodicity, with the Tribonacci chain being a quasicrystal obtained from projecting a 3D cubic lattice onto a line with an irrational slope and the Thue-Morse being an aperiodic sequence not forming a quasicrystal. The Rice-Mele Hamiltonian in Eq. (7.4) is modified to

$$H(t) = \sum_{j=1}^{N} \left(\left\{ [\Delta - V_j \delta(t)]\, c_j^\dagger c_{j+1} + \text{h.c.} \right\} - V_j h(t) c_j^\dagger c_j \right), \tag{7.8}$$

where V_j is the j^{th} component of the aperiodic sequence of potentials distributed according to the aperiodic word W_n, with $N = |W_n|$ sites for periodic boundary conditions (PBC) and $N - 1$ sites for open boundary conditions (OBC). We will consider finite-size words $W_n \in \mathcal{V}$ generated by a substitution rule, where $\mathcal{V}$ denotes the set of finite words that can be generated from an alphabet $\mathcal{A}$ (see Section 7.3).

Now, we apply the first three modulations described in Section 7.3 to the Hamiltonian Eq. (7.8), then numerically compute the time-dependent spectra and plot the results in Fig. 7.2. Additionally, we also calculate the time-dependent Berry phases of the crystalline approximate in the insulating state with a band gap indicated by the green shaded area in Fig. 7.2, which can possibly indicate a crystalline topological phase at the point where the in-gap edge modes cross and become degenerate. In Figs. 7.2(a) and 7.2(b), the results for the periodic modulation are shown. In Fig. 7.2(a), we see that at $t = T/2$, the Berry phase is equal to π, indicating the presence of inversion symmetry [51]. This result is corroborated by the crossing of the in-gap modes at $E = 0$ in Fig. 7.2(b). The color code of the eigenstates indicates whether they are bulk (grey)- or edge-localized (red and blue) modes. This visual confirms that $t = T/2$ is when the chain is in the topological phase. These results are consistent with the fact that the Rice-Mele model realizes topological charge pumping by adiabatically connecting the topological and trivial phases of the SSH model. In Figs. 7.2(c) and 7.2(d), the same information is plotted for the Fibonacci modulation. In Fig. 7.2(c), one can see that the edge modes now intersect at $t = T/4$ and $t = 3T/4$. However, contrary to the SSH model, the Fibonacci chain does not become inversion symmetric at any point in the pumping procedure. In Fig. 7.2(d), the novel feature of multilevel pumping can be observed, as was pointed out in Ref. [24]. The reason for this behavior can be understood from a real-space-renormalization approach. The instantaneous state at the largest gap can mapped to a state in a smaller gap, with renormalized

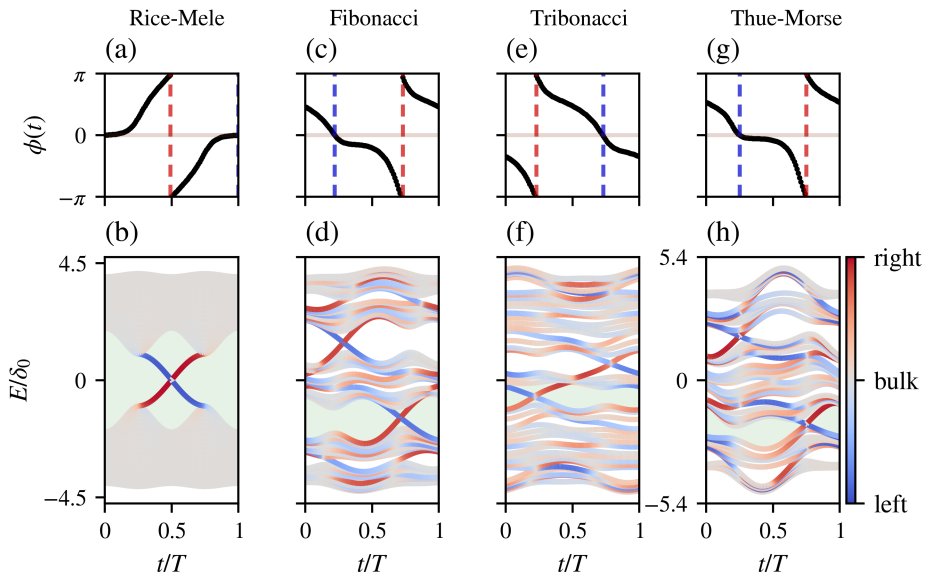

Figure 7.2: Top row: time evolution of the Berry phases of each model studied under a pumping cycle. Vertical dashed lines indicate points when $\phi = 0$ (blue) or $\phi = \pi$ (red). Bottom row: behavior of the eigenvalues under adiabatic time evolution. The colors indicate the localization behavior of each mode, with grey denoting bulk modes and red (blue) indicating localization on the right (left) of the chain. The green shaded area indicates the bulk gap for which the Berry phase was calculated. (a,b) Periodic Rice-Mele, (c,d) Fibonacci Rice-Mele, (e,f) Tribonacci Rice-Mele, (g,h) Thue-Morse Rice-Mele. System sizes are (a,b) $N = 100$, (c,d) $N = 55$, (e,f) $N = 44$, and (g,h) $N = 64$.

Hamiltonian parameters. In Figs. 7.2(e) and 7.2(f), similar behavior is observed for the Tribonacci chain, with multilevel charge pumping and edge state crossing points appearing around $t = T/4$ and $t = 3T/4$. Finally, Figs. 7.2(g) and 7.2(h) show the results for the Thue-Morse chain, also indicating multi-level charge pumping and the edge state crossing points for the largest gaps. Contrary to the two quasiperiodic chains, the Thue-Morse chain is inversion symmetric. This is because the Thue-Morse word is a palindrome for even generations of the word. We will explore palindromic realizations of all the models in section Section 7.5.

To ensure that these features are not dependent on the choice of unit cell, the same calculations were performed using different unit cell configurations. The corresponding results are presented in Section 7.A.

In order to corroborate the claims on multilevel pumping, we also calculate the amount of charge pumped at any time, which is given by the partial sum of

Eq. (7.7), i.e.

$$Q(t) = \frac{1}{2\pi} \sum_{t'=0}^{t} \mathrm{Im}\,\mathrm{Tr}\log\Big(\tilde{V}_{t',t'+\Delta t}\tilde{U}_{t'+\Delta t}\tilde{V}^{\dagger}_{t',t'+\Delta t}\tilde{U}^{\dagger}_{t'}\Big).$$

The results are shown in Fig. 7.3. In Fig. 7.3 (a), the periodic modulation is shown at half-filling, as there is only one gap. This is single-level pumping. In Figs. 7.3 (b) - (d), the charge pumped at three different fillings for the Fibonacci, Tribonacci, and Thue-Morse modulations is shown, respectively. In each case, we see that the charge gradually increases to a maximum of 1 at the end of the pumping cycle for different fillings, a hallmark of quantized multilevel charge pumping. We also note that the form of the curve tends towards a step-like function for decreasing filling in all three cases, generalizing the observations made in Ref. [24].

Finally, we note that for each case, we calculated the Berry phase for a filling corresponding to the largest gap below $E = 0$. This is indicated by the green shaded area in Fig. 7.2, corresponding to the bulk gap considered. In each case, we see that $\phi(t) = \pi$ exactly where the edge modes cross, indicating that the system could be in a nontrivial 1D topological phase (provided it possesses inversion symmetry), with an anomalous polarization of $P = 1/2$. This motivates us to investigate this phase's realization and study it separately to show the anomalous topological response appearing at those points.

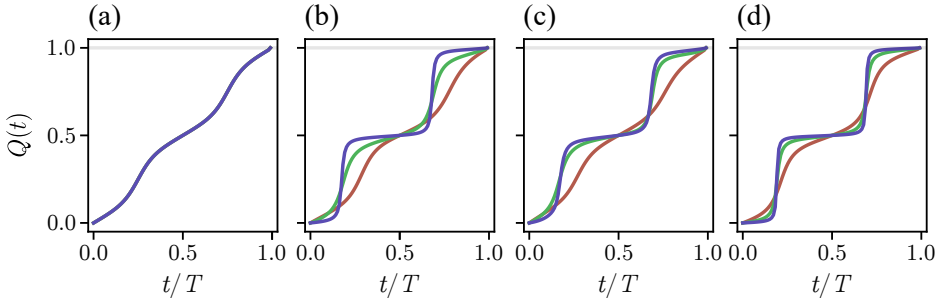

Figure 7.3: Cumulative charge pumped as a function of time. (a) The periodic modulation at half-filling. (b) The Fibonacci modulation at fillings τ (red), τ^3 (green), and τ^6 (blue), with $\tau = (\sqrt{5}-1)/2$ the inverse of the golden ratio. (c) The Tribonacci modulation at fillings β (red), β^3 (green), and β^4 (blue), with $\beta^{-1} \approx 1.8393$ the real root of the cubic equation $x^3 - x^2 - x - 1 = 0$, also called the Tribonacci constant. (d) The Thue-Morse modulation at fillings 1/3 (red), 1/10 (green), and 1/27 (blue). For the aperiodic models, the behavior tends to become step-like for smaller fillings, which is a feature of multi-level charge pumping.

7.5 Topological Signatures in Aperiodic Systems

Before investigating these topological signatures, we shall describe inversion-symmetric realizations of aperiodic chains in more detail.

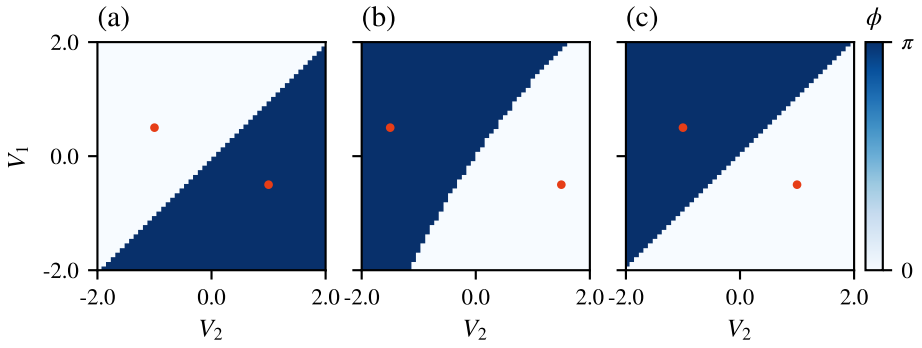

Figure 7.4: Phase diagram of the inversion-symmetric realizations of aperiodic chains. The generations chosen are (a) $n = 9$ for the Fibonacci chain, (b) $n = 8$ for the Tribonacci chain, and (c) $n = 6$ for the Thue-Morse chain. The hopping parameters has been set to $\tilde{t} = 1$ for the Fibonacci and Tribonacci chains, while it has been set to $\tilde{t} = 2$ for the Thue-Morse chain to reflect the phase achieved in the pumping cycle shown in Fig. 7.2(h).

7.5.1 Inversion-symmetric aperiodic chains

As stated earlier, the Thue-Morse chain pumping cycle happens between two realizations of inversion-symmetric chains. This is because of the property that finite Thue-Morse words W_n of even generation n form perfect palindromes. A snapshot of the Hamiltonian when the Berry phase is $\phi = \pi$ reveals that the Hamiltonian is of the form

$$H = \sum_j V_j c_j^\dagger c_j + \tilde{t} \sum_j c_j^\dagger c_{j+1} + \text{h.c.}, \tag{7.9}$$

where $V_j = V_A, V_B$, distributed according to the Thue-Morse sequence, and $\tilde{t} = 2$ (arbitrary units). The on-site potentials take on the values $V_A = -0.25\tilde{t}$ and $V_B = 0.5\tilde{t}$. On the other hand, when $\phi = 0$, $\tilde{t}$ is still the same, but now the on-site potentials are $V_A = 0.25\tilde{t}$ and $V_B = -0.5\tilde{t}$. i.e., the sign has been switched.

With this in mind, we proceed similarly for the Fibonacci and Tribonacci chains. However, we must select palindromic sections of the finite words. For the Fibonacci chain, it is known that for any generation n, the word $W_n = P_n xy$, where P_n is a palindrome and $xy = AB$ or $xy = BA$, depending on the generation. Therefore, we shall work with Fibonacci chains of generation n and omit the last two letters.

For the Tribonacci chain, it is also known [314] that one can factor the generation $n \leq 1$ word as $W_n = P_n E_n$, where

$$P_n = W_{n-1} W_{n-2} \cdots W_1 W_0$$

is a palindrome and E_n is a word of length $|E_n| = (|W_n| - |W_{n-2} + 3)/2$. Thus, we shall be working with the palindrome P_n in this case as well. In all cases, we will use the simple hopping Hamiltonian Eq. (7.9).

In Fig. 7.4(a), we show the phase diagram depicting the quantization of the Berry phase in the $(V_A, V_B) \equiv (V_1, V_2)$ plane for the Fibonacci modulation. Figures 7.4(b) and (c) show the same for the Tribonacci and the Thue-Morse chains. Since the Tribonacci chain has three on-site potentials, we set the most recurrent one equal to $V_A = 0$ and the other two to $(V_B, V_C) = (V_1, V_2)$.

Given the considerations laid down at the end of Section 7.4, we expect a nontrivial insulating phase in 1D, with the corresponding protected anomalous boundary responses at exactly the points where the finite approximants show inversion symmetry. Nevertheless, it was shown that is possible to adiabatically transform a quasiperiodic system, such that the open chain has its edge states pushed into the bulk. Thereby, one may identify the phases as being topologically equivalent to the trivial insulator [139, 308], which renders these topological phases very fragile. This is a common feature of 1D topological insulators, as the SSH chain without chiral symmetry presents very weakly protected edge modes. The presence of both chiral and inversion symmetries renders them more robust, as the former pins down the degenerate edge states at $E = 0$. When chiral symmetry is lifted, one can adiabatically deform the Hamiltonian to move the edge states into bulk bands.

In the following, we will show the existence of these delicate topological phases by using two typical signatures of nontrivial topology in 1D, which do not require the calculation of bulk topological invariants. The first one is the polarization response of an open system, and the second is the ES degeneracy.

7.5.2 Polarization

We use the SSH chain introduced in Eq. (7.1) as a benchmark for anomalous polarization responses. We expect that as soon as an infinitesimal electric field is turned on, the polarization has a value of $|P| = 0.5$ when the chain is in the topological phase. In order to probe the boundary response, we add an electric field along the chain, contributing $H_{\mathcal{E}} = \mathcal{E}\hat{X}$ to the Hamiltonian, where $\mathcal{E}$ is the electric field strength, and the position operator is chosen to be defined as

$$\hat{X} = \sum_{i=1}^{N_c} \sum_{j=1}^{N_s} \left(-\frac{2j-1}{2N_s} - \frac{N_c}{2} + i \right) c_{i,j}^{\dagger} c_{i,j}, \tag{7.10}$$

where N_c is the number of cells and N_s is the number of sites in a cell. This is a generalization of the definition given in the case of the SSH chain in Ref. [220], which takes the form

$$\hat{X} = \sum_{j=1}^{N} \left(-\frac{3}{4} - \frac{N}{2} + j \right) c_{2j-1}^{\dagger} c_{2j-1} + \left(-\frac{1}{4} - \frac{N}{2} + j \right) c_{2j}^{\dagger} c_{2j},$$

where N is the number of unit cells.

The position operator $\hat{X}$ is chosen such that $x = 0$ lies at the boundary of a unit cell. Note that the total amount of sites is $L = N_s N_c$. The full Hamiltonian

is then $H = H_{\text{system}} + H_{\mathcal{E}}$, where H_{system} corresponds to any system that we wish to study. The dielectric response is given by the polarization [220],

$$P(\mathcal{E}) = -\frac{1}{L-1}\sum_{n=1}^{N}\frac{\partial E_n}{\partial \mathcal{E}} \tag{7.11}$$

where $E_n \in \text{Spect}(H)$. In the limit $\mathcal{E} \to 0$, $|P|$ should agree with the polarization mentioned in Section 7.1. In that limit, the adiabatic theorem applies, and one can choose a temporal gauge such that the minimal coupling of the electric field allows for a temporal sweep of the complete BZ [315].

More generally, using a periodic approximation for the aperiodic systems, we shall make use of Eq. (7.10), where each cell represents an approximant of the aperiodic structure.

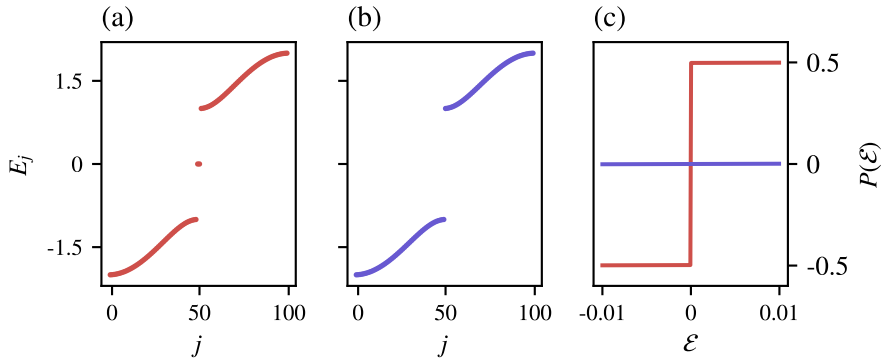

Figure 7.5: Energy and polarization of the SSH chain. (a) The OBC spectrum of the SSH chain in the topological phase: two degenerate edge states are pinned at the Fermi energy. (b) The OBC spectrum in the trivial phase: all states belong to the bulk. (c) The two different polarization responses, in the trivial phase (blue) and in the topological phase (red). The dimerization parameter in Eq. (7.1) has been set to $\delta = \pm 0.5$ [$\delta < 0$ ($\delta > 0$): topological (trivial) phase].

SSH Chain. The spectra and polarization of the SSH chain are shown in Fig. 7.5. The OBC spectra for the topological (red) and the trivial (blue) phase are shown in Figs. 7.5(a) and 7.5(b), respectively. The anomalous response of the SSH chain in the topological phase is shown in Fig. 7.5(c) in red, while the the response in the trivial phase is shown in blue. These results agree with the quantized Berry phase of $\phi = \pi, 0$, respectively.

Aperiodic Chains. We will now analyze the responses of three different aperiodic chains, each one being a representative of a different class of aperiodicity.

The generic system Hamiltonian will be of the form Eq. (7.9), where the on-site potentials are modulated, and the hoppings are constant. The choices for (V_A, V_B) are shown in red in Fig. 7.4, and the system sizes are also the same.

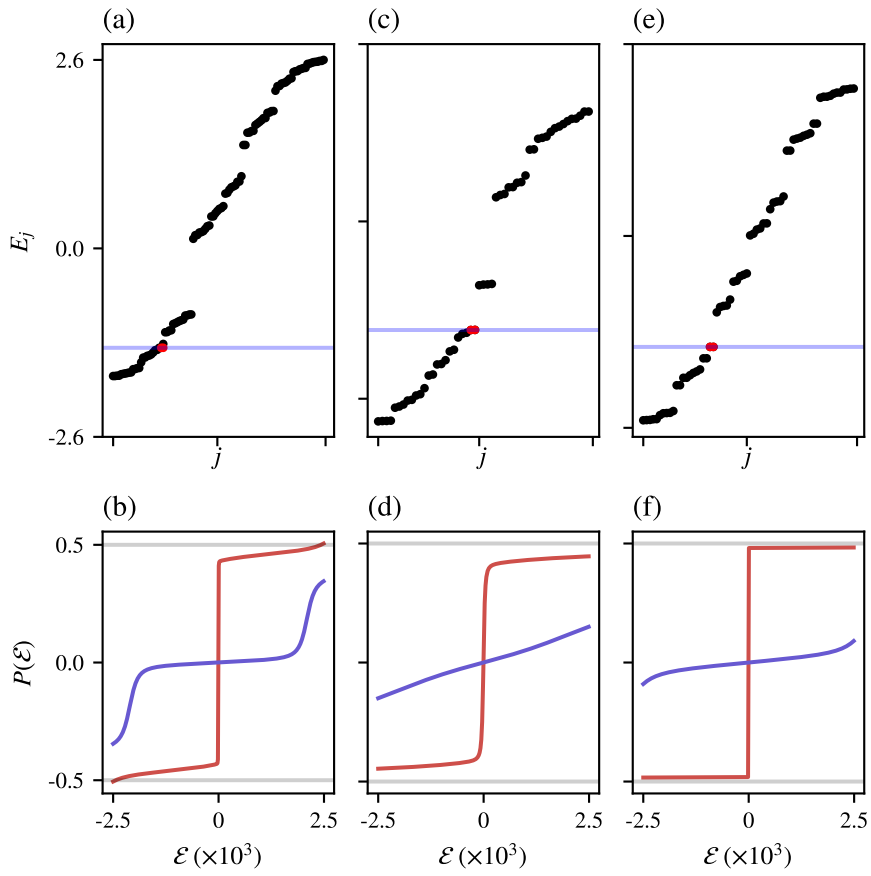

Figure 7.6: Polarization response of the aperiodic chains. OBC spectra (in the nontrivial phase) and polarization responses of the (a,b) Fibonacci chain, (c,d) Tribonacci chain and (e,f) Thue-Morse chain. The fillings are chosen such that the Fermi energies (light blue line) lie in the largest gap in each case. In all cases, the polarization exhibits an anomalous behavior around $\mathcal{E} = 0$, with a jump from -0.5 to 0.5 caused by the eigenstates colored in red in (a), (c), and (e) whenever the system is in the $\phi = \pi$ phase. On the other hand, the polarization does not show a sudden jump in the $\phi = 0$ phase (in blue). For consistency with the phase diagram calculations presented in Fig. 7.4, all unit cell sizes were selected at the same approximant level. Additionally, a two-unit-cell scheme was employed for the Fibonacci chain to enhance numerical stability.

For the Fibonacci modulation, Fig. 7.6(a) depicts the OBC energy levels, with a choice of Fermi energy indicated by the blue line. In Fig. 7.6(b), the corresponding polarization $P(\mathcal{E})$ response is shown. There is a clear anomalous polarization, as indicated by the sudden jump from $P(\mathcal{E}) = -0.5$ to $P(\mathcal{E}) = 0.5$ near $\mathcal{E} \approx 0$, which is caused by the eigenstates colored in red, located at the Fermi level (light blue) in the

$\phi = \pi$ phase. On the other hand, the polarization response does not show a sudden jump in the $\phi = 0$ phase (in blue). The same behavior is observed for the Tribonacci modulation in Figs. 7.6(c) and 7.6(d). For the Thue-Morse chain, in Figs. 7.6(e) and 7.6(f), we also observe a similar behavior. We note that the results plotted in Fig. 7.6 do not show a perfect equality $|P| = 0.5$ (topological), or $P = 0$ (trivial), which we suspect might be due to finite-size effects of the numerical implementation of the calculations. All system sizes have been chosen to be the same as those used to calculate the phase diagram in Fig. 7.4, with parameter values as indicated by the red points in the figures. Namely, we have chosen (a) $(V_1, V_2) = (\mp 0.5\tilde{t}, \pm 1\tilde{t})$, (b) $(V_1, V_2) = (\pm 0.5\tilde{t}, \mp 1.5\tilde{t})$, and (c) $(V_1, V_2) = (\mp 0.25\tilde{t}, \pm 0.5\tilde{t})$ for the topological and trivial phases, respectively.

7.5.3 Entanglement Spectrum

The second signature of nontrivial topological states that we will use is the degeneracy structure of the ES. There exists a one-to-one correspondence between the topological boundary modes of an open system, and the degeneracy of all eigenvalues of the ES of a subsystem taken deep in the bulk of an extended system [31]. In the following, we give a brief overview of how to calculate the ES, and the method

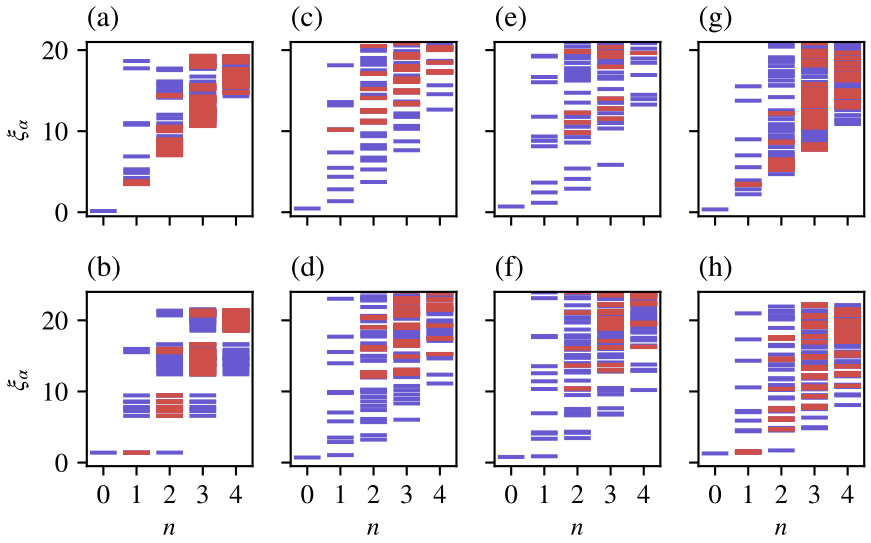

Figure 7.7: First few eigenvalues of the ES plotted against the total particle number of the eigenvalue configuration. The first row indicates all the trivial realizations of the inversion symmetric chains and the lower one indicates all the topological realizations. (a,b) The SSH chain. (c,d) the Fibonacci chain. (e,f) The Tribonacci chain. (g,h) The Thue-Morse chain. A red bar indicates at least double degeneracy at the given particle number. The system sizes chosen are consistent with those computed for charge pumping and for polarization responses.

that we used to obtain the results. We then show that the signatures of nontrivial topology are present in both the SSH chain and in the aperiodic chains.

Let us consider the ground state of a fermionic insulator, described by a quadradic Hamiltonian with a gapped single-particle spectrum. The many-body ground state of such a system is a pure product state, which can be written as

$$|\Psi_0\rangle = \prod_{n<n_F} \alpha_n^\dagger |0\rangle ,$$

where the operator $\alpha_n^\dagger$ creates a particle in the n^{th} eigenstate of the Hamiltonian. The density matrix for this pure state is simply given by $\rho_0 = |\Psi_0\rangle \langle\Psi_0|$. We would like to probe the entanglement between two subsytems, given a certain bipartition of the chain. Let the two systems be labeled by K and L. Then, the ES is defined to be the set of the negative logarithm of the eigenvalues of the reduced density matrix ρ_L (or equivalently ρ_K), i.e.,

$$\text{ES} = \{\xi_\alpha \in \text{Spect}(-\log \rho_L) \mid \rho_L = \text{Tr}_K \rho\}, \tag{7.12}$$

where Tr_K is a partial trace over the subsystem K. In the following, we will plot the ES against particle number configuration (see Section 7.B for more details on how to calculate the ES).

The ES of the SSH chain is shown in Figs. 7.7(a) and 7.7(b). The difference between the trivial Fig. 7.7(a) and topological Fig. 7.7(b) phases is in the increased degeneracy of all eigenvalues in the topological phase. Restricting ourselves to the lowest eigenvalue, we see that its degeneracy goes from $D = 1$ to $D = 4$ (the red bar indicates that the degeneracy is at least of order 2). These results are already known from Ref. [32]. We shall use the degeneracy of the lowest eigenvalue as an indicator of nontrivial topological behavior at the boundary of our 1D models.

In Figs. 7.7 (c)-(h), the ES of the aperiodic chains are shown. For each case, at least a double degeneracy of the lowest eigenvalue can be observed in the bottom row of the figure. It was already known that the bulk entanglement entropy of the Fibonacci quasicrystal carries some type of signatures of the gap labels [316]. Our findings provide an indication of the nontrivial topology that could arise at the boundary when the in-gap modes are inversion-symmetric partners.

7.6 Conclusion

The study of topological phases in quasicrystals has attracted a significant amount of attention in the last decade, and there have been many interesting experimental and theoretical observations [22, 23, 137, 152, 317]. At the same time, it is known that topological phases in 1D band insulators do not exist, except when inversion symmetry gives rise to an obstructed atomic phase. The latter results in a quantized polarization response due to fractionalized charges piling up at the boundary [20].

In this work, we put the recent observation of topological states in quasicrystals in context, and show that multilevel charge pumping is a generic feature of aperiodic chains, rather that it being specific to quasiperiodic models. When these models admit inversion symmetry, such as the Thue-Morse chain, the pumping process

cycles through two topologically distinct phases of the inversion-symmetric configurations. For many chains that admit palindromic factors, it is natural to expect nontrivial topological phases for finite approximants of the aperiodic systems. By calculating three typical signatures of topology in aperiodic chains, we have found genuine 1D topological phases. Namely, we have shown that the Fibonacci and Tribonacci quasicrystals and the Thue-Morse chain – representing different classes of aperiodic systems, exhibit anomalous polarization responses and that their ES possess topological eigenvalue degeneracy.

Our results do not hold for the Rudin-Shapriro modulation because the pumping protocol does not perform an adiabatic evolution of the system. Moreover, it is known that this sequence does not admit any palindromic factor [318]. This might be due to the different measures of the energy and Fourier spectra. As a possible outlook, it would be interesting to understand the relationship between the energy and Fourier spectra, the generic property of multilevel pumping, and the existence of inversion-symmetric aperiodic insulators in general.

7.A Berry phase and edge state level crossing

As stated earlier in the main text, the time at which the level-crossing happens depends on the unit-cell choice. However, as we will empirically show in this appendix, the level crossing seems to always happen when the time-dependent Berry phase is equal to π.

Before we do that, let us briefly explain how the unit cell is chosen for our calculations. As an example, we show the procedure for the Fibonacci word of generation $n = 8$, with $F_9 = 34$ letters. Four choices of unit cells will be taken, where each successive one is shifted by a quarter word length (floored to the nearest integer), as shown below

$$\begin{aligned}
\text{Word: } & ABAABABA\underset{\uparrow}{\,}ABAABABAA\underset{\uparrow}{\,}BABAABAA\underset{\uparrow}{\,}BABAABAAB,\\
\text{Cell 1: } & ABAABABAABAABABAABABAABAABABAABAAB,\\
\text{Cell 2: } & ABAABABAABABAABAABABAABAABABAABABA,\\
\text{Cell 3: } & BABAABAABABAABAABABAABABAABAABABAA,\\
\text{Cell 4: } & BABAABAABABAABABAABAABABAABABAABAA.
\end{aligned}$$

The first unit cell starts from the beginning of the word until its end. The second unit cell starts from where the first arrow points and winds around the word back to the last letter before the arrow. The same is done for the third unit cell, starting from the second arrow and so on... This procedure will be applied to each aperiodic word in this work.

Since the systems under consideration are multiband insulators with valence bands that can cross each other, we must employ a more general definition for the Berry phase that we calculated numerically. To this end, we use [319]

$$\phi = -\mathrm{Im}\log\prod_{k}\sum_{n=1}^{m}\left|\psi_n(k)\right\rangle\left\langle\psi_n(k+\delta k)\right|,$$

where m is the number of filled bands and $|\psi_n(k)\rangle$ is the Bloch state of the n^{th} band, with the following periodic boundary condition imposed in k-space,

$$|\psi_n(k_N)\rangle_j = \exp\left(-2\pi i x_j\right) |\psi_n(k_0)\rangle_j \,.$$

Here, the notation refers to the j^{th} component of the discrete Bloch state, and x_j is the position of the jth lattice point.

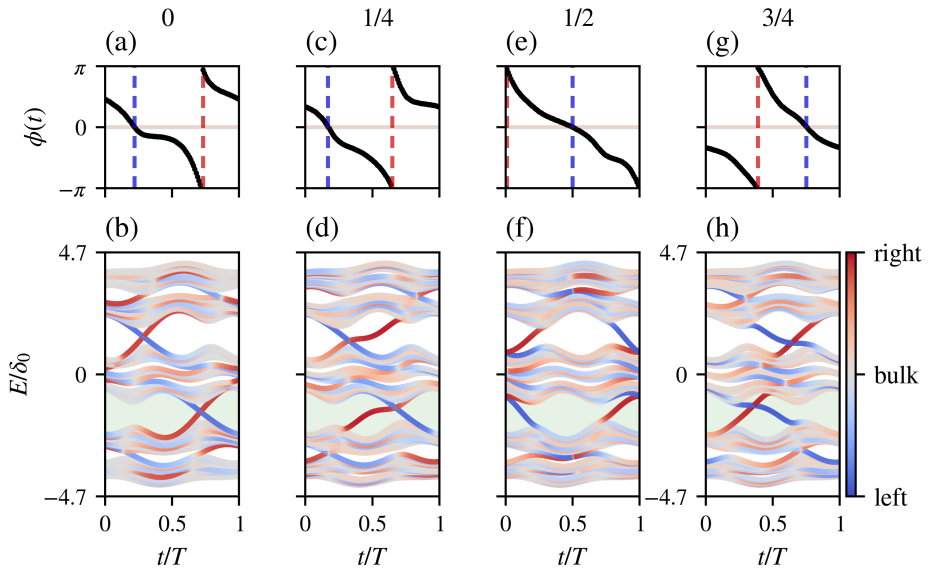

Figure 7.8: Berry Phase and level crossing for the Fibonacci chain. Each column corresponds to a different choice of unit cell, where the number above each column represents the fraction of the length of the generated word using the Fibonacci recursion rule. The green shaded area in the bottom row represents the chosen bulk gap for the Berry phase calculation. The system size is $N = 55$. The red (blue) dashed lines mark the times when $\phi = \pi$ ($\phi = 0$).

The results are plotted in Figs. 7.8, 7.9, and 7.10. In each case, we see in the green shaded region, corresponding to the bulk gap considered, that the edge states cross exactly when $\phi = \pi$, as indicated by the red dotted lines in the upper row.

7.B Entanglement Spectrum of Quadratic Hamiltonians

For quadratic Hamiltonians, it is known that the reduced density matrix takes the exponential form [320]

$$\rho_L = \det \mathcal{M}_L \exp\left[\sum_{i,j\in L} \log\left(G_L \mathcal{M}_L^{-1}\right)_{ij} c_i^\dagger c_j\right] ,$$

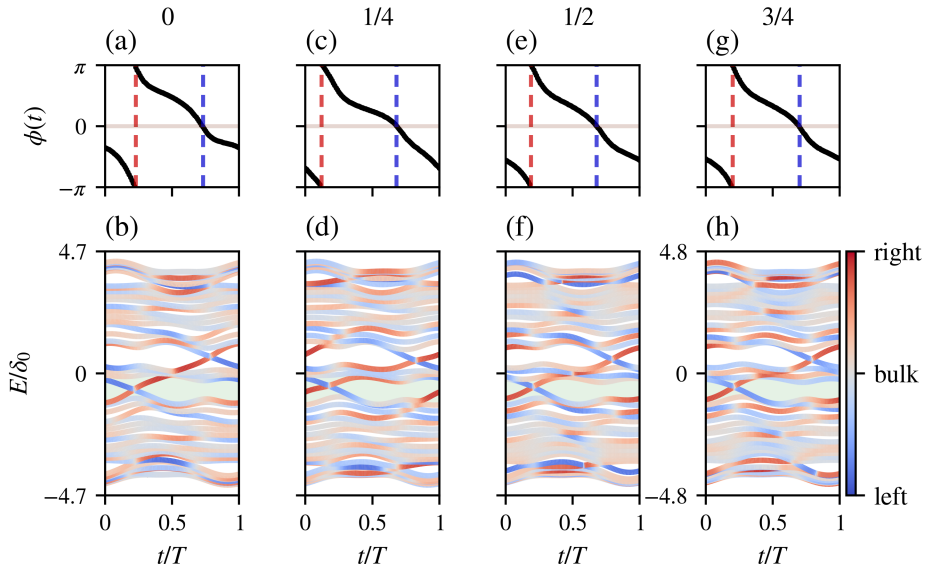

Figure 7.9: Berry Phase and level crossing for the Tribonacci chain. The system size is $N = 44$.

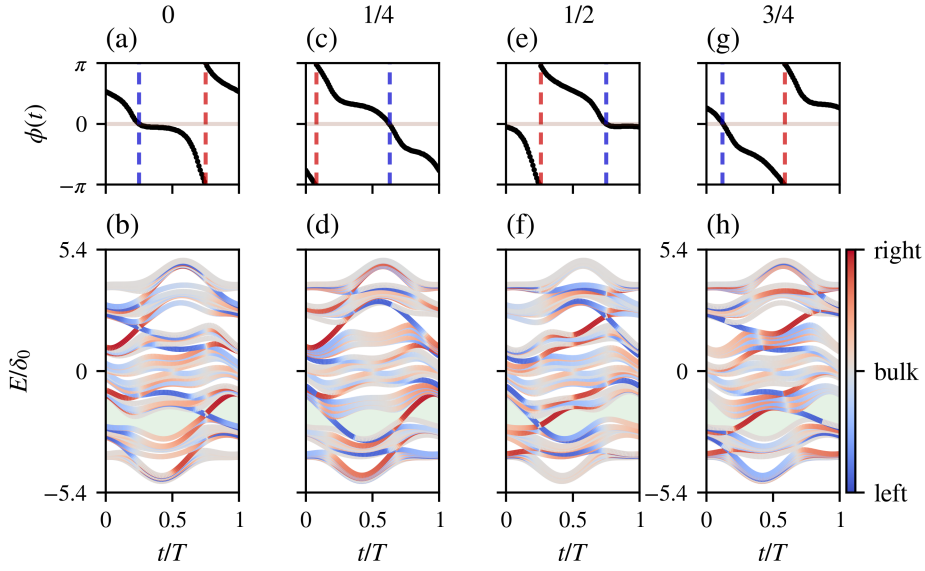

Figure 7.10: Berry Phase and level crossing for the Thue-Morse chain. The system size is $N = 32$.

where $\mathcal{M}_L = \mathbb{1} - G_L$ and $(G_L)_{ij} = \langle c_i^\dagger c_j \rangle$ is the correlation function restricted to subsystem L. Diagonalizing $G_L = M \mathrm{diag}(\lambda_1, \cdots, \lambda_n) M^{-1}$, we obtain

$$\rho_L = \exp\left[\sum_{n=1}^{|L|} \log(1-\lambda_n) + \sum_{n=1}^{|L|} \log\left(\frac{\lambda_n}{1-\lambda_n}\right) d_n^\dagger d_n \right],$$

where $d_n = \sum_j M_{nj} c_j$ and $|L|$ is the number of sites in subsystem L. By considering an occupation configuration of the $|L|$ fermionic eigenstates characterized by the eigenvalues of G_L, e.g. $|0,1,0,0,1,...,0\rangle$, we can generate an eigenvalue of the ES. There are $2^{|L|}$ such configurations, since each of them can be either occupied or not (this is also the number of eigenvalues in the ES). Let $n_\alpha = \{0,1,0,0,1,...,0\}$ be one such configuration. The corresponding ES eigenvalue is obtained through

$$\begin{aligned} \xi_\alpha = &- \sum_{j=1}^{|L|} \log(1-\lambda_j) \left[\frac{1+(-1)^{n_\alpha^{(j)}}}{2} \right] \\ &- \sum_{j=1}^{|L|} \log(\lambda_j) \left[\frac{1-(-1)^{n_\alpha^{(j)}}}{2} \right], \end{aligned} \tag{7.13}$$

where $n_\alpha^{(j)}$ is the occupation number (0 or 1) of the j^{th} eigenstate of G_L. In order to properly visualize the spectrum Fig. 7.7, we plot it against the particle number of the occupation configuration, n_α, i.e. $n = \sum_j n_\alpha^{(j)}$.

Conclusions and outlook

The overarching theme of this thesis has been to uncover hidden structures where none were expected, both in the realm of topological phases and aperiodic systems. The first part of the thesis is directly concerned with topological phases of matter. These have become a cornerstone of condensed-matter physics and have found applications in diverse fields, including mechanical and optical systems. Over the last two decades, their classification has undergone considerable updates, leading to the discovery of novel phases at each turn.

In Chapter 2, we found topological states that would not have been visible using conventional classification methods. Non-Hermitian chains with complicated unit-cell structures were shown to possess topological properties resulting from the concept of latent symmetry, which realizes an energy-dependent version of simpler topological models [1]. More specifically, we demonstrated that by applying the isospectral reduction, one could simplify a complicated system into one that resembles paradigmatic models, albeit with an energy dependence. This energy dependence, in turn, allows the prediction of topological modes and phase transitions using the knowledge about the reduced model. This method was not only applied to accessing topological features but also to predict other phenomena, such as the unusual bipolar non-Hermitian skin effect.

By using field-theoretical methods, we were also able to uncover structures that enabled a simpler understanding of the effect of disorder in non-Hermitian topological phase transitions and to understand the behavior of a one-dimensional Hermitian topological phase in the presence of fermionic *interactions* [2, 3]. In Chapter 3 we examined how disorder drives topological phase transitions in one-dimensional non-Hermitian systems. We derived expressions for the modification of the spectral winding number using perturbation theory for the disorder-averaged Green's function within the self-consistent Born approximation. These methods were applied to two specific examples: the non-Hermitian SSH model and a non-Hermitian s-wave superconductor.

In Chapter 4, we once again resorted to field theoretical methods to study the effect of interactions on a Hermitian SSH model. In this case, by turning the model into a low-energy Thirring field theory, we could use non-perturbative methods to derive exact results on how the polarization density response is modified. This allowed us to understand that interactions do not modify the qualitative features of the topological phases of the noninteracting system. Rather, there is a quantitative renormalization of the fermionic charge, with a term resulting from the one-dimensional system's non-Fermi liquid behavior.

The second part of the thesis details our findings on quasiperiodic systems and, more broadly, on aperiodic systems. Quasiperiodic systems are generated by a projection of a higher-dimensional periodic lattice into a lower-dimensional one. Curiously, the space orthogonal to the physical plane onto which the system is projected often unveils hidden structures. For instance, the eigenstates of the Fibonacci chain demonstrate a pronounced self-similar structure when visualized using conumbers, which represent the numbering of sites in the perpendicular direction. A similar phenomenon is observed in the Tribonacci chain, where the perpendicular space is associated with the Rauzy fractal.

In Chapter 5, we introduced the Fibonacci chain, a fundamental model for a one-dimensional quasiperiodic system, and its generalization to the Tribonacci chain. We demonstrated that both models exhibit multifractal and self-similar spectra and wavefunctions. We then investigated the effect of impurities on the Fibonacci chain and found that quasiperiodic ordering deteriorates in a predictable manner based on the impurity's position. This behavior becomes visually comprehensible through the use of the conumber representation. The behavior can be organized according to the renormalization paths of the sites where the impurity is located [4].

In the Tribonacci chain, the Rauzy fractal emerges as a hidden structure within the perpendicular space, organizing the physical space according to the local environments of the sites. This fractal not only serves as a visual tool to observe the self-similar structure of the wavefunctions but also bridges the concept of local resonators with the perpendicular space of a quasicrystal [5].

In Chapter 6, we examined the spectral properties of two coupled Fibonacci chains. By designing different coupling schemes, we observed that the total system's spectral properties exhibit vastly different behaviors. Notably, we discovered that the system can simultaneously host extended and critical eigenstates or exhibit compact-localized states, resulting in flat bands. Additionally, we found that (i) uniform coupling effectively results in decoupled Fibonacci chain behavior, (ii) single-site coupling leads to effectively decoupled Fibonacci chains with an additional impurity, which can be understood through the insights from Chapter 5, (iii) quasiperiodic coupling results in a different hierarchical structure, which, under the decimation procedure, reverts to the Fibonacci renormalization group flow after a few steps [6].

Finally, in aperiodic chains, we found that the structure at the degenerate point of the adiabatic pumping cycle can result in the emergence of an obstructed atomic-limit realization of the aperiodic insulators [7]. In Chapter 7, we explored how these chains can acquire inversion symmetry at a particular moment during the adiabatic pumping process. When this is the case, they exhibit features characteristic of these unconventional phases: two degenerate edge modes hosting half-charges at the ends of the chain, resulting in a nontrivial polarization response and a degenerate entanglement spectrum.

As an outlook, we believe that the framework of isospectral reductions is quite versatile and can be applied to many more toy models, potentially in higher dimensions, as long as one can design complicated unit cells with appropriate latent

symmetries. An example of work in this direction has already been published on arXiv by our group [8], and another one is currently being prepared [10].

For our work on non-Hermitian field theory, future directions include extending the methods to account for the effects of interactions. Additionally, studying disorder using the replica method might offer deeper insights into the topological aspects and resilience of boundary phenomena.

For Hermitian interacting SSH chains, a direct generalization to study the effects of different types of interactions, especially when including the spin degree of freedom, would be valuable. This approach would yield different effective low-energy models, some of which might not be integrable. Nevertheless, perturbative methods can always be used to derive the scaling exponents and calculate how the polarization in the continuum model might be affected.

On the aperiodic front, a promising direction for addressing the impurity problem might involve using an alternative description with local resonator modes. These modes are local structures that host similarly behaving eigenstates within a particular energy quasi-band. By placing an impurity on one of these local structures, we could predict the typical response and potentially gain additional insights into our analysis. Additionally, the study of coupled Fibonacci chains offers a compelling opportunity to explore the effects of strongly interacting electrons in a quasiperiodic setup, leveraging the existing flat bands.

Finally, a direct follow-up to our results on obstructed atomic limits in aperiodic systems would be to develop topologically robust configurations of these transient realizations. Additionally, there seems to be a relationship between the type of Fourier spectra and the feasibility of performing an adiabatic pumping cycle. For instance, for the Rudin-Shapiro chain, with its absolutely continuous Fourier spectrum, one cannot achieve adiabatic pumping using the same protocol as for other chains. These open questions remain unanswered, providing a clear direction for future research based on our findings.

Layman Summary

"*The scientist does not study nature because it is useful; he studies it because he delights in it, and he delights in it because it is beautiful.*" Henri Poincaré.

In their quest to uncover nature's inner workings, physicists aim to find order in a patchwork of complexity. Their ability to do this relies on the astonishing fact that behind all those complicated layers, one can often find simple fundamental rules underlying the natural ordering of phenomena. This is because, fortunately for physicists, nature is filled with regular patterns that are well-described by the language of mathematics. As physicists become more familiar with these rules, the mathematical tools they employ grow more complex, rendering everyday language and intuition insufficient for explaining increasingly abstract concepts. As a result, a layman often gets lost in translation when talking to physicists.

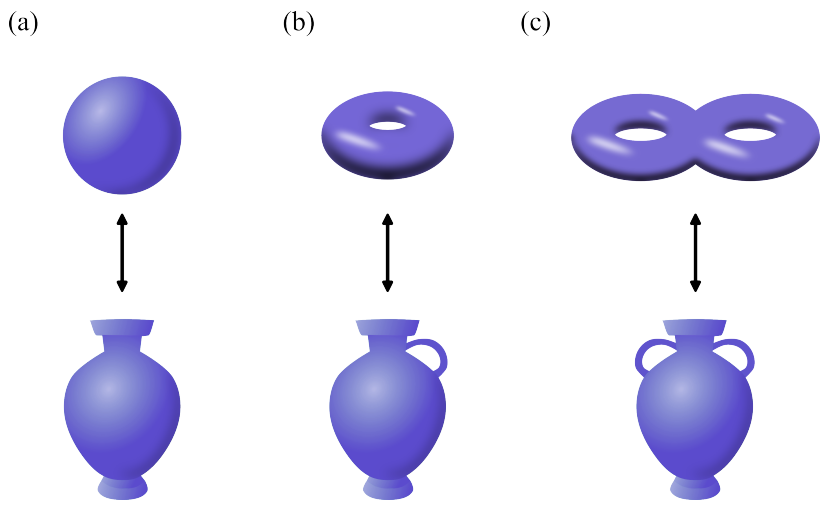

Figure 1: Equivalence between (a) a sphere and a handleless vase, (b) a torus and vase with one handle, and (c) a two-torus and a vase with two handles

This summary attempts to give a lay audience an overview of my research. The generic theme of this thesis is that of topological states. They find applications in many different branches of physics, ranging from fundamental particle physics

all the way to atmospheric physics. In mathematics, topology studies the global properties of abstract spaces. For instance, the number of holes a surface possesses, a concept mathematicians call the genus, is one such property that allows an understanding of the global structure of these surfaces. From this point of view, a sphere is equivalent to a vase without handles, a torus to a vase with one handle, and a two-torus to a vase with two handles, as sketched in Fig. 1. The genus of the space fully characterizes it under continuous deformations. This concept finds its importance in physics whenever a particular property of a system is resilient to changes in the system.

In 2016, the Nobel Prize in Physics was given for the theoretical elucidation of physical phenomena described by the mathematics of topology. Amongst the ramifications of such discoveries is the notable example of a topological insulator. This is a material that is an insulator in the bulk and a conductor on the boundary. More than just being a conductor on the boundary, it can carry a dissipationless current, meaning no energy is lost to heat in the surroundings. This could potentially offer a viable path towards more energy-efficient electronic devices, a fundamental pillar of modern society, which currently only offers between 20% and 50% efficiency.

A second example where topology plays a crucial role that could prove fruitful in a far-away technological future is with superconductors. For the last two decades, many promising realizations of quantum computing machines have seen the light of the day. However, these machines can only operate under extremely delicate conditions, making scalability difficult to achieve. If one can leverage systems with robust topological protection, scalability would be easier to access, as the system could then be perturbed by its surroundings without losing its crucial features.

This is where topological superconductors could offer a viable route towards scalable quantum computers. Superconductors are materials that carry dissipationless currents and expel magnetic fields away from their interior. They are already used in many industrial applications, such as MRI machines or levitating Maglev trains. When topological considerations are taken into account, an elusive emergent particle, called the Majorana particle, can appear in a network of vortices that exist within the superconductor. Manipulating these particles allows basic quantum operations to be performed, which could establish a pathway toward realizing a scalable quantum computer.

The last two examples are but a drop in a sea of phenomena for which the application of topology flourished. This is where the focus of this thesis lies. In the last two decades, much work has been done to classify these topological phases of matter using various mathematical tools. The earliest classification relied on the realization of three discrete symmetries – time-reversal, particle-hole, and chiral symmetries – and the system's dimensionality.

The first of these symmetries is exactly as its name suggests: the equations governing the system's behavior remain unchanged whether the system's evolution is described forward or backward in time. A simple example of this invariance can be found in Newton's second law of motion, $F = ma$, where the force F, equal to the product of the mass m and acceleration a, is unchanged under a reversal of time $t \to -t$. This occurs because acceleration is defined as the rate of change of velocity over time. Under time reversal, both velocity and its rate of change reverse signs, effectively canceling out the overall negative sign. The second symmetry concerns

the charges (e.g., electric charge) associated with the particles in the system. The invariance is now with respect to a transformation of a particle into its antiparticle, changing the signs of all charges. The concept of charge is somewhat more abstract; it represents the strength with which particles interact via a fundamental force (e.g., electric charge dictates how particles interact through the electromagnetic force). Finally, the last one is a combination of both previous symmetries.

Over the past two decades, this classification has undergone essential extensions. These updates occurred, for example, when additional symmetries—such as the spatial symmetries found in solid-state materials—were incorporated or when the mathematical constraints governing physical theories were relaxed. The latter adjustments are rooted in the necessity to simplify the equations used to describe complex systems, often by making assumptions about the nature of interactions to render the system more tractable. For instance, we often isolate the system under consideration, as if it is not interacting with anything from the outside. These assumptions are typically well justified and yield very accurate results. However,

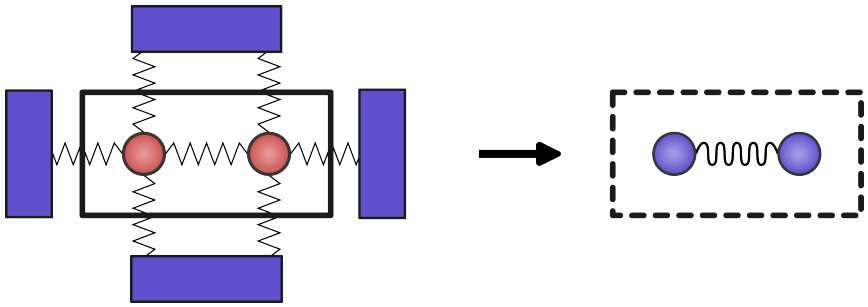

Figure 2: Abstract depiction of the decoupling process. The system, shown here by the larger rectangle with the red beads interconnected by jaggy springs, is decoupled from the surroundings, shown by the blue rectangles outside the system. The result is an effective system of two blue beads and a smoother spring.

interactions with the surroundings are sometimes quite important and cannot be omitted. One possible approximation that can be done under some circumstances is to incorporate these interactions into the system's variables in a new effective model, as sketched in Fig. 2. When one does this in the context of quantum mechanics, the result is generally called a non-Hermitian model.

Along this line of research, we aimed to contribute to this evolving field by finding topological phases that were not yet captured by the existing classifications. In Chapter 2, we used the concepts of latent symmetries and isospectral reductions to predict the existence of topological phases in otherwise complicated one-dimensional non-Hermitian systems. Typically, models that describe topological phases are realized on discrete lattices. This makes numerical computation more accessible and accurately describes most solid-state materials. These lattice points and their interconnections can be viewed as graphs. By leveraging tools from graph theory, a branch of mathematics, we found that another type of symmetry – latent symmetry, only appearing after performing a particular graph reduction scheme,

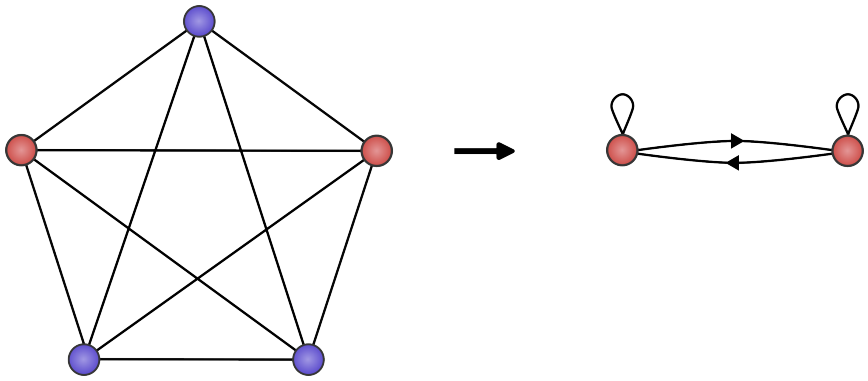

Figure 3: Depiction of the graph reduction technique used in Chapter 2. The original five-vertex connected graph, consisting of three blue and two red vertices and their associated connections, is simplified to a graph with just two red vertices and new connections. This transformation yields a more straightforward graph structure with two vertices, though it includes additional connections that may exhibit directionality and self-loops, where vertices are connected to themselves.

depicted in Fig. 3 – also permitted the existence of certain topological phases. We constructed a general framework that enabled its application to a family of systems that, upon using the graph reductions mentioned previously, are described by paradigmatic models. By then using the properties of those models, we predicted exactly when these topological phases arise, depending on the interplay between the fixed parameters of the system.

Topological phases can be subsumed to their robustness. To test this, we often calculate their resilience to random perturbations. This disorder is introduced everywhere in the system and is completely uncorrelated from one position to the next. In Chapter 3, we developed general tools to analyze one-dimensional non-Hermitian models at their topological phase transitions and used these tools to predict how disorder influences such transitions. The phase transition occurs at a specific point in the parameter space, where the model shifts from a topological to a non-topological phase. At this point, the statistical variables describing physical processes are correlated over very long distances, much larger than the typical lattice spacing. This allows us to approximate them by variables on a continuous space. The advantage of this approach is that it enables us to develop tools that do not rely on numerical calculations, but can be done with pen and paper. It allowed us to derive some exact formulae that tell us how the presence of disorder influences the topological invariant associated with the topological phases. We applied this generic framework to describe how these disorder-driven transitions occur in a one-dimensional topological insulator and a one-dimensional topological superconductor.

Most models that describe topological phenomena in systems consisting of electrons make a bold assumption. They assume that the electrons do not interact with each other but are only subject to the attractive electromagnetic force of the atoms that make up the underlying lattice. This assumption works surpris-

ingly well, forming the foundation for the entire semiconductor industry and the principles on which it operates. The reasons behind this have a deep theoretical understanding, which we shall not delve into. Electron-electron interactions are extremely difficult to describe in a multiparticle system, and since, most of the time, they are not needed to accurately describe the physics of a system, our understanding of topological phases in electronic systems with interactions remains limited. In Chapter 4, we examined the influence of these interactions on the topological phases of a one-dimensional topological insulator. To this end, we made some assumptions like those of the previous chapter that enabled us to describe the model in the continuum rather than on the lattice. This approach allowed us to access tools from quantum field theory, generally used to describe fundamental particle physics. It allowed us to understand that the mechanism driving topology is the same as that without interactions and that when the system is in its topological phase, the topological invariant is only modified to the extent that it takes into account a modification of the charge of the electron brought about by these interactions.

For the second part of the thesis, we turned our attention to aperiodic structures. Contrary to the random disorder described before, these structures feature what is sometimes called correlated disorder. They possess long-range correlations without periodicity, in contrast to the periodic lattices used as the basis for previous systems. While aperiodic structures might initially appear disordered or lacking structure, they possess a distinct form of organization, albeit less immediately apparent than periodic crystals. An example of such systems is quasicrystals, experimentally discovered in 1982 and for which the Nobel Prize in Chemistry in 2011 was awarded to Dan Shechtman. Up to that point, it was believed that the diffraction patterns obtained by shining X-rays on solid-state materials could only be explained if the long-range structure admitted periodicity. This was a defining feature of crystals. This belief was so strong that the results published by Dan Shechtman were publicly mocked, leading him to be completely isolated, even from his research group. However, over the following decades, the notion that quasiperiodic structures could exhibit similar features gained acceptance and mathematical support. A key result for quasicrystals is that they can be understood as projections of a higher-dimensional periodic crystal onto a lower-dimensional plane with a slope that is incommensurate with the periodicity of the higher-dimensional structure. For instance, one can obtain a one-dimensional quasicrystal by projecting a two-dimensional square lattice onto a line that never crosses the vertices of the lattice, as shown in Fig. 4.

Fast-forward to the recent decade, much ink has been spilled on the study of topology in the presence of quasiperiodicity. This has driven our curiosity to understand how these phases arise and how robust and structured quasiperiodicity is. In Chapter 5, we studied simple one-dimensional quasicrystals and their hidden fractal structures in a transverse dimension using the projection method described above. Through the lens of these hidden structures, it was possible to understand how impurities, embodying uncorrelated disorder, start to break the long-range quasicrystalline order. In Chapter 6, we extended the study done in the previous chapter by stacking these one-dimensional chains on top of each other in various ways. We discovered a wide variety of scenarios in which transport properties

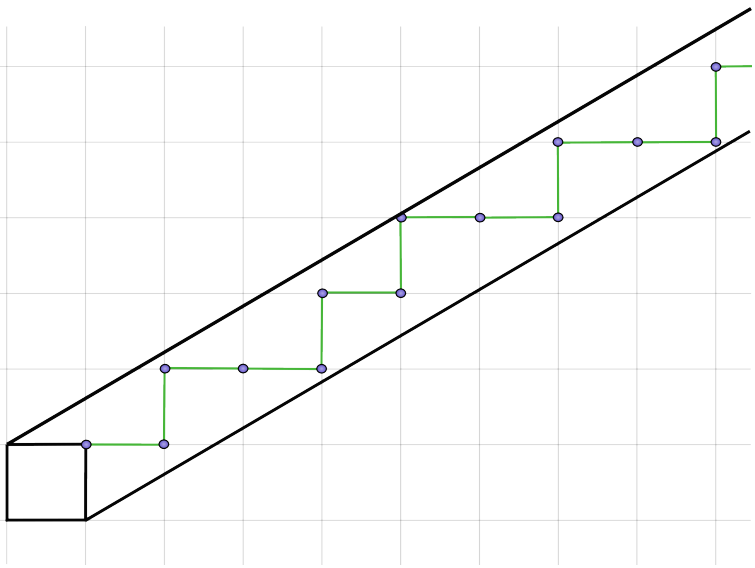

Figure 4: Example of a cut-and-project scheme to construct a one-dimensional quasicrystal from a two-dimensional regular crystal. The black square slides between two lines that never cross any vertex of the two-dimensional lattice. As it covers its track, all the vertices between the two black lines form a chain with edges oriented vertically (V) or horizontally (H). The sequence of orientations $HVHHVHVHH\cdots$, famously known as the Fibonacci sequence, will never repeat after the black square has covered a finite number of edges.

of crystalline and quasicrystalline systems could coexist. Finally, in Chapter 7, we returned to the notion of topology in aperiodic systems. We first showed that topological charge pumping—a phenomenon in which the current pumped in a one-dimensional system is quantized by a topological invariant—can occur in aperiodic systems beyond quasicrystals. While much of the research over the past decade has concentrated on this phenomenon in quasicrystals, our findings show that it is not exclusive to them, but can also be observed in other types of aperiodic systems. We then demonstrated the existence of topological boundary states in aperiodic systems, protected by inversion symmetry—a spatial symmetry where the system remains invariant under reflection through its midpoint.

To conclude this summary, the overarching theme of this thesis has been to uncover hidden structures where none were expected, both in the realm of topological phases and aperiodic systems. Most of our results form a good starting point for further research into the properties of topological phases across all these diverse platforms. Some of this work was already started within our group, but I did not include it in this thesis, while other directions will be pursued by colleagues who will carry on after my departure. The majority of this work was driven by simple and genuine curiosity. While most of it is very theoretical, it will hopefully be observed on experimental platforms and perhaps be helpful to other researchers

working with similar subjects.

Samenvatting

"*De wetenschapper bestudeert de natuur niet omdat het nuttig is te doen. Hij bestudeert het omdat hij er van geniet, en hij geniet ervan omdat het mooi is*", Henri Poincaré.

In hun zoektocht om de innerlijke werking van de natuur te onthullen, proberen natuurkundigen orde te vinden in een lappendeken van complexiteit. Hun vermogen om dit te doen berust op het opmerkelijke feit dat men achter al die ingewikkelde lagen vaak eenvoudige fundamentele regels kan vinden die ten grondslag liggen aan de natuurlijke ordening van verschijnselen. Dit komt doordat de natuur, gelukkig voor natuurkundigen, vol zit met regelmatige patronen die goed kunnen worden beschreven in de taal van de wiskunde. Naarmate natuurkundigen meer vertrouwd raken met deze regels, worden de wiskundige instrumenten die zij gebruiken steeds complexer, waardoor alledaagse taal en intuïtie ontoereikend worden om steeds abstractere concepten te verklaren. Hierdoor raakt een leek vaak de draad kwijt in het gesprek met natuurkundigen.

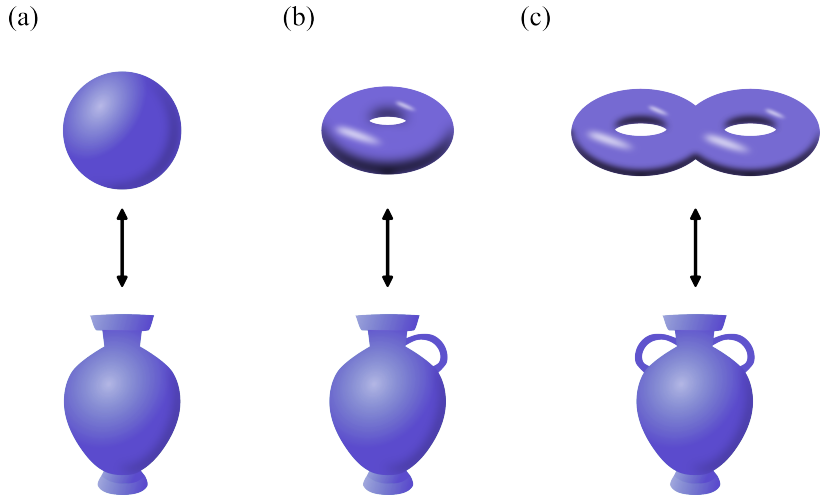

Figuur 1: Equivalentie tussen (a) een bol en een vaas zonder handvat, (b) een torus en een vaas met één handvat, en (c) een twee-torus en een vaas met twee handvatten.

Deze samenvatting probeert een lekenpubliek een overzicht te geven van mijn onderzoek. Het algemene thema van dit proefschrift is dat van topologische toestanden. Deze vinden toepassingen in verschillende takken van de natuurkunde, variërend van fundamentele deeltjesfysica tot atmosferische fysica. In de wiskunde bestudeert de topologie de globale eigenschappen van abstracte ruimten. Zo is het aantal gaten dat een oppervlak heeft—een concept dat wiskundigen het genus noemen—een eigenschap die inzicht geeft in de globale structuur van oppervlakken. Vanuit dit gezichtspunt is een bol gelijkwaardig aan een vaas zonder handvatten, een torus aan een vaas met één handvat, en een twee-torus aan een vaas met twee handvatten, zoals geschetst in Fig. 1. Het genus van de ruimte karakteriseert deze volledig onder continue vervormingen. Dit concept is van belang in de natuurkunde telkens wanneer een bepaalde eigenschap van een systeem bestand is tegen veranderingen in dat systeem.

In 2016 werd de Nobelprijs voor de Natuurkunde toegekend voor de theoretische opheldering van fysische fenomenen die worden beschreven door de wiskunde van de topologie. Een van de gevolgen van dergelijke ontdekkingen is het opmerkelijke voorbeeld van een topologische isolator. Dit is een materiaal dat isolerend is in de bulk, maar geleidend aan de rand. Meer dan alleen een geleider aan de rand, kan het een stroom zonder dissipatie dragen, wat betekent dat er geen energie verloren gaat als warmte in de omgeving. Dit zou een haalbare weg kunnen bieden naar energiezuinigere elektronische apparaten, een fundamentele pijler van de moderne samenleving, die momenteel slechts een efficiëntie van tussen de 20% en 50% bereikt.

Een tweede voorbeeld waarbij topologie een cruciale rol speelt en dat in een verre technologische toekomst veelbelovend zou kunnen zijn, is bij supergeleiders. De afgelopen twee decennia zijn er veelbelovende realisaties van kwantumcomputers tot stand gekomen. Deze machines kunnen echter alleen functioneren onder uiterst delicate omstandigheden, wat schaalbaarheid moeilijk te realiseren maakt. Als men systemen met robuuste topologische bescherming kan benutten, zou schaalbaarheid gemakkelijker toegankelijk worden, aangezien het systeem dan door zijn omgeving verstoord kan worden zonder zijn essentiële eigenschappen te verliezen.

Hier kunnen topologische supergeleiders een haalbare route bieden naar schaalbare kwantumcomputers. Supergeleiders zijn materialen die stromen zonder dissipatie geleiden en magnetische velden uit hun inwendige verdrijven. Ze worden al in veel industriële toepassingen gebruikt, zoals MRI-scanners en zwevende Maglevtreinen. Wanneer topologische aspecten in aanmerking worden genomen, kan een ongrijpbaar, emergent deeltje, het Majorana-deeltje, verschijnen binnen een netwerk van wervels in de supergeleider. Door deze deeltjes te manipuleren, kunnen basale kwantumbewerkingen worden uitgevoerd, wat een weg kan openen naar de realisatie van een schaalbare kwantumcomputer.

De laatste twee voorbeelden zijn slechts een druppel in een zee van fenomenen waarvoor de toepassing van topologie tot bloei is gekomen. Hier ligt de focus van dit proefschrift. In de afgelopen twee decennia is er veel werk verricht om deze topologische fasen van materie te classificeren met behulp van verschillende wiskundige hulpmiddelen. De vroegste classificatie was gebaseerd op het herkennen van drie discrete symmetrieën — tijdsomkering, deeltje-gat, en chirale symmetrieën — en de dimensionaliteit van het systeem.

De eerste van deze symmetrieën is precies wat de naam suggereert: de vergelijkingen die het gedrag van het systeem beschrijven, blijven onveranderd of de evolutie van het systeem nu voorwaarts of achterwaarts in de tijd wordt beschreven. Een eenvoudig voorbeeld van deze invariantie is te vinden in de tweede wet van Newton, $F = ma$, waarin de kracht F, gelijk aan het product van de massa m en de versnelling a, onveranderd blijft onder tijdsomkering $t \to -t$. Dit komt doordat versnelling gedefinieerd is als de snelheid waarmee de snelheid verandert in de tijd. Bij tijdsomkering veranderen zowel de snelheid als de mate van verandering van teken, waardoor het negatieve teken in totaal effectief wordt opgeheven. De tweede symmetrie betreft de ladingen (bijvoorbeeld elektrische lading) die zijn verbonden aan de deeltjes in het systeem. De invariantie betreft hier een transformatie van een deeltje in zijn antideeltje, waarbij de tekens van alle ladingen worden omgekeerd. Het concept van lading is enigszins abstracter; het vertegenwoordigt de sterkte waarmee deeltjes via een fundamentele kracht interacteren (bijvoorbeeld, elektrische lading bepaalt hoe deeltjes via de elektromagnetische kracht interacteren). Tot slot is de laatste symmetrie een combinatie van beide voorgaande symmetrieën.

In de afgelopen twee decennia heeft deze classificatie essentiële uitbreidingen ondergaan. Deze updates vonden plaats wanneer bijvoorbeeld aanvullende symmetrieën—zoals de ruimtelijke symmetrieën in vaste stoffen—werden opgenomen of wanneer de wiskundige beperkingen die fysische theorieën beheersen, werden versoepeld. De laatste aanpassingen zijn geworteld in de noodzaak om de vergelijkingen die complexe systemen beschrijven, te vereenvoudigen, vaak door aannames te maken over de aard van interacties om het systeem beter hanteerbaar te maken. Zo isoleren we bijvoorbeeld vaak het systeem dat we onderzoeken, alsof het geen interactie heeft met iets van buitenaf. Deze aannames zijn doorgaans goed gerechtvaardigd en leveren zeer nauwkeurige resultaten op. Interactie met de omgeving

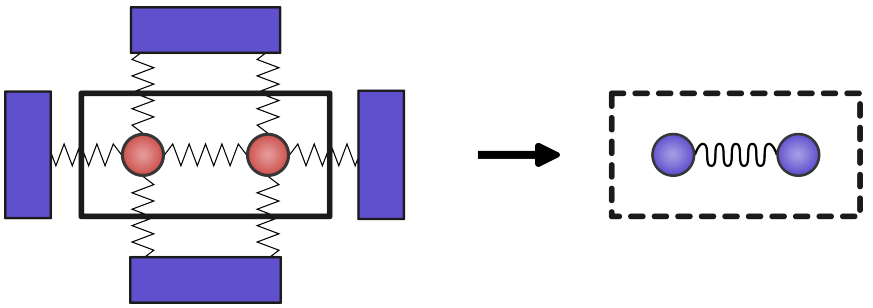

Figuur 2: Abstracte weergave van het ontkoppelingsproces. Het systeem, weergegeven door de grotere rechthoek met rode kralen die onderling verbonden zijn door gekartelde veren, wordt losgekoppeld van de omgeving, weergegeven door de blauwe rechthoeken buiten het systeem. Het resultaat is een effectief systeem van twee blauwe kralen en een veer met meer rondingen.

is echter soms erg belangrijk en kan niet worden weggelaten. Een mogelijke benadering die in sommige gevallen kan worden toegepast, is om deze interacties op te nemen in de variabelen van het systeem in een nieuw effectief model, zoals

geschetst in Fig. 2. Wanneer dit wordt gedaan in de context van de kwantummechanica, wordt het resultaat over het algemeen een niet-Hermitisch model genoemd.

In lijn met dit onderzoekspad streefden we ernaar bij te dragen aan dit zich ontwikkelende vakgebied door topologische fasen te vinden die nog niet door de bestaande classificaties waren vastgelegd. In Hoofdstuk 2 gebruikten we de con-

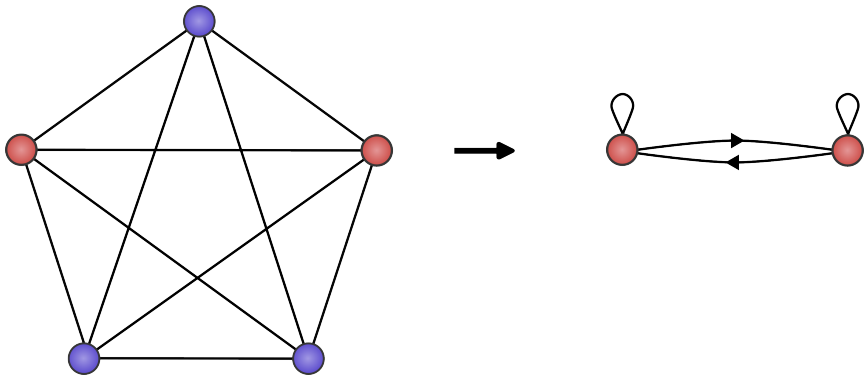

Figuur 3: Weergave van de graafreductietechniek die is gebruikt in Hoofdstuk 2. De oorspronkelijke graaf met vijf verbonden knooppunten, bestaande uit drie blauwe en twee rode knooppunten en hun bijbehorende verbindingen, wordt vereenvoudigd tot een graaf met slechts twee rode knooppunten en nieuwe verbindingen. Deze transformatie resulteert in een vereenvoudigde graafstructuur met twee knooppunten, hoewel er extra verbindingen zijn die richting kunnen vertonen en zelf-lussen kunnen bevatten, waarbij knooppunten met zichzelf verbonden zijn.

cepten van latente symmetrieën en isospectrale reducties om het bestaan van topologische fasen te voorspellen in anderszins ingewikkelde eendimensionale niet-Hermitische systemen. Modellen die topologische fasen beschrijven, worden doorgaans gerealiseerd op discrete roosters. Dit maakt numerieke berekeningen toegankelijker en beschrijft de meeste vaste-stofmaterialen nauwkeurig. Deze roosterpunten en hun onderlinge verbindingen kunnen worden opgevat als grafen. Door gebruik te maken van grafentheorie, een tak van de wiskunde, ontdekten we dat een ander type symmetrie—latente symmetrie, die alleen verschijnt na het uitvoeren van een specifieke graafreductietechniek, weergegeven in Fig. 3—ook het bestaan van bepaalde topologische fasen toestaat. We hebben een algemeen kader geconstrueerd dat de toepassing hiervan mogelijk maakt op een familie van systemen die, na toepassing van de eerder genoemde graafreducties, worden beschreven door paradigmatische modellen. Door vervolgens de eigenschappen van die modellen te gebruiken, voorspelden we precies wanneer deze topologische fasen ontstaan, afhankelijk van het samenspel tussen de vaste parameters van het systeem.

Topologische fasen kunnen worden samengevat door hun robuustheid. Om dit te testen, berekenen we vaak hun veerkracht tegen willekeurige verstoringen. Deze wanorde wordt overal in het systeem geïntroduceerd en is volledig ongecorreleerd van de ene positie naar de andere. In Hoofdstuk 3 hebben we algemene hulpmiddelen ontwikkeld om eendimensionale niet-Hermitische modellen bij hun topologische

faseovergangen te analyseren en gebruikten we deze tools om te voorspellen hoe wanorde dergelijke overgangen beïnvloedt. De faseovergang vindt plaats op een specifiek punt in de parameterruimte, waar het model verschuift van een topologische naar een niet-topologische fase. Op dit punt zijn de statistische variabelen die fysische processen beschrijven over zeer lange afstanden gecorreleerd, veel groter dan de typische roosterafstand. Dit stelt ons in staat deze variabelen te benaderen als continuümvariabelen. Het voordeel van deze benadering is dat we hierdoor tools kunnen ontwikkelen die niet afhankelijk zijn van numerieke berekeningen, maar met pen en papier kunnen worden uitgevoerd. Dit stond ons toe enkele exacte formules af te leiden die aangeven hoe de aanwezigheid van wanorde de topologische invariant beïnvloedt. We hebben dit generieke kader toegepast om te beschrijven hoe deze door wanorde aangedreven overgangen plaatsvinden in een eendimensionale topologische isolator en een eendimensionale topologische supergeleider.

De meeste modellen die topologische fenomenen in systemen van elektronen beschrijven, maken een gedurfde aanname. Ze gaan ervan uit dat de elektronen niet met elkaar interacteren, maar alleen onderhevig zijn aan de aantrekkende elektromagnetische kracht van de atomen die het onderliggende rooster vormen. Deze aanname werkt verrassend goed en vormt de basis voor de gehele halfgeleiderindustrie en de principes waarop deze berust. De achterliggende redenen zijn diep theoretisch verankerd, maar daar zullen we hier niet verder op ingaan. Interactie tussen elektronen is buitengewoon moeilijk te beschrijven in een systeem met meerdere deeltjes. Aangezien deze interacties meestal niet nodig zijn om de fysica van een systeem nauwkeurig te beschrijven, blijft ons begrip van topologische fasen in elektronische systemen met interacties beperkt. In Hoofdstuk 4 onderzochten we de invloed van deze interacties op de topologische fasen van een eendimensionale topologische isolator. Om dit te bereiken, maakten we enkele aannames, zoals die in het vorige hoofdstuk, waardoor we het model in het continuüm konden beschrijven in plaats van op het rooster. Deze aanpak stelde ons in staat gebruik te maken van tools uit de kwantumveldentheorie, die doorgaans worden gebruikt om fundamentele deeltjesfysica te beschrijven. Hiermee konden we begrijpen dat het mechanisme dat de topologie aandrijft hetzelfde blijft zonder interacties, en dat in de topologische fase van het systeem de topologische invariant alleen wordt aangepast om rekening te houden met een wijziging in de lading van het elektron die door deze interacties wordt veroorzaakt.

In het tweede deel van dit proefschrift richtten we onze aandacht op aperiodieke structuren. In tegenstelling tot de willekeurige wanorde die eerder werd beschreven, bevatten deze structuren wat soms gecorreleerde wanorde wordt genoemd. Ze hebben langeafstands-correlaties zonder periodiciteit, in tegenstelling tot de periodieke roosters die als basis voor de eerdere systemen werden gebruikt. Hoewel aperiodieke structuren op het eerste gezicht ongeordend of zonder structuur lijken, bezitten ze een specifieke vorm van organisatie, zij het minder onmiddellijk zichtbaar dan bij periodieke kristallen. Een voorbeeld van zulke systemen zijn quasikristallen, experimenteel ontdekt in 1982 en waarvoor de Nobelprijs voor de Chemie in 2011 werd toegekend aan Dan Shechtman. Tot dat moment werd aangenomen dat de diffractiepatronen die ontstaan bij bestraling van vaste stoffen met röntgenstralen alleen verklaard konden worden als de langeafstandsstructuur periodiciteit toeliet—een kenmerkend aspect van kristallen. Dit geloof was zo sterk

dat de resultaten van Dan Shechtman publiekelijk werden bespot, wat ertoe leidde dat hij volledig geïsoleerd raakte, zelfs van zijn eigen onderzoeksgroep. Echter, in de daaropvolgende decennia werd het idee dat quasiperiodieke structuren vergelijkbare eigenschappen kunnen vertonen, geaccepteerd en wiskundig onderbouwd. Een belangrijk resultaat voor quasikristallen is dat ze kunnen worden begrepen als projecties van een hoger-dimensionaal periodiek kristal op een lager-dimensionaal vlak met een helling die incommensurabel is met de periodiciteit van de hoger-dimensionale structuur. Zo kan men bijvoorbeeld een eendimensionaal quasikristal verkrijgen door een tweedimensionaal vierkant rooster te projecteren op een lijn die nooit de knooppunten van het rooster kruist, zoals weergegeven in Fig. 4.

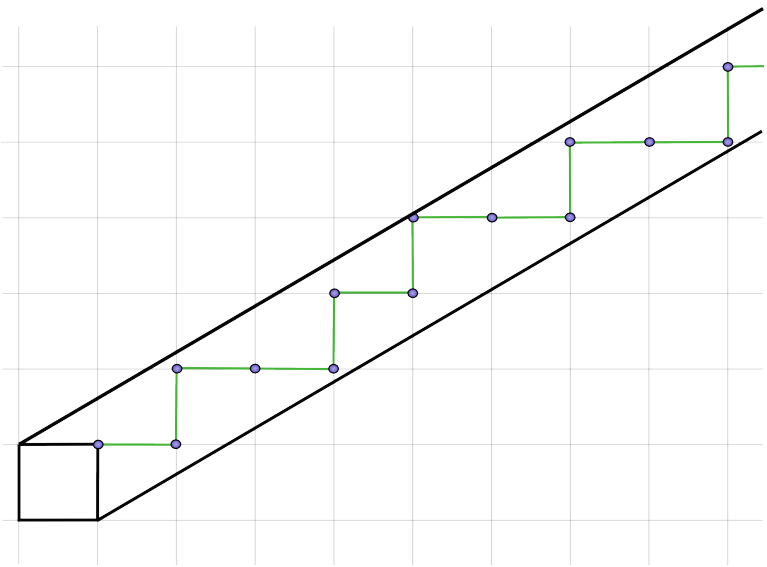

Figuur 4: Voorbeeld van een snij-en-projectieschema om een eendimensionaal quasikristal te construeren uit een tweedimensionaal regulier kristal. Het zwarte vierkant schuift tussen twee lijnen die nooit een knooppunt van het tweedimensionale rooster kruisen. Terwijl het vierkant zijn pad aflegt, vormen alle knooppunten tussen de twee zwarte lijnen een keten met randen die verticaal (V) of horizontaal (H) georiënteerd zijn. De reeks van oriëntaties $HVHHVHVHH\cdots$, bekend als de beroemde Fibonacci-reeks, zal zich nooit herhalen nadat het zwarte vierkant een eindig aantal lijnen heeft bedekt.

In het afgelopen decennium is veel onderzoek gedaan naar de rol van topologie in de aanwezigheid van quasiperiodiciteit. Dit heeft onze nieuwsgierigheid aangewakkerd om te begrijpen hoe deze fasen ontstaan en hoe robuust en gestructureerd quasiperiodiciteit is. In Hoofdstuk 5 onderzochten we eenvoudige eendimensionale quasikristallen en hun verborgen fractale structuren in een transversale dimensie, gebruikmakend van de eerder beschreven projectiemethode. Door deze verborgen structuren konden we begrijpen hoe onzuiverheden, die ongecorreleerde wanorde vertegenwoordigen, beginnen de langeafstands quasikristallijne orde te verstoren. In Hoofdstuk 6 breidden we het onderzoek uit door deze eendimensionale ketens

op verschillende manieren op elkaar te stapelen. Dit leidde tot de ontdekking van een breed scala aan scenario's waarin de transporteigenschappen van kristallijne en quasikristallijne systemen konden samengaan. Ten slotte keerden we in Hoofdstuk 7 terug naar het begrip topologie in aperiodieke systemen. We toonden eerst aan dat topologische ladingspompen—een fenomeen waarbij de stroom in een eendimensionaal systeem wordt gekwantiseerd door een topologische invariant—kunnen optreden in aperiodieke systemen die verder reiken dan alleen quasikristallen. Hoewel veel onderzoek van het afgelopen decennium zich op dit fenomeen in quasikristallen heeft geconcentreerd, laten onze bevindingen zien dat het niet exclusief voor hen is, maar ook in andere soorten aperiodieke systemen kan worden waargenomen. We hebben vervolgens het bestaan van topologische randtoestanden in aperiodieke systemen aangetoond, beschermd door inversiesymmetrie—een ruimtelijke symmetrie waarbij het systeem invariant blijft onder reflectie door zijn middelpunt.

Samenvattend, het overkoepelende thema van dit proefschrift was het blootleggen van verborgen structuren waar die aanvankelijk niet verwacht werden, zowel binnen het domein van topologische fasen als in aperiodieke systemen. De meeste van onze resultaten vormen een goed uitgangspunt voor verder onderzoek naar de eigenschappen van topologische fasen in deze diverse contexten. Een deel van dit werk is al binnen onze onderzoeksgroep voortgezet, maar ik heb dit niet in dit proefschrift opgenomen. Andere richtingen zullen worden opgepakt door collega's die dit onderzoek na mijn vertrek zullen voortzetten. Het merendeel van dit werk werd gedreven door eenvoudige en oprechte nieuwsgierigheid. Hoewel het grotendeels theoretisch van aard is, zal het hopelijk op experimentele platforms waargenomen worden en nuttig blijken voor andere onderzoekers die zich met soortgelijke onderwerpen bezighouden.

Resumé

"*Le savant n'étudie pas la nature parce que cela est utile ; il l'étudie parce qu'il y prend plaisir et il y prend plaisir parce qu'elle est belle.*", Henri Poincaré.

Dans leur quête pour dévoiler les rouages intimes de la nature, les physiciens cherchent à trouver de l'ordre dans un assemblage complexe. Leur capacité à le faire repose sur le fait surprenant que, derrière toutes ces couches compliquées, on trouve souvent des règles fondamentales simples qui sous-tendent l'ordre naturel des phénomènes. Cela s'explique par le fait que, heureusement pour les physiciens, la nature regorge de motifs réguliers, bien décrits par le langage des mathématiques. Au fur et à mesure que les physiciens se familiarisent avec ces règles, les outils mathématiques qu'ils utilisent deviennent de plus en plus complexes, rendant le langage courant et l'intuition insuffisants pour expliquer des concepts de plus en plus abstraits. Par conséquent, un profane se perd souvent dans la traduction lorsqu'il parle avec des physiciens.

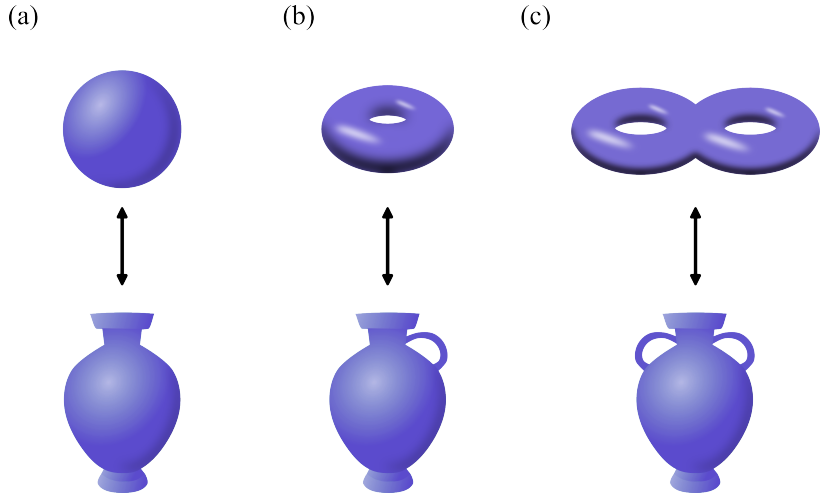

Figure 1: Équivalence entre (a) une sphère et un vase sans anse, (b) un tore et un vase avec une anse, et (c) un deux-tores et un vase avec deux anses.

Ce résumé vise à donner au grand public un aperçu de mes recherches. Le thème général de cette thèse est celui des états topologiques. Ceux-ci trouvent des applications dans de nombreux domaines de la physique, allant de la physique des particules fondamentales à la physique atmosphérique. En mathématiques, la topologie étudie les propriétés globales des espaces abstraits. Par exemple, le nombre de trous qu'une surface possède, un concept que les mathématiciens appellent le genre, est une propriété qui permet de comprendre la structure globale de ces surfaces. De ce point de vue, une sphère est équivalente à un vase sans anses, un tore à un vase avec une anse, et un deux-tores à un vase avec deux anses, comme illustré dans Fig. 1. Le genre de l'espace le caractérise entièrement sous des déformations continues. Ce concept est essentiel en physique dès lors qu'une propriété particulière d'un système résiste aux changements au sein de celui-ci.

En 2016, le prix Nobel de physique a été décerné pour l'élucidation théorique de phénomènes physiques décrits par les mathématiques de la topologie. Parmi les conséquences de telles découvertes, on trouve l'exemple notable de l'isolant topologique. Il s'agit d'un matériau qui est isolant dans son volume, mais conducteur à sa frontière. En plus d'être conducteur à la frontière, il peut transporter un courant sans dissipation, ce qui signifie qu'aucune énergie n'est perdue sous forme de chaleur dans l'environnement. Cela pourrait potentiellement offrir une voie prometteuse vers des dispositifs électroniques plus économes en énergie, un pilier fondamental de la société moderne, qui n'atteint actuellement qu'une efficacité de 20% à 50%.

Un deuxième exemple où la topologie joue un rôle crucial et qui pourrait s'avérer prometteur dans un futur technologique lointain est celui des supraconducteurs. Au cours des deux dernières décennies, de nombreuses réalisations prometteuses de machines de calcul quantique ont vu le jour. Cependant, ces machines ne peuvent fonctionner que dans des conditions extrêmement délicates, rendant leur mise à l'échelle difficile. Si l'on peut exploiter des systèmes dotés d'une protection topologique robuste, la mise à l'échelle deviendrait plus accessible, car le système pourrait alors être perturbé par son environnement sans perdre ses caractéristiques essentielles.

C'est dans ce contexte que les supraconducteurs topologiques pourraient offrir une voie viable vers des ordinateurs quantiques évolutifs. Les supraconducteurs sont des matériaux qui transportent des courants sans dissipation et expulsent les champs magnétiques de leur intérieur. Ils sont déjà utilisés dans de nombreuses applications industrielles, telles que les machines IRM ou les trains à lévitation magnétique (Maglev). Lorsqu'on tient compte des considérations topologiques, une particule émergente insaisissable, appelée particule de Majorana, peut apparaître dans un réseau de vortex présents dans le supraconducteur. La manipulation de ces particules permet d'effectuer des opérations quantiques de base, ce qui pourrait ouvrir la voie à la réalisation d'un ordinateur quantique évolutif.

Les deux derniers exemples ne sont qu'une goutte d'eau dans une mer de phénomènes pour lesquels l'application de la topologie a prospéré. C'est là que se concentre mon travail de thèse. Au cours des deux dernières décennies, de nombreux travaux ont été réalisés pour classifier ces phases topologiques de la matière à l'aide de divers outils mathématiques. La première classification reposait sur la reconnaissance de trois symétries discrètes — la symétrie d'inversion temporelle, la symétrie particule-trou et la symétrie chirale — ainsi que sur la dimensionnalité

du système.

La première de ces symétries est exactement ce que son nom suggère : les équations qui gouvernent le comportement du système restent inchangées, que l'évolution du système soit décrite vers l'avant ou vers l'arrière dans le temps. Un exemple simple de cette invariance se trouve dans la seconde loi de Newton, $F = ma$, où la force F, égale au produit de la masse m et de l'accélération a, reste inchangée sous une inversion du temps $t \to -t$. Cela s'explique par le fait que l'accélération est définie comme le taux de variation de la vitesse dans le temps. Sous une inversion temporelle, la vitesse et son taux de variation changent de signe, annulant ainsi le signe négatif global. La deuxième symétrie concerne les charges (par exemple, la charge électrique) associées aux particules du système. L'invariance s'applique ici à une transformation d'une particule en son antiparticule, ce qui inverse le signe de toutes les charges. Le concept de charge est un peu plus abstrait ; il représente l'intensité avec laquelle les particules interagissent via une force fondamentale (par exemple, la charge électrique détermine comment les particules interagissent par le biais de la force électromagnétique). Enfin, la dernière symétrie est une combinaison des deux symétries précédentes.

Au cours des deux dernières décennies, cette classification a connu d'importantes extensions. Ces mises à jour sont survenues, par exemple, lorsqu'on a intégré des symétries supplémentaires — telles que les symétries spatiales présentes dans les matériaux solides — ou lorsque les contraintes mathématiques régissant les théories physiques ont été assouplies. Ces dernières adaptations découlent de la nécessité de simplifier les équations utilisées pour décrire des systèmes complexes, souvent en formulant des hypothèses sur la nature des interactions afin de rendre le système plus maniable. Par exemple, on isole fréquemment le système étudié, comme s'il n'interagissait avec rien à l'extérieur. Ces hypothèses sont généralement bien justifiées et produisent des résultats très précis.

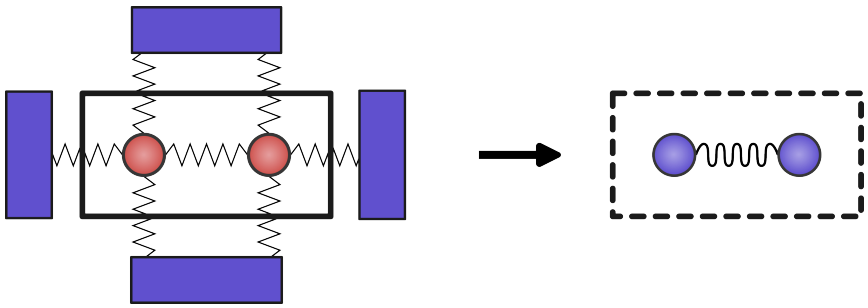

Figure 2: Représentation abstraite du processus de découplage. Le système, illustré ici par le grand rectangle avec des perles rouges interconnectées par des ressorts en zigzag, est découplé de son environnement, représenté par les rectangles bleus à l'extérieur du système. Le résultat est un système effectif composé de deux perles bleues et d'un ressort plus lisse.

Cependant, les interactions avec l'environnement sont parfois très importantes et ne peuvent pas être ignorées. Une approximation possible, dans certaines circonstances, consiste à intégrer ces interactions dans les variables du système dans

un nouveau modèle effectif, comme illustré dans Fig. 2. Lorsqu'on applique cette approche dans le contexte de la mécanique quantique, le résultat est généralement appelé un modèle non-Hermitien.

Dans cette ligne de recherche, nous avons cherché à contribuer à ce domaine en pleine évolution en identifiant des phases topologiques qui n'étaient pas encore incluses dans les classifications existantes. Dans le Chapitre 2, nous avons util-

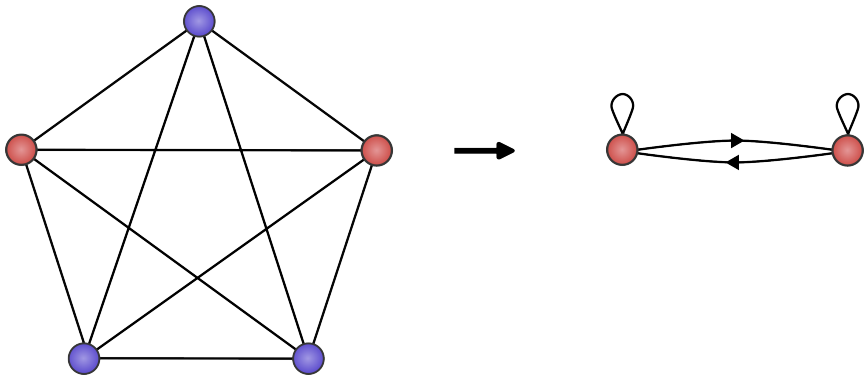

Figure 3: Représentation de la technique de réduction de graphe utilisée dans le Chapitre 2. Le graphe initial, composé de cinq sommets connectés—trois bleus et deux rouges—et de leurs connexions associées, est simplifié en un graphe ne comportant que deux sommets rouges et de nouvelles connexions. Cette transformation produit une structure de graphe plus simple avec deux sommets, bien qu'elle inclut des connexions supplémentaires qui peuvent présenter une directionnalité et des boucles, où des sommets sont connectés à eux-mêmes.

isé les concepts de symétries latentes et de réductions isospectrales pour prédire l'existence de phases topologiques dans des systèmes non-Hermitiens unidimensionnels autrement complexes. Les modèles décrivant les phases topologiques sont généralement réalisés sur des réseaux discrets. Cela rend les calculs numériques plus accessibles et permet de décrire avec précision la plupart des matériaux solides. Ces points de réseau et leurs interconnexions peuvent être vus comme des graphes. En utilisant des outils de la théorie des graphes, une branche des mathématiques, nous avons découvert qu'un autre type de symétrie — la symétrie latente, qui n'apparaît qu'après avoir effectué une certaine réduction de graphe, illustrée dans Fig. 3 — permet également l'existence de certaines phases topologiques. Nous avons construit un cadre général qui permet son application à une famille de systèmes qui, en utilisant les réductions de graphe mentionnées, sont décrits par des modèles paradigmatiques. En exploitant ensuite les propriétés de ces modèles, nous avons prédit précisément quand ces phases topologiques apparaissent, en fonction de l'interaction entre les paramètres fixes du système.

Les phases topologiques peuvent être caractérisées par leur robustesse. Pour tester cela, nous calculons souvent leur résilience face à des perturbations aléatoires. Ce désordre est introduit partout dans le système et est complètement non corrélé d'une position à l'autre. Dans le Chapitre 3, nous avons développé des outils généraux pour analyser des modèles non-Hermitiens unidimensionnels lors de leurs

transitions de phase topologiques et avons utilisé ces outils pour prédire comment le désordre influence ces transitions. La transition de phase se produit en un point spécifique de l'espace des paramètres, où le modèle passe d'une phase topologique à une phase non topologique. À ce stade, les variables statistiques décrivant les processus physiques sont corrélées sur de très longues distances, bien plus grandes que l'espacement typique des réseaux. Cela nous permet de les approximer par des variables dans un espace continu. L'avantage de cette approche est qu'elle nous permet de développer des outils qui ne dépendent pas de calculs numériques, mais peuvent être réalisés sur papier. Elle nous a permis de dériver des formules exactes qui indiquent comment la présence de désordre influence l'invariant topologique associé aux phases topologiques. Nous avons appliqué ce cadre générique pour décrire comment ces transitions induites par le désordre se produisent dans un isolant topologique unidimensionnel et un supraconducteur topologique unidimensionnel.

La plupart des modèles décrivant les phénomènes topologiques dans des systèmes constitués d'électrons font une hypothèse audacieuse. Ils supposent que les électrons n'interagissent pas entre eux, mais sont uniquement soumis à la force électromagnétique attractive des atomes qui composent le réseau sous-jacent. Cette hypothèse fonctionne étonnamment bien et constitue la base de l'ensemble de l'industrie des semi-conducteurs et des principes sur lesquels elle repose. Les raisons de cette validité reposent sur une compréhension théorique profonde, que nous n'aborderons pas ici. Les interactions entre électrons sont extrêmement difficiles à décrire dans un système à plusieurs particules, et comme, la plupart du temps, elles ne sont pas nécessaires pour décrire avec précision la physique d'un système, notre compréhension des phases topologiques dans les systèmes électroniques avec interactions reste limitée. Dans le Chapitre 4, nous avons examiné l'influence de ces interactions sur les phases topologiques d'un isolant topologique unidimensionnel. À cette fin, nous avons fait des hypothèses similaires à celles du chapitre précédent, ce qui nous a permis de décrire le modèle dans le continuum plutôt que sur le réseau. Cette approche nous a permis d'accéder à des outils de la théorie quantique des champs, généralement utilisés pour décrire la physique des particules fondamentales. Elle nous a permis de comprendre que le mécanisme sous-jacent à la topologie reste le même, même en présence d'interactions. Lorsque le système est dans sa phase topologique, l'invariant topologique est uniquement modifié pour tenir compte d'une modification de la charge de l'électron induite par ces interactions.

Dans la deuxième partie de cette thèse, nous avons concentré notre attention sur les structures apériodiques. Contrairement au désordre aléatoire décrit précédemment, ces structures présentent ce que l'on appelle parfois un désordre corrélé. Elles possèdent des corrélations à longue portée sans périodicité, contrairement aux réseaux périodiques utilisés comme base pour les systèmes précédents. Bien que les structures apériodiques puissent initialement sembler désordonnées ou dépourvues de structure, elles possèdent une forme d'organisation distincte, bien que moins évidente que celle des cristaux périodiques. Un exemple de tels systèmes est celui des quasi-cristaux, découverts expérimentalement en 1982, et pour lesquels le prix Nobel de chimie a été décerné à Dan Shechtman en 2011. Jusqu'alors, on croyait que les motifs de diffraction obtenus en exposant les matériaux solides à des rayons

X ne pouvaient être expliqués que si la structure à longue portée était périodique, un critère définissant les cristaux. Cette croyance était si forte que les résultats publiés par Dan Shechtman furent publiquement moqués, le conduisant à un isolement complet, y compris au sein de son propre groupe de recherche. Cependant, au cours des décennies suivantes, l'idée que des structures quasi-périodiques pouvaient présenter des caractéristiques similaires a été acceptée et soutenue mathématiquement. Un résultat clé pour les quasi-cristaux est qu'ils peuvent être compris comme des projections d'un cristal périodique de dimension supérieure sur un plan de dimension inférieure, avec une pente incommensurable par rapport à la périodicité de la structure de dimension supérieure. Par exemple, on peut obtenir un quasi-cristal unidimensionnel en projetant un réseau carré bidimensionnel sur une droite qui ne croise jamais les sommets du réseau, comme illustré dans Fig. 4.

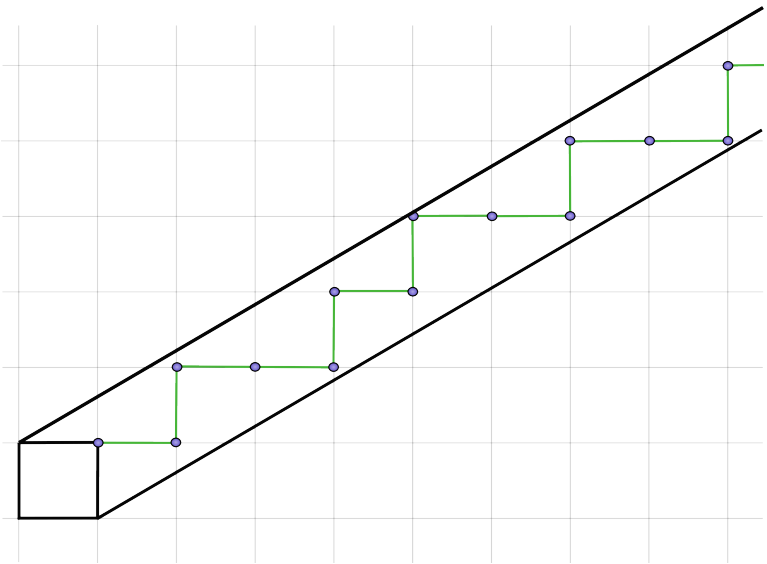

Figure 4: Exemple d'un schéma de coupe-et-projection pour construire un quasi-cristal unidimensionnel à partir d'un cristal bidimensionnel régulier. Le carré noir glisse entre deux lignes qui ne croisent jamais un sommet du réseau bidimensionnel. En suivant son parcours, tous les sommets entre les deux lignes noires forment une chaîne dont les arêtes sont orientées verticalement (V) ou horizontalement (H). La séquence des orientations $HVHHVHVHH\cdots$, connue sous le nom de suite de Fibonacci, ne se répétera jamais après que le carré noir ait couvert un nombre fini d'arêtes.

Avançons jusqu'à la dernière décennie, au cours de laquelle de nombreuses recherches ont été consacrées à l'étude de la topologie en présence de quasi-périodicité. Cela a éveillé notre curiosité pour comprendre comment ces phases apparaissent et dans quelle mesure la quasi-périodicité est robuste et structurée. Dans le Chapitre 5, nous avons étudié des quasi-cristaux unidimensionnels simples et leurs structures fractales cachées dans une dimension transverse en utilisant la méthode de projection décrite ci-dessus. À travers ces structures cachées, nous avons pu com-

prendre comment les impuretés, représentant un désordre non corrélé, commencent à perturber l'ordre quasi-cristallin à longue portée. Dans le Chapitre 6, nous avons prolongé l'étude du chapitre précédent en empilant ces chaînes unidimensionnelles de différentes manières. Nous avons découvert une grande variété de scénarios dans lesquels les propriétés de transport des systèmes cristallins et quasi-cristallins peuvent coexister. Enfin, dans le Chapitre 7, nous sommes revenus à la notion de topologie dans les systèmes apériodiques. Nous avons d'abord montré que le pompage de charge topologique—un phénomène où le courant pompé dans un système unidimensionnel est quantifié par un invariant topologique—peut se produire dans des systèmes apériodiques au-delà des seuls quasi-cristaux. Bien qu'une grande partie des recherches de la dernière décennie se soit concentrée sur ce phénomène dans les quasi-cristaux, nos résultats montrent qu'il n'y est pas exclusif et peut également être observé dans d'autres types de systèmes apériodiques. Nous avons ensuite démontré l'existence d'états de bord topologiques dans des systèmes apériodiques, protégés par la symétrie d'inversion—une symétrie spatiale où le système reste invariant sous réflexion par rapport à son milieu.

Pour conclure ce résumé, le thème central de cette thèse a été de révéler des structures cachées là où l'on n'en attendait pas, que ce soit dans le domaine des phases topologiques ou des systèmes apériodiques. La plupart de nos résultats constituent un bon point de départ pour de futures recherches sur les propriétés des phases topologiques dans ces divers contextes. Une partie de ce travail a déjà été amorcée au sein de notre groupe, bien que je ne l'aie pas incluse dans cette thèse, tandis que d'autres directions seront poursuivies par des collègues qui prendront le relais après mon départ.

La majorité de ce travail a été motivée par une curiosité simple et sincère. Bien que très théorique, il sera, espérons-le, observé sur des plateformes expérimentales et pourra peut-être être utile à d'autres chercheurs travaillant sur des sujets similaires.

Acknowledgement

I'd like to start by thanking my supervisor, Cristiane. Over the last five years, through my master's thesis and PhD, she has been an invaluable mentor. Her imagination knows no bounds, and she always finds inspiration beyond the confines of established knowledge. Her enthusiasm was sometimes hard to level with, but that was only because her ability to foresee outcomes was often beyond my immediate grasp. Starting a PhD during the COVID pandemic was not straightforward. Cristiane's practical advice allowed me to continue my master's thesis work, giving me a clear path forward at a time when it was much needed. Beyond work, she has also always been supportive of life endeavors and shared many great moments with the group and me, such as Sinterklaas dinners or her carnival-themed birthday party. I will forever cherish these moments.

I am also grateful to my direct collaborators, without whom I would not have been able to complete my PhD. I extend my gratitude to Sander Kempkes, Lumen Eek, Malte Röntgen, Christian Morfonios, Peter Schmelcher, Vincent Pagneux, Vassos Achilleos, Julius Krebbekx, Emanuele di Salvo, Chen Xu, Lars Fritz, Dirk Schuricht, Andrew Mitchell, and Zebbedeus Osseweijer.

Among my direct collaborators, three deserve special mention, as I had the privilege of co-supervising their theses: Lumen Eek and Julius Krebbekx, both master's students who have since begun their PhDs, and Zeb, a bachelor's student. All three were exceptionally talented, and I learned a great deal from them during our time together. I am proud that we succeeded in publishing work drawn directly from their theses.

I would also like to thank all the people I have had the pleasure of working alongside in my office, as they have been a great source of inspiration during our very long coffee breaks. In particular, I'd like to thank Rodrigo Arouca and Chongchuo Li, my only office mates at the beginning of my PhD during the COVID pandemic. Then, I'd like to thank all the people who came after them: Robin Verstraten, David Santiago Quevedo Vega, Diego Felipe Muñoz Arboleda, and William Huddie. My gratitude also goes to other group members I haven't mentioned: Tiago Santiago do Espirito Santo, Vinicius Zampronio, and Flavio Noronha. The contributions and teamwork from the different talks and scientific discussions have been invaluable throughout my journey of research.

Last but not least, I want to thank all the institute members for the wonderful lunch breaks, borrels, and PLaNETs we shared. These moments made my time at the institute truly enjoyable.

Finally, beyond the professional realm, I extend my deepest gratitude to my friends and family for believing in me and for a supportive environment that perfectly resulted in an ideal work-life balance. I'd like to thank my father and brothers, who are always close to my heart despite being far away. Special thanks to my aunt Fouzia, who I lived with for an extended period when I came to Utrecht. I should not forget to thank my cousins Taha and Ayoub, who I also lived with and shared many great moments, especially during our holiday road trip through Europe. Additionally, I'd like to thank all the members of NMATAR. Thank you for being a part of my life and believing in me.

Most importantly, I'd like to thank my mother, who is not here with us anymore to witness the end of a milestone. Without the upbringing you have instilled in me, I would have never made it this far.

The translations were accomplished with the assistance of ChatGPT and Lumen Eek (for Dutch), based on the English summary I composed myself.

Curriculum Vitae

Anouar Moustaj was born on March 5, 1993, in Marrakesh, Morocco. In 2011, he obtained his French baccalaureate from the Lycée Français Vincent van Gogh in The Hague. He then pursued a Bachelor of Arts in Audio Engineering at Middlesex University, graduating in 2013. After working as an audio engineer in various locations until 2015, he enrolled in a Bachelor of Science program in Physics and Astronomy at the University of Groningen. He graduated *Cum Laude* in 2018, with a focus on theoretical physics. His bachelor's thesis examined a modification of special relativity to address symmetry violations observed in particle physics. He continued his studies with a Master of Science in Theoretical Physics, initially focusing on high-energy physics but later shifting to condensed matter theory for his master's thesis. His thesis, conducted under the supervision of Cristiane Morais Smith, investigated topics in quasicrystals, topology, and local symmetries. Following this, he remained in Cristiane's research group to pursue a PhD, culminating in the current thesis.

Bibliography

[1] L. Eek, A. Moustaj, M. Röntgen, V. Pagneux, V. Achilleos, and C. Morais Smith, *Emergent non-Hermitian models*, Phys. Rev. B **109**, 045122 (2024).

[2] A. Moustaj, L. Eek, and C. Morais Smith, *Field theoretical study of disorder in non-Hermitian topological models*, Phys. Rev. B **105**, L180503 (2022).

[3] E. Di Salvo, A. Moustaj, C. Xu, L. Fritz, A. K. Mitchell, C. M. Smith, and D. Schuricht, *Topological phases of the interacting Su-Schrieffer-Heeger model: An analytical study*, Phys. Rev. B **110**, 165145 (2024).

[4] A. Moustaj, S. Kempkes, and C. Morais Smith, *Effects of disorder in the Fibonacci quasicrystal*, Phys. Rev. B **104**, 144201 (2021).

[5] J. P. J. Krebbekx, A. Moustaj, K. Dajani, and C. Morais Smith, *Multifractal properties of Tribonacci chains*, Phys. Rev. B **108**, 104204 (2023).

[6] A. Moustaj, M. Röntgen, C. V. Morfonios, P. Schmelcher, and C. Morais Smith, *Spectral properties of two coupled Fibonacci chains*, New J. Phys. **25**, 093019 (2023).

[7] A. Moustaj, J. P. J. Krebbekx, and C. Morais Smith, *Anomalous polarization in one-dimensional aperiodic insulators*, arXiv: 2404.14916 (2024).

[8] L. Eek, M. Röntgen, A. Moustaj, and C. Morais Smith, *Higher-order topology protected by latent crystalline symmetries*, arXiv: 2405.02704 (2024).

[9] Z. Osseweijer, L. Eek, A. Moustaj, M. Fremling, and C. Morais Smith, *Haldane model on a Sierpinski gasket*, arXiv: 2407.20075 (2024).

[10] A. Moustaj, L. Eek, M. Rontgen, and C. Morais Smith, *Latent Haldane models*, arXiv: 2411.08202 (2024).

[11] A. Moustaj, L. Eek, and C. Morais Smith, *Nearest-neighbour hopping Haldane models*, (in preparation) (2024).

[12] A. Moustaj, M. Stålhammar, and C. Morais Smith, *Properties of exceptional fractal nodal band structures in two and three dimensions*, (in preparation) (2024).

[13] J. M. Kosterlitz and D. J. Thouless, *Ordering, metastability and phase transitions in two-dimensional systems*, J. Phys. C **6**, 1181–1203 (1973).

[14] K. von Klitzing, T. Chakraborty, P. Kim, V. Madhavan, X. Dai, J. McIver, Y. Tokura, L. Savary, D. Smirnova, A. M. Rey, C. Felser, J. Gooth, and X. Qi, *40 years of the quantum Hall effect*, Nat. Rev. Phys. **2**, 397–401 (2020).

[15] X. Chen, Z.-C. Gu, and X.-G. Wen, *Classification of gapped symmetric phases in one-dimensional spin systems*, Phys. Rev. B **83**, 035107 (2011).

[16] C. K. Chiu, J. C. Teo, A. P. Schnyder, and S. Ryu, *Classification of topological quantum matter with symmetries*, Rev. Mod. Phys. **88**, 035005 (2016).

[17] G. Ma, M. Xiao, and C. T. Chan, *Topological phases in acoustic and mechanical systems*, Nat. Rev. Phys. **1**, 281–294 (2019).

[18] A. Altland and M. R. Zirnbauer, *Nonstandard symmetry classes in mesoscopic normal-superconducting hybrid structures*, Phys. Rev. B **55**, 1142–1161 (1997).

[19] V. F. Schindler, *Higher-Order Topology in Quantum Matter*, Tech. Rep. (Universitat Zurich, Zurich, 2020).

[20] B. Bradlyn, L. Elcoro, J. Cano, M. G. Vergniory, Z. Wang, C. Felser, M. I. Aroyo, and B. A. Bernevig, *Topological quantum chemistry*, Nature **547**, 298–305 (2017).

[21] W. A. Benalcazar, B. A. Bernevig, and T. L. Hughes, *Electric multipole moments, topological multipole moment pumping, and chiral hinge states in crystalline insulators*, Phys. Rev. B **96**, 245115 (2017).

[22] M. Verbin, O. Zilberberg, Y. E. Kraus, Y. Lahini, and Y. Silberberg, *Observation of Topological Phase Transitions in Photonic Quasicrystals*, Phys. Rev. Lett. **110**, 076403 (2013).

[23] M. Verbin, O. Zilberberg, Y. Lahini, Y. E. Kraus, and Y. Silberberg, *Topological pumping over a photonic Fibonacci quasicrystal*, Phys. Rev. B **91**, 064201 (2015).

[24] M. Yoshii, S. Kitamura, and T. Morimoto, *Topological charge pumping in quasiperiodic systems characterized by the Bott index*, Phys. Rev. B **104** (2021).

[25] R. Chen, C.-Z. Chen, J.-H. Gao, B. Zhou, and D.-H. Xu, *Higher-Order Topological Insulators in Quasicrystals*, Phys. Rev. Lett. **124**, 036803 (2020).

[26] Z. Gong, Y. Ashida, K. Kawabata, K. Takasan, S. Higashikawa, and M. Ueda, *Topological Phases of Non-Hermitian Systems*, Phys. Rev. X **8**, 31079 (2018).

[27] K. Kawabata, K. Shiozaki, M. Ueda, and M. Sato, *Symmetry and Topology in Non-Hermitian Physics*, Phys. Rev. X **9**, 41015 (2019).

[28] X.-G. Wen, *Colloquium: Zoo of quantum-topological phases of matter*, Rev. of Mod. Phys. **89**, 041004 (2017).

[29] X. Chen, Z.-C. Gu, and X.-G. Wen, *Complete classification of one-dimensional gapped quantum phases in interacting spin systems*, Phys. Rev. B **84**, 235128 (2011).

[30] B. Zeng, X. Chen, D.-L. Zhou, and X.-G. Wen, *Quantum Information Meets Quantum Matter* (Springer New York, New York, NY, 2019).

[31] L. Fidkowski, *Entanglement Spectrum of Topological Insulators and Superconductors*, Phys. Rev. Lett. **104**, 130502 (2010).

[32] J. Sirker, M. Maiti, N. P. Konstantinidis, and N. Sedlmayr, *Boundary fidelity and entanglement in the symmetry protected topological phase of the SSH model*, J. Stat. Mech. **2014**, P10032 (2014).

[33] T. Micallo, V. Vitale, M. Dalmonte, and P. Fromholz, *Topological entanglement properties of disconnected partitions in the Su-Schrieffer-Heeger model*, SciPost Physics Core **3**, 012 (2020).

[34] A. Kitaev, *Anyons in an exactly solved model and beyond*, Ann. Phys. **321**, 2–111 (2006).

[35] L. Savary and L. Balents, *Quantum spin liquids: a review*, Rep. Prog. Phys. **80**, 016502 (2017).

[36] M. Iqbal and N. Schuch, *Entanglement Order Parameters and Critical Behavior for Topological Phase Transitions and Beyond*, Phys. Rev. X **11**, 041014 (2021).

[37] D. E. Feldman and B. I. Halperin, *Fractional charge and fractional statistics in the quantum Hall effects*, Rep. Prog. Phys. **84**, 076501 (2021).

[38] X.-G. Wen, *Choreographed entanglement dances: Topological states of quantum matter*, Science **363**, eaal3099 (2019).

[39] F. D. M. Haldane, *Nonlinear Field Theory of Large-Spin Heisenberg Antiferromagnets: Semiclassically Quantized Solitons of the One-Dimensional Easy-Axis Néel State*, Phys. Rev. Lett. **50**, 1153–1156 (1983).

[40] A. Y. Kitaev, *Unpaired Majorana fermions in quantum wires*, Phys. Usp. **44**, 131–136 (2001).

[41] W. P. Su, J. R. Schrieffer, and A. J. Heeger, *Solitons in Polyacetylene*, Phys. Rev. Lett. **42**, 1698–1701 (1979).

[42] A. Kitaev, V. Lebedev, and M. Feigel'man, in *AIP Conference Proceedings* (AIP, 2009) pp. 22–30.

[43] L. Fu, C. L. Kane, and E. J. Mele, *Topological Insulators in Three Dimensions*, Phys. Rev. Lett. **98**, 106803 (2007).

[44] A. W. W. Ludwig, *Topological phases: classification of topological insulators and superconductors of non-interacting fermions, and beyond*, Phys. Scr. **T168**, 014001 (2016).

[45] M. Karoubi, in *Handbook of K-Theory* (Springer Berlin Heidelberg, Berlin, Heidelberg, 2005) Chap. 4, pp. 111–137.

[46] M. Z. Hasan and C. L. Kane, *Colloquium : Topological insulators*, Rev. Mod. Phys. **82**, 3045–3067 (2010).

[47] D. Hsieh, Y. Xia, D. Qian, L. Wray, J. H. Dil, F. Meier, J. Osterwalder, L. Patthey, J. G. Checkelsky, N. P. Ong, A. V. Fedorov, H. Lin, A. Bansil, D. Grauer, Y. S. Hor, R. J. Cava, and M. Z. Hasan, *A tunable topological insulator in the spin helical Dirac transport regime*, Nature **460**, 1101–1105 (2009).

[48] A. M. Essin, J. E. Moore, and D. Vanderbilt, *Magnetoelectric Polarizability and Axion Electrodynamics in Crystalline Insulators*, Phys. Rev. Lett. **102**, 146805 (2009).

[49] F. Wilczek, *Two applications of axion electrodynamics*, Phys. Rev. Lett. **58**, 1799–1802 (1987).

[50] R. D. King-Smith and D. Vanderbilt, *Theory of polarization of crystalline solids*, Phys. Rev. B **47**, 1651–1654 (1993).

[51] J. Zak, *Berry's phase for energy bands in solids*, Phys. Rev. Lett. **62**, 2747–2750 (1989).

[52] D. J. Thouless, M. Kohmoto, M. P. Nightingale, and M. den Nijs, *Quantized Hall Conductance in a Two-Dimensional Periodic Potential*, Phys. Rev. Lett. **49**, 405–408 (1982).

[53] S.-Q. Shen, W.-Y. Shan, and H.-Z. Lu, *Topological insulator and the Dirac equation*, SPIN **01**, 33–44 (2011).

[54] M. F. Atiyah and I. M. Singer, *The index of elliptic operators on compact manifolds*, Bull. Amer. Soc. Math **69**, 422–433 (1963).

[55] W. A. Benalcazar, T. Li, and T. L. Hughes, *Quantization of fractional corner charge in Cn -symmetric higher-order topological crystalline insulators*, Phys. Rev. B **99**, 245151 (2019).

[56] F. D. M. Haldane, *Model for a Quantum Hall Effect without Landau Levels: Condensed-Matter Realization of the "Parity Anomaly"*, Phys. Rev. Lett. **61**, 2015–2018 (1988).

[57] B. A. Bernevig and T. L. Hughes, *Topological Insulators and Topological Superconductors* (Princeton University Press, New Jersey, 2013).

[58] K. S. Novoselov, A. K. Geim, S. V. Morozov, D. Jiang, M. I. Katsnelson, I. V. Grigorieva, S. V. Dubonos, and A. A. Firsov, *Two-dimensional gas of massless Dirac fermions in graphene*, Nature **438**, 197–200 (2005).

[59] P. W. Anderson, *Absence of Diffusion in Certain Random Lattices*, Phys. Rev. **109**, 1492–1505 (1958).

[60] A. P. Schnyder, S. Ryu, A. Furusaki, and A. W. W. Ludwig, *Classification of topological insulators and superconductors in three spatial dimensions*, Phys. Rev. B **78**, 195125 (2008).

[61] C. Brouder, G. Panati, M. Calandra, C. Mourougane, and N. Marzari, *Exponential Localization of Wannier Functions in Insulators*, Phys. Rev. Lett. **98**, 046402 (2007).

[62] I. V. Lerner, in *Strongly Correlated Fermions and Bosons in Low-Dimensional Disordered Systems* (Springer Netherlands, Dordrecht, 2002) pp. 341–373.

[63] L. Fidkowski and A. Kitaev, *Effects of interactions on the topological classification of free fermion systems*, Phys. Rev. B **81**, 134509 (2010).

[64] L. Fidkowski and A. Kitaev, *Topological phases of fermions in one dimension*, Phys. Rev. B **83**, 075103 (2011).

[65] C. Zhang and M. Zubkov, *Influence of interactions on Integer Quantum Hall Effect*, Ann. Phys. **444**, 169016 (2022).

[66] M. Levin and A. Stern, *Fractional Topological Insulators*, Phys. Rev. Lett. **103**, 196803 (2009).

[67] Y.-M. Lu and A. Vishwanath, *Theory and classification of interacting integer topological phases in two dimensions: A Chern-Simons approach*, Phys. Rev. B **86**, 125119 (2012).

[68] C. L. Kane and E. J. Mele, *Quantum Spin Hall Effect in Graphene*, Phys. Rev. Lett. **95**, 226801 (2005).

[69] S. L. Sondhi, A. Karlhede, S. A. Kivelson, and E. H. Rezayi, *Skyrmions and the crossover from the integer to fractional quantum Hall effect at small Zeeman energies*, Phys. Rev. B **47**, 16419–16426 (1993).

[70] H. L. Stormer, D. C. Tsui, and A. C. Gossard, *The fractional quantum Hall effect*, Rev. of Mod. Phys. **71**, S298–S305 (1999).

[71] S. de Léséleuc, V. Lienhard, P. Scholl, D. Barredo, S. Weber, N. Lang, H. P. Büchler, T. Lahaye, and A. Browaeys, *Observation of a symmetry-protected topological phase of interacting bosons with Rydberg atoms*, Science **365**, 775–780 (2019).

[72] T. Neupert, C. Chamon, T. Iadecola, L. H. Santos, and C. Mudry, *Fractional (Chern and topological) insulators*, Phys. Scr. **T164**, 014005 (2015).

[73] X.-G. Wen, *Topological orders in rigid states*, Int. J. Mod. Phys. B **04**, 239–271 (1990).

[74] M. Dzero, K. Sun, V. Galitski, and P. Coleman, *Topological Kondo Insulators*, Phys. Rev. Lett. **104**, 106408 (2010).

[75] S. Raghu, X.-L. Qi, C. Honerkamp, and S.-C. Zhang, *Topological Mott Insulators*, Phys. Rev. Lett. **100**, 156401 (2008).

[76] M. B. Hastings, *An area law for one-dimensional quantum systems*, J. Stat. Mech. **2007**, P08024–P08024 (2007).

[77] Z.-C. Gu and X.-G. Wen, *Symmetry-protected topological orders for interacting fermions: Fermionic topological nonlinear σ models and a special group supercohomology theory*, Phys. Rev. B **90**, 115141 (2014).

[78] D. S. Freed, *Short-range entanglement and invertible field theories*, arXiv 1406.7278 https://doi.org/10.48550/arXiv.1406.7278 (2014).

[79] A. Kapustin, *Symmetry Protected Topological Phases, Anomalies, and Cobordisms: Beyond Group Cohomology*, arXiv: 1404.6659 https://doi.org/10.48550/arXiv.1404.6659 (2014).

[80] A. Kapustin, R. Thorngren, A. Turzillo, and Z. Wang, *Fermionic symmetry protected topological phases and cobordisms*, J. High Energy Phys. **2015** (12), 1–21.

[81] S. Ryu, J. E. Moore, and A. W. W. Ludwig, *Electromagnetic and gravitational responses and anomalies in topological insulators and superconductors*, Phys. Rev. B **85**, 045104 (2012).

[82] C. L. Kane and T. C. Lubensky, *Topological boundary modes in isostatic lattices*, Nat. Phys. **10**, 39–45 (2014).

[83] R. Süsstrunk and S. D. Huber, *Observation of phononic helical edge states in a mechanical topological insulator*, Science **349**, 47–50 (2015).

[84] F. D. M. Haldane and S. Raghu, *Possible Realization of Directional Optical Waveguides in Photonic Crystals with Broken Time-Reversal Symmetry*, Phys. Rev. Lett. **100**, 013904 (2008).

[85] Z. Wang, Y. Chong, J. D. Joannopoulos, and M. Soljačić, *Observation of unidirectional backscattering-immune topological electromagnetic states*, Nature **461**, 772–775 (2009).

[86] C. H. Lee, S. Imhof, C. Berger, F. Bayer, J. Brehm, L. W. Molenkamp, T. Kiessling, and R. Thomale, *Topolectrical Circuits*, Commun. Phys. **1**, 39 (2018).

[87] A. McDonald and A. A. Clerk, *Exponentially-enhanced quantum sensing with non-Hermitian lattice dynamics*, Nat. Commun. **11**, 5382 (2020).

[88] P. San-Jose, J. Cayao, E. Prada, and R. Aguado, *Majorana bound states from exceptional points in non-topological superconductors*, Sci. Rep. **6**, 21427 (2016).

[89] A. Ghatak, M. Brandenbourger, J. van Wezel, and C. Coulais, *Observation of non-Hermitian topology and its bulk–edge correspondence in an active mechanical metamaterial*, Proc. Natl. Acad. Sci. **117**, 29561–29568 (2020).

[90] K. Sone, Y. Ashida, and T. Sagawa, *Exceptional non-Hermitian topological edge mode and its application to active matter*, Nat. Commun. **11**, 5745 (2020).

[91] F. K. Kunst, E. Edvardsson, J. C. Budich, and E. J. Bergholtz, *Biorthogonal Bulk-Boundary Correspondence in Non-Hermitian Systems*, Phys. Rev. Lett. **121**, 26808 (2018).

[92] E. J. Bergholtz, J. C. Budich, and F. K. Kunst, *Exceptional topology of non-Hermitian systems*, Rev. Mod. Phys. **93**, 15005 (2021).

[93] T. E. Lee, *Anomalous Edge State in a Non-Hermitian Lattice*, Phys. Rev. Lett. **116**, 133903 (2016).

[94] S. Yao and Z. Wang, *Edge States and Topological Invariants of Non-Hermitian Systems*, Phys. Rev. Lett. **121**, 86803 (2018).

[95] N. Okuma, K. Kawabata, K. Shiozaki, and M. Sato, *Topological Origin of Non-Hermitian Skin Effects*, Phys. Rev. Lett. **124**, 86801 (2020).

[96] L. Zhang, Y. Yang, Y. Ge, Y.-J. Guan, Q. Chen, Q. Yan, F. Chen, R. Xi, Y. Li, D. Jia, S.-Q. Yuan, H.-X. Sun, H. Chen, and B. Zhang, *Acoustic non-Hermitian skin effect from twisted winding topology*, Nat. Commun. **12**, 6297 (2021).

[97] S. Liu, R. Shao, S. Ma, L. Zhang, O. You, H. Wu, Y. J. Xiang, T. J. Cui, and S. Zhang, *Non-Hermitian Skin Effect in a Non-Hermitian Electrical Circuit*, Research **2021**, 10.34133/2021/5608038 (2021).

[98] Z. Gu, H. Gao, H. Xue, J. Li, Z. Su, and J. Zhu, *Transient non-Hermitian skin effect*, Nat. Commun. **13**, 7668 (2022).

[99] Q. Liang, D. Xie, Z. Dong, H. Li, H. Li, B. Gadway, W. Yi, and B. Yan, *Dynamic Signatures of Non-Hermitian Skin Effect and Topology in Ultracold Atoms*, Phys. Rev. Lett. **129**, 070401 (2022).

[100] F. K. Kunst and V. Dwivedi, *Non-Hermitian systems and topology: A transfer-matrix perspective*, Phys. Rev. B **99**, 245116 (2019).

[101] L. Li, C. H. Lee, and J. Gong, *Topological Switch for Non-Hermitian Skin Effect in Cold-Atom Systems with Loss*, Phys. Rev. Lett. **124**, 250402 (2020).

[102] Z. Yang, K. Zhang, C. Fang, and J. Hu, *Non-Hermitian Bulk-Boundary Correspondence and Auxiliary Generalized Brillouin Zone Theory*, Phys. Rev. Lett. **125**, 226402 (2020).

[103] C. M. Bender and S. Boettcher, *Real Spectra in Non-Hermitian Hamiltonians Having PT Symmetry*, Phys. Rev. Lett. **80**, 5243–5246 (1998).

[104] C. M. Bender, S. Boettcher, and P. N. Meisinger, *PT-symmetric quantum mechanics*, J. Math. Phys. **40**, 2201–2229 (1999).

[105] C. E. Rüter, K. G. Makris, R. El-Ganainy, D. N. Christodoulides, M. Segev, and D. Kip, *Observation of parity–time symmetry in optics*, Nat. Phys. **6**, 192–195 (2010).

[106] H. Hodaei, M.-A. Miri, M. Heinrich, D. N. Christodoulides, and M. Khajavikhan, *Parity-time–symmetric microring lasers*, Science **346**, 975–978 (2014).

[107] Z. Lin, H. Ramezani, T. Eichelkraut, T. Kottos, H. Cao, and D. N. Christodoulides, *Unidirectional Invisibility Induced by PT-Symmetric Periodic Structures*, Phys. Rev. Lett. **106**, 213901 (2011).

[108] W. Chen, S. Kaya Ozdemir, G. Zhao, J. Wiersig, and L. Yang, *Exceptional points enhance sensing in an optical microcavity*, Nature **548**, 192–196 (2017).

[109] A. Yariv, *Coupled-mode theory for guided-wave optics*, IEEE J. Quantum Electron. **9**, 919–933 (1973).

[110] A. Szameit and S. Nolte, *Discrete optics in femtosecond-laser-written photonic structures*, J. Phys. B **43**, 163001 (2010).

[111] S. Weimann, M. Kremer, Y. Plotnik, Y. Lumer, S. Nolte, K. G. Makris, M. Segev, M. Rechtsman, and A. Szameit, *Topologically protected bound states in photonic parity–time-symmetric crystals*, Nat. Mater. **16**, 433–438 (2017).

[112] S. Longhi, D. Gatti, and G. D. Valle, *Robust light transport in non-Hermitian photonic lattices*, Sci. Rep. **5**, 13376 (2015).

[113] G. M. Krause, *Bounds for the variation of matrix eigenvalues and polynomial roots*, Linear Algebra Appl. **208-209**, 73–82 (1994).

[114] Y. Xiong, *Why does bulk boundary correspondence fail in some non-hermitian topological models*, J. Phys. Commun. **2**, 035043 (2018).

[115] N. Hatano and D. R. Nelson, *Vortex pinning and non-Hermitian quantum mechanics*, Phys. Rev. B **56**, 8651–8673 (1997).

[116] S. Noschese, L. Pasquini, and L. Reichel, *Tridiagonal Toeplitz matrices: properties and novel applications*, Numer. Linear Algebra Appl. **20**, 302–326 (2013).

[117] S. Lieu, *Topological phases in the non-Hermitian Su-Schrieffer-Heeger model*, Phys. Rev. B **97**, 45106 (2018).

[118] C. Yin, H. Jiang, L. Li, R. Lü, and S. Chen, *Geometrical meaning of winding number and its characterization of topological phases in one-dimensional chiral non-Hermitian systems*, Phys. Rev. A **97**, 52115 (2018).

[119] C. H. Lee, L. Li, R. Thomale, and J. Gong, *Unraveling non-Hermitian pumping: Emergent spectral singularities and anomalous responses*, Phys. Rev. B **102**, 085151 (2020).

[120] R. Arouca, C. H. Lee, and C. Morais Smith, *Unconventional scaling at non-Hermitian critical points*, Phys. Rev. B **102**, 245145 (2020).

[121] D. Shechtman, I. Blech, D. Gratias, and J. W. Cahn, *Metallic Phase with Long-Range Orientational Order and No Translational Symmetry*, Phys. Rev. Lett. **53**, 1951–1953 (1984).

[122] A. L. Pope and T. M. Tritt, in *Thermal Conductivity: Theory, Properties, and Applications*, edited by T. M. Tritt (Springer US, Boston, MA, 2004) pp. 255–259.

[123] C. Berger, T. Grenet, P. Lindqvist, P. Lanco, J. C. Grieco, G. Fourcaudot, and F. Cyrot-Lackmann, *The new AlPdRe icosahedral phase: Towards universal electronic behaviour for quasicrystals?*, Solid State Commun. **87**, 977 – 979 (1993).

[124] J. M. Dubois, in *Quasicrystals, An Introduction to Structure, Physical Properties and Applications* (Springer, 2002) pp. 507–538.

[125] E. Maciá, *The role of aperiodic order in science and technology*, Rep. Prog. Phys. **69**, 397–441 (2006).

[126] A. B. Harris, *Effect of random defects on the critical behaviour of Ising models*, J. Phys. C **7**, 1671–1692 (1974).

[127] J. M. Luck, *Critical Behavior of the Aperiodic Quantum Ising Chain in a Transverse Magnetic Field*, J. Stat. Phys. **72** (1993).

[128] J. Hermisson, *Aperiodic and correlated disorder in XY chains: exact results*, J. Phys. A **33**, 57–79 (2000).

[129] Q. Niu and F. Nori, *Renormalization-Group Study of One-Dimensional Quasiperiodic Systems*, Phys. Rev. Lett. **57**, 2057–2060 (1986).

[130] M. Kohmoto and Y. Oono, *Cantor spectrum for an almost periodic Schrödinger equation and a dynamical map*, Phys. Lett. A **102**, 145–148 (1984).

[131] M. Kohmoto, B. Sutherland, and C. Tang, *Critical wave functions and a Cantor-set spectrum of a one-dimensional quasicrystal model*, Phys. Rev. B **35**, 1020–1033 (1987).

[132] M. Kolář, M. K. Ali, and F. Nori, *Generalized Thue-Morse chains and their physical properties*, Phys. Rev. B **43**, 1034–1047 (1991).

[133] J. Bellissard, B. Lochum, E. Scoppola, and D. Testard, *Spectral Properties of One Dimensional Quasi-Crystals*, Commun. Math. Phys **125**, 527–543 (1989).

[134] C. Sire and R. Mosseri, *Spectrum of 1D quasicrystals near the periodic chain*, J. Phys. **50**, 3447–3461 (1989).

[135] C. Sire and R. Mosseri, *Excitation spectrum, extended states, gap closing : some exact results for codimension one quasicrystals*, J. Phys. **51**, 1569 – 1583 (1990).

[136] Q. Niu and F. Nori, *Spectral splitting and wave-function scaling in quasicrystalline and hierarchical structures*, Phys. Rev. B **42**, 10329–10341 (1991).

[137] Y. E. Kraus, Y. Lahini, Z. Ringel, M. Verbin, and O. Zilberberg, *Topological States and Adiabatic Pumping in Quasicrystals*, Phys. Rev. Lett. **109**, 106402 (2012).

[138] V. Goblot, A. Štrkalj, N. Pernet, J. L. Lado, C. Dorow, A. Lemaître, L. Le Gratiet, A. Harouri, I. Sagnes, S. Ravets, A. Amo, J. Bloch, and O. Zilberberg, *Emergence of criticality through a cascade of delocalization transitions in quasiperiodic chains*, Nat. Phys. **16**, 832–836 (2020).

[139] M. Röntgen, C. V. Morfonios, R. Wang, L. Dal Negro, and P. Schmelcher, *Local symmetry theory of resonator structures for the real-space control of edge states in binary aperiodic chains*, Phys. Rev. B **99**, 214201 (2019).

[140] A. Jagannathan, *The Fibonacci quasicrystal: Case study of hidden dimensions and multifractality*, Rev. Mod. Phys. **93** (2021).

[141] M. Brin and G. Stuck, in *Introduction to Dynamical Systems* (Cambridge University Press, 2002) Chap. 3, pp. 54–68.

[142] M. Baake and U. Grimm, *Aperiodic Order* (Cambridge University Press, 2013).

[143] S. Akiyama, M. Barge, V. Berthé, J.-Y. Lee, and A. Siegel, in *Mathematics of Aperiodic Order* (Birkhäuser, Basel, 2015) Chap. 2, pp. 33–72.

[144] F. Adiceam, D. Damanik, F. Gähler, U. Grimm, A. Haynes, A. Julien, A. Navas, L. Sadun, and B. Weiss, *Open Problems and Conjectures Related to the Theory of Mathematical Quasicrystals*, Arnold Math. J. **2**, 579–592 (2016).

[145] M. Baake, P. Gohlke, M. Kesseböhmer, and T. Schindler, *Scaling properties of the thue–morse measure*, Discrete Contin. Dyn. Syst. **39**, 4157–4185 (2019).

[146] M. Dulea, M. Johansson, and R. Riklund, *Trace-map invariant and zero-energy states of the tight-binding Rudin-Shapiro model*, Phys. Rev. B **46**, 3296–3304 (1992).

[147] E. Hewitt and K. R. Stromberg, in *Real and Abstract Analysis* (Springer Berlin Heidelberg, Berlin, Heidelberg, 1965) Chap. 5, pp. 256–376.

[148] L. Bursill, P. J. Lin, and X. Fan, *Spiral Lattice Concepts*, Mod. Phys. Lett. B **01**, 195–206 (1987).

[149] J. Bellissard, in *From Number Theory to Physics* (Springer Berlin Heidelberg, 1992) pp. 538–630.

[150] J. M. Luck, *Cantor spectra and scaling of gap widths in deterministic aperiodic systems*, Phys. Rev. B **39**, 5834–5849 (1989).

[151] G. A. Domínguez-Castro and R. Paredes, *The Aubry–André model as a hobbyhorse for understanding the localization phenomenon*, Eur. J. Phys. **40**, 045403 (2019).

[152] Y. E. Kraus and O. Zilberberg, *Topological Equivalence between the Fibonacci Quasicrystal and the Harper Model*, Phys. Rev. Lett. **109**, 116404 (2012).

[153] D. R. Hofstadter, *Energy levels and wave functions of Bloch electrons in rational and irrational magnetic fields*, Phys. Rev. B **14**, 2239–2249 (1976).

[154] J. Zak, *Magnetic Translation Group*, Phys. Rev. **134**, A1602–A1606 (1964).

[155] A.-S. Walter, Z. Zhu, M. Gächter, J. Minguzzi, S. Roschinski, K. Sandholzer, K. Viebahn, and T. Esslinger, *Quantization and its breakdown in a Hubbard–Thouless pump*, Nat. Phys. **19**, 1471–1475 (2023).

[156] L. A. Bunimovich and B. Z. Webb, *Isospectral graph transformations, spectral equivalence, and global stability of dynamical networks*, Nonlinearity **25**, 211–254 (2012).

[157] L. Bunimovich, D. Smith, and B. Webb, *Finding Hidden Structures, Hierarchies, and Cores in Networks via Isospectral Reduction*, Applied Mathematics and Nonlinear Sciences **4**, 231–254 (2019).

[158] L. Bunimovich and B. Webb, *Isospectral graph reductions and improved estimates of matrices' spectra*, Linear Algebra Appl. **437**, 1429–1457 (2012).

[159] F. G. Vasquez and B. Z. Webb, *Pseudospectra of isospectrally reduced matrices*, Numer. Linear Algebra Appl. **22**, 145–174 (2015).

[160] L. Brillouin, *Les problèmes de perturbations et les champs self-consistents*, Journal de Physique et le Radium **3**, 373–389 (1932).

[161] J. Hubbard, *Calculation of Partition Functions*, Phys. Rev. Lett. **3**, 77–78 (1959).

[162] D. Chruściński and A. Kossakowski, *Feshbach Projection Formalism for Open Quantum Systems*, Physical Review Letters **111**, 050402 (2013).

[163] D. Smith and B. Webb, *Hidden symmetries in real and theoretical networks*, Physica A: Statistical Mechanics and its Applications **514**, 855–867 (2019).

[164] M. Kempton, J. Sinkovic, D. Smith, and B. Webb, *Characterizing cospectral vertices via isospectral reduction*, Linear Algebra Appl. **594**, 226–248 (2020).

[165] A. J. Schwenk, in *New Directions in the Theory of Graphs*, edited by F. Harary (Academic Press, New York, 1973) pp. 275–307.

[166] C. Godsil and J. Smith, *Strongly Cospectral Vertices*, arXiv (2017).

[167] M. Röntgen, N. E. Palaiodimopoulos, C. V. Morfonios, I. Brouzos, M. Pyzh, F. K. Diakonos, and P. Schmelcher, *Designing pretty good state transfer via isospectral reductions*, Phys. Rev. A **101**, 042304 (2020).

[168] C. V. Morfonios, M. Röntgen, M. Pyzh, and P. Schmelcher, *Flat bands by latent symmetry*, Phys. Rev. B **104**, 035105 (2021).

[169] M. Röntgen, M. Pyzh, C. Morfonios, N. Palaiodimopoulos, F. Diakonos, and P. Schmelcher, *Latent Symmetry Induced Degeneracies*, Phys. Rev. Lett. **126**, 180601 (2021).

[170] M. Röntgen, C. Morfonios, P. Schmelcher, and V. Pagneux, *Hidden Symmetries in Acoustic Wave Systems*, Phys. Rev. Lett. **130**, 077201 (2023).

[171] M. Röntgen, O. Richoux, G. Theocharis, C. V. Morfonios, P. Schmelcher, P. del Hougne, and V. Achilleos, *Equireflectionality and customized unbalanced coherent perfect absorption in asymmetric waveguide networks*, arXiv (2023).

[172] J. Sol, M. Röntgen, and P. del Hougne, *Covert Scattering Control in Metamaterials with Non-Locally Encoded Hidden Symmetry*, Adv. Mat. **36**, 10.1002/adma.202303891 (2024).

[173] Z. Lin, L. Ding, S. Ke, and X. Li, *Steering non-Hermitian skin modes by synthetic gauge fields in optical ring resonators*, Optics Letters **46**, 3512 (2021).

[174] H. Xin, W. Song, S. Wu, Z. Lin, S. Zhu, and T. Li, *Manipulating the non-Hermitian skin effect in optical ring resonators*, Physical Review B **107**, 165401 (2023).

[175] M. Röntgen, X. Chen, W. Gao, M. Pyzh, P. Schmelcher, V. Pagneux, V. Achilleos, and A. Coutant, *Topological states protected by hidden symmetry*, Phys. Rev. B **110**, 035106 (2024).

[176] L. Bunimovich and B. Webb, *Isospectral Transformations* (Springer New York, New York, NY, 2014).

[177] A. Clerk, *Introduction to quantum non-reciprocal interactions: from non-Hermitian Hamiltonians to quantum master equations and quantum feedforward schemes*, SciPost Physics Lecture Notes , 44 (2022).

[178] F. Song, S. Yao, and Z. Wang, *Non-Hermitian Topological Invariants in Real Space*, Physical Review Letters **123**, 246801 (2019).

[179] M. Creutz, *End States, Ladder Compounds, and Domain-Wall Fermions*, Phys. Rev. Lett. **83**, 2636–2639 (1999).

[180] C. Morfonios, M. Pyzh, M. Röntgen, and P. Schmelcher, *Cospectrality preserving graph modifications and eigenvector properties via walk equivalence of vertices*, Linear Algebra Appl. **624**, 53–86 (2021).

[181] M. Röntgen, Latent symmetries: An introduction (2022).

[182] S. Liu, S. Ma, C. Yang, L. Zhang, W. Gao, Y. J. Xiang, T. J. Cui, and S. Zhang, *Gain- and Loss-Induced Topological Insulating Phase in a Non-Hermitian Electrical Circuit*, Phys. Rev. App. **13**, 014047 (2020).

[183] J. Dong, V. Juričić, and B. Roy, *Topolectric circuits: Theory and construction*, Phys. Rev. Res. **3**, 023056 (2021).

[184] S. Liu, S. Ma, Q. Zhang, L. Zhang, C. Yang, O. You, W. Gao, Y. Xiang, T. J. Cui, and S. Zhang, *Octupole corner state in a three-dimensional topological circuit*, Light: Science & Applications **9**, 145 (2020).

[185] S. Imhof, C. Berger, F. Bayer, J. Brehm, L. W. Molenkamp, T. Kiessling, F. Schindler, C. H. Lee, M. Greiter, T. Neupert, and R. Thomale, *Topolectrical-circuit realization of topological corner modes*, Nat. Phys. **14**, 925–929 (2018).

[186] S. Datta, in *Electronic Transport in Mesoscopic Systems* (Springer-Verlag, Heidelberg, Germany, 2006).

[187] M. A. Bandres, S. Wittek, G. Harari, M. Parto, J. Ren, M. Segev, D. N. Christodoulides, and M. Khajavikhan, *Topological insulator laser: Experiments*, Science **359**, 10.1126/science.aar4005 (2018).

[188] A. Cerjan, S. Huang, M. Wang, K. P. Chen, Y. Chong, and M. C. Rechtsman, *Experimental realization of a Weyl exceptional ring*, Nat. Photonics **13**, 623 (2019).

[189] T. Helbig, T. Hofmann, and S. Imhof, *Generalized bulk–boundary correspondence in non-Hermitian topolectrical circuits*, Nat. Phys. **16**, 747 (2020).

[190] D. Leykam, K. Y. Bliokh, C. Huang, Y. D. Chong, and F. Nori, *Edge Modes, Degeneracies, and Topological Numbers in Non-Hermitian Systems*, Phys. Rev. Lett. **118**, 40401 (2017).

[191] S. Yao, F. Song, and Z. Wang, *Non-Hermitian Chern Bands*, Phys. Rev. Lett. **121**, 136802 (2018).

[192] H. Zhou and J. Y. Lee, *Periodic table for topological bands with non-Hermitian symmetries*, Phys. Rev. B **99**, 235112 (2019).

[193] S. Longhi, *Probing non-Hermitian skin effect and non-Bloch phase transitions*, Phys. Rev. Research **1**, 23013 (2019).

[194] C. H. Lee and R. Thomale, *Anatomy of skin modes and topology in non-Hermitian systems*, Phys. Rev. B **99**, 201103 (2019).

[195] D. S. Borgnia, A. J. Kruchkov, and R.-J. Slager, *Non-Hermitian Boundary Modes and Topology*, Phys. Rev. Lett. **124**, 56802 (2020).

[196] K. Kawabata, K. Shiozaki, and S. Ryu, *Topological Field Theory of Non-Hermitian Systems*, Phys. Rev. Lett. **126**, 216405 (2021).

[197] S. Longhi, *Spectral deformations in non-Hermitian lattices with disorder and skin effect: A solvable model*, Phys. Rev. B **103**, 144202 (2021).

[198] J. Y. Lee, J. Ahn, H. Zhou, and A. Vishwanath, *Topological Correspondence between Hermitian and Non-Hermitian Systems: Anomalous Dynamics*, Phys. Rev. Lett. **123**, 206404 (2019).

[199] P. Coleman, in *Introduction to many-body physics* (Cambridge university press, Cambridge, UK, 2015).

[200] A. Udupa, A. Banerjee, K. Sengupta, and D. Sen, *One-dimensional spinorbit coupled Dirac system with extended s-wave superconductivity: Majorana modes and Josephson effects*, Journal of Physics: Condensed Matter **33**, 145301 (2021).

[201] A. M. M. Pruisken and L. Schäfer, *Field Theory and the Anderson Model for Disordered Electronic Systems*, Phys. Rev. Lett. **46**, 490–492 (1981).

[202] K.-M. Kim and M. J. Park, *Disorder-driven phase transition in the second-order non-Hermitian skin effect*, Phys. Rev. B **104**, L121101 (2021).

[203] Y. X. Zhao and Z. D. Wang, *Disordered Weyl Semimetals and Their Topological Family*, Phys. Rev. Lett. **114**, 206602 (2015).

[204] X.-L. Qi and S.-C. Zhang, *Topological insulators and superconductors*, Rev. Mod. Phys. **83**, 1057–1110 (2011).

[205] C. L. Kane and E. J. Mele, *Z2 Topological Order and the Quantum Spin Hall Effect*, Phys. Rev. Lett. **95**, 146802 (2005).

[206] F. D. M. Haldane, *'Luttinger liquid theory' of one-dimensional quantum fluids. I. Properties of the Luttinger model and their extension to the general 1D interacting spinless Fermi gas*, J. Phys. C **14**, 2585–2609 (1981).

[207] J. Voit, *One-dimensional Fermi liquids*, Rep. Prog. Phys. **58**, 977–1116 (1995).

[208] T. Giamarchi, *Quantum Physics in One Dimension* (Oxford University Press, 2003).

[209] S. Rachel, *Interacting topological insulators: a review*, Rep. Prog. Phys. **81**, 116501 (2018).

[210] V. Gurarie, *Single-particle Green's functions and interacting topological insulators*, Phys. Rev. B **83**, 085426 (2011).

[211] S. R. Manmana, A. M. Essin, R. M. Noack, and V. Gurarie, *Topological invariants and interacting one-dimensional fermionic systems*, Phys. Rev. B **86**, 205119 (2012).

[212] W. Chen, *Weakly interacting topological insulators: Quantum criticality and the renormalization group approach*, Phys. Rev. B **97**, 115130 (2018).

[213] A. M. Marques and R. G. Dias, *Multihole edge states in Su-Schrieffer-Heeger chains with interactions*, Phys. Rev. B **95**, 115443 (2017).

[214] M. Yahyavi, L. Saleem, and B. Hetényi, *Variational study of the interacting, spinless Su–Schrieffer–Heeger model*, J. Phys. Condens. Matter **30**, 445602 (2018).

[215] T. Jin, P. Ruggiero, and T. Giamarchi, *Bosonization of the interacting Su-Schrieffer-Heeger model*, Phys. Rev. B **107**, L201111 (2023).

[216] P. B. Melo, S. A. S. Júnior, W. Chen, R. Mondaini, and T. Paiva, *Topological marker approach to an interacting Su-Schrieffer-Heeger model*, Phys. Rev. B **108**, 195151 (2023).

[217] X. Zhou, J.-S. Pan, and S. Jia, *Exploring interacting topological insulator in the extended Su-Schrieffer-Heeger model*, Phys. Rev. B **107**, 054105 (2023).

[218] A. A. Nersesyan, *Phase diagram of an interacting staggered Su-Schrieffer-Heeger two-chain ladder close to a quantum critical point*, Phys. Rev. B **102**, 045108 (2020).

[219] J. K. Asbóth, L. Oroszlány, and A. Pályi, *A Short Course on Topological Insulators*, Vol. 919 (Springer International Publishing, Cham, 2016).

[220] Y. Aihara, M. Hirayama, and S. Murakami, *Anomalous dielectric response in insulators with the π Zak phase*, Phys. Rev. Res. **2**, 033224 (2020).

[221] W. E. Thirring, *A soluble relativistic field theory*, Ann. Phys. **3**, 91–112 (1958).

[222] V. E. Korepin, *Direct calculation of the S matrix in the massive Thirring model*, Theor. Math. Phys. **41**, 953–967 (1979).

[223] B. Perez-Gonzalez, M. Bello, A. Gomez-Leon, and G. Platero, *Interplay between long-range hopping and disorder in topological systems*, Phys. Rev. B **99**, 035146 (2019).

[224] P.-J. Chang, J. Pi, M. Zheng, Y.-T. Lei, D. Ruan, and G.-L. Long, *Topological phases of extended Su-Schrieffer-Heeger-Hubbard model*, arXiv: 2405.10351 (2024).

[225] B. Sbierski and C. Karrasch, *Topological invariants for the Haldane phase of interacting Su-Schrieffer-Heeger chains: Functional renormalization-group approach*, Phys. Rev. B **98**, 165101 (2018).

[226] S. Coleman, *Quantum sine-Gordon equation as the massive Thirring model*, Phys. Rev. D **11**, 2088–2097 (1975).

[227] A. B. Zamolodchikov, *Mass scale In the sine–Gordon model and its reductions*, Int. J. Mod. Phys. A **10**, 1125–1150 (1995).

[228] S. Lukyanov and A. Zamolodchikov, *Form factors of soliton-creating operators in the sine-Gordon model*, Nucl. Phys. B **607**, 437–455 (2001).

[229] G. Mussardo, in *Statistical Field Theory* (Oxford University PressOxford, 2020) pp. 863–881.

[230] A. B. Zamolodchikov, in *Integrable Sys Quantum Field Theory* (Elsevier, 1989) pp. 641–674.

[231] J. K. Asbóth, L. Oroszlány, and A. Pályi, in *A Short Course on Topological Insulators* (Springer International Publishing, 2016) pp. 55–68.

[232] V. E. Korepin, N. M. Bogoliubov, and A. G. Izergin, *Quantum Inverse Scattering Method and Correlation Functions* (Cambridge University Press, 1993).

[233] G. Mussardo, in *Statistical Field Theory* (Oxford University PressOxford, 2009) pp. 605–654.

[234] F. A. Smirnov, *Form Factors in Completely Integrable Models of Quantum Field Theory*, Vol. 14 (World Scientific, 1992).

[235] P. Goodard, A. Kent, and D. Olive, *Virasoro algebras and coset space models*, Phys. Lett. B **152**, 88–92 (1985).

[236] P. Goddard, A. Kent, and D. Olive, *Unitary representations of the Virasoro and super-Virasoro algebras*, Comm. Math. Phys. **103**, 105–119 (1986).

[237] V. Fateev, *The exact relations between the coupling constants and the masses of particles for the integrable perturbed conformal field theories*, Phys. Lett. B **324**, 45–51 (1994).

[238] G. Mussardo, in *Statistical Field Theory* (Oxford University PressOxford, 2009) Chap. 19, pp. 655–688.

[239] J. Cardy, *Scaling and Renormalization in Statistical Physics* (Cambridge University Press, 1996).

[240] J. C. Collins, in *Renormalization* (Cambridge University Press, 1984) Chap. 3, pp. 38–61.

[241] N. G. de Bruijn, *Algebraic theory of Penrose's non-periodic tilings of the plane. II*, Indagationes Mathematicae (Proceedings) **84**, 53 – 66 (1981).

[242] M. de Boissieu, *Ted Janssen and aperiodic crystals*, Act. Crystall. Sect. A **75(Pt 2)**, 273–280. (2019).

[243] T. Janssen, *Crystallography of quasi-crystals*, Act. Crystall. Sect. A **42**, 261–271 (1986).

[244] L. Bindi, P. J. Steinhardt, N. Yao, and P. J. Lu, *Natural Quasicrystals*, Science **324**, 1306–1309 (2009).

[245] F. Flicker and J. van Wezel, *One-Dimensional Quasicrystals from Incommensurate Charge Order*, Phys. Rev. Lett. **115**, 236401 (2015).

[246] M. Kohmoto and J. Banavar, *Quasiperiodic Lattice: Electronic Properties, Phonon Properties, and Diffusion*, Phys. Rev. B **34**, 563–566 (1986).

[247] N. Macé, A. Jagannathan, and F. Piéchon, *Fractal dimensions of wave functions and local spectral measures on the Fibonacci chain*, Phys. Rev. B **93**, 205153 (2016).

[248] E. Levy, A. Barak, A. Fisher, and E. Akkermans, *Topological properties of Fibonacci quasicrystals : A scattering analysis of Chern numbers*, arXiv:1509.04028 (2016).

[249] G. Rai, S. Haas, and A. Jagannathan, *Proximity effect in a superconductor-quasicrystal hybrid ring*, Phys. Rev. B **100**, 165121 (2019).

[250] G. Rai, S. Haas, and A. Jagannathan, *Superconducting proximity effect and order parameter fluctuations in disordered and quasiperiodic systems*, Phys. Rev. B **102**, 134211 (2020).

[251] G. G. Naumis and J. L. Aragón, *Substitutional disorder in a Fibonacci chain: Resonant eigenstates and instability of the spectrum*, Phys. Rev. B **54**, 15079–15085 (1996).

[252] A. Jagannathan, P. Jeena, and M. Tarzia, *Nonmonotonic crossover and scaling behavior in a disordered one-dimensional quasicrystal*, Phys. Rev. B **99**, 54203 (2019).

[253] A. Jagannathan and M. Tarzia, *Re-entrance and localization phenomena in disordered Fibonacci chains*, Eur. Phys. J. B **93** (2020).

[254] F. Piéchon, M. Benakli, and A. Jagannathan, *Analytical Results for Scaling Properties of the Spectrum of the Fibonacci Chain*, Phys. Rev. Lett. **74**, 5248–5251 (1995).

[255] T. C. Halsey, M. H. Jensen, L. P. Kadanoff, I. Procaccia, and B. I. Shraiman, *Fractal measures and their singularities: The characterization of strange sets*, Phys. Rev. A **33**, 1141–1151 (1986).

[256] A. Brauer, *On algebraic equations with all but one root in the interior of the unit circle. To my teacher and former colleague Erhard Schmidt on his 75th birthday*, Mathematische Nachrichten **4**, 250–257 (1950).

[257] G. Rauzy, *Nombres algébriques et substitutions*, Bull. Soc. Math. France **79**, 147–178 (1982).

[258] M. Janssen, *Multifractal analysis of broadly-distributed observables at criticality*, Int. J. Mod. Phys. B **08**, 943–984 (1994).

[259] H. Hentschel and I. Procaccia, *The infinite number of generalized dimensions of fractals and strange attractors*, Physica D: Nonlinear Phenomena **8**, 435–444 (1983).

[260] P. Grassberger and I. Procaccia, *Dimensions and entropies of strange attractors from a fluctuating dynamics approach*, Physica D: Nonlinear Phenomena **13**, 34–54 (1984).

[261] D. A. Moreira, E. L. Albuquerque, and C. G. Bezerra, *Specific heat spectra for quasiperiodic ladder sequences*, Eur. Phys. J. B **54**, 393–398 (2006).

[262] B. Pal and A. Chakrabarti, *Absolutely continuous energy bands in the electronic spectrum of quasiperiodic ladder networks*, Physica E **60**, 188–195 (2014).

[263] A. Mukherjee, A. Nandy, and A. Chakrabarti, *Controlled delocalization of electronic states in a multi-strand quasiperiodic lattice*, Eur. Phys. J. B **90**, 52 (2017).

[264] M. Saha and S. K. Maiti, *Particle current rectification in a quasi-periodic double-stranded ladder*, J. Phys. D **52**, 465304 (2019).

[265] S. Roy, S. K. Maiti, L. M. Pérez, J. H. O. Silva, and D. Laroze, *Localization Properties of a Quasiperiodic Ladder under Physical Gain and Loss: Tuning of Critical Points, Mixed-Phase Zone and Mobility Edge*, Materials **15**, 597 (2022).

[266] E. Kilic, *The Binet formula, sums and representations of generalized Fibonacci p-numbers*, Eur. J. Comb. **29**, 701–711 (2008).

[267] M. Kohmoto, L. P. Kadanoff, and C. Tang, *Localization Problem in One Dimension: Mapping and Escape*, Phys. Rev. Lett. **50**, 1870–1872 (1983).

[268] E. Lazo, in *Instabilities and Nonequilibrium Structures VI. Nonlinear Phenomena and Complex Systems*, Vol. 5 (Springer, Dordrecht, 2000) pp. 387–392.

[269] P. Archambault and C. Janot, *Thermal Conductivity of Quasicrystals and Associated Processes*, MRS Bull. **22**, 48–53 (1997).

[270] C. Janot, *The Properties and Applications of Quasicrystals*, Europhys. News **27**, 60–64 (1996).

[271] A. Sütő, *Singular continuous spectrum on a cantor set of zero Lebesgue measure for the Fibonacci Hamiltonian*, J. Stat. Phys. **56**, 525–531 (1989).

[272] A. Ramachandran, C. Danieli, and S. Flach, in *Fano Resonances in Optics and Microwaves* (Springer, 2018) pp. 311–329.

[273] D. Leykam, A. Andreanov, and S. Flach, *Artificial flat band systems: from lattice models to experiments*, Adv. Phys. X **3**, 1473052 (2018).

[274] D. Leykam, J. D. Bodyfelt, A. S. Desyatnikov, and S. Flach, *Localization of weakly disordered flat band states*, Eur. Phys. J. B **90**, 1 (2017).

[275] A. Mielke, *Pair Formation of Hard Core Bosons in Flat Band Systems*, J. Stat. Phys. **171**, 679–695 (2018).

[276] P. Pudleiner and A. Mielke, *Interacting bosons in two-dimensional flat band systems*, Eur. Phys. J. B **88**, 207 (2015).

[277] S. Takayoshi, H. Katsura, N. Watanabe, and H. Aoki, *Phase diagram and pair Tomonaga-Luttinger liquid in a Bose-Hubbard model with flat bands*, Phys. Rev. A **88**, 063613 (2013).

[278] B. Grémaud and G. G. Batrouni, *Haldane phase on the sawtooth lattice: Edge states, entanglement spectrum, and the flat band*, Phys. Rev. B **95**, 165131 (2017).

[279] M. Shayegan, *Wigner crystals in flat band 2D electron systems*, Nat. Rev. Phys. **4**, 212–213 (2022).

[280] M. R. Slot, T. S. Gardenier, P. H. Jacobse, G. C. P. van Miert, S. N. Kempkes, S. J. M. Zevenhuizen, C. M. Smith, D. Vanmaekelbergh, and I. Swart, *Experimental realization and characterization of an electronic Lieb lattice*, Nat. Phys. **13**, 672–676 (2017).

[281] R. Drost, T. Ojanen, A. Harju, and P. Liljeroth, *Topological states in engineered atomic lattices*, Nat. Phys. **13**, 668–671 (2017).

[282] R. A. Vicencio, C. Cantillano, L. Morales-Inostroza, B. Real, C. Mejía-Cortés, S. Weimann, A. Szameit, and M. I. Molina, *Observation of Localized States in Lieb Photonic Lattices*, Phys. Rev. Lett. **114**, 245503 (2015).

[283] S. Mukherjee, A. Spracklen, D. Choudhury, N. Goldman, P. Öhberg, E. Andersson, and R. R. Thomson, *Observation of a Localized Flat-Band State in a Photonic Lieb Lattice*, Phys. Rev. Lett. **114**, 245504 (2015).

[284] S. Kajiwara, Y. Urade, Y. Nakata, T. Nakanishi, and M. Kitano, *Observation of a nonradiative flat band for spoof surface plasmons in a metallic Lieb lattice*, Phys. Rev. B **93**, 075126 (2016).

[285] S. Taie, H. Ozawa, T. Ichinose, T. Nishio, S. Nakajima, and Y. Takahashi, *Coherent driving and freezing of bosonic matter wave in an optical Lieb lattice*, Sci. Adv. **1**, 10.1126/sciadv.1500854 (2015).

[286] S. Taie, T. Ichinose, H. Ozawa, and Y. Takahashi, *Spatial adiabatic passage of massive quantum particles in an optical Lieb lattice*, Nat. Comm. **11**, 257 (2020).

[287] S. Peotta and P. Törmä, *Superfluidity in topologically nontrivial flat bands*, Nat. Comm. **6**, 8944 (2015).

[288] A. Julku, S. Peotta, T. I. Vanhala, D.-H. Kim, and P. Törmä, *Geometric Origin of Superfluidity in the Lieb-Lattice Flat Band*, Phys. Rev. Lett. **117**, 045303 (2016).

[289] K. Kobayashi, M. Okumura, S. Yamada, M. Machida, and H. Aoki, *Superconductivity in repulsively interacting fermions on a diamond chain: Flat-band-induced pairing*, Phys. Rev. B **94**, 214501 (2016).

[290] M. Tovmasyan, S. Peotta, P. Törmä, and S. D. Huber, *Effective theory and emergent SU(2) symmetry in the flat bands of attractive Hubbard models*, Phys. Rev. B **94**, 245149 (2016).

[291] L. Liang, T. I. Vanhala, S. Peotta, T. Siro, A. Harju, and P. Törmä, *Band geometry, Berry curvature, and superfluid weight*, Phys. Rev. B **95**, 024515 (2017).

[292] W. Maimaiti, A. Andreanov, H. C. Park, O. Gendelman, and S. Flach, *Compact localized states and flat-band generators in one dimension*, Phys. Rev. B **95**, 115135 (2017).

[293] J.-W. Rhim and B.-J. Yang, *Singular flat bands*, Adv. Phys. X **6**, 10.1080/23746149.2021.1901606 (2021).

[294] J.-W. Rhim and B.-J. Yang, *Classification of flat bands according to the band-crossing singularity of Bloch wave functions*, Phys. Rev. B **99**, 045107 (2019).

[295] M. Röntgen, C. Morfonios, I. Brouzos, F. Diakonos, and P. Schmelcher, *Quantum Network Transfer and Storage with Compact Localized States Induced by Local Symmetries*, Phys. Rev. Lett. **123**, 080504 (2019).

[296] S. N. Kempkes, P. Capiod, S. Ismaili, J. Mulkens, L. Eek, I. Swart, and C. Morais Smith, *Compact localized boundary states in a quasi-1D electronic diamond-necklace chain*, Quantum Front. **2**, 1 (2023).

[297] R. A. Vicencio and C. Mejía-Cortés, *Diffraction-free image transmission in kagome photonic lattices*, J. Opt. **16**, 015706 (2014).

[298] E. H. Lieb, *Two theorems on the Hubbard model*, Phys. Rev. Lett. **62**, 1201–1204 (1989).

[299] S. Flach, D. Leykam, J. D. Bodyfelt, P. Matthies, and A. S. Desyatnikov, *Detangling flat bands into Fano lattices*, Europhys. Lett. **105**, 30001 (2014).

[300] B. Sutherland, *Localization of electronic wave functions due to local topology*, Phys. Rev. B **34**, 5208–5211 (1986).

[301] H. Ha and B.-J. Yang, *Macroscopically degenerate localized zero-energy states of quasicrystalline bilayer systems in the strong coupling limit*, Phys. Rev. B **104**, 165112 (2021).

[302] M. Kohmoto and B. Sutherland, *Electronic and vibrational modes on a Penrose lattice: Localized states and band structure*, Phys. Rev. B **34**, 3849–3853 (1986).

[303] S. Ryu, A. P. Schnyder, A. Furusaki, and A. W. W. Ludwig, *Topological insulators and superconductors: tenfold way and dimensional hierarchy*, New J. Phys. **12**, 065010 (2010).

[304] A. Agarwala and V. B. Shenoy, *Topological Insulators in Amorphous Systems*, Phys. Rev. Lett. **118**, 236402 (2017).

[305] A. G. Grushin, in *Low-Temperature Thermal and Vibrational Properties of Disordered Solids* (WORLD SCIENTIFIC (EUROPE), 2022) pp. 435–486.

[306] S.-g. Cheng, Y. Wu, H. Jiang, Q.-F. Sun, and X. C. Xie, *Transport measurement of fractional charges in topological models*, npj Quantum Mater. **8**, 30 (2023).

[307] W. Kohn, *Analytic Properties of Bloch Waves and Wannier Functions*, Phys. Rev. **115**, 809–821 (1959).

[308] K. A. Madsen, E. J. Bergholtz, and P. W. Brouwer, *Topological equivalence of crystal and quasicrystal band structures*, Phys. Rev. B **88**, 125118 (2013).

[309] R. B. Laughlin, *Quantized Hall conductivity in two dimensions*, Phys. Rev. B **23**, 5632–5633 (1981).

[310] D. J. Thouless, *Quantization of particle transport*, Phys. Rev. B **27**, 6083–6087 (1983).

[311] M. J. Rice and E. J. Mele, *Elementary Excitations of a Linearly Conjugated Diatomic Polymer*, Phys. Rev. Lett. **49**, 1455–1459 (1982).

[312] T. A. Loring and M. B. Hastings, *Disordered topological insulators via C*-algebras*, Europhys. Lett. **92**, 67004 (2010).

[313] M. B. Hastings and T. A. Loring, *Almost commuting matrices, localized Wannier functions, and the quantum Hall effect*, J. Math. Phys. **51**, 15214 (2010).

[314] B. Tan and Z. Y. Wen, *Some properties of the Tribonacci sequence*, Eur. J. Comb. **28**, 1703–1719 (2007).

[315] B. Bradlyn and M. Iraola, *Lecture notes on Berry phases and topology*, SciPost Physics Lecture Notes , 51 (2022).

[316] G. Rai, H. Schlömer, C. Matsumura, S. Haas, and A. Jagannathan, *Bulk topological signatures of a quasicrystal*, Phys. Rev. B **104**, 184202 (2021).

[317] J. Kellendonk and E. Prodan, *Bulk–Boundary Correspondence for Sturmian Kohmoto-Like Models*, Ann. Henri Poincaré **20**, 2039–2070 (2019).

[318] J. P. Allouche, *Schrödinger operators with Rudin-Shapiro potentials are not palindromic*, J. Math. Phys. **38**, 1843–1848 (1997).

[319] R. Resta, *Macroscopic polarization in crystalline dielectrics: the geometric phase approach*, Rev. Mod. Phys. **66**, 899–915 (1994).

[320] S.-A. Cheong and C. L. Henley, *Many-body density matrices for free fermions*, Phys. Rev. B **69**, 075111 (2004).